Multi–Objective Optimization Framework For Wave Energy Farms Combining Machine Learning, Genetic Algorithms And Numerical Modeling

Felipe Teixeira Duarte

PH.D. THESIS PRESENTED TO THE
FACULTY OF ENGINEERING OF THE UNIVERSITY OF PORTO

Doctoral Program in Civil Engineering
Hydraulics, Water Resources and Environment

Supervisor: Prof. Francisco de Almeida Taveira Pinto

Co–Supervisor: Prof. Paulo Jorge Rosa Santos

PORTO, SEPTEMBER 11, 2025

DOUTORAMENTO EM ENGENHARIA CIVIL 2024/2025

DEPARTAMENTO DE ENGENHARIA CIVIL E GEORRECURSOS

Tel. +351–22–508 1901

Fax +351–22–508 1446

✉ prodec@fe.up.pt

Edited by

FACULDADE DE ENGENHARIA DA UNIVERSIDADE DO PORTO

Rua Dr. Roberto Frias

4200–465 PORTO

Portugal

Tel. +351–22–508 1400

Fax +351–22–508 1440

✉ feup@fe.up.pt

http://www.fe.up.pt

MULTI–OBJECTIVE OPTIMIZATION FRAMEWORK FOR WAVE ENERGY FARMS COMBINING MACHINE LEARNING, GENETIC ALGORITHMS AND NUMERICAL MODELING

FELIPE TEIXEIRA DUARTE

DOCTORAL PROGRAM IN CIVIL ENGINEERING

SEPTEMBER 11, 2025

ABSTRACT

The escalating global demand for energy has intensified the need for sustainable alternatives to fossil fuels. Among the array of renewable energy sources, wave energy stands out as a promising solution, as it offers high energy density and predictability, making it a viable option for consistent power generation. However, the successful implementation of wave energy farms must address several critical factors, including the site selection, grid connectivity, suitable devices, and deploying multiple wave energy converters (WEC) within a farm.

This thesis presents a framework for optimizing the layout of WECs farms, integrating multi–objective approaches to enhance energy production while addressing environmental constraints. The traditional optimization strategies often emphasize single objectives, such as maximizing energy output or cost–efficiency. This research introduces a novel, dynamic, continuous–domain methodology combining hydrodynamic modeling with advanced optimization techniques to achieve more balanced and sustainable solutions for offshore energy systems. The framework is built on three pillars: representative sea–state selection, fitness function definition, and multi–objective genetic algorithm (GA) optimization. Representative sea states are identified using statistical analysis and machine learning techniques, ensuring computational efficiency while preserving wave energy. The fitness function incorporates environmental impacts, and energy production metrics to evaluate layouts holistically. A customized GA was developed, leveraging domain–specific operators and the SNL–SWAN hydrodynamic model to optimize WEC placement in a continuous domain, enhancing flexibility and solution quality.

Case studies demonstrate the framework's adaptability across offshore and nearshore environments. For offshore farms, the methodology optimized layouts for co–located wind–wave energy parks. Nearshore applications highlighted the potential for shoreline erosion mitigation through targeted WEC placement, balancing energy production with coastal protection. These applications underscore the versatility of the framework in addressing diverse stakeholder priorities and site–specific constraints. Key innovations include the integration of k–means clustering for efficient sea–state representation, significantly reducing computational demands, and the implementation of a continuous optimization domain. This approach overcomes the limitations of grid–based methods, allowing for more nuanced and realistic solutions. Sensitivity analyses reveal the critical role of wave distribution, device spacing, and WEC positioning in optimizing energy capture and environmental outcomes, highlighting the importance of trade–offs in multi–objective optimization.

The framework's effectiveness was evaluated through rigorous testing under varying boundary conditions, device types, and environmental settings. By harmonizing energy generation with environmental sustainability, the research provides valuable insights for stakeholders, policymakers, and researchers in the field of renewable marine energy. Additionally, the open–source implementation promotes reproducibility and facilitates further research on WEC farm optimization and coastal morphodynamic evolution, contributing to a future powered by clean and reliable ocean energy.

KEYWORDS:

Marine renewable energy; Wave energy converter; Numerical modelling; Layout optimization; Genetic algorithm; SNL–SWAN; Co–located wave–wind energy farms; k–means.

RESUMO

A crescente procura global por energia tem intensificado a necessidade de alternativas sustentáveis aos combustíveis fósseis. Entre as diversas fontes de energia renovável, a energia das ondas destaca–se como uma solução promissora, devido à sua elevada densidade energética e previsibilidade, tornando–a uma opção viável para a geração consistente de energia. No entanto, a implementação bem–sucedida de parques de energia das ondas exige a consideração de diversos fatores críticos, incluindo a seleção do local, a ligação à rede, a escolha de dispositivos adequados e a implementação de múltiplos conversores de energia das ondas (WEC) num parque.

Esta tese apresenta uma nova metodologia para a otimização do *layout* de parques de WEC, integrando abordagens multiobjectivo para maximizar a produção de energia elétrica, ao mesmo tempo que são consideradas restrições ambientais. As estratégias mais tradicionais de otimização frequentemente têm objetivos únicos (e.g., a maximização da produção de energia ou a redução de custos). Esta investigação introduz uma metodologia dinâmica, que considera um domínio espacial contínuo e combina modelação hidrodinâmica com técnicas avançadas de otimização, de forma a alcançar soluções mais equilibradas e sustentáveis para os sistemas energéticos *offshore*. A metodologia é sustentada por três pilares: seleção de estados de mar representativos, definição da função de fitness e otimização por algoritmo genético (GA) multiobjectivo. Os estados de mar representativos são identificados através de análises estatísticas e técnicas de aprendizagem automática, assegurando eficiência computacional e preservando a energia dos estados de mar. A função de fitness incorpora impactos ambientais e métricas de produção de energia para avaliar os layouts de forma holística. Um GA personalizado foi desenvolvido, utilizando operadores específicos do domínio e o modelo hidrodinâmico SNL–SWAN para otimizar a colocação dos WEC num domínio contínuo, aumentando a flexibilidade e a qualidade das soluções.

Os estudos de caso demonstram a adaptabilidade da metodologia a ambientes *offshore* e costeiros. Para parques *offshore*, a metodologia otimizou *layouts* de parques de energia eólica–ondas integrados. As aplicações costeiras destacaram o potencial desses parques na mitigação da erosão costeira através da colocação estratégica de WEC, equilibrando a produção de energia elétrica com a proteção costeira. Estas aplicações sublinham a versatilidade da metodologia na abordagem das prioridades de diferentes *stakeholders* (partes interessadas), assim como as restrições específicas do local. Entre as principais inovações, destaca–se a integração do agrupamento k–means para representação eficiente dos estados de mar, reduzindo significativamente as exigências computacionais, e a implementação de um domínio espacial de otimização contínuo. Esta abordagem supera as limitações dos métodos baseados em grelha, permitindo soluções mais detalhadas e realistas. As análises de sensibilidade revelam o papel crítico da distribuição do recurso energético das ondas, do espaçamento entre dispositivos e da posição dos WEC na otimização da captura de energia e resultados ambientais, evidenciando a importância de estabelecer compromissos em otimizações multiobjectivo.

A eficácia da metodologia foi avaliada através de testes rigorosos para diferentes condições de fronteira, tipos de dispositivos e restrições ambientais. Ao harmonizar a geração de energia com a sustentabilidade ambiental, esta investigação fornece informações valiosas para *stakeholders*, definidores de políticas e investigadores a trabalhar na área da energia marinha renovável. Adicionalmente, a implementação de código aberto promove a reprodutibilidade e facilita futuras investigações sobre a otimização de parques de WEC e a evolução morfodinâmica costeira, contribuindo para um futuro alimentado por energia mais limpa e confiável proveniente dos oceanos.

PALAVRAS–CHAVE:

Energia renovável marinha; Conversor de energia das ondas; Modelação numérica; Otimização de layout; Algoritmo genético; SNL–SWAN; Parques de energia eólica–ondas co–localizados; k–means.

Para Bernardo, Henrique e Gustavo

For neither good nor evil can last forever;

and so it follows that as evil has lasted a long time,

good must now be close at hand.

Miguel de Cervantes (Don Quixote de la Mancha)

“One cannot prove anything here, but it is possible to be convinced.'

Fyodor Dostoevsky (1821-1881)

ACKNOWLEDGMENTS

Pursuing a PhD is a journey marked by immense challenges, sacrifices, and personal growth. It is a path that demands relentless dedication, resilience, and an unwavering commitment to the pursuit of knowledge. Along the way, there are moments of uncertainty, long hours of work, and the constant balancing of professional ambitions with personal responsibilities. Achieving this milestone requires not only intellectual effort but also the support and understanding of those around us. Reflecting on this journey, I recognize the sacrifices made, the obstacles overcome, and the invaluable contributions of the people and institutions that have shaped this achievement. I wish to express my heartfelt gratitude to all those who contributed to this achievement.

First, I extend my deepest thanks to my supervisor, Professor Doctor Francisco Taveira Pinto, and my co-supervisor, Professor Doctor Paulo Rosa Santos. Your unwavering belief in my capabilities, insightful guidance, and numerous reviews throughout this process were instrumental in shaping this thesis. Your mentorship has been a cornerstone of my academic growth, and for that, I am profoundly grateful.

I am immensely grateful to my family, whose love and support made this journey possible. To my wife, Glayds, and my wonderful sons, Bernardo, Henrique, and Gustavo. Your love, patience, and support have been my greatest source of strength and motivation. To my father, José Ernesto, and my mother, Maria Bernarda, thank you for instilling in me the values of perseverance and dedication. This achievement is as much yours as it is mine.

I am also grateful to my colleagues Victor Ramos, Daniel Clemente, and Gianmaria Giannini. Your collaboration, encouragement, and camaraderie were invaluable in navigating the challenges of academic research and writing. To the members of the NEMAR group, thank you for your constant support, insightful discussions, and willingness to help whenever needed.

I would like to acknowledge the Faculty of Engineering of the University of Porto (FEUP) and the Interdisciplinary Centre of Marine and Environmental Research (CIIMAR) for providing an excellent environment for research and academic development.

Special thanks to the Portuguese Foundation for Science and Technology (FCT) for funding this research through the Ph.D. scholarship with reference 2020.09157.BD. I am also thankful for the support provided by the projects ATLANTIDA - Platform for the monitoring of the North Atlantic Ocean and tools for the sustainable exploitation of the marine resources (NORTE-01-0145-FEDER-000040) and HYDEA - Boosting the hydrogen transition in the Atlantic Area ports, funded by the European Union under the Interreg Atlantic Area Programme 2021-2027.

To all those who have supported me, directly or indirectly, along this journey, I express my sincere gratitude. This milestone is a testament to the collective efforts and encouragement I have received, and I carry each of you in my heart as I embark on the next chapter of my professional life.

Thank you all for being part of this journey.

NOMENCLATURE

ABBREVIATIONS

Abs	Absorption
AEP	Annual Energy Production
AI	Artificial Intelligence
AOI	Area Of Interest
ANN	Artificial Neural Networks
AWS	Archimedes Wave Swing
AWT_k	Percentage of Accessible Wind Turbines during a given percentage of time
BEM	Boundary element methods
BLI	Bed Level Impact
BLV	Level Variation Indicator
B–OF	Bottom–fixed Oscillating Flap
CaPEX	Capital Expenditure
CEA	Cumulative Eroded Area
CFD	Computational fluid dynamics
CI	Computational Intelligence
CMA–ES	Covariance matrix adaptation–based evolutionary strategy
CoV	coefficient of variation
CPU	Central Processing Unit
CRF	Capital Recovery Factor
CWR	Capture Width Ratio
DE	Differential evolution algorithm
DGRM	Directorate–General for Natural Resources, Safety and Maritime Services
DIA	Discrete Interaction Approximation
DOF	Directions of Freedom
DtN	Dirichlet–to–Neumann
E	East
EA	Evolutionary Algorithms
ECMWF	European Centre for Medium–Range Weather Forecasts
EI	Erosion Impact
ENE	East–Northeast
ERA5	ECMWF Reanalysis v5
ESE	East–Southeast
FEA	Beach Face Eroded Area
FSI	Fluid–structure interaction
FVM	Finite–volume method
FWT	Floating Wind Turbines
GA	Genetic Algorithm
GEBCO	The General Bathymetric Chart of the Oceans
GMM	Gaussian Mixture models
GSO	Glowworm swarm optimization

HCCA	Hybrid cooperative co–evolution algorithm
HI	Hydrographic Institute
HRF	Significant Wave Height Reduction within the Farm
HRA	Significant wave height reduction in the area of interest index
IHO	International Hydrographic Organization
IOC	Intergovernmental Oceanographic Commission
LCoE	Levelized Cost of Energy
LMM	lateral mobile modules
MAPE	Mean Absolute Percentage Error
MODE	Multi–Objective Differential Evolution Algorithm
N	North
NE	Northeast
NER	Non–dimensional Erosion
NDA	Non–uniformly Distributed Arrays
NLSW	Non–hydrostatic, nonlinear shallow water equations
NNE	North–Northeast
NNW	North–Northwest
NOMAD	Mesh Adaptive Direct Search algorithm
NSE	Navier–Stokes equation
NSEM	Navier–Stokes equation model
NSWE	Nonlinear Shallow Water Equation
NW	Northwest
NWT	Numerical Wave Tank
O&M	Operation and Maintenance
OpEX	Operating Expenses
OWC	Oscillation water columns
OWSC	Oscillating wave surge converter
OWT	Offshore Wind Turbine
PDA	Peripherally Distributed Arrays
PSO	Particle Swarm Optimization
PTO	Power–Take–off
RANS	Reynolds Averaged Navier–Stokes
RAO	Response Amplitude Operators
RCW	Relative Capture Width
RMS	Root mean square
RMSE	Root mean squared error
RNI	Average Relative Nearshore Impact
RWP	Reduction of Wave Energy Potential
P2M	Peak–to–Mean index
S	South
SE	Southeast
SED	Squared Euclidean distances
SHRHA	Hydraulics, Water Resources and Environment Division
SIMAR	Spanish Port Authority (*Puertos del Estado*)

SNL	Sandia National Laboratory
SPH	Smoothed Particle Hydrodynamics
SQP	Sequential quadratic programming
SSE	South–Southeast
SSW	South–Southwest
Std	Standard Deviation
SW	Southwest
SWAN	Simulating WAves Nearshore
TRL	Technology Readiness Level
UDA	Uniformly Distributed Arrays
VBGMM	Variational Bayesian Gaussian Mixture models
WEC	Wave Energy Converter
WFA	WindFloat Atlantic wind turbines
WLA	Wave Energy Park Layout Assessment Index
W	West
WNW	West–Northwest
WSW	West–Southwest

SYMBOLS

a	Wave amplitude
A	Area
C	Wave phase velocity
C_b	bottom friction coefficient
C_g	Wave group velocity
D	Device characteristic width
$E(\sigma,\theta)$	Variance density spectrum
E_p	Potential energy
E_k	Kinetic energy
$\vec{F}$	Resulting Forces
g	Gravitational acceleration
h	Water depth
H	Wave Height
H_s	Significant Wave Height
Hs_i	H_s of baseline, scenario without WECs
Hs_{wec_i}	H_s of scenario with WECs for each i position of wind turbines
J	Wave power (energy flux) per meter of wave front
$J_b^{20}(s,t)$	Wave power per meter of wave front at 20 m depth without WEC farm
$J_{f,i}^{20}(s,t)$	Wave power per meter of wave front at 20 m depth with WEC farm
J_x	Wave power x component
J_y	Wave power y component
k	Wave number
k_c	Cluster
K_t	Transmission coefficient
m_i	Coefficient of linear term of the i curve
$N(\sigma,\theta)$	Wave action density
N	Total number of data values
N_c	Total number of data values inside a cluster
$N(x)$	Normalized value of x
p	WLA weight for energy production
P	Pressure
P_{abs}	Wave power captured by the WEC
P_{array}	Power of a wave farm
$P_{centroid}$	Wave energy per wave front for each sea state
p_d	Dynamic pressure
P_{wec}	Power of an array of WECs
P_i	Incident power
s	WLA weight for shield protection
S_{bfr}	Source term for dissipation due to interaction with the bottom
S_{wc}	Source term for dissipation due to “white–caping”
S_{in}	Source term for atmospheric input from wind
S_{nl}	Source term for nonlinear interactions between spectral components
S_p	Total number of points along the contour

S_{surf}	Source term for depth–induced breaking
S_{tot}	Source term total
T	Period
t	Time
T_b	Access time without WECs
T_e	Wave energy period
T_p	Peak wave period
T_{cf}	Cut–off wave period
T_W	Access time with WECs
U	Magnitude of the velocity in a given direction
u_x	Velocity in x direction
u_y	Velocity in y direction
u_z	Velocity in z direction
U_{rms}	Orbital bottom velocity
U_{10}	Wind speed used is measured at a 10–meter elevation

GREEK SYMBOL

α	Calibration coefficient
β	Power Production Density
γ	Peak enhancement parameter
∇	Gradient
Δb	Bottom slope
Δd	Distance from the first run position
$\Delta T_{O\&M}$	Access Time Increase for O&M
ε	Wave steepness
η	Displacement of the water free surface above the still water level
θ	Wave phase angle
θ_m	Wave propagation direction
λ	Wavelength
μ	Density
π	Number pi
ρ	Mass density
σ	Relative radian frequency
φ_p	Power representativeness
ϕ	Velocity potential
X	Variable of integration
ω	Angular frequency
ω_{cf}	Cut–off wave frequency
$\zeta_b(x, y)$	Seabed level at the point of coordinates (*x,y*) without WEC farm
$\zeta_f(x, y)$	Seabed level at the point of coordinates (*x,y*) with WEC farm

TABLE OF CONTENTS

LIST OF FIGURES

LIST OF TABLES

1

INTRODUCTION

1.1.Scope of the research

The rising demand for energy caused by the growth of a more energy–intensive society associated with higher concerns about the environment boost innovations that could bring alternative sources of energy. The presently most common sources of energy, *i.e.*, the fossil fuels, are limited, nonrenewable, and immensely polluting, having an adverse effect on the environment on a worldwide scale. Nevertheless, a growing number of technologies to produce electricity from renewable and sustainable energy sources are being developed and tested aiming to expand and diversify the present electricity production matrix.

Advancements in the understanding and utilization of the ocean have steadily progressed across various fields, including shipping, transportation, health, industry, and energy. These developments significantly impact marine ecosystems and the Earth's climate system. In the future, the ocean has the potential to emerge as a primary energy source, for instance, through the harvesting of waves and tidal energy, or function as a host for the extraction of other sources like offshore wind and solar energy.

Ocean waves are generated by wind, storing potential and kinetic energy. The total theoretical potential estimated for this resource is of about 32000 TWh per year [1], slightly higher than the world electricity production in 2023 (29479 TWh) [2]. Because of this high potential, the European Commission introduced its Strategy on Offshore Renewable Energy, outlining ambitious targets for ocean energy development. The Strategy aims to support the deployment of 100 MW of ocean energy projects by 2025, scale up to at least 1 GW by 2030, and achieve a long–term goal of 40 GW by 2050 [3]. The effective exploitation of this renewable energy potential will contribute to the reduction of carbon emissions and stimulate economic growth in coastal and remote areas.

Therefore, waves can provide a sustainable, power–dense, predictable, and widely available source of energy, with wave energy converters (WECs) employing multiple principles (*e.g.*, oscillating water column, point absorber, overtopping, and bottom–hinged systems) to transform the kinetic and potential energy of ocean waves into electricity.

In the last decades, more than 1000 technologies for harvesting ocean wave energy have been patented. However, only a few dozen have reached the demonstration phase at sea, and none have yet reached the commercial exploration phase. In other words, it has not reached a technological maturity level that allows it to be competitive with more traditional technologies [1].

Additionally, the high Levelized Cost of Energy (LCoE) caused mainly by immature technologies hinders its progress. Understanding wave farm effects (*e.g.*, diffraction, reflection, radiation) on energy capture and their dependence on WECs' layout is crucial for their optimized design [3], which usually aims to maximize the electrical energy output and eventually explore co–location benefits (*e.g.*, with offshore wind farms), as well as to minimize costs and environmental impacts [4].

The wave energy sector needs to improve its competitiveness by gaining scale. For that purpose, several devices are required to be installed in arrays forming an energy farm/park, which has an impact on the propagation of incident waves. The interaction of WECs with waves results in diffraction, reflection, and radiation phenomena, generating a complex wave field, especially on the lee side of the farm, with potential influence on local and coastal hydro–morphodynamics, as well as on the energy production itself. Constructive or destructive interference can occur with a local decrease in energy in the latter case [5–8]. Therefore, local and regional impacts of marine renewable developments must be well understood as they can interfere with the natural marine environment.

The influence of WEC arrays on the local wave climate affects the flow over the water column and, subsequently, the sediment dynamics. It has been hypothesized that wave height reductions in the lee side of WECs, particularly nearshore, could benefit coastal protection [9–22]. The morphology of the coastline is closely linked to the wave climate, and the requirement for accurate modelling of the effects of WECs has been identified. A change in the longshore littoral transport process can have implications further along a coastline, as well as in the vicinity of a WEC.

Additionally, the integration of WECs into an existing offshore wind park can create a shadow effect by reducing wave heights, and extending the period allocated for the operation and maintenance of wind turbines, thus enhancing the efficiency of wind energy generation [23]. This shadow effect, also known as the park effect, may be affected by the spatial orientation of the park, wave direction and intensity, bathymetry, and the absorption characteristics of the WEC array. Combined wave–wind systems can be classified by technology, water depth, or location relative to the shoreline.

Co–locating wave–wind energy parks may offer benefits such as more effective resource utilization, lower financial expenses, and improved energy output [24]. The combined use of these technologies in the same area can take advantage of potential synergies, such as shadow effects, smoothing of power output, and the sharing of grid infrastructure, operation and maintenance, logistics, and mooring. This may also allow for smooth grid integration and lower installation costs [25,26].

By expanding co–location benefits, offshore wave farms can also serve the purpose of coastal protection through wave attenuation and "*shadowing*" of sensitive shorelines [11,12], leading to lower mean wave heights [27].

Furthermore, as offshore wind technology matures, following a hybridization strategy may accelerate the progress of WECs from the pre–operational stage to a fully functioning wave park. A major focus of present research regarding the hybridization of wave and wind farms is on the coupling of bottom–

fixed or floating wind turbines (FWT) and WECs, as well as on the developments onshore that combine power generation with harbor protection [28,29].

However, the traditional approaches to model offshore farms often oversimplify key aspects. These simplifications include assuming invariant transmission coefficients, fixed power ratings, and limited farm configurations. Additionally, they may neglect local marine space restrictions or utilize a small number of WEC units.

Optimizing the layout of wave farms is complex due to the numerous variables involved (WEC position, array shape), constraints (space available, already allocated areas), and conflicting objectives (energy output vs. costs vs. environment). Current design methods often neglect these aspects, focusing solely on maximizing the energy output [3]. Additionally, computational demands increase significantly with multi–objective functions or high–fidelity wave–WEC interaction models.

With limited field data available, WEC development usually relies on physical and numerical modeling. Numerical modeling, particularly through wave propagation models, is well–suited for assessing multi–variable combinations. These tools can be adapted to forecast local wave climates, wave farm energy outputs, and both near–field and far–field effects [17,30].

Phase–averaged models provide a computationally efficient approach for the simulation of waves and nearshore wave–induced current fields. However, most of them rely on parametrizations to represent WECs and other relevant wave characteristics. A common technique involves representing WECs as porous structures acting as sources or sinks for wave energy extraction [31,32]. The SWAN spectral wave model is widely used and validated for coastal wave transformation modeling. A modified version, SWAN–SNL [33–36], allows for WEC representation as power sinks using device–specific power performance data.

The use of evolutionary algorithms (EAs), specifically genetic algorithms (GAs), provides an efficient solution to this optimization problem. EAs, inspired by natural selection, offer flexible and robust optimization frameworks, with GAs operating on candidate solutions to mimic the survival of the fittest, optimal layout, considering factors like energy output, environmental impact, and economic viability.

Interactions between devices in an array have been a recurring topic of investigation [3,37]. Most studies on the design optimization of wave energy farms have been based on comparisons of some different configurations [3,37]. However, the use of machine learning techniques for optimization schemes is growing, with one example being the evolutionary algorithms, specifically the genetic algorithm, which mimics the process of natural selection and incorporates heredity, mutation, and recombination [38].

1.2.Objectives

This thesis aims to develop a systematic optimization framework for designing multi–purpose offshore wave energy farms. The multi–objective optimization framework will go beyond maximizing electricity production or revenue, by considering the impact of offshore farms on wave climate and other potential uses, such as the co–location with offshore wind farms or coastal protection structures. By incorporating machine learning to define/select representative sea states, a wide range of influencing parameters, and advanced numerical modelling, the optimization framework will be able to predict with reliability the best wave farm layout that balances the electricity generation with the far field wave impacts (positive or negative) making use of genetic algorithms.

To achieve these goals, complementary approaches will be employed. First, a combined method of statistical analysis and machine learning is used for representative sea–state selection. This approach identifies a compact set of sea states that accurately reflects the local wave climate. Second, a custom–designed multi–objective genetic algorithm (GA) optimizes wave farm layouts for the selected number of devices (*i.e.*, WECs). To achieve this, the GA seamlessly integrates environmental impact considerations (defined by the user) and energy production estimation using an automatic routine integrated into the wave numerical model.

1.3. Thesis structure

This thesis is structured to provide a comprehensive overview of the research, from its background and motivation to its findings and conclusions. The report is organized into the following chapters:

- Chapter 2 provides a comprehensive literature review on fundamental topics related to the optimization of offshore WEC farms and their near and far–field effects. Key areas of focus include the resource assessment of offshore renewable energy, an overview of WEC concepts, the theoretical background of water wave mechanics used in numerical modeling, an evaluation of widely utilized numerical models, a discussion of parameters influencing layout optimization, and an examination of existing studies and methodologies for WEC farm layout optimization;
- Chapter 3 outlines the optimization framework developed. It details the numerical models employed, the workflow of the customized genetic algorithm developed for this research, and the simulation parameters used to develop, verify, and demonstrate the model's applicability. This includes a description of the chosen location and the characterization of the devices analyzed in the study;
- Chapter 4 elaborates on the foundational developments required to construct the optimization model. This includes an in–depth comparison of phase–resolving and phase–averaging wave numerical models, the development of a multi–objective assessment tool (fitness function) for the genetic algorithm, and the establishment of a framework to identify representative sea states through machine learning techniques;
- Chapter 5 presents the applications of the novel genetic algorithm developed in this research. It describes the sensitivity analysis conducted to optimize computational costs and convergence rates, the verification of the algorithm through repeated simulations and single–objective runs, and a series of case studies. These case studies encompass an offshore scenario that integrates economic parameters to refine the objective function and two nearshore scenarios, which evaluate the model's performance in achieving coastal protection and minimizing environmental impact;

- Chapter 6 concludes the thesis by summarizing the main findings concerning the research objectives and proposing directions for future developments in this field.

1.4. List of Publications

The following original research papers authored by the thesis author correspond to the chapters of this thesis:

i. Teixeira–Duarte F, Clemente D, Giannini G, Rosa–Santos P, Taveira–Pinto F. Review on layout optimization strategies of offshore parks for wave energy converters. Renewable and Sustainable Energy Reviews 2022;163:112513. https://doi.org/10.1016/J.RSER.2022.112513.

ii. Teixeira–Duarte F, Ramos V, Rosa–Santos P, Taveira–Pinto F. Multi–objective decision tool for the assessment of co–located wave–wind offshore floating energy parks. Ocean Engineering 2024;292:116449. https://doi.org/10.1016/J.OCEANENG.2023.116449.

iii. Teixeira–Duarte F, Rosa–Santos P, Taveira–Pinto F. Multi–objective optimization of co–located wave–wind farm layouts supported by genetic algorithms and numerical models. Renew Energy 2025:122362. https://doi.org/10.1016/J.RENENE.2025.122362

The thesis author also contributed as a co–author to the following papers during the Ph.D. period:

iv. Clemente D, Teixeira–Duarte F, Rosa–Santos P, Taveira–Pinto F. Advancements on Optimization Algorithms Applied to Wave Energy Assessment: An Overview on Wave Climate and Energy Resource. Energies 2023, Vol 16, Page 4660 2023;16:4660. https://doi.org/10.3390/EN16124660.

v. Clemente D, Ramos V, Teixeira–Duarte F, Taveira–Pinto FVC, Rosa–Santos P, Taveira–Pinto F. Assessment of electricity production and coastal protection of a nearshore 500 MW wave farm in the north–western Portuguese coast. Appl Energy 2025;379:124950. https://doi.org/10.1016/J.APENERGY.2024.124950.

vi. Clemente, Daniel; Majidi, Ajab; Margarida–Bento, Ana; Queirós, Beatriz; Teixeira–Duarte, Felipe; Miranda, Filipe; Sarmento, Francisca; *et al*. "Avanços Tecnológicos e o Futuro das Energias Renováveis Marinhas e Proteção Costeira [PT]". In *Argos – Revista do Museu Marítimo de Ílhavo [PT]*, 116–123. Ílhavo, Portugal: Museu Marítimo de Ílhavo [PT], 2025.

2

LITERATURE REVIEW & THEORETICAL BACKGROUND

2.1.Offshore Renewable Energy

Offshore Renewable Energy covers a broad spectrum of renewable energy sources such as ocean waves, tides (tidal streams and tidal range), ocean currents, salinity and thermal gradients, which are extracted directly from ocean waters. Notwithstanding, the ocean space can also be used to explore wind and solar energy as well as to produce biomass than can be later converted into electricity [1]. Figure 1 summarizes the current status (data from 2023) of tidal and wave energy deployment that was prepared by Ocean Energy Europe [39].

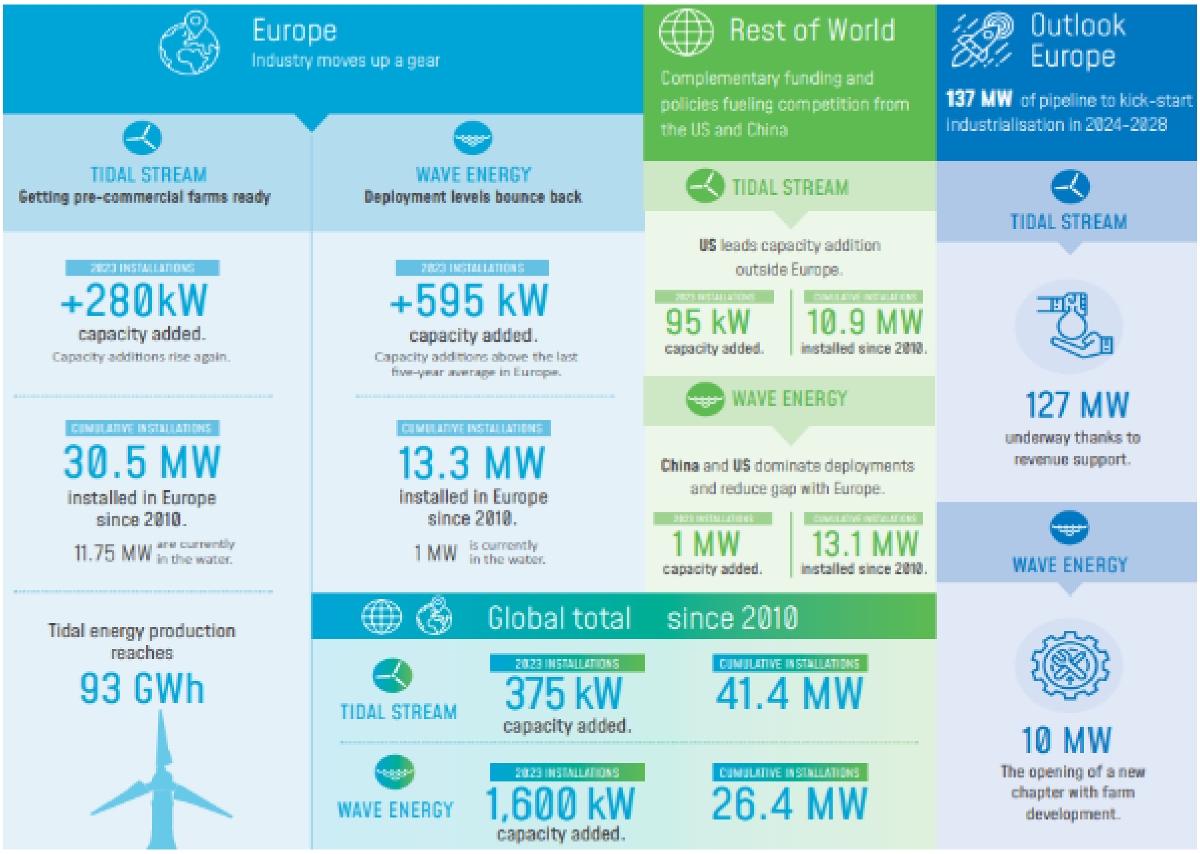

Figure 1 – Ocean energy key trends and statistics 2023, report from Ocean Energy Europe [39].

Offshore wind energy technology has already achieved commercial–scale, with a year–by–year decrease in associated costs. However, there is still a lack of competitiveness when compared, in terms of cost per kWh of electricity produced, with other renewable energy technologies, such as hydropower, solar photovoltaic or onshore wind. Wave and tidal energy technologies are not yet market competitive, being some steps behind, in terms of development, the offshore wind [40]. Since 2010, the overall installed capacity worldwide was circa 26.4 MW for wave energy and circa 41.4 MW for tidal stream energy [39].

2.1.1. Wave energy

Wave energy potential is largely discussed, but despite all research carried out so far, the real potential remains to a certain extent indeterminate. Nevertheless, some credible estimates point to a theoretical potential estimated of about 32000 TWh/yr [1]. Figure 2 presents the annual mean wave power (kWh) around the globe. The wave energy potential is linked to wind characteristics (speed, duration, direction) and the fetch length.

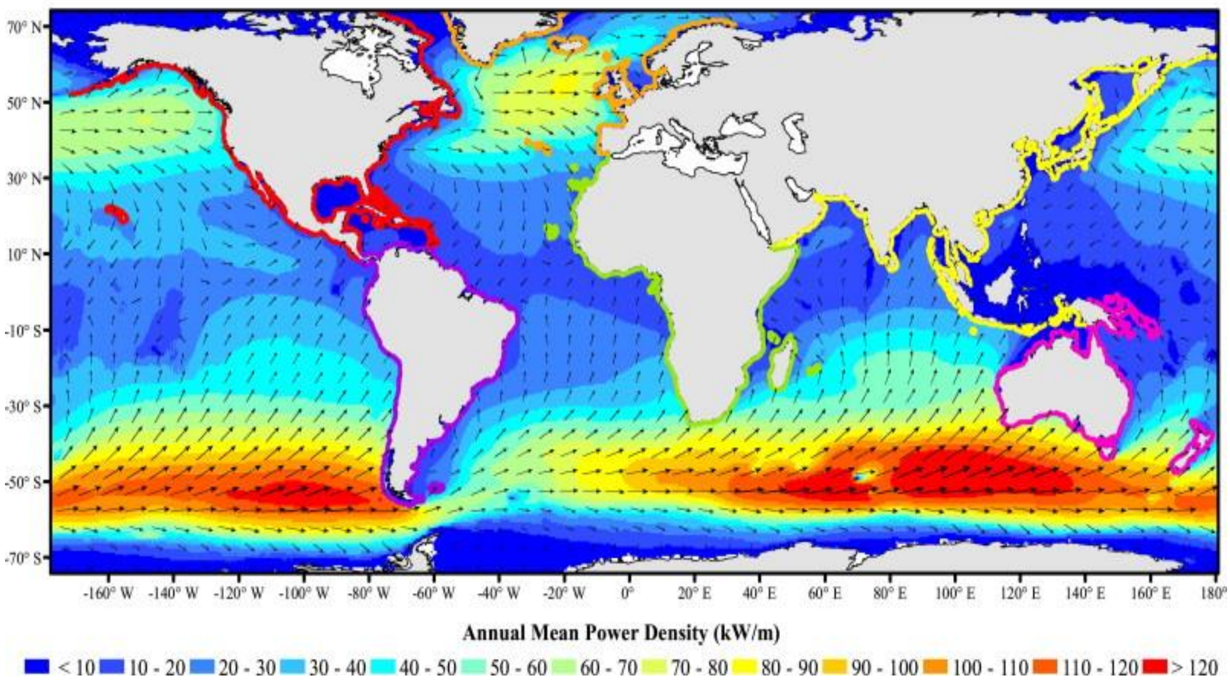

Figure 2 – The global wave energy resource [41].

The wave energy sector is still considered to be at a pre–commercial stage, demanding further research and development, to improve the performance and reliability of wave energy conversion technologies, reduce their overall costs and consequently reduce the Levelized Cost of Energy (LCoE) [1]. Moreover, these technologies also need continued demonstration and validation in real ocean conditions for long periods of time.

Europe concentrates over half of the WEC developments, with most research and development dedicated to point absorbers [42]. Those technologies can be used as independent WECs or as part of breakwaters or harbor infrastructures. At the moment, the number of systems beyond the research and development stage is relatively small, with some point absorbers being developed to be integrated into pilot wave farms for demonstration purposes [43].

It is important to mention that nearly 95% of the energy in an ocean wave is located between the water free surface and a water depth equal to a quarter of its wavelength. This energy could be harvested by several methods, which consequently generate a substantial range of technological developments. Wave energy is extracted essentially from surge, sway and heave modes of motion of the WEC, despite the possibility of conversion through other modes of motion [42].

2.1.2. Wind Energy

Offshore wind energy conversion technologies are increasing their importance globally and already have an important role in the energy systems of several countries (*e.g.*, UK, Belgium and Germany). Wind turbines are becoming more efficient and larger, and consequently increasing their rated power, improving also their cost–effectiveness. Benefitting from constant technology enhancements, the worldwide offshore wind market expanded by approximately 30% per year between 2010 and 2023. In addition, the new projects have capacity factors of 40%–50%, as larger turbines and technology improvements are helping to make the most of available wind resources [44]. These capacity factors are competitive with gas–fired power plants and some coal–fired power plants, and exceed those of traditional onshore wind farms and solar photovoltaic parks.

The rising attraction of building wind farms offshore is supported by their advantages compared with the onshore counterparts, such as: the higher wind power resource offshore results in a higher electricity production when large turbines are used; more constant wind fields offshore; virtually no limitations in the transport of components for the offshore wind farms; and the huge potentially areas available for the installation of wind farms. In addition, the distance from the shore and human settlements minimize the issue of visual and noise impacts. As a result, it is possible to raise efficiency using cheaper or noisier wind turbines, like two–blades and downwind technologies.

The oil and gas industry, as a long and mature user of offshore technologies, was the major developer of the support structure/foundation concepts employed. Therefore, the younger wind industry has taken advantage of existing knowledge and adopted some of them. The typical offshore structure/foundation concepts can be divided in: bottom–mounted structures, rigidly connected to the seabed (*i.e.*, fixed), or floating–support structures with no rigid connections [45]. The solution implemented depends on the local seabed, water depth and financial constraints.

The bottom–mounted structures can be divided in: gravity foundations, monopile foundations and braced support structures, such as tripod and jacket/truss. The concept most commonly used in swallow waters is the monopile foundation (which, is similar to the support of onshore turbines). The gravity foundation is also used on swallow water, but the braced support structures are more appropriate for intermediate waters. Figure 3 represents the evolution of wind turbines' structures/foundations as a function of water depth.

The design requirements of turbine structures for offshore wind farms are generally complex, including aspects like the survivability in the harsh marine environment and the prolonged exposure to large wave loading.

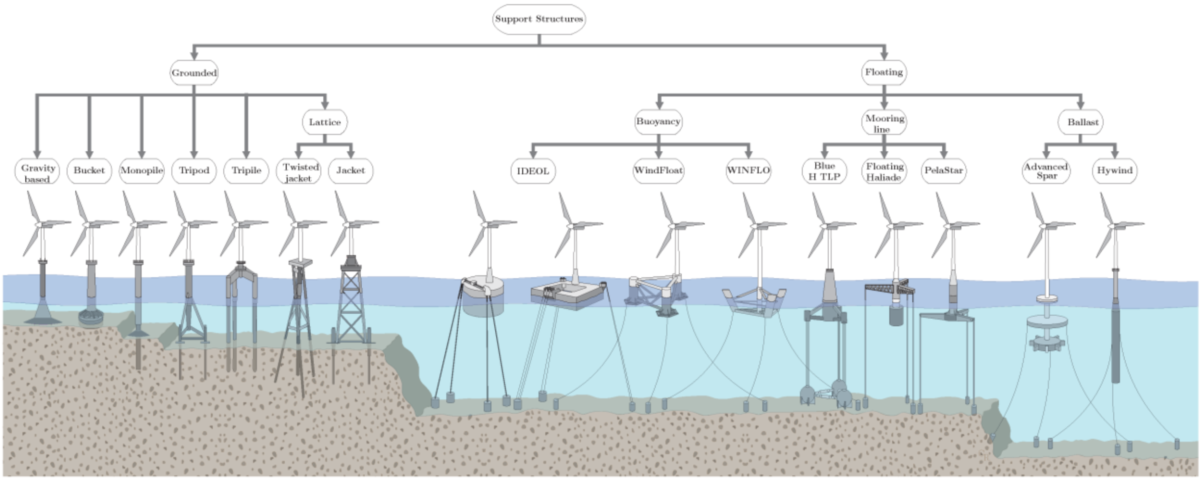

Figure 3 – Support structure/foundation options for OWTs [46].

While fixed structures are more mature given their longest use, floating structures are still at the beginning of their path, with the first full–scale commercial floating wind farm only commissioned in 2017. Floating structures are recommended for large water depths, mainly because the cost of bottom–fixed structures increases with the depth.

The majority of offshore wind farms are currently in China, followed by northern Europe. China alone accounts for more than half of the total offshore wind power capacity installed worldwide, while Europe accounts for about 45%, as can be seen in the Figure 4. A total of 236 MW net floating wind has been installed globally in Norway, the UK, Portugal, China, Japan, France, and Spain [44].

2.1.3. Wave energy converters

Over the years, several alternative ways to classify or categorize wave energy conversion technologies have been proposed. The classification can be made according to: location and water depth; the way wave energy is converted into mechanical energy; position/orientation in relation to wave propagation; or by the technology used.

Wave energy can be harvested onshore, nearshore, or offshore. The wave harvesting principle most used onshore is the oscillating water column (OWC), in which the water free surface oscillation induced by incident waves creates compression and decompression of the air inside a semi–submerged chamber. The air flow produced then rotates an air turbine. In the nearshore and shallow water area, a common solution is the oscillating wave surge converter (OWSC) acting like a pendulum under the wave action. Finally, in offshore regions, there are mainly three types of technologies: the point absorbers, the attenuators, and the overtopping/terminator devices.

The point absorbers have a small size compared to the predominant wavelength [42] (*e.g.*, a buoy, in which the active part moves predominantly along a vertical axis). The attenuators have large horizontal extensions oriented in parallel to the wave direction, gradually generating energy as the wave passes through the system length. The terminator devices have a large horizontal extension perpendicular to the wave direction [42].

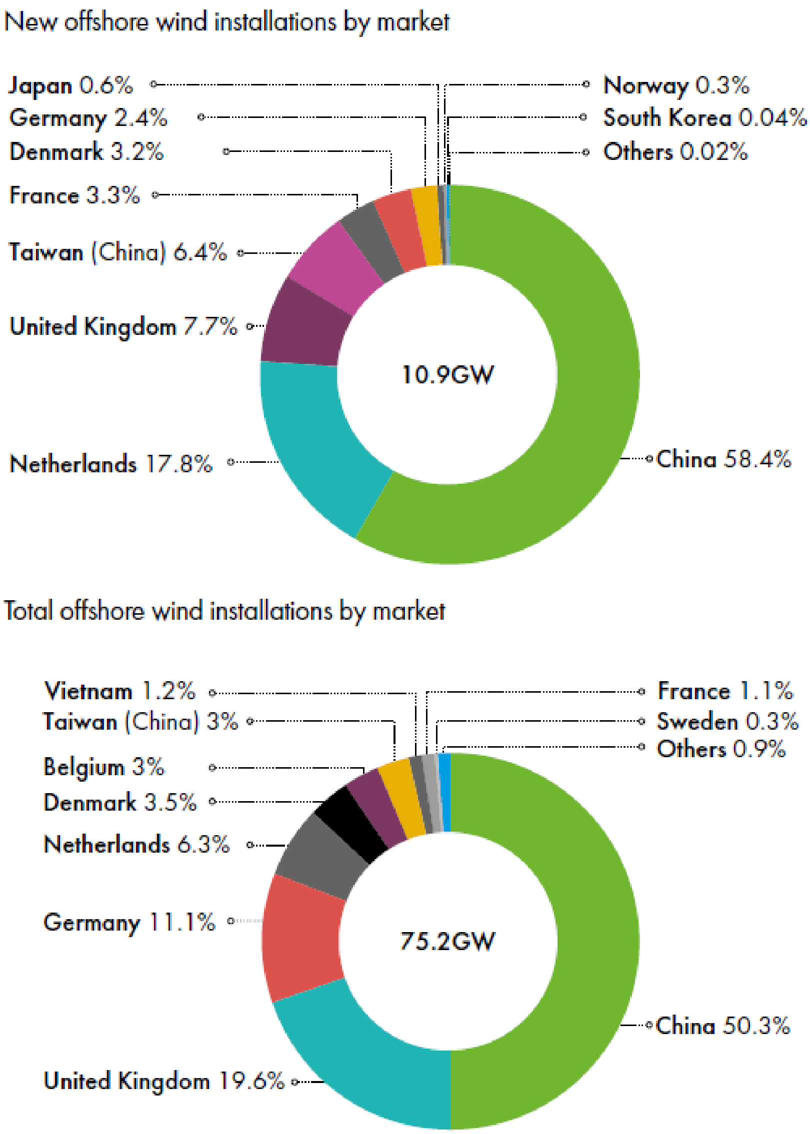

Figure 4 – The 2023 new and the total installed capacity for offshore wind energy [44].

The mechanism in which wave energy is extracted could be used to categorize the converters. A typical point absorber uses the "heave" to move a piston up and down, terminators and OWSCs use the "surge" as a propelling motion, and attenuators convert the "pitch" to activate an engine rotation [2].

The subdivision of WECs in oscillating water columns, oscillating body converters, and overtopping converters is well accepted in the sector and presented in Figure 5, based on IRENA categorization [47]. Figure 5 also illustrates the subdivisions of each category.

The OWCs usually have a high level of reliability, and because the only moving part is the air turbine, these technologies are simpler than the others. On the other hand, their present performance level still demands improvements, namely by implementing advanced control strategies and turbine concepts that are under development. The floating OWCs integrated on spar–buoys are considerably improving their power performance [42].

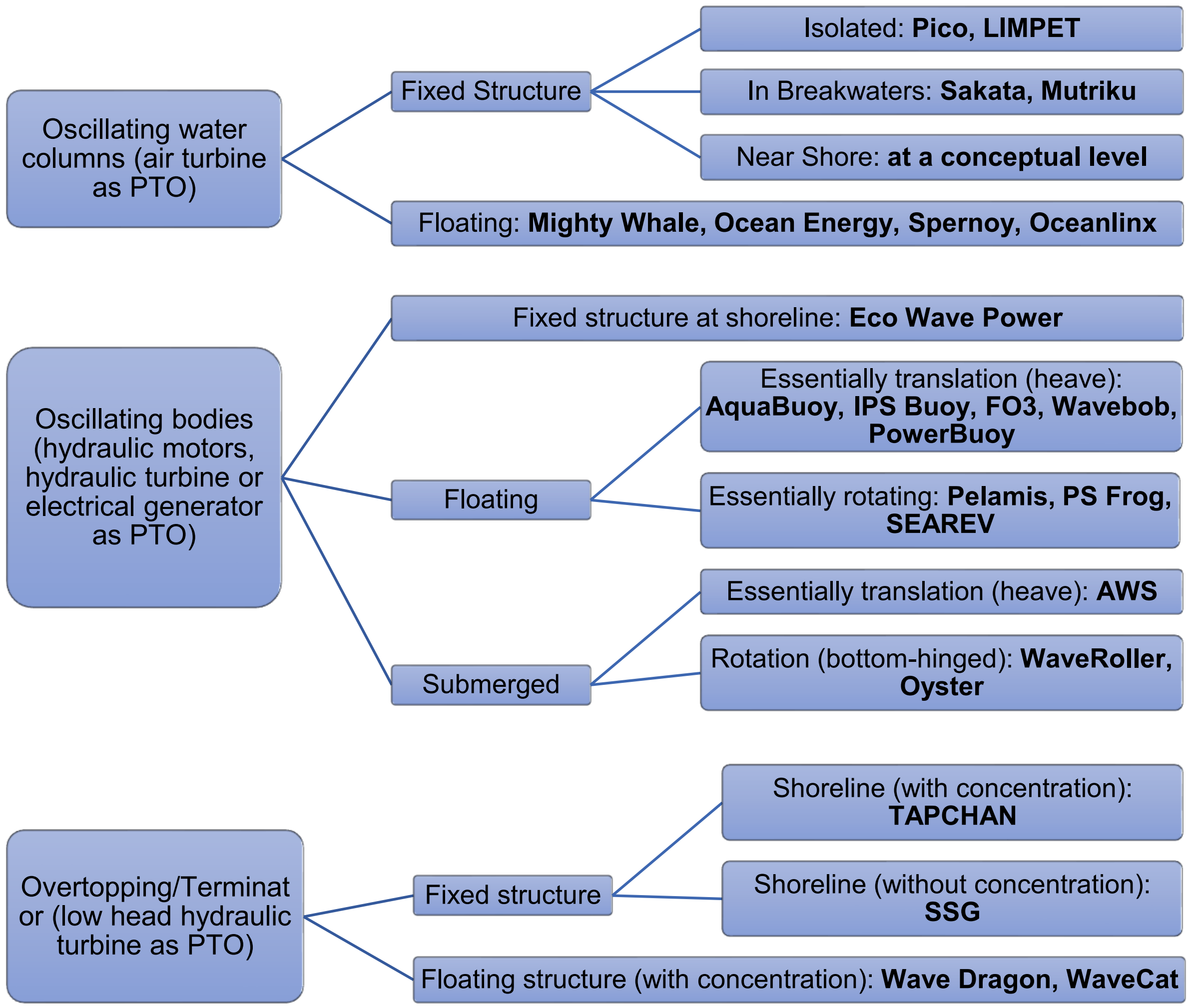

Figure 5 – Categorization of wave energy converters and examples [47].

The oscillating bodies category includes a significant range of concepts. Although the most common ones are floating devices, these concepts can also be submerged, fixed to the seabed or not. They are more common in deep waters (over 40 m), where typically more energetic wave regimes occur. The large variety of concepts has given rise to a wide diversity of PTO systems, *e.g.*, hydraulic generators with linear hydraulic actuators, linear electric generators, and piston pumps [47]. Among the advantages of oscillating bodies are their size and versatility since most of them are floating devices. Nevertheless, a prevalent technology has yet to emerge, and more research needs to be undertaken to increase PTO performance and avoid certain mooring system issues [42].

An overtopping device is, in simple terms, a water reservoir structure with a front ramp, fixed or floating, that can also include concentration walls or arms. Incident waves run up over the front ramp structure and overtop their crest, entering the water reservoir. This converter uses the potential energy of the water collected in the reservoirs to move a conventional low-head hydro turbine, such as in a small hydropower plant [43].

The concept of water storage for electricity purposes is well known and developed along with human history, which is an advantage for overtopping devices. Still, some downsides related to its application for marine/wave energy harvesting include the availability and performance of hydro turbines for such low-heads and large discharges, as well as the impact of sediments and marine growth on their operational costs. There have been developments in the integration of overtopping devices into port breakwaters, in which the device can be installed in existing structures and add the benefits of local electricity production and enhanced protection [29].

2.1.4. Combined wave–wind systems

The integration of technologies that exploit similar resources offers notable advantages, including greater efficiency in resource utilization, reduced financial costs, and enhanced overall energy production. This principle applies to offshore renewable energy technologies, such as wind and wave energy harvesting, which can be co–located. The differing temporal variability of these natural resources allows for smoother integration into the grid network. Additionally, shared infrastructure between generators reduces installation costs. Given the maturity of offshore wind technology, a hybrid approach could accelerate the transition of WECs from the research and development phase to fully operational wave parks.

The synergies between the offshore wind and wave energy sectors present significant research opportunities, particularly in combining floating wind turbines with WECs. These opportunities extend beyond co–location projects to the development of advanced hybrid systems. Additionally, hybrid onshore systems integrating electricity production with harbor protection could be implemented using new or existing harbor infrastructure. Several projects, including MARINA platform [48], ORECCA [49], TROPOS [50] and MERMAID [51], have advanced such concepts in recent years.

Recent policy initiatives, such as Portugal's ambitious target of 2 GW of offshore wind capacity by 2030 [52], create further opportunities for co–location with wave energy [53,54]. This approach offers various synergies, including dual energy conversion, cost reductions, and enhanced accessibility for offshore wind farm maintenance [55–62]. Wave energy parks, acting as wave attenuators, can generate a "shadowing" effect that protects offshore wind turbines from harsh sea conditions [63,64].

This protection is particularly relevant given the high operational and maintenance (O&M) costs of offshore wind farms, which account for 30%–35% of their lifetime expenses [53]. To address these expenses, the offshore wind industry is increasingly adopting preventive and predictive maintenance strategies [54]. Similarly, wave energy farms face high costs related to construction and O&M [65]. However, integrating these systems allows them to share infrastructure, such as foundations and electrical connections, significantly reducing overall expenditures [27].

The potential for higher energy output is another compelling reason to combine wind and wave energy systems [66]. While wind energy can be highly variable, wave energy tends to be more predictable [6]. This predictability can complement wind energy production, ensuring a steadier energy supply over time. For example, during periods of low wind, wave energy may still generate electricity, helping to smooth out fluctuations in power output. This complementary behavior can also reduce the demand for large–scale battery storage systems and lower the total power capacity needed to meet grid requirements. Additionally, combining wave and wind energy systems can help mitigate the costs associated with managing intermittency in the power grid, providing more reliable and consistent energy to the network [52].

Combined wave–wind systems can be categorized by technology type, water depth (shallow, transitional, or deep), or location relative to the shoreline (onshore, nearshore, or offshore). Pérez–Collazo *et al*. [27] proposed a classification framework based on the degree of connectivity between offshore technologies, distinguishing co–located, hybrid, and island systems, as illustrated in Figure 6.

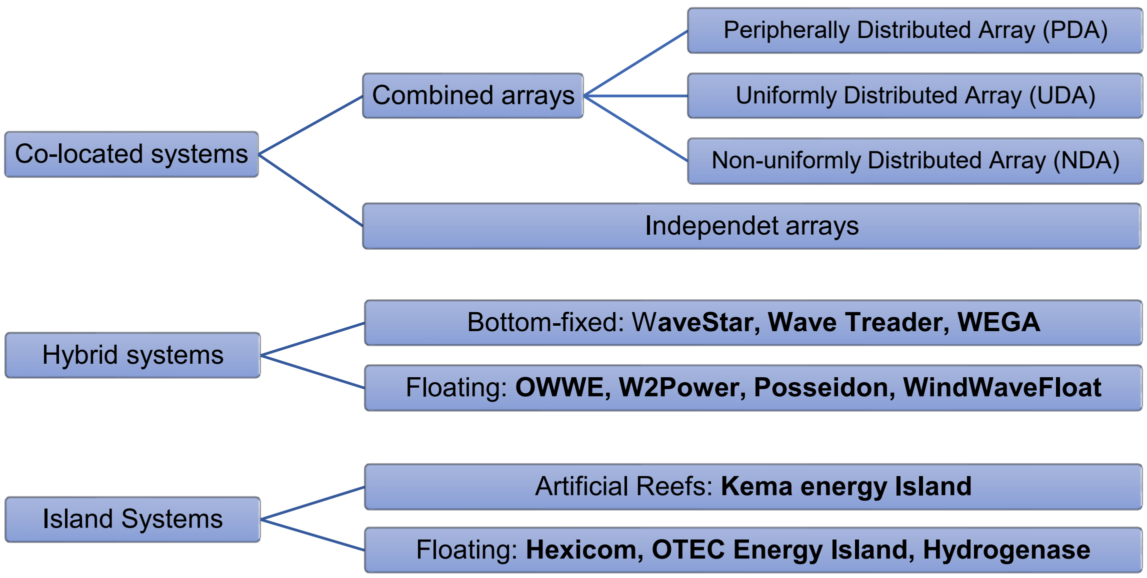

Figure 6 – Classification of combined wave–wind technologies [27].

Co–located systems occupy the same marine area while employing separate foundation systems. These systems typically share essential infrastructure, such as grid connections, O&M resources, and port facilities. Given the advanced maturity of wind energy technology, co–located systems are frequently designed with a primary focus on wind farms, either bottom–fixed or floating, and subsequently integrate the WECs with minimal modifications to the existing grid infrastructure. Co–located systems are categorized into two configurations: independent and combined arrays.

Independent arrays are located within the same general region, though not in the exact same position. While spatially distinct, these arrays are sufficiently close to share grid connections, O&M resources, and associated services. An example of such an independent configuration is illustrated in Figure 7.

Combined arrays, in contrast, occupy the same marine location and share infrastructure, forming a unified array. These arrays can adopt various layouts, categorized as Peripherally Distributed Arrays

(PDA), Uniformly Distributed Arrays (UDA), and Non–uniformly Distributed Arrays (NDA), based on the positioning of WECs relative to wind turbines.

In the Peripherally Distributed Array the WECs are positioned before the wind turbines according to the prevailing wave direction. This arrangement serves as a wave shield, reducing wave energy and enhancing stability within the inner section of the array. Uniformly Distributed Arrays intersperse WECs and wind turbines throughout the array, with WECs evenly positioned in the gaps between turbines. Non–uniformly Distributed Arrays optimize the placement of WECs to maximize energy extraction, considering interactions with surrounding devices. This layout offers flexibility and adaptability to site–specific conditions. Figure 8 illustrates these configurations, although their precise arrangement may vary significantly depending on environmental, technical, and operational requirements.

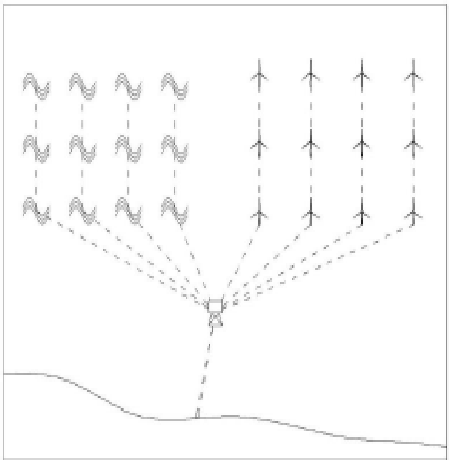

Figure 7 – Schematic of a co–located independent array [27].

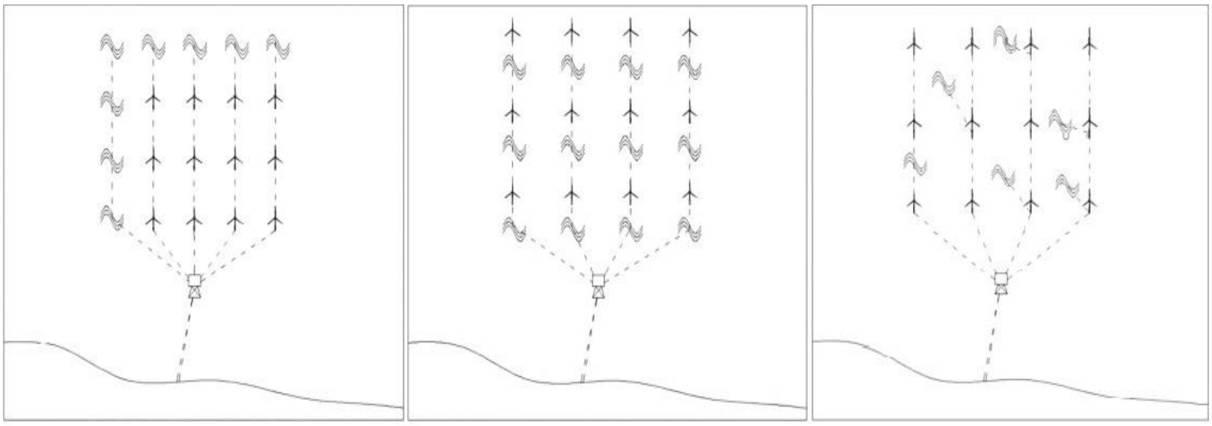

Figure 8 – Peripherally Distributed Array (left)), Uniformly Distributed Array (center) and Non–uniformly Distributed Array (right) [27].

2.1.5. Marine renewable energy in Portugal

The Portuguese continental coast, extending approximately 900 km along the Atlantic Ocean, is marked by distinct atmospheric oscillations throughout the year, with frequent depressions during winter and anticyclones in summer [67]. These climatic conditions, coupled with Portugal's geographical location and the long fetch of the Atlantic near its coast, create favorable conditions for the development of offshore renewable energy. However, while the coast presents significant potential for renewable energy exploitation, it also faces challenges related to coastal erosion, climate resilience, and the need for effective protection measures.

Historically, coastal erosion and rising sea levels have been pressing issues in Portugal, exacerbated by certain engineering practices. From 1990 to 2017, approximately 12.5 million cubic meters of sand were used to stabilize 20 beach sectors covering an area of 75 km [68]. Despite these efforts, the hard engineering solutions, such as seawalls and groins, have often accelerated erosion by disrupting the natural sediment flow [69]. In the past, safety concerns frequently overshadowed comprehensive impact assessments. Coastal retreat continues at an average rate of 1 to 5 m per year [68].

The coastal defense may be even more important if the sea level rise scenarios are considered. By 2050, sea levels are projected to rise between 0.18 m (likely range: 0.15 to 0.23 m) under the SSP1–1.9 scenario and 0.23 m (likely range: 0.20 to 0.29 m) under the SSP5–8.5 scenario. By 2100, this rise is expected to be between 0.38 m (likely range: 0.28 to 0.55 m) for SSP1–1.9 and 0.77 m (likely range: 0.63 to 1.01 m) for SSP5–8.5, relative to 1990 levels [70]. This increase is expected to intensify wave conditions, particularly along the western coast.

In response to these challenges, Portugal has implemented a variety of coastal protection measures aimed at preserving the socio–economic and ecological value of its coastal areas. These measures include constructing artificial reefs, restoring dunes, and reinforcing natural barriers such as salt marshes and wetlands. These interventions are designed to mitigate the physical impacts of erosion and storm surges while also preserving and enhancing coastal ecosystems. The integration of nature–based solutions with traditional engineering approaches reflects a more sustainable and holistic approach to managing coastal dynamics.

Simultaneously, Portugal has recognized the strategic importance of marine renewable energies. In its National Strategy for the Sea 2013–2020 [71] and the Maritime Spatial Plan [72], the country designated significant areas along its coast for the deployment of marine renewable energy technologies. Notably, Portugal has allocated a 400 km² area with depths ranging from 30 to 90 m off São Pedro de Moel, in central Portugal, as a pilot zone for testing maritime technology. Additionally, there is a test area approximately 6.5 km off Aguçadoura, in northern Portugal, with a water depth of circa 45 m and grid connection capability. These designated areas underscore Portugal's commitment to advancing offshore renewable energy technologies.

The country's coastline, characterized by strong and persistent wind regimes, particularly in the northern and central regions, has positioned Portugal as a strategic player in both onshore and offshore wind energy projects. The WindFloat Atlantic project [73], located off the coast of Viana do Castelo, exemplifies Portugal's innovative approach to offshore wind energy. This floating wind farm, one of the first of its kind globally, utilizes advanced technology to harness wind energy in deep waters where traditional fixed–bottom turbines are not feasible.

In addition to wind energy, Portugal is advancing wave energy technology through significant investment in research and pilot projects aimed at optimizing the efficiency and scalability of these devices. With a mean annual wave power of 15 to 35 kW/m, Portugal's coastline provides diverse testing environments, from shallow nearshore zones to deeper offshore waters, facilitating the development of wave energy technologies adaptable to various marine conditions [74].

In 2024, over 83% of Portugal's electricity was generated from renewable energy sources, primarily hydropower, wind, bioenergy, and solar [75]. The commercialization of wave energy could further diversify Portugal's renewable energy portfolio, contributing to energy self–sufficiency and positioning the country as a potential electricity exporter. This aligns with both national and European strategies for a green energy transition and increased autonomy [76].

Several companies have deployed or plan to deploy WEC devices in Portuguese waters, including AW–Energy's WaveRoller® (350 kW) [77] and CorPower's C4 (1.2 MW, 300 kW/unit) [78]. Additionally, the Portuguese government has promoted an auction for offshore renewable energy sources, with a target of 10 GW by 2030 [52]. While the focus is primarily on offshore wind, there is considerable potential for co–locating wave energy systems or even adopting hybridization approaches [55,58]. These strategies could result in dual energy conversion, reduced overall costs, and enhanced accessibility for offshore wind maintenance. Moreover, WEC parks could act as wave attenuators, reducing the wave energy impacting wind farms and thus mitigating coastal erosion [9–12,18,59–63].

Integrating renewable energy infrastructure with coastal protection measures can offer several additional advantages. For example, the presence of renewable energy systems, such as offshore wind turbines or WECs, could facilitate the installation of monitoring equipment, such as sensors or data collection platforms. These devices can track key environmental parameters, such as wave heights, water quality, sediment movement, and coastal erosion patterns. By collecting and analyzing this data, researchers and policymakers can gain a deeper understanding of coastal dynamics and the long–term impacts of both climate change and human intervention. This integrated approach enables more effective monitoring of the coastline and can provide valuable insights for adapting coastal protection strategies to changing conditions.

2.2.Wave energy converter farms

To harness the energy from waves in a sustainable way, the WEC must be placed in an array, frequently called a park or farm, in order to exploit the gain of scale. The design of these parks should take into account many variables and complex interactions; hence a specialized design and engineering are required to ensure that they can effectively capture and convert wave energy into electricity.

The selection of the initial layout or design assumes a huge importance for the development of offshore energy parks since the selected design will have a significant and continuous effect on device operation throughout its life–cycle, which usually spans at least two decades [42]. A complete offshore energy park design includes many variables, components and/or sub–systems, such as the type, number, and location of the devices, foundations or moorings, electrical grid integration, land connection, environmental constraints, and access to operation and maintenance [42].

Design optimization usually utilizes advanced computation to balance costs, objectives, or a fitness function, like minimizing cost or maximizing the park performance. The process of optimization consists of adjusting the variables, device characteristics, or the process to achieve some objective, such as minimum cost or maximum production [40]. There are several factors that can influence the design and optimization of WEC farms. From the review of layout optimization [3] the main parameters include:

i. **Wave conditions**: The design of a WEC farm must take into account the local wave conditions; the majority of the studies use the significant wave height, peak period, and main wave direction as input to determine the optimal layout and spacing of the WECs, as well as the size and type of WECs that should be used.

ii. **WEC technology**: The choice of the technology can have a significant impact on the performance and efficiency of a wave energy farm. Most optimization studies use point absorbers, while there are some optimizations of floating OWC of terminators arrays. The WEC technology and the wave conditions are intrinsically connected, hence it is important to analyze the cost beneficial of every possibility when designing a farm.

iii. **Environmental impact**: WEC farms can have an impact on the local marine environment, including impacts on marine life and habitats. The inclusion of the potential environmental impacts constrains on the park design helps minimizing negative effects or maximizing positive ones, such as coastal protection.

iv. **Cost**: The cost of designing and building a WEC farm usually is the main factor impacting its feasibility and profitability. The main parameter associated with cost is the Levelized Cost of Energy, LCoE, while the one associated with the electricity production is the *q-factor* (see section 2.2.2). The costs of different design options, when integrated in the optimization, minimize costs while still meet the performance and efficiency goals of the park.

v. **Maintenance**: The maintenance requirements of a WEC farm can also be an important factor in its design. WECs maintainability influence the cost–effectiveness over long periods, and the layout can also influence the local wave conditions. Therefore, providing a larger maintenance weather window in a smoother environment.

The minimization of the cost of energy produced usually guides the park design. As stated before, the most common tool to evaluate this is the LCoE, which is a measure of the cost of generating energy from a specific source over the lifetime of the project. A simple model for the LCoE is,

$$\boldsymbol{LCOE} = \frac{\boldsymbol{CaPEX} \times \boldsymbol{CRF} + \boldsymbol{OpEX}}{\boldsymbol{AEP}} \tag{1}$$

where CaPEX represents the Capital Expenditure, CRF the Capital Recovery Factor, OpEX the Operating Expenses, and AEP the Annual Energy Production.

From equation 1, it can be inferred that, once the technology is chosen, the optimization of the park layout has great importance to achieve the best results in terms of energy production with minimum operational costs and externalities, particularly the environmental ones.

There are many other factors that can also influence the design and optimization of WEC farms, and the specific design of a park will depend on the specific goals and constraints of the project. It is important to work with experts in wave energy and engineering to ensure that the design of a WEC farm is optimized for the local wave conditions and the specific needs of the project.

To properly understand interactions of WEC arrays and their effects on the environment, it is necessary to understand the physical process of how a WEC interacts and absorbs energy from the incident wave field [6].

2.2.1. WECs interference on the waves

Absorption of energy from gravity waves on the ocean should be understood as wave interference following the same basic principles of absorption of other types of waves, like electromagnetic and sound waves. The WEC extracts the energy by generating a "counter–wave" that disturbs the incident wave, and the energy provided by the destructive interaction is absorbed by the device [42].

When an incident wave hits some structure, it will be reflected and diffracted. However, if the structure is mobile, like a floating body, it will also produce its wave field related to its motion, creating a radiating wave field. Hence, applying the energy conservation principle all these effects generate waves with the same total energy minus the absorbed by the structure. Figure 9 presents a simple visual representation of the phenomena occurring with a WEC array [79].

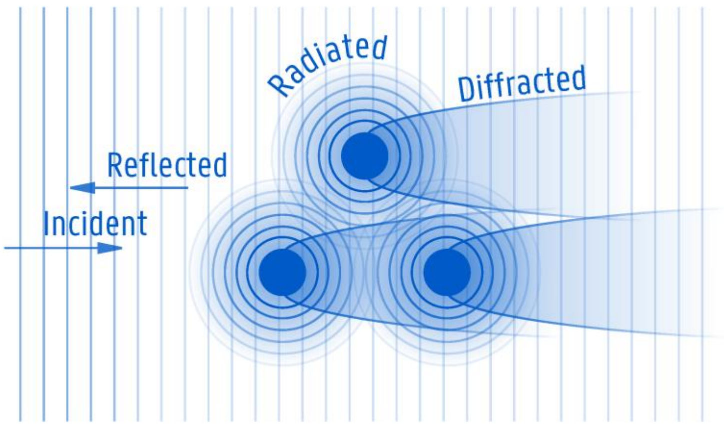

Figure 9 – Representation of incident, reflected, radiated and diffracted caused by a WEC farm [79].

The governing laws are the same for radiated, diffracted and incident waves. However, the incident wave, given its long path from the origin, is a plane–wave propagating in only one direction. On the contrary, diffracted/radiated waves, have origin in the oscillating structure and propagate in every direction.

Given this multidirectional wave field created by the oscillating body, the energy from the incident wave is redistributed to all directions, causing interferences around the structure.

In a WEC, the Power–Take–Off (PTO) is responsible for extracting energy from incoming waves. This extraction is observed as a variation in the phase of the radiated wave, which indicates a reduction in wave amplification or an increase in wave cancellation. As a result, the disparity in the overall energy balance reflects the absorbed energy by the device.

Both air and water are fluids and as so the study of the mechanics of waves in them has several similarities. However, when considering the influence of devices on the extraction of energy there is a significant difference between both. As illustrated in Figure 10, the perturbation caused by a WEC has a significant impact not only after the device but all around it. On the contrary, in the case of a wind turbine, the effect could be neglected to the front. In a wind turbine, this effect is usually called the wake effect.

The wake effect is a downstream region where the wind speed is modified, creating a shadow, affecting a cone–shaped region behind the turbine. Hence, wind turbines in the first row of a wind farm are not affected by the others.

In WEC farms, the concept of a wake is not typically employed since the influence extends throughout the entire system. Hence, each WEC interacts with all the others, irrespective of their positions. The devices positioned upstream experience the influence of those downstream, thereby altering their wave response. It is noteworthy that the potential impact of the park effect on the energy absorption of the foremost row may surpass that experienced by subsequent rows [6]. Thus, when evaluating the park effect, it is imperative to regard a WEC array as a cohesive entity.

The influence exerted by the park effect on the wavefield diminishes as the distance from the source increases. Consequently, the potential for recuperating the wave energy flux may be attainable when the distance surpasses a certain threshold.

2.2.2. The Park Effect

The investigation on the park effects in the wind energy industry has experienced great development in the last decades, and it has shown that the park effect, or wake effect, is inversely proportional to the distance between wind turbines. This led to some separation parameters for the longitudinal and lateral distances between wind turbines.

The park effect is also very important for the wave energy conversion and must be carefully investigated to design an optimal layout. Nevertheless, given its higher complexity and the high number of different technologies and WEC devices, even with several investigations dealing with this matter published over the past 40 years, there are no guidelines at present for their separating distance [6].

A definition of park effect shall consider that the exploration of renewable energy from the environment, in a particular place, by the conservation laws, reduces the available energy at that location with consequences to its neighborhood. As a result, the total power from an array of several WECs should be lower than the sum of the power of the devices when measured as an isolated unit. This is a highly complex issue, because the efficiency of WEC depends not only on the device parameters, but also on environmental parameters, such as the wave height, period, and mean direction.

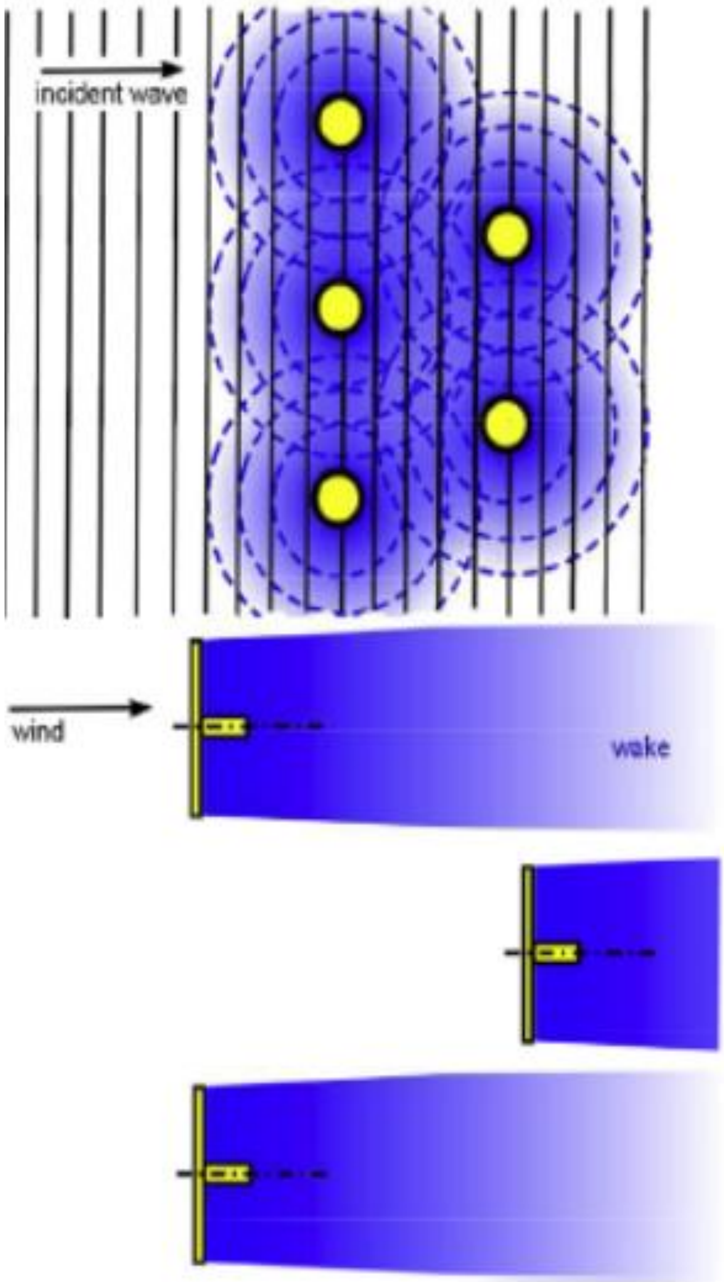

Figure 10 – Illustration of the difference in the effect of a WEC (left) and a Wind Turbine (right) [6].

The *q-factor* is frequently used to quantify the park effect. This factor is a simple way to quantify how wave interactions interfere with power absorption in an array. The *q-factor* is defined as the ratio between the power of the entire array, P_{array}, and the summation of the power of each single isolated device in the array, P_{wec},

$$\boldsymbol{q\text{-}factor} = \frac{\boldsymbol{P_{array}}}{\sum \boldsymbol{P_{wec}}} \tag{2}$$

If "$q\text{-}factor$" is lower than 1, the average power per converter in the array is less than the power of an isolated converter. Consequently, destructive effects prevailed among wave interactions on the wave farm. On the other hand, if q is greater than 1, there are more converters positioned on constructive points than the other way around.

As seen before, since the first investigations of Budal [80,81], it was shown that there is the possibility, in some layout combinations, to achieve a $q\text{-}factor$ considerably higher than 1. Nevertheless, these achievements were made on a theoretical basis with optimally controlled axisymmetric heaving buoys and controlled sea states. In real cases, due to the complexity of waves, given their irregularity, achieving optimal control is not realistically possible. Hence the majority of researchers in this field argue that the best practice should be to minimize destructive interactions instead of seeking to maximize the constructive ones [37].

The first row of the array often receives constructive interactions from the rows behind due to the diffracted waves. However, this is usually not enough to compensate for the decrease in wave energy remaining for the other rows.

In small arrays with less than ten converters with traditional layouts, the park effect usually has a small influence on the total energy absorbed, when the distance between devices is greater than one order of magnitude in comparison to the dimensions of the WEC [6]. In other words, separation of 100–200 m for a converter diameter of 10–20 m. Hence, this opens a discussion of the importance of the park effect to such small parks, even more, because of the uncertainties associated with the wave modeling, the positioning of the WECs, and local conditions, like the bathymetry.

As the number of converters increases, the importance of the park effect increases as well, due to the higher number of wave interactions, with the absorbed power of a given row in the array being smaller than the one in front, and greater than the one behind. Consequently, the number of rows of parks arranged on a traditional grid geometry like square or triangular should be maintained as small as possible. However, the number of devices in a row does not have a limitation, mostly because the lateral separation is habitually large when compared to the converter dimensions.

The influence of the park effect on extensive arrays was observed to be approximately 5% [6]. This finding was derived from an array comprising 25 oscillating surge WECs positioned at a separation distance of 200 m. Moreover, it was observed that the fifth row in the array experienced a decline of 20% in terms of mean annual energy absorption. Section 2.5 provides a comprehensive review of various studies that have investigated the park effect in order to identify an optimal configuration and understand its consequences. These studies have delved into the intricate aspects of the park effect and its impact on wave energy conversion, thereby contributing valuable insights to the field.

2.2.3. WEC farm evaluation

The evaluation of wave energy farms involves a multifaceted approach that considers both the performance of the farm itself and its broader environmental and operational impacts. A significant body of research has focused on developing and refining a variety of indicators to assess these dimensions, with particular emphasis on the economic feasibility, power production efficiency, environmental consequences, and operational challenges associated with WEC systems.

A key area of evaluation for wave farms pertains to their economic performance. In studies of layout optimization, such as those reviewed by several authors [3], economic indicators like the LCoE and Annual Energy Production (AEP) are often prioritized. These indicators provide essential insights into the cost–effectiveness and energy output of WEC arrays, helping to gauge their viability as a sustainable energy source. Alongside LCoE and AEP, additional performance metrics such as the *q-factor* and capacity factor are frequently employed to further assess energy production. These metrics offer valuable information regarding the operational efficiency of the farm, helping to evaluate the overall energy yield relative to the array's design and operational parameters.

In terms of economic viability, the LCoE remains a central metric, with co–located wind and wave farms benefiting from shared infrastructure, such as grid connections and maintenance facilities, which reduce costs compared to standalone installations. Astariz *et al*. [61] demonstrated that co–located systems could achieve cost reductions and improved energy yield per unit area. For instance, the authors showed that sharing resources between wind and wave energy systems could lead to a 3.4% increase in energy yield compared to wind–only systems.

In addition to these primary economic and energy–related indicators, several metrics are specifically designed to assess the quality of power production from wave farms. Power production density, for instance, measures the ratio of energy output to the area occupied by the farm [82], providing a useful gauge of spatial efficiency. Power smoothing is another critical aspect of wave farm performance, and it is evaluated using statistical parameters such as the standard deviation (std), coefficient of variation (CoV), and the range of power absorption by different WECs within the array. These indicators reveal the extent of variability in energy production, with measures like the P2M (the difference between the most absorbing WEC and the farm average) highlighting disparities that may inform optimization strategies to improve energy capture balance across the farm.

Engström *et al*. [82] utilized potential linear wave theory to evaluate WEC arrays, emphasizing key performance metrics: the Capture Width Ratio (CWR), which measures absorbed power relative to incident wave energy transport; Power Production Density (β), defined as total absorbed power divided by the array's convex hull area; and Normalized Variance of Power, which quantifies output fluctuations. These metrics were analyzed in the context of hydrodynamic forces (excitation and radiation) and power absorption using spectral properties such as energy period (T_e) and significant wave height.

Beyond evaluating internal power production, wave farms are also assessed for their broader environmental impacts, particularly in terms of how they influence their surrounding marine and coastal environments. One prominent phenomenon, the "park effect," refers to the changes in wave dynamics and energy distribution caused by the presence of the farm itself. Various indices have been developed to quantify this effect, with a particular focus on offshore energy parks that combine wind and wave energy systems. For example, studies by Astariz *et al*. [23,56–62,66,83–86] have proposed metrics such as the significant wave height reduction within the farm (HRF), which quantifies the reduction in significant wave height (H_s) within the farm area, specifically at locations of the wind turbines. This indicator offers insights into the influence of wave farms on wave patterns, which can affect not only energy capture but also operational logistics, such as accessibility for maintenance tasks.

$$\boldsymbol{HRF} = \frac{\mathbf{100}}{\boldsymbol{n}}\sum_{\boldsymbol{i=1}}^{\boldsymbol{n}}\frac{H_{s_i} - H_{s_{\boldsymbol{wec_i}}}}{H_{s_i}} \tag{3}$$

where H_{s_i} is the baseline scenario without WECs and $H_{s_{wec_i}}$ is with WECs, for each i position of wind turbines.

Operational and maintenance (O&M) efficiency is another vital aspect of wave farm evaluation. To assess the effectiveness of O&M processes, metrics like the Access Time Increase for O&M ($\boldsymbol{\Delta T_{O\&M}}$), which relate the hours per year when H_s is lower than or equal to 1.5 m within the wind farm with co-located WECs (T_W) and in the baseline scenario (T_b), and the Percentage of Accessible Wind Turbines during a given percentage of time (AWTk) are commonly used. These indicators reflect logistical challenges in offshore energy park operations, particularly in terms of how wave farms influence accessibility to turbines for maintenance. Research carried out by Astariz *et al.* [56] demonstrated that non–uniformly distributed WEC arrays could reduce wave heights by up to 19%, thus improving accessibility during maintenance windows and enhancing operational efficiency.

$$\boldsymbol{AWT_k} = \frac{\textbf{Accessible wind turbines}}{\boldsymbol{Total\ number\ of\ wind\ tubines}}\ \boldsymbol{x}\ \mathbf{100} \tag{4}$$

$$\Delta \boldsymbol{T_{O\&M}}(\%) = \frac{\boldsymbol{T_W} - \boldsymbol{T_b}}{\boldsymbol{T_W}}\ \boldsymbol{x}\ \mathbf{100} \tag{5}$$

Another important concept explored in the context of wave farm performance is the "shadow effect". Astariz *et al*. [57] showed that the presence of WECs leads to a reduction in wave heights, which in turn extends weather windows and reduces the variability of power production. This phenomenon has significant implications for both operational efficiency and economic viability, as it can increase the predictability of energy output and improve grid integration. Astariz *et al*. [84] further explored this effect, highlighting the potential for co–located wind and wave energy systems to reduce the variability in power production through statistical analysis methods such as cross–correlation and standard deviation.

The environmental impacts of wave farms on coastal areas are another essential aspect of the evaluation of wave farms. The work of Abanades *et al*. [9–12,18] introduced various indicators such as the Bed Level Impact (BLI), Beach Face Eroded Area (FEA), Non–dimensional Erosion Reduction (NER), and Cumulative Eroded Area (CEA), which quantify the effects of wave farms on sediment dynamics and coastal morphology. These metrics are crucial for understanding how wave farms affect the coastline, particularly in terms of erosion and sediment transport. By measuring the morphological changes caused by wave farms, these indicators help to assess the potential for wave energy systems to either mitigate or exacerbate coastal erosion.

Other researchers have focused on wave power and coastal conditions. Carballo and Iglesias [87] introduced the Average Relative Nearshore Impact (RNI) to evaluate the impact of wave farms on nearshore wave power distribution. Similarly, Berrio *et al*. [88] proposed the Reduction of Wave Energy Potential (RWP), which is the difference between the simulated and baseline scenario for wave energy flux per wave front length, and the Level Variation Indicator (BLV) to assess changes in wave conditions and seabed stability due to wave farm installations. These indicators compare baseline (no wave farm) and project scenarios, providing a detailed framework for understanding the intricate interactions between wave farms, coastal systems, and marine environments.

The Average Relative Nearshore Impact (RNI) is a key non–dimensional indicator for evaluating the effect of wave energy farms on coastal wave power. It compares wave power at specific locations, typically at the 20–meter depth contour, with and without the farm's presence. The results, averaged across spatial and temporal domains, provide insights into the farm's influence on wave energy distribution and coastal processes. This non–dimensional indicator offers a detailed understanding of how wave farms influence wave energy distribution along the coastline. Results are averaged spatially and temporally, providing a clear picture of the farm's impact on wave dynamics and coastal processes.

$$\mathbf{RNI} = \frac{\mathbf{1}}{\boldsymbol{T}}\frac{\mathbf{1}}{\boldsymbol{S_p}}\sum_{\boldsymbol{T}=\mathbf{1}}^{\boldsymbol{T}}\sum_{\boldsymbol{S_p}=\mathbf{1}}^{\boldsymbol{S_p}}\frac{\boldsymbol{J_b^{20}(s,t) - J_{f,i}^{20}(s,t)}}{\boldsymbol{J_b^{20}(s,t)}} \tag{6}$$

where $J_b^{20}(s,t)$ is the base line scenario power, $J_{f,i}^{20}(s,t)$ the scenario with farms and with S_p and t the total number of points along the contour and in time.

The Bed Level Impact (BLI) and the Eroded Area (A) are other crucial indicators used to evaluate the impact of wave farms on coastal erosion. BLI measures the change in seabed elevation caused by the farm, while A quantifies the volume of sediment displaced during erosion events. Together, these metrics provide a clear indication of how wave farms influence coastal stability and the potential for mitigating or exacerbating erosion. The Erosion Impact (EI) index further quantifies the farm’s role in reducing coastal erosion, offering a measure of its effectiveness in preserving beach profiles.

$$\boldsymbol{BLI\,(x,y) = \ \zeta_f(x,y) \ - \ \zeta_b(x,y)} \tag{7}$$

where $\zeta_f(x,y)$ and$\zeta_b(x,y)$ are the seabed level with the farm and without it.

In addition to the BLI, the Eroded Area (A) is quantified to assess the volume of material displaced from the beach during erosion events. The eroded area in the baseline scenario is compared to the eroded area in the presence of the wave farm. This comparison allows for the assessment of the farm's effectiveness in reducing or mitigating coastal erosion. The Erosion Impact (EI) index is then defined to represent the reduction in eroded area due to the wave farm, expressed as a percentage of the total eroded area in the baseline scenario. The EI index provides a clear measure of the wave farm’s contribution to mitigating erosion and preserving the integrity of the beach profile.

For long–term coastal protection, additional advanced indicators such as the Beach Face Eroded Area (FEA), Non–dimensional Erosion Reduction (NER), and Cumulative Eroded Area (CEA) are employed. These indicators help assess the ongoing impact of wave farms on coastal erosion, providing a more comprehensive view of their role in protecting shorelines over time.

$$\boldsymbol{FEA}_{f}(\boldsymbol{y}) = \int_{x_1}^{x_{max}} \left[\zeta_b(x,y) - \zeta_f(x,y)\right] dx \tag{8}$$

$$\boldsymbol{NER}\,(\boldsymbol{y}) = 1 - (x_{max} - x_1) \int_{x_1}^{x_{max}} \left[\zeta_b(x,y) - \zeta_f(x,y)\right]\left[\zeta_0(x,y) - \zeta_f(x,y)\right]^{-1} dx \tag{9}$$

$$\boldsymbol{CEA}_{f}^{N}(\boldsymbol{x}) = (y_{max} - y_P)^{-1} \int_{y_P}^{y_{max}} \int_{x_0}^{x} \left[\zeta_b(\chi,y) - \zeta_f(\chi,y)\right] dx\, dy \tag{10}$$

where $\zeta_b(x,y)$ is the seabed level at the point of coordinates (*x,y*) at the initial condition and $\zeta_f(x,y)$ with the farm. where the variable of integration, χ, represents the coordinate along the profile, and *x* and x_0, and y_0 , and y_{max} and y_P are the limits of integration along the profile and along the coast, respectively. x_0 is the value of the *x*–coordinate corresponding to the first point of the profile and *x* takes values from x_0 to x_{max}. Along the beach, y_0 is the value of the *y*–coordinate corresponding to the southernmost point of the beach, y_{max} the northernmost point of the beach and y_P the value corresponding to the reference profile.

The Beach Face Eroded Area (FEA) measures the volume of sediment eroded from the beach face per unit length of beach, both in the baseline and farm scenarios. This parameter is defined as a function of the beach profile, with erosion occurring along the entire profile from the seaward end to the landward end. The FEA provides a clear measurement of the farm's impact on the beach face and its potential to reduce or increase erosion over time.

The Non–dimensional Erosion Reduction (NER) is a dimensionless indicator that expresses the variation in eroded area as a fraction of the total eroded area in a specific beach profile. A positive NER indicates a reduction in erosion, while a negative value suggests that the wave farm has exacerbated erosion at that particular location. The NER provides a straightforward way to assess the farm's role in mitigating or intensifying coastal erosion.

The Cumulative Eroded Area (CEA) represents the total volume of material eroded along a specific section of the beach, taking into account both the northern and southern parts of the reference profiles. By considering different reference profiles the CEA offers a holistic view of the erosion dynamics across a broader spatial scale.

The methodologies and indicators outlined above align with ongoing coastal protection and monitoring initiatives such as the CONSCIENCE [89] and EUROSION [90] projects, which aim to evaluate and manage coastal erosion over medium– to long–term periods. These projects utilize a variety of impact indicators to assess erosion dynamics and the effectiveness of coastal protection measures, including wave energy farms. By integrating these well–established frameworks, the evaluation of wave farms provides valuable insights into their role in mitigating coastal erosion and supporting sustainable coastal management practices.

The SWAN model combined with Kamphuis' formulae is often employed to evaluate H_s and T_p to assess the morphological impact of wave farms, as these influence sediment transport processes. They play a vital role in understanding the energy dynamics at the shoreline, which is essential for predicting the potential impacts of wave farms on beach morphology and sedimentation processes.

The evaluation of wave energy farms involves a robust set of indicators that address both the operational performance of the farm and its environmental impact on coastal systems. By integrating these metrics into the evaluation process, it is possible to develop a holistic understanding of the potential benefits and challenges of wave energy farms. This comprehensive approach ensures that the development of wave energy projects is not only economically viable but also environmentally sustainable, offering a solid foundation for informed decision–making in the renewable energy sector. Through continued research and refinement of these evaluation methodologies, wave energy can be positioned as a critical component of sustainable energy solutions for the future.

2.3.Water Waves Theory

In nature, ocean waves are rarely exactly the same in their neighborhood or propagate in the same direction. They are affected by a variety of factors, such as wind, currents, water depth, and bottom bathymetry, which can cause the waves to vary in height, frequency, direction, and shape. In addition, the interaction of waves with each other, known as wave–wave interactions, can cause waves to change their characteristics, merge, or even break.

To account for these natural variations in the wave field, many wave models use a stochastic or probabilistic approach, which involves simulating a range of possible wave conditions that are statistically representative of the natural variability of the wave field. These models use statistical distributions to represent the variation in wave height, period, and direction, and may also incorporate random phase offsets and other sources of variability [91].

For example, SWAN, which is a widely used wave model, includes a number of options for representing wave variability, including random phase offsets, directional spreading functions, and spectral shape functions. These options allow the model to simulate a range of wave conditions that are consistent with the natural variability of the wave field.

Similarly, OpenFOAM includes a range of options for simulating stochastic waves, including the use of random phase offsets and amplitude modulation functions to represent the variability of the wave field. These stochastic modeling techniques can help to improve the accuracy of the simulation and provide a more realistic representation of the natural variability of the wave field.

The most applied theory to describe the characteristics of waves is the Airy linear wave theory. However, for nonlinear effects, other theories like Stokes' theory and Boussinesq equations are applied. *Figure 11* illustrates the ranges of applicability of the various wave theories.

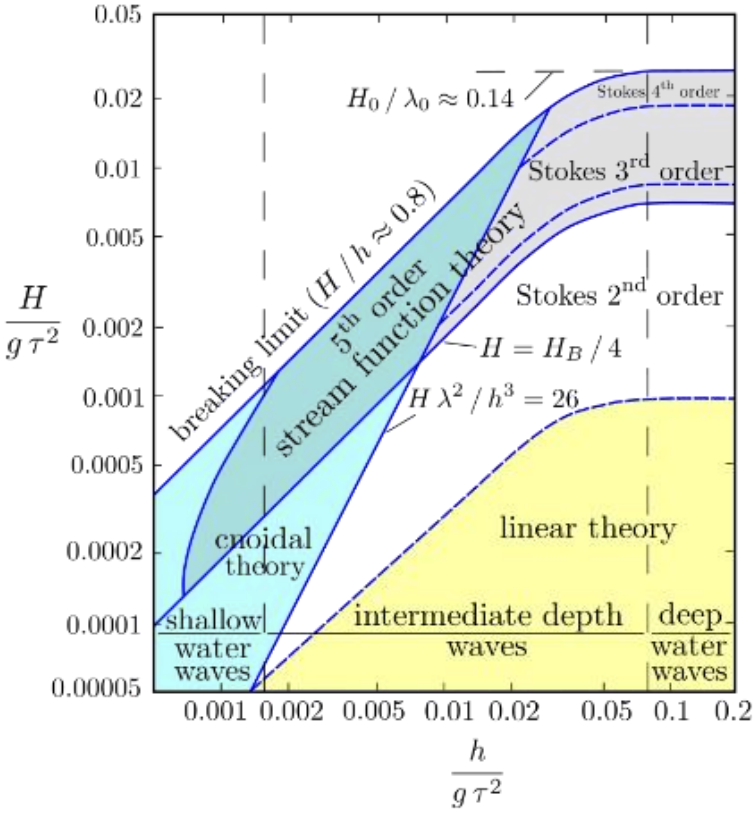

Figure 11 – Ranges of applicability of the various wave theories [92].

2.3.1. Water wave governing equations

Ocean waters are Newtonian fluids, hence the equation of motion of a fluid particle is obtained based on Newton's second law of conservation of momentum. The Navier–Stokes equations mathematically express conservation of momentum and conservation of mass for Newtonian fluids. The balance equation could be inferred by the diagram shown in Figure 12.

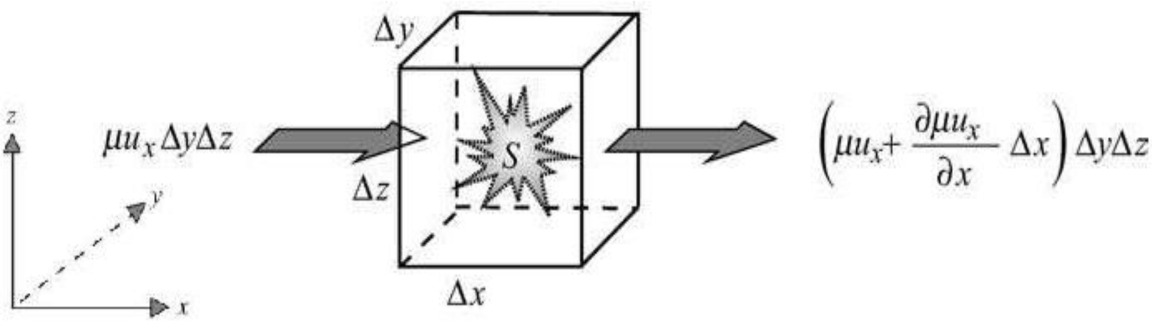

Figure 12 – Three–dimensional control volume to characterize the transport of a property μ by the water in the x–direction [92].

In cartesian coordinates (x, y, z), consider a control volume of a fluid that carries through it some arbitrary, conservative attribute μ (density). The balancing equation for μ per unit volume, per unit time is obtained by:

$$\frac{\partial \mu}{\partial t} + \frac{\partial \mu\, u_x}{\partial x} + \frac{\partial \mu\, u_y}{\partial y} + \frac{\partial \mu\, u_z}{\partial z} = S \tag{11}$$

Considering that water is an incompressible fluid with constant mass density ($\rho \approx 1025\ kg/m^3$ for sea water), it is possible to infer that there is no mass production (water production) or loss inside the control volume, which gives the *continuity equation:*

$$\nabla . u = \frac{\partial\, u_x}{\partial x} + \frac{\partial\, u_y}{\partial y} + \frac{\partial\, u_z}{\partial z} = 0 \tag{12}$$

The balance of momentum is reached by considering the pressure gradient in the water and the balance equation for $\mu = \rho\vec{u}$. The momentum balance equations, or the Euler equations, can be derived from the resulting forces, $\vec{F}$, on a water particle,

$$\vec{F} = \frac{D\vec{u}}{Dt} = -\frac{1}{\rho}\nabla P + \vec{g} \tag{13}$$

Due to the large size of the structures and the intensity of the motion of the water particles, viscous effects of the fluid are considered insignificant in the majority of the medium in wave motion research and many technical applications. This, together with the assumption of irrotational flow, can help to ease the challenge of establishing a wave theory by allowing the inclusion of velocity potentials in the basic differential equations, reducing the number of fluid unknowns while raising the order of the equations (potential flow problem) [18]. In essence, this converts the continuity equation to a Laplacian (linear equation) of the velocity potential, which must be solved when linear and nonlinear boundary conditions are introduced. Therefore, when wave kinematics can be characterized by a velocity potential φ, the continuity equation is defined as:

$$\nabla^2 \phi = \frac{\partial^2\, \phi}{\partial x^2} + \frac{\partial^2\, \phi}{\partial y^2} + \frac{\partial^2\, \phi}{\partial z^2} = 0 \tag{14}$$

The NSEs are integrated in a set of three nonlinear partial differential Equations using the Euler technique for incompressible fluid in Cartesian coordinates, with the components of velocity $u\ (x, y, z)$ and pressure p. The density ρ can be treated as a known constant since the fluid is presumed to be incompressible. The fluid's kinematic viscosity is denoted by ν. The system of equations corresponds to the NSEs and is provided for the scenario where the external or body force is just gravity,

$$\frac{\partial u_x}{\partial t} + u_x \frac{\partial\, u_x}{\partial x} + u_y \frac{\partial\, u_x}{\partial y} + u_z \frac{\partial\, u_x}{\partial z} = -\frac{1}{\rho}\frac{\partial p}{\partial x} + \nu.\left(\frac{\partial^2\, u_x}{\partial x^2} + \frac{\partial^2\, u_x}{\partial y^2} + \frac{\partial^2\, u_x}{\partial z^2}\right) + g_x \tag{15}$$

$$\frac{\partial u_y}{\partial t} + u_x \frac{\partial\, u_y}{\partial x} + u_y \frac{\partial\, u_x}{\partial y} + u_z \frac{\partial\, u_y}{\partial z} = -\frac{1}{\rho}\frac{\partial p}{\partial y} + \nu.\left(\frac{\partial^2\, u_y}{\partial x^2} + \frac{\partial^2\, u_y}{\partial y^2} + \frac{\partial^2\, u_y}{\partial z^2}\right) + g_y \tag{16}$$

$$\frac{\partial u_z}{\partial t} + u_x \frac{\partial u_z}{\partial x} + u_y \frac{\partial u_z}{\partial y} + u_z \frac{\partial u_z}{\partial z} = -\frac{1}{\rho}\frac{\partial p}{\partial z} + \nu.\left(\frac{\partial^2 u_z}{\partial x^2} + \frac{\partial^2 u_z}{\partial y^2} + \frac{\partial^2 u_z}{\partial z^2}\right) + g_z \tag{17}$$

in a vectorial form,

$$\frac{\partial \vec{u}}{\partial t} + \vec{u}.\nabla\vec{u} = \frac{\nabla P}{\rho} + \nu\nabla^2\vec{u} + \vec{g} \tag{18}$$

The Euler equations may be rearranged to yield the generalized Bernoulli equation, which is an integral form of the equations of motion, in the situation of irrotational flow ($\nabla \times \vec{u} = 0$).

$$gz + \frac{P}{\rho} + \frac{1}{2}\left(\left(\frac{\partial \phi}{\partial x}\right)^2 + \left(\frac{\partial \varphi}{\partial z}\right)^2\right) + \frac{\partial \phi}{\partial t} = C(t) \tag{19}$$

Wave theories can be split into two broad types, Linear and Nonlinear, depending on how nonlinear boundary conditions are treated. Within each category, there are a number of wave theories that may be used to predict wave motion under various sea circumstances. According to the usage made of the wave theories in this research, the following sections present a brief description of linear and nonlinear wave theories.

2.3.2. Linear wave theory

The linear, or small amplitude, theory of surface gravity waves has been the basic theory for ocean waves since Airy proposed it in 1847. It is presented in many books, usually with a scientific or engineering approach against the background of mathematics, physics, oceanography, ocean engineering, or coastal engineering [92].

Water waves in real conditions propagate in a viscous fluid over an irregular bottom of varying permeability. However, in the majority of the situations, the main body of the fluid motion is almost irrotational. This effect is provided by the fact that the viscous effects are typically restricted to thin “boundary” layers near the surface and the bottom. In addition, because the water could be considered reasonably incompressible, velocity potential and a stream function would exist for waves. To develop the theory and simplify the mathematical analysis, several other assumptions must be made [91].

First, the fluid is assumed to be homogeneous and incompressible, which implies that the density (ρ) remains constant throughout. Additionally, surface tension effects are considered negligible, as is the Coriolis effect arising from the Earth's rotation. The pressure at the free surface is presumed to be uniform and constant. Furthermore, the fluid is treated as ideal or inviscid, meaning that it lacks viscosity.

The theory also assumes that the wave under consideration does not interact with other water motions. The flow is regarded as irrotational, signifying that water particles do not rotate; only normal forces are significant, while shearing forces are negligible. The bed is modeled as a horizontal, fixed, and impermeable boundary, implying that the vertical velocity at the bed is zero. The wave amplitude is assumed to be small, with the waveform remaining invariant in both time and space. Lastly, the waves are considered to be plane or long-crested, corresponding to a two-dimensional representation.

The assumption of irrotationality is particularly noteworthy, as it permits the use of a mathematical construct known as the velocity potential (ϕ). The velocity potential is a scalar function whose gradient, the rate of change of ϕ with respect to the horizontal and vertical directions, yields the velocity vector at any point in the fluid. This theory is fundamental for understanding higher order-theories and for the analysis of irregular waves.

The linearization is reached by assuming that the wave height is too small compared to the wavelength, small wave steepness, and the water depth is taken as constant with a flat bottom. The theory is built on only two equations: a mass balance equation and a momentum balance equation. The water free surface elevation of one wave component is sinusoidal, and can be expressed as a function of the horizontal position, x, and time, t, by:

$$\boldsymbol{\eta(x,t) = \mathrm{a}\cos(kx - \omega t) = \frac{H}{2}\cos\left(\frac{2\pi x}{L} - \frac{2\pi t}{T}\right) = a\, cos\theta} \tag{20}$$

where “a” is the wave amplitude, “k” the angular wavenumber and “ω” the angular frequency.

By integrating the velocity of the water particle in time it is possible to calculate its path. The underwater particle follows an orbital path, which can be observed by fixing the point of interest to the crest and following its movement. In different water depths this orbital path changes shapes. Like Figure 13 illustrates, the orbital shape becomes more elongated as the wave moves to shallower waters, because of the seabed influence.

It turns out that the boundary conditions can be linearized and η can be eliminated from the mass balance and momentum balance equations. The linearization of the boundary conditions is described in the following section.

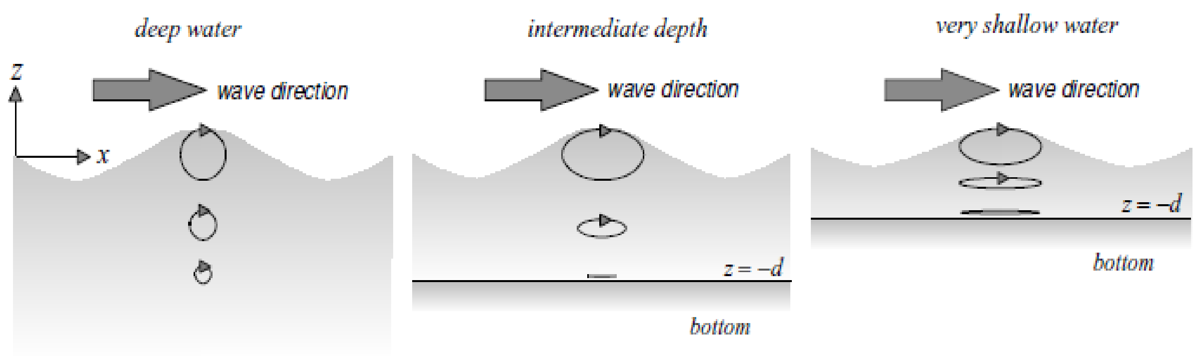

Figure 13 – The orbital motion in deep water, intermediate–depth water and very shallow water [92].

2.3.2.1. Linearization boundary conditions for flat horizontal bottom

For the theory to be linear, certain aspects of wave kinematics (motion) and wave dynamics (forces) need to be neglected. For this, it is enough that the amplitude of the waves is small relative to the wavelength and to the water depth. Figure 14 presents a scheme of the linear theory mathematical problem.

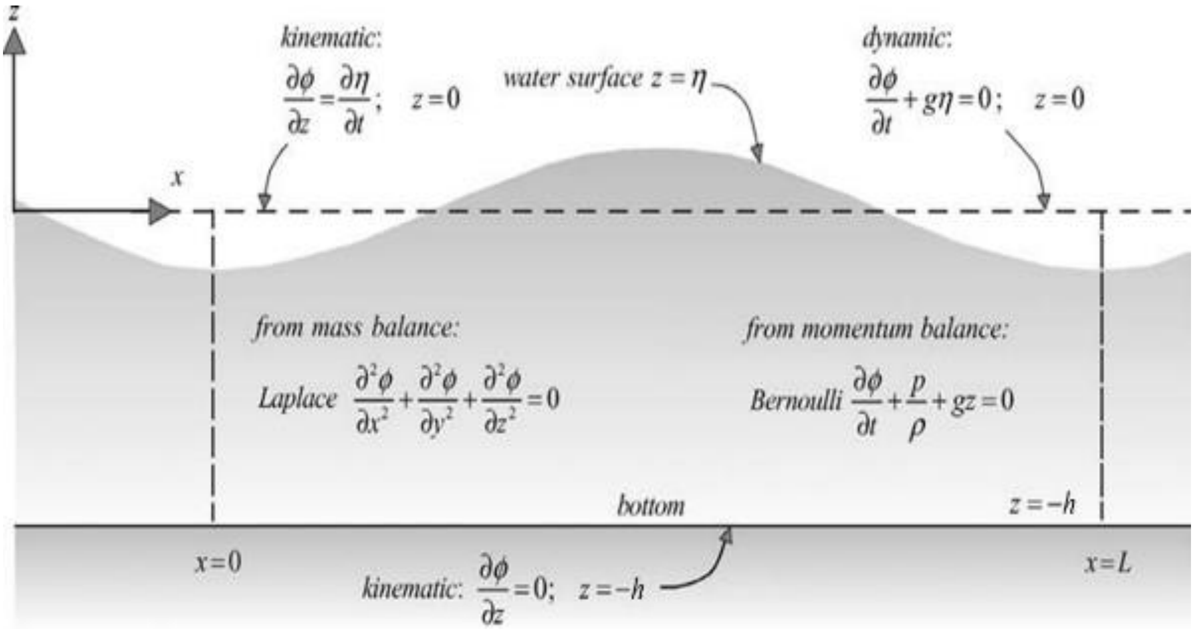

Figure 14 – The linearized basic equations and boundary conditions for the linear wave theory, adapted from [92].

Kinematic free surface boundary conditions:

Considering the premise of the theory, the small amplitude ($\frac{H}{L} \ll 1$), it can be inferred that the slope of the water free surface will be close to zero, *i.e.*, $z \approx 0$, given,

$$\frac{\partial \varphi}{\partial z} = \frac{\partial \eta}{\partial t} \quad at\ z = 0 \tag{21}$$

Dynamic free surface boundary condition:

Because of small amplitude, velocity and pressure are also supposed to be small. Therefore, the products of these variables should result in extremely small values, which can be neglected in the linearization. The Bernoulli equation can be written, for $z \approx 0$, as:

$$g\eta + \frac{\partial \phi}{\partial t} = 0 \quad at\ z = 0 \tag{22}$$

2.3.2.2. Wave energy and Energy Transportation

Wave energy is the combination of kinetic energy, due to the movement of the fluid particles, and potential energy, due to the displacement of the fluid from its horizontal equilibrium position. The propagation of waves is intrinsically linked to the direction of energy propagation. In essence, the wave propagation direction is determined by the direction in which the energy is being transmitted through the medium.

i. Potential Energy

The displacement of a mass of water from its equilibrium position against a gravitational field generates potential energy in water waves. All potential energy comes from gravitational forces since the fluid is considered to be incompressible, and surface tension is ignored,

$$\boldsymbol{E_p(\theta) = \int_{-h}^{\eta} \rho g z dz - \int_{-h}^{0} \rho g z dz = \int_{0}^{\eta} \rho g z dz} \tag{23}$$

$$\boldsymbol{E_p(\theta) = \frac{1}{2}\rho g \eta^2 = \frac{1}{4}\rho g a^2} \tag{24}$$

$$\boldsymbol{E_p = \frac{1}{16}\rho g H^2} \tag{25}$$

where $E_p(\theta)$ is the potential energy of a fluid element at a phase angle θ, ρ the density of the fluid, g the acceleration due to gravity, z the height above a reference level (usually the still water level), h is the water depth at the location and η the displacement of the water free surface above the still water level. The mean potential energy of the wave is obtained by time–averaging the potential energy over one wave period or length–averaging over one wavelength.

The term $H/2$ represents the amplitude of the wave measured from the mean water level to the wave crest, and the factor of 1/4 in the equation accounts for the fact that the wave amplitude is measured from the mean water level to the wave crest, while the potential energy is measured from the mean water level to the center of gravity of the fluid element.

ii. Kinetic Energy

In an ideal fluid, there is no turbulent kinetic energy, as turbulence is a property of viscous fluids. The flow is assumed to be frictionless and non–viscous, so there is no mechanism for the production and dissipation of turbulent kinetic energy.

When considering waves in an ideal fluid, the fluid particles move in a regular and predictable manner, and the wave motion can be described using linear wave theory. In this case, the particle velocities induced by the wave can be calculated using the wave height, wavelength, and wave period, and the flow is assumed to be laminar and non–turbulent.

The term "E_k" typically stands for turbulent kinetic energy. However, it is still possible to calculate the instantaneous kinetic energy per unit volume of the fluid due to the wave motion, which is related to the wave velocity and the density of the fluid. Time (period) or space (length) averaging gives the mean value of the kinetic energy. The time–averaged in the entire column, is then, per unit surface area,

$$\boldsymbol{E_k(\theta)} = \overline{\int_{-h}^{\eta} \frac{1}{2}\rho(ux^2 + uz^2)dz} \tag{26}$$

$$\boldsymbol{E_k} = \frac{1}{16}\rho g H^2 \tag{27}$$

The magnitude of kinetic and potential energy been the same is typical of conservative (nondissipative) systems in general [91]. The sum of the potential and kinetic energy is the overall average energy per unit surface area of the wave. The total average energy per unit surface area is denoted by the letter E.

$$\boldsymbol{E} = E_p + E_k = \frac{1}{8}\rho g H^2 \tag{28}$$

Energy transport in water waves is directly tied to wave energy flux, which quantifies the rate at which wave energy propagates in the direction of wave advance. Wave energy flux is defined as the energy transmitted through a vertical plane perpendicular to the wave direction, spanning the entire water depth. In linear wave theory, the average energy flux per unit wave crest width is mathematically expressed as:

$$\mathrm{P} = \frac{1}{T}\int_{t}^{t+T}\int_{-h}^{\eta} p_d\, u\, dz\, dt \tag{29}$$

where T represents the wave period, p_d the dynamic pressure ($p_d = p + \rho g z$), u the horizontal velocity, dz the vertical coordinate, and dt temporal averaging over a wave cycle. The integration is performed over the vertical domain from the seabed ($-h$) to the free surface (η) and across one complete wave period (t to $t + T$).

Upon integration, this expression simplifies to:

$$\overline{P} = \overline{E}nC = \overline{E}C_g \tag{30}$$

Here, P is referred to as wave energy flux, or wave power per unit length of wave front (Wm^{-1}), E is the wave energy density, C is the wave phase velocity, and C_g is the group velocity. The variable n, which is dimensionless, is defined as the ratio of group velocity to phase velocity (C_g/C), as described in prior formulations. This parameter n adjusts for the distribution of energy between wave components, depending on the wave type and water depth.

The concept of wave energy flux is pivotal in understanding the transport of energy in ocean waves. In practical applications, it forms the foundation for estimating the potential of wave energy as a renewable resource. The wave energy flux quantifies how much energy can be harnessed per unit width of wave crest and is a key metric in the design and optimization of WECs. For deep-water waves the group velocity can be approximated as half the phase velocity ($C_g = \frac{1}{2}C$), and the parameter n to 0.5. In shallow-water conditions the group velocity and phase velocity converge ($C_g \approx C$), leading to $n \approx 1$.

The group velocity C_g depends on the wave dispersion relation and can be written in terms of the wave phase velocity C as:

$$\boldsymbol{C_g = nC = \frac{1}{2}\frac{g\,T}{2\pi} = \frac{g\,T}{4\pi}} \tag{31}$$

Substituting equations 28 and 31 in equation 30, it is possible to rewrite the wave energy flux function of the wave height (H) and period (T) as:

$$\overline{\mathbf{P}} = \boldsymbol{\overline{E}C_g = \frac{\rho g^2 H^2 T}{32\pi}} \tag{32}$$

2.4.Numerical Modeling of wave propagation

Free surface flow simulation is a subject of great interest for coastal and maritime researchers, not only because of its complexity, but also due to its importance to marine structures design and optimization. When the focus is on the numerical modeling of a physical event, different approaches have been used to simulate the propagation of nonlinear waves and the fluid–structure interaction. It is common to divide such models into three major classes: Boussinesq, potential flow, and Navier–Stokes models.

To accurately model the extremely complex behavior of free surface flows along with maritime and coastal structures, where viscous forces have higher relevance, models based on the Navier–Stokes equations (NSEM) are needed to consider the viscous effects of boundary layer separation, turbulence, wave breaking, and overtopping [93].

The computational fluid dynamics (CFD) models require a significant computational processing capacity, which has become feasible with the advancements in modern computational power. This progress has enabled the efficient solution of the Navier–Stokes equations (NSEs), in conjunction with the continuity equations, for fluid–structure scenarios. Consequently, CFD simulations can now be employed to accurately analyze and understand fluid–structure interactions within reasonable timeframes.

Wave prediction requires a combination of environmental data, such as local wind–generated sea and swell, spatially and temporally varying winds, and irregular bathymetry and coastlines. Numerical models will attempt to mimic the physical processes that occur in nature, and predict waves as realistically as possible.

A comprehensive model that integrates the complete knowledge of wind–wave physics and could be appropriate in all situations is, still nowadays, computationally expensive. Instead, several models have been proposed for applications that consider particular circumstances.

The selection of the most suitable model for each situation demands an understanding of the target domain and the relative importance of the different physical processes involved. The main four areas of interest for wave prediction are:

- Deep Oceans – the area where bottom effects could be neglected;

- Shelf Seas – transition area from deep oceans to shoaling zone;
- Shoaling Zone – area sensitive to the shoaling effects;
- Artificial Structures – areas where there is an interaction between waves and any artificial structure (*e.g.*, breakwater, oil platform, island, reef).

Table 1 presents the relevance of each physical process to them [94]:

Table 1 – Relative importance of the physical mechanisms in different domains. The color scale represents the importance: negligible (white), minor importance (light blue), significant (blue), and dominant (dark blue). Adapted from [94].

Physical Process	Artificial Structures	Shoaling zone	Deep Water	Shelf Seas
Diffraction				
Depth refr./shoaling				
Current refraction				
Quad. Interactions				
Triad Interactions				
Atmospheric Input				
White–capping				
Depth Breaking				
Bottom Friction				

This difference in the importance of physical mechanisms in different domains leads to distinctive approaches to simulate water wave propagation. Usually, two major categories of models can be identified [95]:

(i) Deterministic (phase–resolving) models are usually derived from the Euler equation for potential flows (Laplace equation + boundary conditions) under the hypothesis of weak nonlinearity and in the limit of shallow water. The amplitudes and phases of each individual wave component are resolved in these models, which aim to simulate the time–varying water surface [95];

(ii) Stochastic (phase–averaged) models are derived from deterministic equations by applying a turbulence–like closure hypothesis to the infinite set of coupled equations governing the evolution of the spectral moments. For any given deterministic wave equation, with a suitable closure hypothesis, a stochastic model can be developed. Since the closure approximation invariably introduces errors, the underlying deterministic model is, in principle, more accurate than its stochastic counterpart [95].

As waves approach the shore, effects such as bottom friction and depth–induced wave breaking must be considered [95]. However, ocean waves are generally not modeled in all their detail as they propagate across the ocean, into shelf seas, and finally into coastal waters.

Except for simulations of small scales, such as a detailed survey on the reliability of a structure or local hydrodynamic of beaches, great detailing is generally not required since it leads to prohibitive computational requirements. So, some models use the statistical characteristics of waves, represented by the wave spectrum, which can be determined either from observations or with computer simulations based on wind, tides, and seabed topography [92].

2.4.1. Phase–resolving Models

The phase–resolving models attempt to represent the time–varying water free surface, resolving both the amplitudes and phases of the individual wave components. Phase–resolving models have generally been used for the propagation of waves in nearshore regions where there are relatively rapid changes in water depth and shoreline [96,97].

Phase–resolving models could be categorized according to the values of the nonlinearity parameters (ak or a/h), the relative water depth (kh), or the bottom slope (Δb). Where "a" is the wave amplitude, "k" is the wave number, and "h" is the water depth [94].

Models that do not rely on simplifying assumptions about the magnitude of the aforementioned parameters in their formulation are referred to as "exact" models. However, it is important to note that these models do not yield exact solutions, as their implementation requires numerical methods. This class of models is typically solved using *boundary integral methods* [94,98], also referred to as *boundary element methods, BEM*.

For conditions with a small bottom slope ($a << kh$) and with waves weakly nonlinear ($ak << 1$), it is possible to expand the velocity potential as a Taylor series, leading to the *mild–slope equation models* [94].

When both the relative depth parameter and the bottom slope are small ($kh << 1, \Delta b << 1$), combined with a weak nonlinearity ($a/h << 1$), *Boussinesq equation models* result. If a no-reflection situation with waves only propagation forward is assumed, the Boussinesq equations can be reduced to the Korteweg–de Vries equations [94].

The fluid can be depth–averaged or multi–layered. These models can be used for simulating wave transformation in the surf and swash zones, complex changes in rapidly varied flows (wave breaking and coastal flooding), density–driven flows in coastal seas, estuaries, lakes, and rivers, and large–scale oceanic circulation [99].

In general, there are two sets of equations that belong to this class of depth–integrated, wave–resolving models: nonlinear shallow water equations – NSWEs [100,101]; and the numerous equations of Boussinesq type, all of which stem from the work of Peregrine [39].

NSWE modeling approaches present good response where nonlinearity predominates, with good performance from the surf zone shoreward, modeling breaking wave, run–up, in a depth–integrated form [102], and the moving shoreline. However, the absence of frequency dispersion leads to an incorrect propagation of ocean waves in deeper waters, causing an abnormal wave breaking [99].

2.4.2. Phase–averaging Models

Phase–averaging models predict average or integral properties of the wave field, considering the evolution of the directional wave spectrum. There is no attempt made to predict the phases of the spectral components, instead, it assumes a Gaussian random wave model [94].

Some of the simplest properties calculated are the significant wave height or peak wave period. Nevertheless, these models can predict the spatial and temporal development of the directional spectrum.

An important aspect to understand phase–averaging models is the source term, which represents all physical processes that transfer energy to, from, or within the spectrum. This term is composed by the summation of independent processes like atmospheric input from wind (S_{in}), nonlinear interactions between spectral components (S_{nl}), dissipation due to "*white–capping*" (S_{ds}), dissipation due to interaction with the bottom (S_b), among others. Thus, the source term represents all effects of generation, wave–wave interactions, and dissipation.

Those four parameters are the major ones to describe the source term for wind–generated waves. Nonetheless, in deep waters, usually aiming simplicity, the source term could be reduced to include just three, removing the bottom dissipation ($S_{tot} = S_{in} + S_{nl} + S_{ds}$).

The review of phase–averaging models, along with the examples of their implementation, is discussed in detail in following sections. These sections provide a comprehensive overview of the specific models employed in various research studies. Furthermore, the limitations associated with these models are also examined, shedding light on the constraints and considerations that need to be taken into account when applying such approaches.

2.4.2.1. Spectral modelling of waves in deep waters

In deep water environments, where seabed influence on wave motion is negligible, wave characteristics are primarily shaped by wind speed, fetch, and the duration of sustained wind [92]. Spectral wave models, such as JONSWAP [103] and Pierson–Moskowitz [104], effectively describe wave spectra under idealized conditions. However, real–world complexities necessitate a spectral energy balance approach that is able of considering the wave generation process, propagation, nonlinear interactions, and energy dissipation [105]. Eulerian methods are preferred for computational efficiency due to wave interactions [106].

Oceanic environments can be described using a deep-water condition, where seabed influence on wave motion is negligible. Typically found along straight or gently curving coastlines without significant currents or obstacles, these environments allow for simplified wave modeling [92]. Under such ideal conditions, wave characteristics, including significant wave height, period, and spectral distribution, are primarily determined by wind forcing, fetch, and duration. Spectral models like JONSWAP and Pierson–Moskowitz accurately represent wave spectra for young and fully developed seas, respectively, with directional spreading typically around 30º.

However, real–world oceanic conditions often deviate significantly from these idealized scenarios, necessitating more sophisticated modeling approaches. The concepts of fetch and duration become inadequate in complex oceanic environments. Consequently, the spectral energy balance equation emerges as a fundamental tool for describing the temporal evolution of wave spectra. This equation accounts for various physical processes, including wave propagation, generation through wind input, nonlinear wave–wave interactions, and energy dissipation due to wave breaking [105].

The formulation of this energy balance can be approached through two primary methodologies: the Lagrangian method, based on the tracking of wave rays, and the Eulerian method, which utilizes a fixed grid on the ocean surface. Given the inherent complexity arising from the interactions among numerous wave components, the Eulerian approach generally proves more suitable for computational purposes [106].

Wave generation in deep water is primarily attributed to atmospheric pressure fluctuations induced by wave–induced airflow, rather than direct wind stress [107]. Energy dissipation predominantly occurs through wave breaking, commonly referred to as whitecapping. Nonlinear quadruplet wave–wave interactions play a crucial role in redistributing energy within the wave spectrum without altering its total energy content [108].

These interactions contribute to a downshift in peak frequency and stabilize the spectral shape, reinforcing the characteristic JONSWAP spectrum for wind–sea conditions. As waves propagate away from their generation area, they evolve into swell, characterized by a narrower frequency and directional spectrum, reflecting the imprint of the generating storm rather than the local wind conditions [94].

To accurately model wave spectra in deep water, it is essential to employ short–term statistical descriptions. Time series of sea surface elevation, typically ranging from 15 to 30 minutes, provide the necessary data for characterizing wave conditions through parameters such as significant wave height and period [109].

A more comprehensive statistical representation is achieved through the random–phase/amplitude model, which treats the sea surface as a superposition of numerous independent harmonic waves. This model leads to the concept of the variance density spectrum, offering a detailed description of how the wave energy is distributed across different frequencies and directions [109]. For stationary and Gaussian sea surfaces, the variance density spectrum provides a complete statistical characterization of the wave field.

Third–generation phase–averaged spectral wave models, such as WAM [110] and WAVEWATCH III [111], are widely used for large–scale wave forecasting [109]. These models assume weak forcing and quasi–linear wave evolution, governed by the energy balance equation. The quasi–Gaussian, quasi–homogeneous, and quasi–stationary nature of wave fields allows for efficient and accurate large–scale predictions [105].

While WAM and WWIII excel in deep waters, models like SWAN are better suited for coastal regions [112]. Nested modeling systems can combine these models to cover various spatial scales.

Wave energy assessments worldwide have highlighted the potential of this resource using WAN, WWIII and/or SWAN. Studies in the United States, Chile, China, Europe, and various other regions have reported significant wave power levels [67]. For Portugal, studies analyzed wave power under various sea states along the northern and central coasts. These studies identified maximum wave power values ranging from 30 kW/m to 600 kW/m, depending on the sea state [113]. A comprehensive 3–year simulation along the Iberian Peninsula's north and west coasts showed significant seasonal variations, peaking at 90 kW/m during winter, and 10 kW/m in summer time [114]. These findings emphasize the importance of accurate wave modeling for assessing and exploiting wave energy resources.

Summarizing, phase–averaged spectral wave models simulate large–scale ocean wave evolution by solving the energy balance equation with a computational grid with resolutions that can reach hundreds of kilometers. These models track the distribution of wave energy across frequencies and directions, capturing essential wave dynamics while averaging out rapid phase fluctuations. By incorporating physical processes like wind input, wave–wave interactions, and dissipation, these models predict key wave parameters and inform various oceanographic applications.

2.4.2.2. Spectral modelling of waves in shallow waters

Coastal waters are defined as bodies of water that are close to the coast, shallow enough to affect waves, and may include (small) islands, headlands, reefs, tidal flats, estuaries, harbors, or other features. They also have ambient currents that are influenced by tides, storm surges, or river discharge, and their water levels vary over time. Under certain idealized conditions, such as a constant wind blowing perpendicularly off a long and straight coastline, over shallow water with constant depth, the significant wave height is determined by the wind speed, fetch, wind duration, and depth. These factors also influence the significant wave period and the energy density spectrum.

Under these idealized conditions, the spectrum has a universal shape known as the TMA spectrum [115], which is a generalization of the JONSWAP spectrum. The directional width of this TMA spectrum remains consistent with that in deep water [92]. In more realistic, arbitrary coastal–water conditions, the spectral energy balance of the waves is used to compute wave conditions. This shallow–water version of the energy balance is conceptually a straightforward extension of the energy balance in oceanic waters, with the wave spectrum based on the wave–wave interactions, generation, dissipation and propagation of spectral components individually.

As in oceanic waters, computations using the spectral energy balance should employ a Eulerian representation based on a computational grid projected onto the coastal region. Ambient currents are accounted for by replacing the energy density with the action density (*i.e.*, the energy density divided by the relative frequency) in the energy–balance equation and applying other relatively simple conceptual measures. Refraction is included in the energy or action balance equation through an additional transport term, while diffraction is only experimentally formulated in the energy balance equation.

As the water depth decreases, the processes of wave generation by wind, quadruplet wave–wave interactions, and dissipation by white–capping intensify, joined by bottom dissipation. In very shallow water, just outside and within the surf zone, triad wave–wave interactions and depth–induced breaking become significant, dominating wave evolution in the surf zone. The combination of triad wave–wave interactions and depth–induced wave breaking tends to stabilize the spectrum into the universal TMA shape. However, in fully developed, shallow–water conditions near the outer edge of the surf zone, triad interactions may create an additional (secondary) high–frequency peak in the spectrum.

The success of the phase–averaged approach in the open ocean [116] has inspired its application to large–scale coastal water domains. Consequently, phase–averaged models like SWAN [112] and TOMAWAC [117] were developed and are now commonly used for coastal applications [118]. These models solve a single energy balance equation, originally developed for global wave forecasting, with some modifications to account for finite depth effects [119] and important shallow water processes, such as near–resonant triad interactions [120] and depth–induced breaking [121]. These adjustments are made using designated source/sink terms.

These modifications are based on the assumption that coastal wave fields can be considered quasi–Gaussian, quasi–homogeneous, and quasi–stationary random processes [92]. However, as waves in shallower waters, waves develop faster as the mean forcing becomes stronger. Additionally, the dispersion effect weakens in shallower waters. This diminishes the validity of the statistical properties (*i.e.*, weakly forced and strongly dispersed wave fields) that underpin the energy balance equation in coastal phase–averaged models. This raises questions about the adequacy of these models in providing a complete statistical description of coastal wave fields.

Two key assumptions become particularly questionable in coastal waters. The first is quasi–homogeneity, which, to the leading order, ignores possible coherent structures induced by simple linear interference effects. These effects are frequently observed in coastal seas, where bathymetry and smaller–scale ambient current patterns cause wave fields to change rapidly [122]. The second questionable assumption is quasi–Gaussianity. In shallow coastal waters, wave triads are nearly resonant, leading to strong correlations over relatively small scales. The weakening of the dispersion effect, which typically promotes Gaussian statistics, further challenges the assumption of Gaussianity. In other words, shallow water coastal waves are non–Gaussian [123].

Phase–averaged models for shallow water nonlinearity are based on a quadratic model and a statistical truncation assumption. The quadratic model allows for the formulation of the evolution equations for the statistical moments of a wave field. The quadratic term generates a hierarchical dependency between the moments, leading to an infinite set of equations, which requires a truncation assumption, thus expressing the famous closure problem of turbulence theory [124]. The common truncation strategy is the fourth–cumulant discard, resulting in a coupled set of two equations for the second–order spectrum and third–order bispectrum [125,126].

However, as nonlinearity intensifies, the fourth–cumulant neglection leads to over–predicted bispectral values [127,128]. This observation has motivated the development of heuristic closure strategies to limit significant deviations from Gaussian statistics [127–129]. These solutions emphasize the challenges posed by the closure problem and the need for further research and development. Furthermore, the numerical solution of the coupling between the spectrum and bispectrum over large scales is computationally demanding, prompting further simplifications for practical use [120,130–132].

The formulation of the quadratic model neglects higher–order nonlinear terms, which can lead to a lack of reliability of this approach, particularly in areas with high nonlinearity such as shallow waters. Despite this, efforts have focused on improving the linear properties of models [126,133–139], and improving linear characteristics, such as dispersion and shoaling. However, there is uncertainty regarding the prediction of nonlinear evolution because of the truncation error associated with the changes in the quadratic coefficients.

The Whitham equation [140] is an example of how refining the linear dispersion relation can significantly influence nonlinear model behavior. As a generalized Korteweg–de Vries (KdV) equation [141], the Whitham equation incorporates a more complete representation of the linear dispersion relation. While this improvement is aimed to yield a more accurate representation of wave field evolution, particularly for shorter wave components, it can strongly alter the characteristics of modulational instability [142,143]. This shift can lead to instability in shallower water depths higher than predicted by the KdV equation.

Consequently, the Whitham equation, unlike the modulationally stable KdV equation, exhibits modulational instability. This instability can result in erroneous predictions of narrowband field recurrence in shallow waters, potentially leading to incorrect energy transfers and inaccurate evolution of peak frequency components. Furthermore, these errors can also impact the development of infragravity components due to improper modulations of the wave field.

The dynamics of waves in coastal waters are complex and influenced by factors such as shoaling, refraction, and breaking. These phenomena arise from nonlinear wave–wave interactions and the interaction of waves with varying bottom topography and currents. Accurate wave prediction is crucial for coastal communities, engineers, and municipalities, as it informs decisions related to nearshore circulation, sediment transport, shipping operations, coastal safety, and erosion prevention.

Traditional deterministic wave prediction models often employ dimensional reduction techniques like the Boussinesq or mild–slope approach. However, these approaches can limit the accuracy of wave propagation simulations, especially for waves with a wide spectral width or in regions with complex bathymetry. To address these limitations, non–local formulations based on the Dirichlet–to–Neumann (DtN) operator have been developed. The DtN operator allows for a fully dispersive representation of wave propagation, preserving the accuracy of the linear dispersion relation.

While the DtN approach has been successfully applied to wave propagation in deep water and over constant depth, its extension to varying bathymetry presents challenges. Existing formulations often assume small bottom perturbations, which may not be accurate in coastal areas with mild slopes and significant bottom amplitudes. Consequently, these formulations may struggle to accurately predict wave field parameters, particularly as waves transition from deep to shallow water.

While phase–averaged spectral models have been designed to include basic shallow water effects, they tend to focus on deep and intermediate depth waves. Several limitations are associated with using phase–averaged models in coastal domains: (1) they are based on an energy balance equation for weakly nonlinear waves; (2) they rely on linear wave theory to relate the wave field to the bathymetry and ambient current patterns; (3) they assume that nonlinear interactions are weak, and energy is primarily exchanged through resonant four–wave interactions; and (4) they employ simple parameterizations for shallow water processes such as wave breaking, bottom friction, and wave–wave interactions.

In practice, these limitations mean that phase–averaged models may not accurately predict the details of wave transformation in shallow waters, especially for complex coastal environments where strong nonlinear interactions and wave–breaking processes dominate. To address these challenges, alternative approaches, such as phase–resolving models, directly solve the nonlinear governing equations of wave motion, including higher–order interactions. These models can provide more accurate predictions of wave evolution in coastal regions but are computationally demanding and may not be suitable for large–scale applications.

Overall, the accuracy and reliability of wave models in coastal waters depend on the balance between the complexity of the physical processes included and the computational resources available. Advances in numerical techniques, computational power, and the understanding of coastal wave dynamics continue to drive the development of more accurate and efficient wave models for coastal applications.

2.4.3. Modeling the WEC park effect

Phase–averaged and phase–resolving models should not be directly compared, since they are complementary tools. However, their application domains could be the same in specific areas [94].

The phase–resolving approach applies hydrodynamic laws to calculate the movement of the water free surface, the velocity of water particles, and the wave–induced pressure in the water with great precision at any time and space in the domain. Thus, the description and modeling of waves are fully deterministic, being possible to compute every change in the evolution of the waves, like waves' breaking in the surf zone or on a breakwater [92].

However, for larger scale domains, the phase–resolving models are not commonly applied [144], mostly because of the overwhelming calculation requirements and the lower capability to obtain feasible detailed wind data for this scale. On the other hand, in practice, this level of detail is not required [92].

Ocean waves' description at a large spatial domain could ignore this level of detail aiming at characteristics that are relevant and predictable. This could be achieved by applying specific averages of the waves in space and time, *i.e.*, applying the phase–averaging approach, in which statistical properties are defined and modeled. However, to achieve feasible results with the averaging data, the wave situation must be homogeneous and stationary in the space and time interval considered. For waves not extremely steep in not shallow waters, the physically and statistically most significant phase–averaged characteristic is the wave spectrum [92].

In summary, if the wave properties vary rapidly, on an order of a few wavelengths, then it will be required the application of a phase–resolving model. On the other hand, if the wave properties vary slowly, on a scale of several wavelengths, then phase–averaging models would be adopted [94].

The effect of WEC farms could be divided into two classes regarding the distance from the devices: the near field and the far field effects. In terms of computer processing capacity, the simulations can be divided into two categories. One that fully couples the WEC motion and wave kinematics, but relies on extensive simplifications on what concerns the environment (*e.g.*, wave conditions and bathymetry) and device geometry. And the other with less accuracy on wave–structure interaction (WSI), but that can better simulate several devices in real conditions, such as realistic irregular wave, over long periods and large domains.

Near field effects are commonly simulated by BEM models, such as, WAMIT [145] and NEMOH [146]. The use of CFD models, resolving the NSEs, or Smoothed Particle Hydrodynamics (SPH) methods, for modeling the fluid–structure interaction is growing with the advances in the computer processing capacity [147–149]. BEM models require a flat bottom, while CFD solvers rapidly increase the computational time with irregular bathymetry. Hence, these models are framed in the first category and it is not feasible to use them for far field effects.

The employment of wave propagation models takes place in far field effects simulations. Several studies have compared the environmental impacts of WECs in different wave scenarios. It is suggested that the energy extraction capabilities of a specific device can be incorporated into nearshore wave propagation modeling software using semi–empirical models that represent the natural generation, dissipation, and transmission of energy. These models can be used to predict the impact of the WEC on the wave energy resource and nearshore wave behavior.

Phase–averaging models are a computationally efficient option for modeling wave properties and nearshore wave–induced current fields, but they rely on parametrizations to represent the WEC and other relevant wave characteristics. Typically, the device is represented as a porous structure [150] that work as either a source or a sink term [32], extracting a specific amount of wave energy. Spectral wave propagation models, such as the MIKE 21 SW [151] and the TOMAWAC [152], have been applied, however the most common and broadly used is the SWAN [9–12,18,23,31,56–62,66,83–87,153–163] and its modified version the SNL–SWAN [32,164], introduced by Smith [13].

In order to accurately simulate currents and sediment transport, phase–averaging models are often coupled with other models, such as ROMS for circulation and XBeach for sediment transport. Another viable option is the utilization of the Delft3D application, which integrates multiple models within a user–friendly graphical user interface (GUI). This comprehensive software tool enables the coupling of a wave model (SWAN) with current flows and morphological changes, facilitating a more comprehensive analysis of coastal processes.

The porous layer method in SWAN was pioneered by Millar *et al.* [31], which represented the WEC's impact on wave conditions with generalized transmission coefficients. However, this method ignores intrinsic information, such as the WEC viscous power losses, and treats the devices as barriers with an idealized reflection and transmission coefficient.

Carbalo and Iglesias [87] applied in SWAN the transmission coefficient (k_t) of WAVECAT device measured in wave tank tests at the Hydraulics Laboratory of FEUP. Abanades *et al.* [9–11,18] applied this k_t to assess the impact of wave farms on coastal morphodynamics and have found that wave farms decrease erosion but also decrease beach accretion. While Astariz *et al*. [23,56–62,66,83–86] applied similar techniques to study the influence of WEC arrays on co–located wind–wave offshore energy parks.

The SNL–SWAN refers to the improvements that the Sandia National Lab made to the code of SWAN, including new types of obstacles that calculate the k_t based on the WEC power matrix or the Relative Capture Width curve [34–36] and allow frequency–dependent wave energy transmission through the obstacle. Luczko *et al*. [32] improved the model fidelity and accuracy including viscous drag and moorings into k_t calculation.

The use of phase–resolving models to simulate the coastal impacts of wave farms is rising. Those application used models like REFDIF [16], Boussinesq Wave [165,166], Mild–slope (Mildwave) [167–170] and non–hydrostatic wave–flow models (SWASH) [171–173]. These models can more accurately depict wave transformation processes, such as shoaling, refraction, diffraction, and nonlinear wave–wave interactions, by resolving individual waves and solving mass and momentum balance equations. Additionally, by including phase information and capturing dynamic wave–WEC interactions, wave–resolving models can produce more accurate downstream predictions of the influence of individual or groups of WECs. Rijnsdorp *et al*. [172] demonstrated the capabilities of SWASH in simulating wave–WEC interactions under linear and nonlinear wave conditions.

Nearshore shallow waters have highly nonlinear hydrodynamic processes, and SWASH has been successfully used and validated there [174–177]. These findings show how SWASH could be used to validate phase–averaged models. David *et al*. [173] compared the coastal impacts of a WEC farm using both a coupled wave–averaged flow model (Delft3D–SNL–SWAN) and a non–hydrostatic wave–resolving model (SWASH). The simulations showed that both models predicted similar impacts, including reduced wave heights near shore and the generation of converging nearshore currents. However, significant differences were observed between the models in the wave farm region, likely due to differences in the representation of WECs.

To summarize, phase–averaged wave models are used to predict the average properties of waves over a certain period of time, such as the mean wave height or the mean wave period. These models are useful for predicting the long–term behavior of waves and for design purposes, such as determining the required strength of a coastal structure or predicting the loads on an offshore platform. Phase–resolving wave models, on the other hand, are used to predict the detailed time–dependent behavior of waves and are able to provide more accurate and detailed predictions of wave behavior, particularly for highly nonlinear wave phenomena such as breaking waves or wave–structure interactions. Both phase–averaged and phase–resolving wave models can be useful tools for assessing the environmental impacts of wave energy conversion technologies. The choice of model will depend on the specific application and the level of accuracy and detail required.

2.5.Offshore energy park layout optimization

The overall performance of an offshore wave energy array is influenced by the size, shape, and characteristics of each device, as well as the local wave climate [42]. Layout optimization of a wave energy farm has been broadly investigated; however, the process remains incomplete. Hence, this remains a pertinent research topic in WEC farm design [178].

Several investigations on the layout optimization problem have been conducted, some based on numerical software and others on analytical models. However, a few numerical models also relied on experimental results [179]. To perform optimization of large wave energy farms with many devices and parameters, semi–analytical methods were often the most selected, while studies applying analytical models were usually for single or a few floating bodies.

The effect of changing the distance between WECs in an array was studied by Ringwood and Korde [180], with arrays having up to four devices considering four arbitrary geometries of the layout. The work demonstrated that an improvement of 40% in *q-factor* can be obtained when control and separation distances were selected properly [178].

These research works did not investigate the optimal layout or propose new algorithms to maximize the *q-factor*. The layouts rely on a researcher's educated judgment, and only WECs with simple geometry were considered, like spheres, arranged in a simple way, such as rows [181]. The basic conclusion made was that the spacing between converters has a higher impact on *q-factor* than the device geometry [182,183].

This section presents a review on the main methods of WEC farm layout optimization applied until now. The methods are divided into two large groups: the analytical methods, and the computational intelligence methods. A deeper review can be seen in Teixeira–Duarte *et al*. [3].

The layout optimization of offshore WECs is a multidisciplinary task with high complexity, mainly due to the many interrelated purposes, restrictions and variables involved. Hence, the achievement of a final solution usually results from empirical procedures with numerous rounds of trial and error [42]. The decision on the layout is established by the team planner following *Ad Hoc* and heuristic approaches. However, over time, it has been growing the research and utilization of more automated, holistic, and repeatable approaches, mainly using computational procedures to achieve the optimal arrangement of the layout for enhancing energy production and reducing the cost of operation, maintenance, and distribution [38,184].

The layout of an offshore park defines the position of all devices relative to one another and the electrical grid, mutually. A variety of trade–offs should be considered when selecting an optimal layout, depending mostly on two factors: the distance from shore and the spacing between devices [42].

To resolve optimization layout problems, there are mainly three types of techniques:

- Experimental methods – can be applied in the laboratory or in the field, however, they are commonly highly expensive, time–consuming, and have low parameters flexibility, hence, usually, they are used often just at the last stage of development to validate some other technique;
- Analytical methods or mathematical techniques – are used to increase the understanding of problems, using equations to provide exact solutions. Although as the problem grows in complexity and variability, it becomes more and more challenging to fit some analytical method.

They are efficient at finding local optima, although they do not assure to achieve the global optima;

- Numerical methods – utilize probabilistic approaches to iteratively generate a sequence of approximations close to the exact solution and have become more popular with the development of more powerful computer hardware.

Both analytical and numerical methods could utilize optimization algorithms, which can be of different types: a deterministic method, such as the analytical itself or an exhaustive search method; a stochastic method; or a heuristic technique.

An exhaustive search ensures the global optimal utilizing a systematic approach to sample the entire solution domain at a satisfactory resolution. Nevertheless, they are extremely computationally expensive for complex solutions, turning challenging the data analysis in some cases.

Stochastic algorithms, like the Monte Carlo method, randomly sample the solution domain a sufficient number of times to ensure that a global optimal solution is found. Although these approaches are commonly more computationally efficient than an exhaustive search method, they are still computationally expensive for complex cases.

Heuristic algorithms use the previous experience of the researcher to sample the solution domain, aiming to fit the most optimal solution, with the least number of function evaluations possible. However, by definition, they do not ensure global optimization. The inclusion of randomness in some algorithms allows a search through multiple optima, avoiding entrapment in a local optimum. A heuristic algorithm is commonly used when the stochastic approach becomes unreasonably computationally expensive. Some examples of heuristic methods utilized for layout optimization of offshore WEC farms are Evolutionary Algorithms, including genetic algorithms, Covariance Matrix Adaptation – Evolution Strategy, and Differential Evolution. Figure 15 presents a taxonomy of optimization algorithms.

To settle a baseline on the layout optimization methodologies, the following sub–sections present a brief explanation of the most used techniques applied, until this moment, to layout optimization of WEC farms, explaining the founding theory of each one, their working logic, and application in the wave energy field.

2.5.1. Analytical and Semi–Analytical methods

Analytical methods are specific, precise, accurate, and reliable. However, as the complexity of a system increases, the difficulty of fitting a precise and computationally feasible analytical equation to the problem reaches situations that are impossible to process, becoming necessary other approaches. A possibility is to integrate an analytical method to the parts that are well-known and developed and a numerical method to explore other more complex parts of the system. This is the basic concept of the semi–analytic approach.

In a semi–analytic framework, the system is manipulated to reduce the computational load and complexity required by a stochastic simulation. Hence, a method that combines the best of both analytical and stochastic methods could be a powerful tool for the analysis of complex systems.

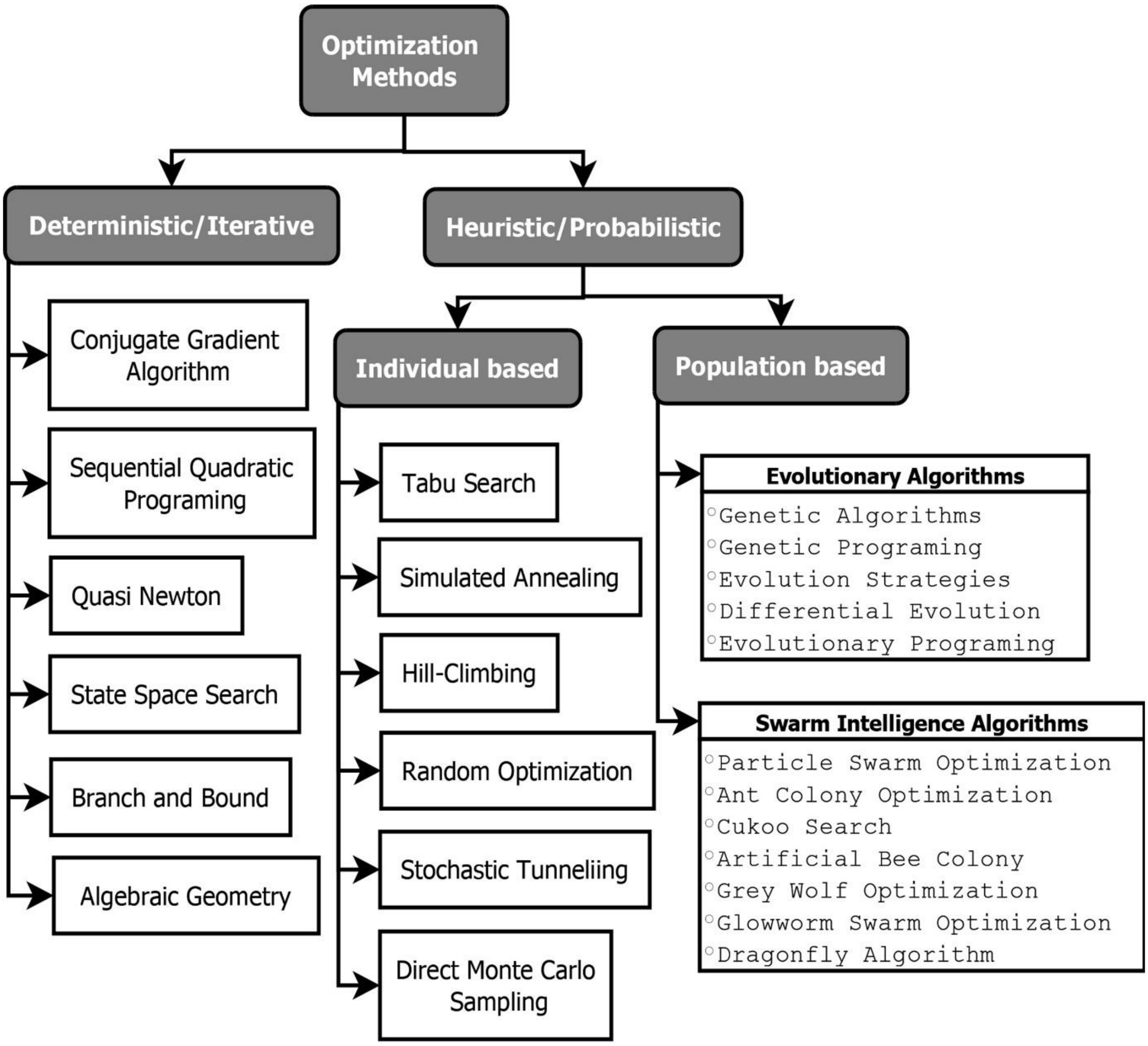

Figure 15 – Taxonomy of optimization algorithms (adapted from [92,93]).

Commonly, it is possible to distinguish three different parts of a semi–analytical framework: simulation, estimation, and analytical model. The simulation parts are used to determine the decision variable employed for recovering the transmitted symbol, the analytical model utilizes the system properties to define the quantities of interest. The estimation part is the connection between the simulated and analytical.

In the sequential framework, Figure 16, the chain of events is straightforward, with no feedback between the different elements. This usually requires beginning with a simulation to generate the processes and system functions that are too complex to describe analytically. Then, the estimation process applies the values received by the simulation to achieve key parameters for the analytical model, where these parameters integrate the variables of a known equation to obtain the final result. In this structure, the simplifications permitted by the analytical model provide the computational gain.

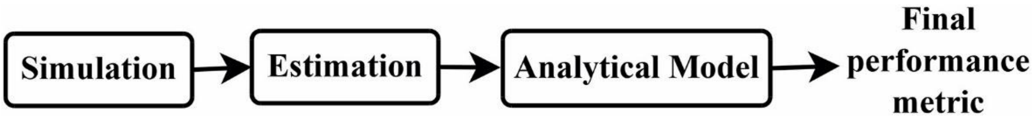

Figure 16 – Flowchart of a sequential semi–analytical approach.

In stochastic simulations, the computational complexity increases as more communication systems coexist inside the same environment, making it important to include the interaction of the separated systems and determine their inner potential interference. Furthermore, processing requirements have significant growth of random elements of each part of the communication chain. Given that, the semi–analytic techniques enable a reduction of these computational requirements by the expression of the evaluated metric analytically as a function of parameters projected during simulations. This assumption is the basic concept of the sequential semi–analytic approach, presented in Figure 16.

In the closed–loop approach, *Figure* 17, the simulation part processes the analytical model outputs, with the nonlinear segments fully simulated and quantities like, for example, the loop discriminator and filter outputs being calculated. The estimation block is, like in the sequential approach, used to integrate the simulation and analytical components of the scheme, with the new estimate parameter obtained used to generate new correlator outputs. Nevertheless, the estimation part also computes performance metrics according to the ending parameters.

Since the initial studies on wave energy, analytical techniques have been largely used to determine hydrodynamic parameters, because of the low computational costs required, the interaction wave–device, the power output of the park, and the spacing between WECs. However, they lose accuracy as the systems get larger and more complex, due to the simplification made to fit the equations.

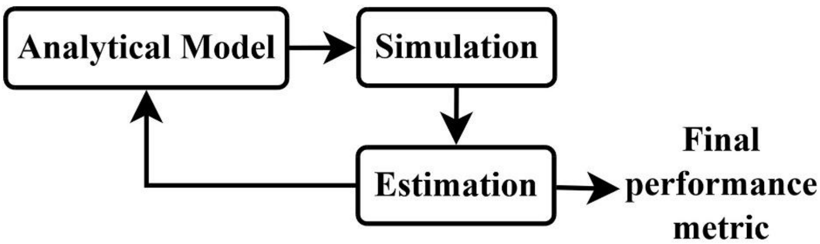

Figure 17 – Flowchart of a closed–loop semi–analytical approach.

The first investigations on wave energy farms made by Budal [80,81], Falnes [187] and Evans [188] employed analytical methods for hydrodynamic modeling. These investigations adopted the point absorber approximation, considering the devices to be sufficiently small that the interaction resulting from scattered waves could be disregarded. Similarly, in the plane–wave approximation utilized by Simon [189] the structures are assumed to be sufficiently separated, allowing their interaction to be treated as an approximation of plane waves with complex amplitudes. This approach facilitated the treatment of wave interactions as additional incident waves, while neglecting the contribution of evanescent modes.

The point absorber approximation performs fairly well at low frequencies and for large separating distances, while the plane–wave approximation performs better at high frequencies [190]. Nevertheless, it is expected an error increase with more interacting units.

Falnes and Budal [191] observed that the wave period and the array configuration could lead the *q-factor* to be higher or lower than one. Nonetheless, higher *q-factor* (equation 33) values suffer great variations, and considering the polychromatic nature of real waves, it was suggested that a properly designed array configuration should focus on minimizing the destructive influences [192].

In the iterative multiple scattering method, developed by Ohkusu [193] and later applied in wave energy, the diffraction and radiation properties of isolated bodies are utilized, and the reflected waves inside the array are added iteratively until convergence is reached.

Simon [189] combined the iterative multiple scattering method with the direct matrix method, solving the wave amplitude around every structure simultaneously. This approach eliminated the need for iterative procedures and provided exact solutions within the assumptions of linear potential flow theory. For floating bodies, the resulting infinite matrices must be truncated, leading to a semi–exact method.

Fitzgerald and Thomas [194] investigated a layout optimization problem without using the small body approximation to simulate the motions of bodies. They consider the general layout of arrays in the plane. They applied the small body approximation instead of the point absorber approximation and performed a local layout optimization for five devices using the sequential quadratic programming (SQP) solver with multiple manually selected initial points [194].

Child and Venugopal [195], applied the interaction theory to solve interactions within the WEC array [196], and also introduced a method called parabolic intersection [197]. They claim it is beneficial to position the devices at the intersection points of certain parabolas centered at the other devices. The authors considered wave directionality and array layouts for five identical generic point absorbers and compared their method with a traditional genetic algorithm, using the MATLAB GA and Direct Search Toolbox. It was concluded that the parabolic intersection was more efficient but less accurate [178,197]. However, the accurate computation of the *q-factor* requires a BEM code and is presently computationally prohibitive within an optimization context [181].

Göteman *et al*. [198] investigated the use of devices with different dimensions in the same array and concluded that it could lead to an increase in total power production. Consequently, it is possible to achieve a reduction in costs and an improvement in production at the same time, being economically beneficial to deploy smaller and larger devices together in a wave energy farm. The authors also investigated different array configurations to minimize the output power fluctuations, optimizing the power variance for some wave conditions and array geometries.

Göteman *et al*. [199] used a semi–analytical method to study the performance of wave energy farms of over 1000 devices. Instead of numerical models to calculate the hydrodynamics, the authors used the potential flow theory to reduce computational costs. The power performances of layouts are similar, on the other hand, the variance of rectangular geometry (higher) was three times larger than that of the random geometry (lower). Figure 18 presents the layout comparison.

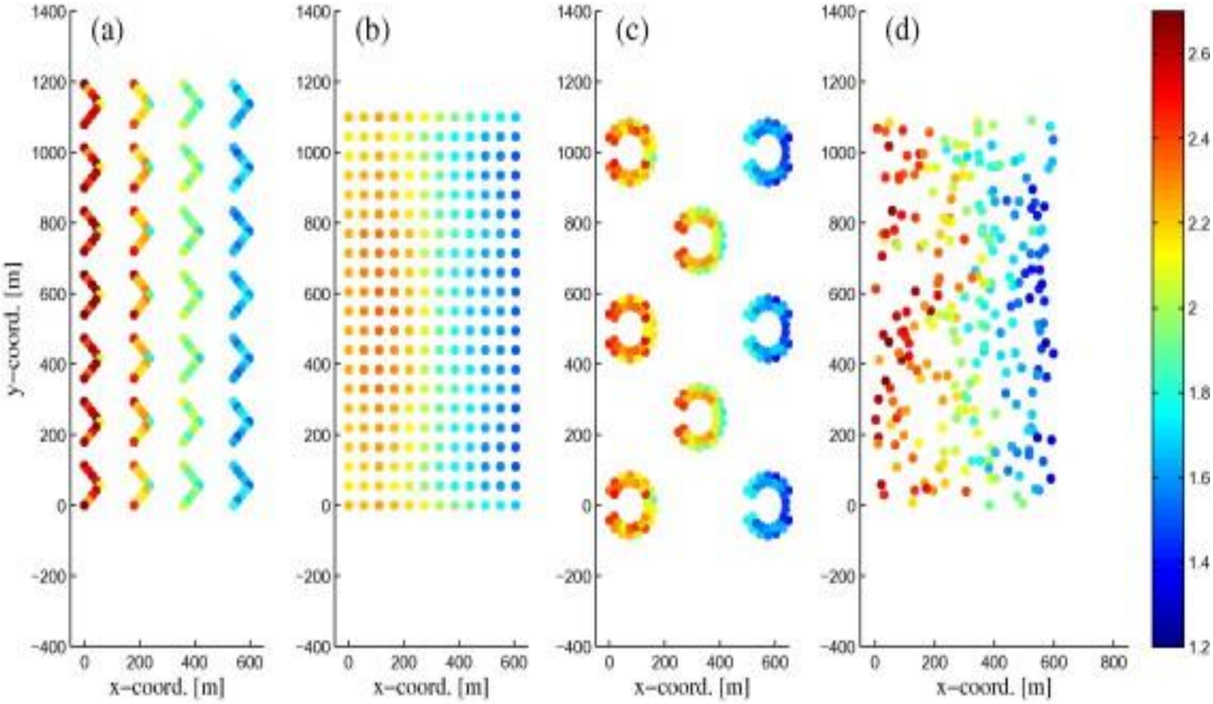

Figure 18 – Layout comparison of time–averaged power per WEC. The power scale ranges from 1.2 to 2.7 kW per WEC. The sea state is categorized by the energy period, T_e = 5.47 s, and the significant wave height, H_s = 1.02 m. Wave moving in the positive x–direction [199].

Göteman *et al*. [200] developed a method based on analytical multiple scattering theory and used time series of irregular wave amplitudes to compute the instantaneous power of each device, to model the hydrodynamic interactions and power output of very large wave energy farms.

McGuinness and Thomas [201] applied an analytical method, the sequential quadratic programming method, to identify the minimum value of an objective function for optimization of the spacing between heave–constrained, spherical point absorbers lay on a parallel line to the wave direction. In another study [202], the authors investigated three devices in a line perpendicular to the incoming waves, regular and irregular, and indicated the important possible variability in power development.

An expanded multiple scattering method was applied by Göteman [179], which used cylindrical bodies with changes in size, demonstrating a higher performance when different sizes are together.

Jianyang *et al.* [178] explored the optimal configuration of both dimension and layout of arrays of heaving buoys with full interaction and exact hydrodynamics using BEM, and a point absorber approximation for the initial setup for the array.

Analytical approaches are numerically efficient and capable of obtaining good results, even nowadays. However, they lose accuracy in more complex cases such as devices with multiple Degrees of Freedom or irregular waves.

2.5.2. Computational intelligence

Computational Intelligence (CI) is the theory, design, application, and development of biologically inspired computational paradigms [185]. It is inserted into Artificial Intelligence (AI), which is a concept for advanced information processing. The focus is to build algorithms capable of processing a huge amount of raw, incomplete, imprecise, or uncertain data, for approximating solutions for those complex problems [203]. These methods implement new approaches for analyzing and creating flexible information processed by humans, such as sensing, understanding, learning, recognizing, and thinking [186].

Conventionally, the three main areas of Computational Intelligence have been Neural Networks, based on the human brain; Fuzzy Systems, based on the way humans think, and Evolutionary Computation, based on natural evolution [204]. Table 2 summarize the main characteristics of each one.

Table 2 – Main areas of computational intelligence.

	Artificial Neural Networks	Fuzzy Systems	Evolutionary Computation
Description	Basic Computational analytical tools, with complex communication network	Data handling methodology that allows ambiguity	Based on natural evolution process
Algorithms	Multi–Layer feedforward; backpropagation algorithm; gradient descent	Fuzzy control language; Continuous set membership from 0 to 1	Stochastic search and optimization algorithms
Wave energy applications	Predict wave parameters (H_s T_e); estimate missing data; energy flux; control strategy	Control strategies; predict wave parameters	Missing data; estimate wave parameters; optimization of WEC shape and park layout
References	[203,205,206]	[203,207,208]	[203,207–209]

New approaches are presented frequently in addition to the three main areas, like ambient intelligence, artificial life, cultural learning, artificial endocrine networks, social reasoning, and artificial hormone networks [185].

2.5.2.1. Genetic Algorithms

Evolutionary Computation refers to a category of CI techniques inspired by biological theories. The algorithms could be classified as a metaheuristic optimization method, being capable of finding the global optimum, hence it is widely used in engineering optimization problems. Nevertheless, it has a significant computational requirement, as it needs a huge quantity of fitness function evaluations to achieve the global optimum [210].

Evolutionary computation includes several techniques, such as genetic programming, genetic algorithms, evolution strategies, swarm intelligence, differential evolution, evolvable hardware, multi–objective optimization, among others [185]. These techniques usually can be distinguished by the used approaches in terms of how they represent the individuals.

The genetic algorithms (GA) are the most recognized type of evolutionary algorithm and have been applied several times as function optimization and search method [211]. These are robust methods that do not necessitate derivative information and can manage a huge number of variables to achieve the minimum or the maximum of a function. Usually, this algorithm has a binary representation, a low probability of mutation, and an emphasis on genetically inspired recombination to determine the selection of the fittest, to generate the new candidate solutions.

The route is inspired by the continuous Darwinian improvement cycle of evaluation [212]. In GA, the survivability, or fitness, is evaluated by a selection operator, which determines the solutions that best solve the problem with minimum error. Figure 19 presents a GA cycle.

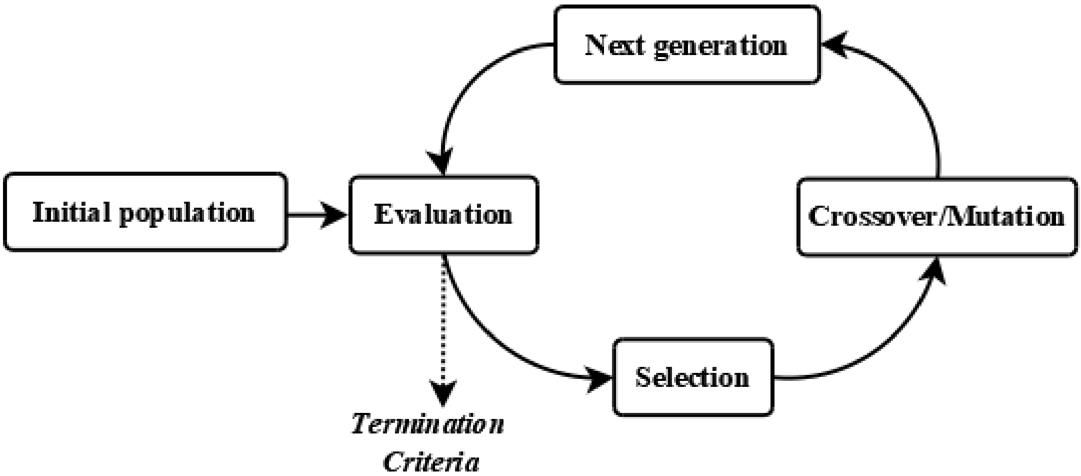

Figure 19 – A genetic Algorithm cycle (adapted from [212]**).**

The individuals of the populations are evaluated according to the objective function, the fitness. An evaluation step is a non–deterministic approach. The repetition of the process for several generations, the probability disseminates genes that promote higher fitness, creating better solutions and extinguishing the worse suited [203].

The initial population can be settled both randomly and heuristically. Then, the workflow of genetic algorithms enters an endless loop. Each individual is evaluated, and the best fitted are choosen to the next generation. The reproduction is performed by creating random pairs, or "mating partners", and applying some basic genetic operators, like crossover, that combine each pair, and mutation, which basically apply noise to the strings of genes with different probabilities, generating an entirely novel array of individuals. Although, it is possible that pieces, or even complete individuals, from the previous generations survive crossover and mutation without being modified, the likelihood of this hypothesis is relatively improbable [211].

The objective function does a similar job as the gradient or the derivative in conventional optimization techniques, where the selection is made following a selection strategy which picks individuals with probability proportional to their relative value and explores the solution domain searching for better solutions [212].

While the value of each fitness is important to determine the chances of its survival, there is no guarantee that the ones with the higher fitness values will survive or the smaller ones will perish, because of the non–deterministic nature of the method [213]. Given that, it could occur that some individuals with low fitness value genes might prove to be useful when recombined in new chromosomes, which is a low probability "second chance", offered by the process flexibility that would be impossible in a more deterministic setting [213].

A pseudocode of the steps for a Genetic algorithm approach could be synthesized as**:**

I. Setting a population
II. Assess the fitness of every individual
III. While termination criteria are not achieved
    a. select parents
    b. apply genetic operators to the selected individuals
        i. select mating partners
        ii. chromosome recombination
        iii. random mutation
    c. assess fitness values of new individuals
    d. select individuals for the next generation
IV. End while
V. Return the best sample

2.5.3. Computational intelligence applications

Blanco *et al*. [214] investigated a Multi–Objective Differential Evolution Algorithm (MODE) to optimize the energy production of a 2–Body Point absorber, with positioning, PTO system, control strategy, and hydrodynamic design as parameters. In another investigation [215], this approach was enhanced by the application of PTO constraints and two cost functions, which include the mean annual power produced and device surface.

Sharp and DuPont [216] presented a multi–objective method, using binary and continuous genetic algorithms, to determine array configurations considering as parameters the power output and costs in the evaluation function [217]. In another investigation [184], they used a coupled genetic algorithm and heuristics to investigate the minimum separation for a small number of devices, five, in a discretized space and a unidirectional wave. The method uses several layout evaluations, which could limit their application to more complex wave energy models. Figure 20 shows one of the layouts found by the authors in one case and its effect on the wave field simulated with WAMIT.

Wu *et al*. [218] used a variation of an evolutionary algorithm, and a covariance matrix adaptation–based evolutionary strategy (CMA–ES) aiming to achieve an improvement and a fast process in the optimization when considering a fully submerged three–tether buoy array. The investigation considered

25 and 50 devices and a unidirectional irregular wave model. The results indicate that the variation of EA, called 1+1EA, performed better for a small number of layout evaluations.

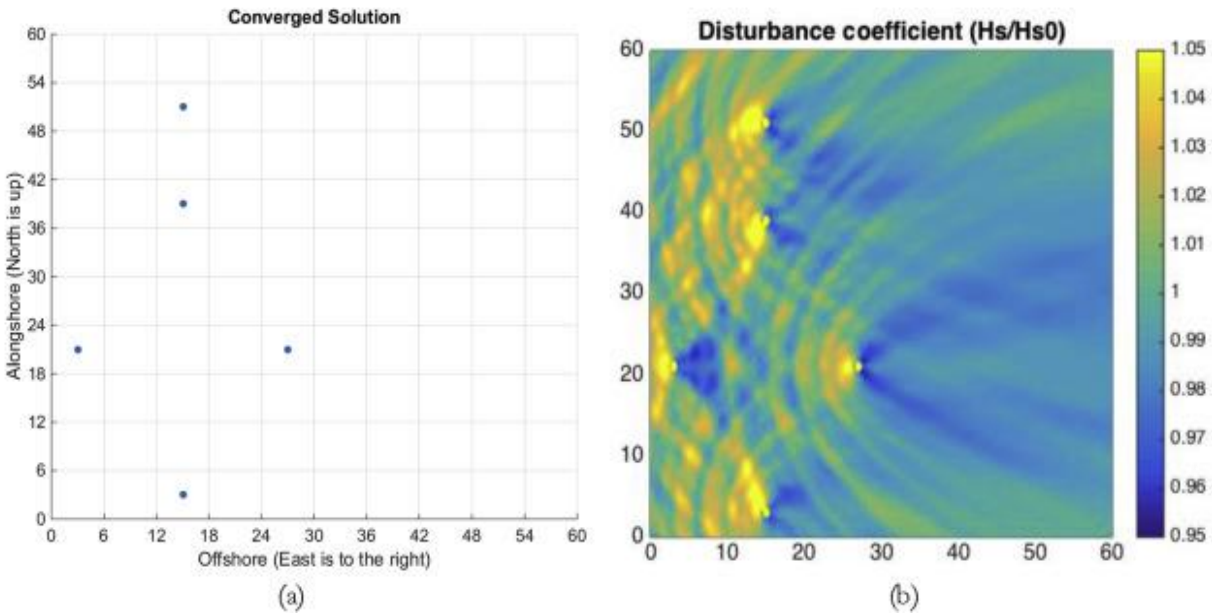

Figure 20 – Layout from case one of the compared cases with 6 m minimum separation distance (a). Corresponding wave characterized by the disturbance coefficient (ratio between significant wave height after and before the WEC) (b).

Sarkar *et al*. [192] applied an array optimization for 40 OWSC using machine learning, a Monte Carlo method, and a genetic algorithm. The hydrodynamic interaction was constrained between nearest neighbors for fast evaluations, and a machine learning approach was applied to identify optimal three–WEC clusters. Then, the optimization of the park used the genetic algorithm, with the same number of evaluations, 16 million, which outperformed the Monte Carlo method. This investigation also concluded also that clustering should be avoided for this type of device, although a positive interaction could be achieved.

The project DTOcean (optimal design tools for ocean energy arrays) developed a set of tools for the optimization of ocean energy systems [209].

Snyder and Moarefdoost [181,182] investigated the layout optimization using the point absorber approximation introduced by Budal [81], instead of simulating the exact hydrodynamics and proposed a greedy search heuristic to optimize the wave farm layout. They concluded that this method outperforms a specific GA and the general–purpose global solvers PSWARM (PSO) and NOMAD (Mesh Adaptive Direct Search algorithm). Figure 21 shows the layouts obtained, and Figure 22 the *q-factor* comparison between techniques.

Ruiz *et al*. [219] compared the convergence rate and efficiency of three Evolutionary Algorithms: a CMA–ES from DTOcean, a modified GA, and a GSO in a discrete search space with a simple wave energy model. The study concludes that CMA–ES converged faster but with less accuracy, in terms of energy production, when compared to the other two.

Ferri [220] compared the CMA–ES from DTOcean and a metamodel algorithm, surrogate–model based optimization method, to compare computational cost and energy production. The metamodel algorithm converged rapidly, but with less accuracy (estimation error of 10%), being suitable just to be used as an initial step on a hybrid method.

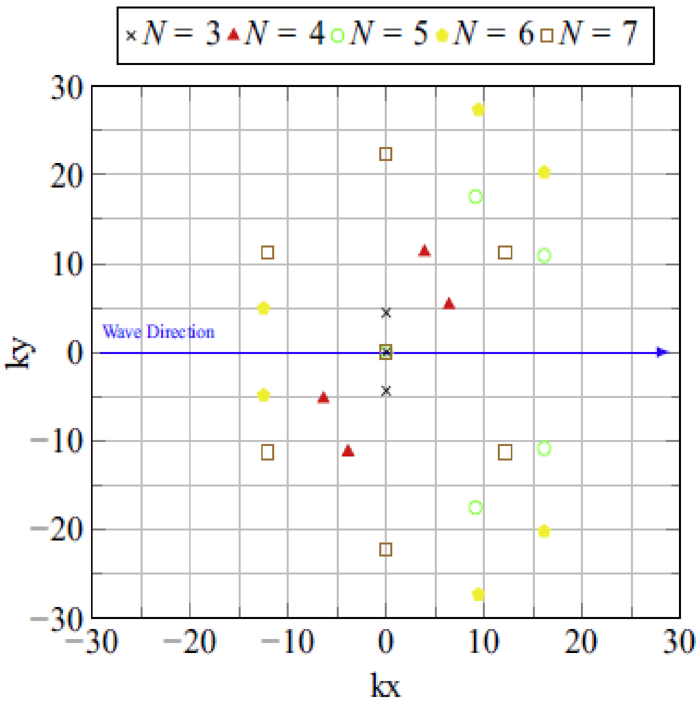

Figure 21 – Layouts configuration obtained by Snyder and Moarefdoost [182] for 3,4,5,6 and 7 WECs. All layouts have a WEC at the origin.

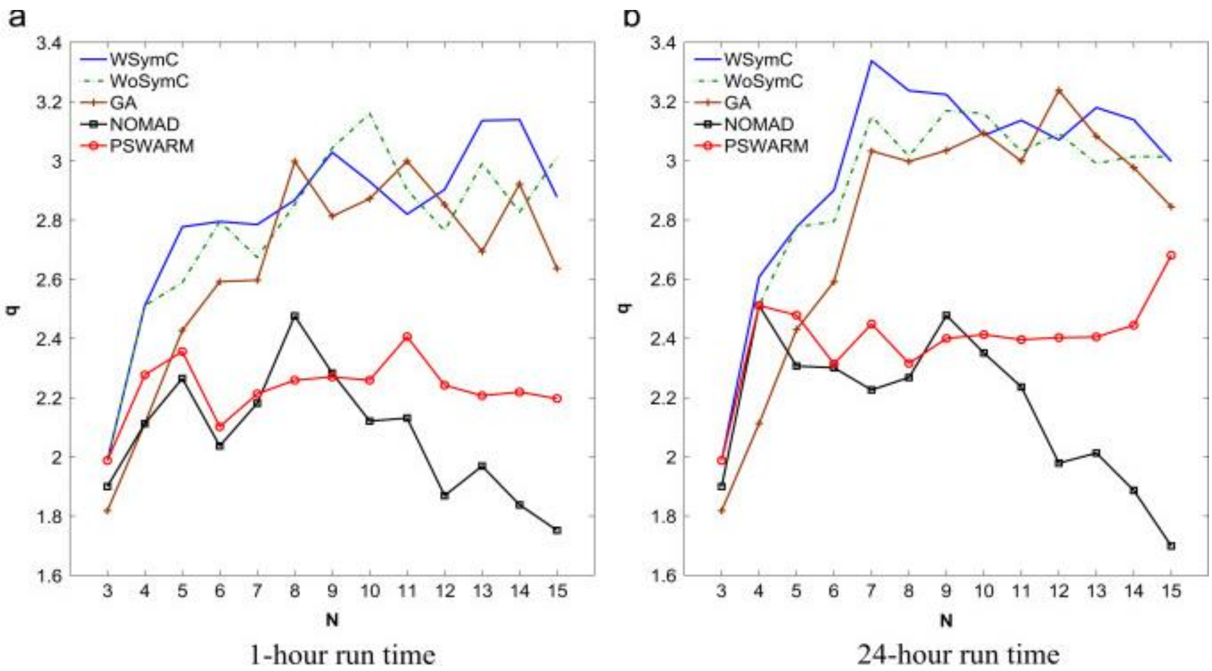

Figure 22 – Comparison of *q-factor* performance for different heuristic methods and the one developed by Snyder and Moarefdoost [182].

Giassi *et al*. [217] investigated the optimization of arrays using GA, varying the diameter and the gridded spacing. The results show that the diameter affects the cost of a device more than power production, and changes in the mass have a greater impact on the energy absorption. In [221], Giassi *et al*. studied the dimensions of the array, optimizing WECs position and buoy dimensions, concluding that the array performance can be increased using different WEC dimensions. Giassi and Göteman [38] continued this investigation to optimize arrays of four to fourteen converters achieving a *q-factor* larger than one. In this study, a hybridization of GA with a multiple analytical scattering method was proposed, to adjust the geometry and control parameters of a small wave farm.

Fang *et al.* [222] used a DE, with an adaptive mutation operator, to improve the convergence rate of the array optimization for a wave energy farm with three, five, and eight devices in a unidirectional wave scenario. Configurations with higher energy production were obtained, although the study did not consider large arrays.

Neshat *et al*. [223] compare some metaheuristic optimization evolutionary algorithms, like CMA–ES, DE, and partial evaluation, using a population from 2 to 100 devices. They observed that differences in the mean output energy obtained by the methods were less than 20%. The hybrids of stochastic buoy placements and the uphill local search performed better for energy absorption. In another investigation [224], the same sea state was used to assess and optimize a 16 devices array using an adaptive neuro–surrogate optimization method. Optimization strategies were compared in different ways; for example, all parameters were optimized simultaneously, the device coordinates and PTO parameters were optimized alternately, or the converters were positioned one–by–one using a local search to fit the best positioning.

Vatchavayi [225] used real wave data, applied a CMA–ES to optimize the positioning of WECs and the Nelder–Mead method to find the optimal parameters for each WEC. The proposed optimization was not suitable for all scenarios studied. In the ones with the best performance, the smaller arrays achieved the best results.

Faraggiana *et al*. [226] compared different metaheuristic optimization strategies, particle swarm optimization, and genetic algorithm, to optimize the separation distance between devices, the PTO tuning, and the rated power of a system of three WaveSub WECs. PSO presented better results for two converters, but not for larger arrays.

Neshat *et al*. [227] compared their previous results with 17 different optimization approaches (Figure 23), three of them with a hybrid heuristic framework, for optimizing the arrangement of large wave farms with 49 and 100 generators in two real wave regimes. The study concludes that the multi–strategy evolutionary algorithm created by symmetric local search and Nelder–Mead search, with an embedded rotation operator, combined with an improved binary DE and a hybrid backtracking strategy (DLS+CLS), achieved the best performance. In another investigation [228], the authors applied 15 state–of–the–art evolutionary, swarm, alternating (cooperative), and hybrid optimization algorithms, showing that the new hybrid cooperative co–evolution method can outperform other heuristic search methods in convergence speed and the quality of layouts.

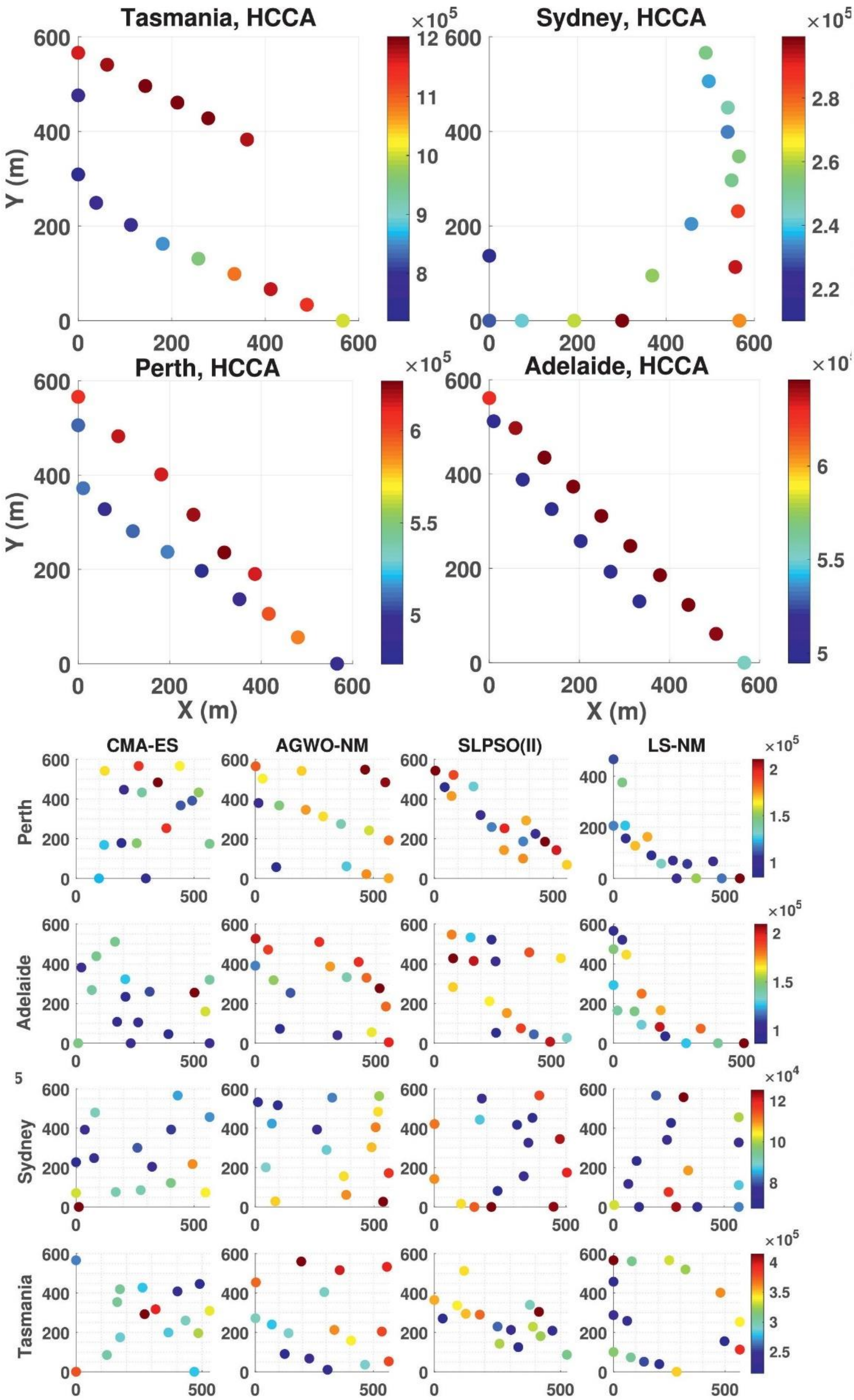

Figure 23 – Best layouts for an array of 16 devices using HCCA, CMA– ES, AGWO–NM, SLPSO II, and LS–NM in four real wave scenarios, adapted from [228].

3

METHODOLOGY

This chapter aims to present an overview of the research methodology. Initially, a summary of the following sections will be presented, followed by a comprehensive description of the tasks undertaken.

3.1.Overview of the framework

In order to accomplish the aforementioned goals, and allow the understanding and reproducibility of the research framework, the following sections addresses the challenge of wave farm layout optimization by proposing a novel, multi–objective framework. The framework integrates three key components:

(i) **Representative sea–state selection**: a statistical analysis coupled with machine learning techniques is used to identify a representative set of sea states that accurately capture the local wave climate.

(ii) **Definition of the fitness function**: a multi–objective decision tool for assessment of wave energy park, the WLA index, is created and presented in a case study.

(iii) **Multi–objective genetic algorithm optimization**: a tailored GA is developed to optimize wave farm layouts for multiple objectives. This includes energy production estimated using the SNL–SWAN model, alongside environmental impact considerations seamlessly integrated into the fitness function. Domain–specific operators are implemented in the GA to ensure physically feasible solutions based on established knowledge of wave–WEC interaction.

(iv) **Applicability to offshore and nearshore environments:** The framework's versatility is demonstrated through various case studies. An economic approach is employed to determine constants in the WLA index for offshore co–located scenarios. Additionally, the algorithm is applied to distinct WECs and coastal regions. These applications highlight the framework's potential to mitigate shoreline erosion by reducing incoming wave energy and to optimize wave farms for minimal shoreline impact.

(v) **Open–source framework for reproducibility:** The entire codebase is publicly accessible to promote replication and extend research on WEC farm optimization and coastal morphodynamic evolution.

Previous studies in WEC array optimization have extensively used fixed or small arrays in a much greater area [3,229], where the optimizations merely find the best separation distance between WECs [37,203,230], focused on discrete positioning strategies. For instance, many works employ grid–based methods, limiting WEC placements to predefined locations [37,38,181,221,231–237]. While these methods simplify computational demands, they inherently restrict the flexibility needed to achieve optimal layouts in realistic scenarios [238,239]. Moreover, the majority of existing studies emphasize single–objective optimization, such as maximizing the power output [3,203] or focus on specific environmental conditions [23,27,240], limiting their generalizability.

As the computational demands of evaluating WEC arrays grow exponentially with the number of converters, developing a fast and effective optimization approach for large–scale wave farms becomes crucial [241]. To address this challenge, the proposed multi–objective evolutionary algorithm optimizes both power output and hydrodynamic interactions within large–scale farms. The methodology combines a smart initialization process, a population–based evolutionary algorithm, a third–generation wave numerical model, and continuous global optimization. This integrated approach effectively handles the complexities of large–scale wave farm optimization, scaling up the array size without sacrificing computational efficiency, while accurately capturing significant interactions between WECs and managing the extensive search space dimensions inherent to the problem.

This approach departs from prior studies that often focus on single or limited objectives. It offers a more realistic solution by simultaneously considering a large number of WECs on a continuous deployment domain, variable installed capacity, and a robust statistical representation of local wave conditions. The versatile SNL–SWAN model [34,35,242], effectively captures complex interactions and provides greater adaptability to site–specific constraints and stakeholder priorities. The proposed multi-objective GA framework is implemented and evaluated through rigorous simulations and case studies. These evaluations assess key performance metrics, including convergence speed, solution quality, and overall robustness, in comparison to existing methods. The framework is designed to effectively balance energy extraction with environmental considerations, ensuring a comprehensive analysis of its capabilities.

The research discusses future directions, including applicability to diverse wave farm configurations, integration with advanced computational models for accuracy, and the development of self–adaptive frameworks for dynamic optimization under varying wave conditions. Overall, the work highlights the power of GA as a tool for optimizing wave farm layouts. By facilitating efficient wave energy harvesting while considering environmental and economic constraints, GA–based optimization holds significant promise for unlocking the potential of wave energy and contributing to a sustainable future powered by ocean renewables.

3.2.Numerical Modeling

Wave–averaged models are a computationally efficient option for modeling wave propagation and nearshore wave–induced current fields, but they rely on parametrizations to represent WECs and other relevant wave characteristics, such as refraction from depth and current, shoaling, wind forcing, white–capping, wave breaking, and non–linear wave interaction. Furthermore, these models do not account for the evolution and transformation of individual waves. Typically, the device is represented as a porous structure [31,150] that works as either a source or a sink term [32], extracting a specific amount of wave energy. Several spectral wave propagation models have been applied to simulate the far–field impacts of wave energy parks. However, the most common and broadly used is the SWAN model [9–12,18,23,31,56–62,66,83–87,153–163] and its modified version, the SNL–SWAN [32,34–36,162,164], introduced by Smith *et al*. [13].

3.2.1. SWAN model

The SWAN (Simulating Waves Nearshore) model, a widely utilized phase–averaged spectral wave model, was developed at Delft University of Technology [112]. As an open–source, third–generation model, SWAN is designed to simulate and propagate waves from deep water to nearshore environments. Its versatility and efficiency make it suitable for a range of scenarios, from complex, time–dependent, two–dimensional simulations using spherical coordinates to more straightforward, stationary, one–dimensional energy balance calculations in Cartesian coordinates. Although it accurately captures wave transformations induced by bottom bathymetry and currents, such as shoaling and refraction, its representation of diffraction is estimated. In addition, the model has undergone extensive testing and validation against real–world wave conditions [92].

SWAN operates by solving the energy balance equation, which incorporates the interactions between waves and currents and accounts for various physical processes, including wave generation, wind–driven growth, wave–wave interactions, propagation, refraction, diffraction, shoaling, bottom friction, and white–capping dissipation. At its core, SWAN uses the spectral action balance equation to model wave–current interactions. This equation is adaptable to both cartesian and spherical coordinate systems, facilitating applications at both small and large scales. Furthermore, SWAN accommodates complex geometries by supporting curvilinear and nested grids, which allow for high–resolution simulations in areas of particular interest.

The wave action density, denoted as N, is a critical concept in wave modeling, defined as the ratio of the variance density spectrum $E(\sigma,\theta)$ to the relative frequency σ:

$$\boldsymbol{N(\sigma,\theta)} = \frac{\boldsymbol{E(\sigma,\theta_m)}}{\boldsymbol{\sigma}}, \tag{34}$$

Here, $E(\sigma,\theta)$ represents the wave variance spectrum, which distributes wave energy across relative radian frequencies (σ) and propagation directions (θ_m). This formulation provides a mean of understanding how wave energy is distributed within the spectral space, considering both the frequency and direction of wave propagation.

The wave action density, N, along with the variance spectrum, E, vary in space and time, particularly in the presence of ambient currents. This dynamic behavior is captured by expressing N as a function of $(\sigma, \theta_m, x, y, t)$, where x and y are spatial coordinates, and t represents time. The governing equation that describes the evolution of wave action density is the action balance equation, which accounts for the propagation of wave action through both physical and spectral spaces. This equation is central to understanding wave dynamics as it integrates the effects of wave–current interactions, energy flux, and various physical processes.

The action balance equation, as formulated by Ris *et al*. [243] and Holthuijsen [92], is expressed as:

$$\frac{\partial N}{\partial t} + \nabla_{x,y}.\left[(\vec{c}_g + \vec{U})N\right] + \frac{\partial}{\partial \sigma}(c_\sigma N) + \frac{\partial}{\partial \theta}(c_\theta N) = \frac{S_{tot}}{\sigma} \tag{35}$$

This equation consists of several key components. The first term on the left–hand side represents the local rate of change of wave action density in time, which can also be interpreted as the rate of change of energy in the absence of currents. The second term describes the propagation of wave action in the geographical space, considering the propagation velocities $\vec{c}_g$ in the x and y directions and the influence of ambient currents $\vec{U}$. This term also encompasses shoaling, the phenomenon where wave heights increase as waves move into shallower water. The third term accounts for the shifting of wave action density in the frequency domain, primarily due to variations in depth and currents, with the propagation velocity in the spectral domain C_σ . The fourth term captures depth–induced and current–induced refraction, where the propagation velocity C_θ represents changes in the directional space θ.

On the right–hand side of the action balance equation lies the source term S_{tot}, which encapsulates the various processes of energy generation and dissipation within the wave field:

$$S_{tot} = S_{in} + S_{wc} + S_{nl4} + S_{bfr} + S_{surf} + S_{nl3} \tag{36}$$

Each component of the source term plays a distinct role in the wave dynamics. The term S_{in} represents the energy transferred from wind to waves, a process dependent on local wind velocity and the wave spectrum itself. S_{wc} accounts for the dissipation of wave energy due to white–capping, a phenomenon that becomes significant in the wave generation area and is primarily influenced by wave steepness. The term S_{nl4} represents the nonlinear transfer of wave energy through quadruplet interactions (four–wave interactions), which are dominant in deep water.

As waves propagate into intermediate and shallow waters, additional processes become more influential. The term S_{bfr} captures the effects of bottom friction, which depends on the orbital velocity near the seabed and the bottom roughness. Depth–induced breaking, represented by S_{surf}, is another significant factor, especially in shallow waters, and is dependent on the ratio of significant wave height to water depth. Finally, S_{nl3} accounts for nonlinear interactions among three wave components (triads), which also contribute to the evolution of the wave spectrum.

The versatility of the SWAN model allows it to be used in various computational contexts. For small–scale computations, the action balance equation is typically expressed in Cartesian coordinates, denoted as $S(\sigma,\theta,x,y,t)/\sigma$. In contrast, for large–scale computations, the equation is often formulated in spherical coordinates $S(\sigma,\theta,\lambda,\varphi,t)$, where λ and φ represent longitude and latitude, respectively. Additionally, in scenarios where ambient currents are absent, the relative frequency σ can be replaced by the radian frequency ω, simplifying the action balance equation to the energy balance or density equation $S(\omega,\theta,x,y,t)$.

Other simplifications are also possible within the SWAN framework. For instance, under stationary conditions, the time component can be omitted from the equation, leading to a static formulation. Furthermore, for one–dimensional scenarios, where seabed topography varies only in the direction normal to the coast, the variation in the y–direction can be removed, thus further simplifying the energy balance equation and reducing computational demands.

The SWAN model incorporates the mechanisms of wind energy transfer to waves through two primary processes: the resonance mechanism as described by Phillips [107] and the Miles–Janssen feedback mechanism [244,245]. Initially, waves are manually introduced into the model, and the wind speed used is measured at a 10–meter elevation (U_{10}). The resonance mechanism plays a critical role in the early stages of wave growth, with wave energy increasing linearly over time. In contrast, the Miles–Janssen mechanism functions through a feedback loop, where energy and pressure are transferred to the wave system in a manner proportional to the existing wave energy, thereby enhancing wave growth in a sustained manner.

SWAN is capable of simulating non–linear wave interactions through the inclusion of two key terms: three–wave interactions (triads) and four–wave interactions (quadruplets). Triads are crucial in shallow waters, facilitating the transfer of energy from lower to higher frequencies, often leading to the formation of higher harmonics [246]. This mechanism is particularly important for steep waves. In contrast, quadruplets dominate in deep and intermediate waters, redistributing energy within the spectrum by transferring it from the spectral peak to both lower and higher frequencies, where energy is eventually dissipated through white–capping. SWAN handles these complex interactions using the Discrete Interaction Approximation (DIA) [247], which models the energy transfer processes essential for accurate wave spectrum evolution.

Energy dissipation within the SWAN model is accounted for through three primary mechanisms: white–capping $S_{wc}(\sigma,\theta)$,bottom friction $S_{bfr}(\sigma,\theta)$, and depth–induced breaking $S_{surf}(\sigma,\theta)$. White–capping serves as the dominant energy dissipation process in deep water, being directly proportional to the energy density and heavily influenced by the steepness of the wave field. The formulation for white–capping in SWAN is based on the pulse model proposed by Hasselmann [108], and it effectively controls and limits wave heights, especially in the presence of wind input.

The dissipation of wave energy due to seabed interactions is modeled as a function of the bottom friction coefficient (C_b) and the root mean square (RMS) orbital bottom velocity (U_{rms}). Given the diverse characteristics of seabed properties, SWAN incorporates several friction models, including the empirical JONSWAP model [103], the drag law model by Collins [248], and the eddy–viscosity model by Madsen *et al*. [249]. These models allow SWAN to simulate a wide range of bottom interaction scenarios, adapting to different seabed compositions and roughness.

In shallow waters, the mechanism of depth–induced breaking, particularly within the surf zone, becomes the primary process governing wave energy dissipation. SWAN employs the spectral version of the bore model by Eldeberky and Battjes [121], which is an extension of the original formulation by Battjes and Janssen [246]. This approach preserves the spectral shape while modeling the total wave energy and its dissipation rate due to wave breaking, thus ensuring accurate predictions of wave behavior in shallow coastal areas.

Refraction effects are fully incorporated in SWAN, particularly in the fourth term of the wave energy balance equation. To address diffraction, which was not originally included, Holthuijsen *et al.* [250] introduced a phase–decoupled refraction–diffraction approximation. This method combines the processes of diffraction, typically handled by phase–resolving models through the mild–slope equation, with refraction, shoaling, generation, dissipation, and wave–wave interactions. This hybrid approach enables SWAN to simulate the complex interactions of random, short–crested waves in varying coastal environments.

SWAN also models the reflection and transmission of wave energy through or over obstacles like breakwaters, dams, and WECs. The degree of reflection is influenced by factors such as the shoreface slope, mean wave frequency, and incident wave height. The model computes absorption by structures or coastlines as the difference between the incident energy and the combined reflected and transmitted energy. Reflection within SWAN is treated as specular, assuming that the angle of incidence equals the angle of reflection [92]. Recent updates to SWAN have introduced variations in transmission that depend on the wave frequency and direction, providing more nuanced simulations of wave–structure interactions.

Gradients in wave–induced radiation stresses, which typically generate currents and water level set–up, are standard outputs of SWAN. These can be used as input for subsequent computations in separate hydrodynamic models [92]. This allows for the simulation of feedback mechanisms between waves, currents, and water levels. For stationary cases, the exchange between wave and hydrodynamic models can be iterated until convergence is achieved. In non–stationary cases, SWAN can exchange data with hydrodynamic models at regular intervals, ensuring that dynamic feedbacks are accurately captured over time.

Regarding the wave energy, SWAN utilizes the full wave spectrum $E(\sigma, \theta)$ to calculate the wave power components per meter of wave front in the x and y directions, as defined by the following equations:

$$\boldsymbol{J_x = \rho g \int_0^{2\pi} \int_0^{\infty} c_g\,(\sigma, d) E(\sigma, \theta) \cos\theta d\sigma\, d\theta}, \tag{37}$$

$$\boldsymbol{J_y = \rho g \int_0^{2\pi} \int_0^{\infty} c_g\,(\sigma, d) E(\sigma, \theta) \sin\theta\, d\sigma\, d\theta}, \tag{38}$$

in these equations, ρ denotes the water density, g represents gravitational acceleration, and c_g indicates the group velocity. The x and y coordinates correspond to the spatial directions on the grid. The total wave power per meter of wave front, J, is then derived as:

$$\boldsymbol{J} = \sqrt{\boldsymbol{J}_x^2 + \boldsymbol{J}_y^2}\,. \tag{39}$$

SWAN has proven effective in a range of studies for assessing wave resources across various wave climates and coastal environments [251–253]. It has also been employed to evaluate the potential impacts of WECs on the surrounding wave climate, including the impact on shoreline [13,16,31,68,153,156,158,254–256].

In such applications, WECs are represented as porous obstacles spanning at least two grid cells, functioning as energy sinks in the wave action balance equation, which results in the extraction of a portion of the incoming wave energy [87]. The absorption of energy by the WECs is quantified using a transmission coefficient, K_t, which measures the ratio of absorbed energy to the incoming significant wave height (H_s). However, it is important to note that this approach assumes a constant energy absorption rate, which is an oversimplification since actual absorption depends on both wave period and height. Despite these limitations, this methodology is widely used to assess the effectiveness of wave energy farms in mitigating extreme wave conditions, particularly in conjunction with offshore wind farms and coastal areas [12,23,56–62,83,84,157]. The coefficient K_t is usually defined empirically based on the characteristics of the specific WECs [87].

SWAN's versatility extends across various domains, including coastal engineering, offshore engineering, and marine renewable energy. Its modular structure allows for the integration of additional physical processes, enhancing its flexibility for different wave modeling scenarios. Nevertheless, it is crucial to acknowledge some limitations of SWAN, such as its reliance on the Gaussian distribution assumption and the challenges associated with parameterization.

SWAN relies on a series of input and computational grids to define the spatial and temporal boundaries of the simulation. Users need to configure three primary spatial grids: (1) the input grids, which detail the bathymetry, water levels, bottom friction, and wind conditions (especially if wind is not uniform across the area of interest); (2) a computational grid where SWAN performs its calculations; and (3) one or more output grids where the simulation results will be displayed. Similarly, users can define distinct time frames with varying time steps, including a computational time window, input time windows for variables such as water levels and wind fields, and output time windows, for example, to generate hourly results.

A comprehensive bathymetric grid is critical for effective SWAN simulations, particularly in shallow or intermediate water conditions where waves interact with the seabed. While in deep offshore waters, precise bathymetric details are less critical due to the lack of seabed interaction, in coastal areas, factors like bottom friction, depth–induced breaking, and refraction become significant. In addition to bathymetry, grids for variables like wind fields (if not uniform), bottom friction, currents, and water levels can be input by the user, especially when these variables fluctuate over time, requiring non–stationary inputs.

The computational grid, defined by the user, sets the geographical scope (X, Y coordinates), size (X and Y dimensions), orientation, and resolution (grid spacing). This grid should encompass the area of interest and ideally overlap with the input grids to allow for interpolation of data such as bottom depth, currents, and wind conditions. The boundaries of this grid should extend beyond the area where accurate results are desired, especially when boundary conditions are uncertain. SWAN supports various grid types, including uniform rectangular, curvilinear, and unstructured (triangular mesh) grids.

As a spectral model, SWAN also requires the user to define the characteristics of the computational spectral grid, including the frequency range (minimum and maximum), resolution (number of frequencies), and directional domain. The minimum frequency should be less than 0.7 times the lowest expected peak frequency, while the maximum should be approximately three times the highest peak frequency [112]. The frequency resolution is determined within this range.

SWAN needs boundary conditions defined by incoming wave parameters to solve the wave action balance equation. These boundary conditions can be derived from various sources: (1) parametric spectra from offshore data (*e.g.*, H_{m0}, T_p or T_{m01}); (2) 1D/2D spectra, either measured or modeled; and (3) outputs from other wave models like WWIII, WAM, or previous SWAN simulations. For parametric spectral inputs or stationary/non–stationary spectra, users can select the spectral shape at the computational grid boundary, with options such as JONSWAP (default), PM spectra, or Gaussian spectra. The seaward boundary is typically aligned parallel to the coast, close to the data source, assuming uniform wave conditions along this boundary.

When boundary conditions are derived from earlier simulations, a nesting approach is often used. This involves an initial broad–area simulation with coarse resolution, which then provides boundary conditions for a finer, more detailed SWAN grid. If the initial simulation uses a model other than SWAN (*e.g.*, WAM, WWIII), extra care is needed to allow SWAN to adjust the wave conditions to its internal physics, typically by setting boundaries far enough from the area of interest. Guidelines for designing nested grids in terms of dimensions, resolution, and spectral parameters are provided in the SWAN user manual [257] and scientific and technical documentation [258].

Users can customize the physical processes included in the simulation, such as white–capping, wave interactions (quadruplets and triads), wave breaking, bottom friction, diffraction, and obstacles. These processes can be activated or deactivated based on the study area's characteristics, and users can choose between different generations of wave modeling (first, second, or third–generation) to match the requirements of their specific scenario.

Finally, the output grid must be configured to specify the spatial and temporal resolution of the results. The output grid, which should align with or be smaller than the computational grid, can present results in various formats, including grids, curves, contour lines, or specific points. SWAN offers over 20 output commands, with results available in table formats, matrices, or as 1D/2D energy density spectra.

Since SWAN outputs are purely numerical, users typically require additional software to visualize and interpret the results. When outputting data in a matrix format, the user can choose between binary or ASCII file formats. Plotting and analyzing SWAN results generally necessitate familiarity with complementary software tools.

3.2.2. SNL–SWAN

SNL–SWAN [33,259] is a software tool specifically designed by the Sandia National Lab to simulate the effects of WEC arrays on ocean waves. It is an open–source code derived from the well–established SWAN model developed by TU Delft, and has been verified and preliminary validated by comparison to experimental data [34–36].

A key enhancement introduced by SNL–SWAN is the WEC module. This module significantly improves SWAN's ability to account for the power performance of WECs and their subsequent impact on the wave field. SNL–SWAN employs five distinct methods to determine the transmission coefficient, which represents the ratio of transmitted over incoming significant wave height (H_s) and is determined using either the WEC power matrix or the Relative Capture Width curve, activated through specific switches within the WEC module. This transmission coefficient is then utilized to estimate either a frequency–variable coefficient within SWAN's Action Density Evolution Equation or a frequency–constant coefficient. The frequency–dependent wave energy transmission allows for a more accurate evaluation of WEC farm effects on wave propagation considering also the dependence of WEC performance on it.

To effectively model WECs within SNL–SWAN, it is essential to provide accurate information regarding their power performance. This information is typically presented in two primary formats. The power matrix represents the absorbed power (in kilowatts, kW) by a WEC device across a range of significant wave heights and peak wave periods. The Relative Capture Width (RCW) quantifies the ratio of power absorbed by the WEC to the incident wave power in a wave front equal to the characteristic dimensions of the WEC at a specific frequency. It can be calculated for each individual frequency.

The WEC Obstacle Case (Obcase) parameter within SNL–SWAN determines the method used to calculate the obstacle transmission coefficient (K_t). This coefficient quantifies the amount of wave energy that is transmitted through the WEC. The baseline SWAN model, equivalent to Obcase 0, does not account for WECs, the K_t is specified directly in the input file. Obcase 1 and 2 employ simplified approaches, calculating a constant K_t based on the power matrix and incident wave field (H_s, T_p) or the RCW value at the peak incident wave period, respectively. For more accurate simulations, Obcase 3 and 4 utilize the power matrix and incident wave spectra or the RCW curve, respectively, to calculate a frequency–dependent K_t, allowing for a more realistic representation of WEC energy absorption across different wave periods.

The normalization width, a crucial parameter in WEC modeling, represents the physical dimension of the WEC along its face. It is essential to provide this information to ensure accurate simulation results. It is important to note that the power matrix typically relies on bulk sea state parameters, such as significant wave height (H_s) and peak wave period (T_p), to characterize wave conditions. However, it does not provide information about the shape of the wave spectrum. Consequently, if spectral information is unavailable, only Obcase 1 can be employed. Conversely, if a power matrix is available for discrete wave periods (frequencies) and amplitudes, Obcase 3 can theoretically be utilized.

The RCW curve, which illustrates the absorbed power ratios of a WEC device at varying wave periods, can be estimated through experimental or numerical methods. While RCW values exceeding 1.0 have been observed experimentally, SNL–SWAN imposes a limit of 1.0 to ensure physical accuracy. This constraint prevents the model from removing more power from the wave field than is physically available to the obstacle. Furthermore, SNL–SWAN cannot simulate the "antenna effect," where a WEC focuses wave energy beyond its physical dimensions.

This method enables the transmission coefficient (directly linked to wave power absorption) to vary when wave conditions change over a relatively broad range of temporal and spatial scales. To date, most studies assessing the park effects of wave farms and potential synergies with offshore wind farms have been conducted using SWAN, which simulates WECs as obstacles with an empirically defined K_t, which, as previously stated, has serious limitations in reproducing wave energy absorption.

SNL–SWAN models WECs as linear obstacles within a computational grid. When a grid line intersects an obstacle, a transmission coefficient is applied to the wave energy flux between the grid points. It is crucial to note that the width of the obstacle does not directly influence its impact on the model. Instead, the intersection of the obstacle with grid lines determines its effect. A wide obstacle that does not intersect any grid lines will have no impact on the simulation, while a narrow obstacle that intersects multiple grid lines can significantly affect the wave field.

To ensure accurate WEC simulations, the grid resolution should be sufficiently fine to capture the physical dimensions of the WECs. This ensures that the obstacles intersect multiple grid lines, allowing for a more accurate representation of their impact on the wave field. Additionally, the RCW should be within the range of 0 to 1.0 , as values outside this range will be automatically adjusted by SNL–SWAN, and the sum of transmitted, reflected, and absorbed energy should not exceed the incident wave energy. SNL–SWAN will flag any violation of this principle.

The choice of the obstacle case depends on the availability of information about the WEC's power performance. Obcase 3 and 4 are suitable when detailed spectral information is available, while Obcase 1 and 2 are more appropriate for average sea state conditions.

SNL–SWAN determines transmission coefficients by interpolating values from either the Power Matrix or the RCW curve. This interpolation process ensures a smooth transition between data points, allowing for accurate estimation of the transmission coefficient for any given frequency and significant wave height combination. If a specific frequency or significant wave height falls outside the range defined by the Power Matrix or RCW curve, SNL–SWAN assigns a transmission coefficient of 1.0. This implies an absorption coefficient of 0.0, indicating that the WEC does not absorb any wave energy at those conditions.

In addition to the standard outputs, SNL–SWAN generates a file named POWER_ABS.OUT, which provides detailed information on the absorbed power for each modeled WEC (obstacle). This file is crucial for analyzing the power capture performance of WEC arrays.

SNL–SWAN offers a higher level of accuracy in assessing the performance of a WEC array compared to the original SWAN code, including more detailed physics and processes, and a greater control over the simulation, allowing for the input of more accurate data and the adjustment of parameters to fine–tune simulations. It can also be adapted to specific scenarios and conditions, providing more flexibility.

Overall, SNL–SWAN is a powerful tool that significantly improves upon the original SWAN model for simulating ocean waves and assessing the performance of WECs.

For the present work, a frequency–dependent transmission was used, calculated according to the WEC's power absorption matrix at each of the binned incident wave frequencies. As a result, SNL–SWAN does not consider the diffracted or radiated waves resulting from WEC operation. On these grounds, SNL–SWAN does not take into account resonance phenomena and possible standing waves in the WEC array.

Based on the aforementioned characteristics, SNL–SWAN shares with the standard SWAN model an inherent limitation to accurately model WEC power absorption [230]. Nonetheless, nowadays, SNL–SWAN emerges as the most suitable choice for modeling environmental and far–field impacts, over RANS/SPH–CFD, coupled BEM and Boussinesq, Mild–Slope, and non–hydrostatic models, primarily owing to its ability to model wave propagation over large coastal areas with varying bathymetries, all at a very reasonable computational cost [230]. In contrast, the potential flow models lack the flexibility to work with varying bathymetries.

3.2.3. SNL–SWAN Model setup

The performance of each wave farm is evaluated by the application of SNL–SWAN using stationary mode in each sea state. The model domain is discretized into a curvilinear grid and the bathymetry is defined over the model domain, applying a triangular interpolation, followed by internal diffusion, using the Delft3D–QUICKIN toolbox [260]. This ensured adequate aspect ratio, Courant number and orthogonality values towards high–fidelity simulations [261]. All grid resolution was planned to provide at least 10 crossings of each obstacle line.

The spectral resolution used was a circle in 36 directions with frequency interval varying from 0.05 to 1 Hz in 24 bins. Depth–induced breaking with $\alpha = 1$ and $\gamma = 0.73$. The bottom friction used the JONSWAP parameter with a coefficient of $0.067\ \mathrm{m^2s^{-3}}$. To calculate the transmission coefficient the Obcase 3 (power matrix with frequency dependent values) was applied.

Wave conditions are specified at the four boundaries of the model domain. JONSWAP wave spectra are used to define the wave height, peak period, and spectral shape. The boundary conditions vary according to the defined sea state and the area is automatically adjusted by the algorithm.

3.3.Unsupervised classification for minimal representative sea states

Unsupervised classification is a fundamental method in machine learning and data mining, allowing for the automatic discovery of hidden patterns and structures within unlabeled datasets, attributes or characteristics. The process involves representing the data, defining a distance or similarity measure, initializing the clusters, assigning data points to the clusters, iteratively refining those clusters, and evaluating the results. The group assignment is done based on the similarity to cluster centroids. The quality of the clusters can be evaluated using both internal or external metrics. Different clustering algorithms exist, each employing different strategies and assumptions based on the nature of the data and the problem at hand.

K–Means clustering approach involves partitioning a dataset into a specified number of clusters, where data points within each cluster exhibit high similarity, while clusters are distinct from one another. The clustering process iteratively minimizes the sum of squared Euclidean distances (SED) between data points and their respective cluster centroids:

$$\boldsymbol{SED} = \sum_{k=1}^{K} \sum_{x_i \in M_{k_c}} \left\| \boldsymbol{x_i} - \boldsymbol{\mu_{k_c}} \right\|^2 \tag{40}$$

where x_i is the individual data point, and μ_k the centroid of cluster k_c.

k–Means offers a computationally efficient method for reducing a large dataset into a smaller number of representative subgroups. Some studies applied clustering methods to wave climate estimation, mostly k–means, to deal with the huge amount of data [262–270]. The k–means clustering algorithm can be applied to metocean data (*e.g.*, significant wave heights, H_S, peak wave periods, T_P, peak wave directions, θ_m) to analyze and understand local extreme events, as well as to characterize waves and currents.

In this context, k–means clustering aims to identify distinct groups or clusters within the dataset based on the values of H_S, T_P, and θ_m [268], to reduce the number of sea states needed for the study. However, it is important to note that k–Means can only guarantee a local optimum, and its performance may be influenced by the initial choice of centroids. Therefore, data standardization is often recommended to mitigate the impact of differing scales.

The unsupervised classification methods utilized included k–means, Gaussian Mixture models (GMM), and Variational Bayesian Gaussian Mixture models (VBGMM). These methods were implemented using the python scikit–learn library [271] with the full and filtered dataset. The approach followed the normalization procedure outlined by Camus [262], to equalize the scales.

To assess the effectiveness of sea state clustering, this study employed two common error metrics: Mean Absolute Percentage Error (MAPE) and Root Mean Squared Error (RMSE). These metrics are widely used to evaluate model predictions providing valuable insights into the representativeness of each cluster regarding the corresponding sea states [272]. Notably, previous research [264–267] used metrics similar to MAPE to evaluate input wave parameters within k–means clustering applications.

$$\boldsymbol{MAPE} = \frac{\boldsymbol{1}}{\boldsymbol{n}} \sum_{i=1}^{n} \left| \frac{\boldsymbol{x_i} - \boldsymbol{x_i'}}{\boldsymbol{x_i}} \right| * \boldsymbol{100} \tag{41}$$

$$\boldsymbol{RMSE} = \sqrt{\frac{\boldsymbol{1}}{\boldsymbol{n}} \sum_{i=1}^{n} (\boldsymbol{x_i} - \boldsymbol{x_i'})^2} \tag{42}$$

where x_i is the measured value, x_i' the estimated value and n the number of data points.

The definition of the optimal number of sea states was determined by locating the number of clusters that could provide sea states that represent at least 90% of the incoming wave energy. In this process, power representativeness (φ_p) was used,

$$\boldsymbol{\varphi_p} = \frac{\sum_{c=1}^{n}(\boldsymbol{P_{centroid}} \times \boldsymbol{N_c})}{\sum_{i=1}^{N} \boldsymbol{P_i}} \tag{43}$$

where $P_{centroid}$ represents the wave energy per meter of wave front for each sea state, represented by the centroid of the cluster, N the total number of data values, N_c the values inside a cluster, n the number of clusters, and P_i the incoming wave energy per meter of wave front for each data value.

3.4.Genetic Algorithm

Achieving the stated objective of building a Genetic Algorithm (GA) with a novel multi–objective function, while integrating SNL–SWAN as the Hydrodynamic model for array evaluation, involves a sequential chain of development. The process starts with an initial assessment of the WEC, determining key farm characteristics, including the type, number, location, and orientation of the devices, alongside defining the optimization metric. Moreover, as part of the whole package of optimization some side algorithms were needed to support the GA, such as an algorithm to automate the process of input creation and execution of multiple simulations using the SNL–SWAN model, which is the core of layout evaluation.

The first step before entering the new tailored GA loop of generations is the definition of sea states, which using the data from the clustering and a side algorithm (included in the provided GA code), create the SWAN input files and simulate them to define the baseline scenarios. The second step is the random creation and simulation of an initial population in the deployment area. In all simulations in this work, the initial population size was 500 individuals (WEC farm layouts).

Then the workflow of GA enters in a loop, Figure 24. The SNL–SWAN model is incorporated inside the GA loop. At the beginning, the model simulates all initial populations for every sea state, generating 2 outputs: the power absorption of each WEC and the H_S of every node in the AOI. Those outputs are processed in the evaluation code, and generate a table with weighted mean H_S reduction and power absorption for each layout.

The fitness evaluation uses the WLA index [63] to classify the layouts and determine the elite that will be granted in the next generation. The parents' selection is done using the probability according to the individual ranking, *i.e.*, individuals of higher rank have higher chances to be picked, independently of their WLA value. It is worth noting that even with a low probability of choosing the same pair of parents more than once, the creation of new individuals is forced to be different from the ones already in the offspring. The reproduction was performed by applying the crossover, according to the flowchart in Figure 25 and mutation, Figure 26 , using the function "*create child layout*" described in the flowchart presented in Figure 27, which combines the WECs from the parents regarding the minimal distance between WECs constrain.

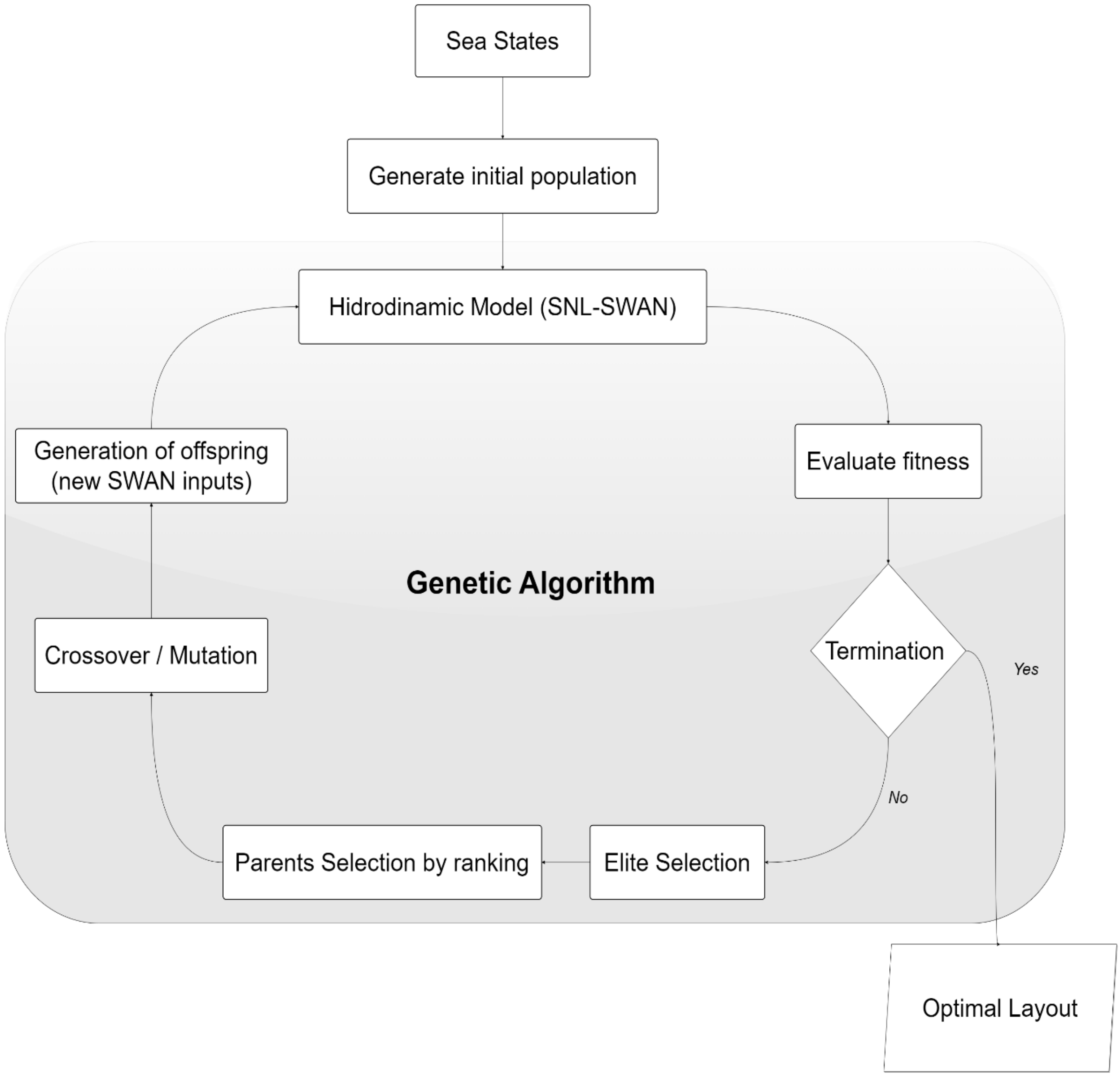

Figure 24 – Genetic Algorithm loop.

The crossover flowchart outlines the selection process for elite individuals and best parents, which are individuals preserved even when the crossover operation is bypassed due to the crossover rate used to populate the next generation. This ensures the retention of valuable genetic information from the previous generation. The information for all individuals, including offspring generated by crossover and elite members from the prior generation, is retrieved from a dictionary data structure. Then, the crossover loop iterates through each crossover rate, determining whether crossover should be applied based on the predefined probability.

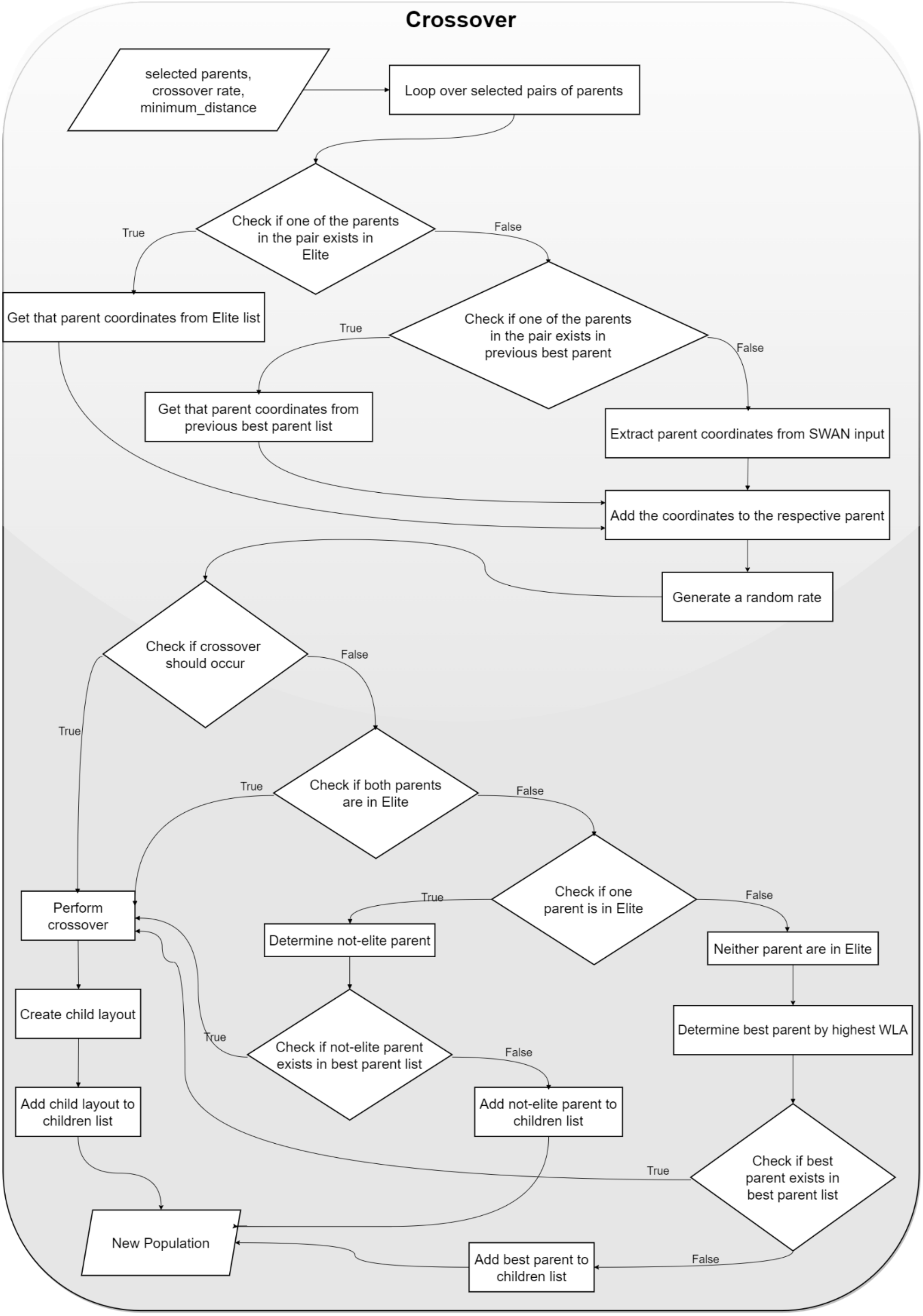

Figure 25 – Flowcharts of crossover and mutation functions inside the genetic algorithm.

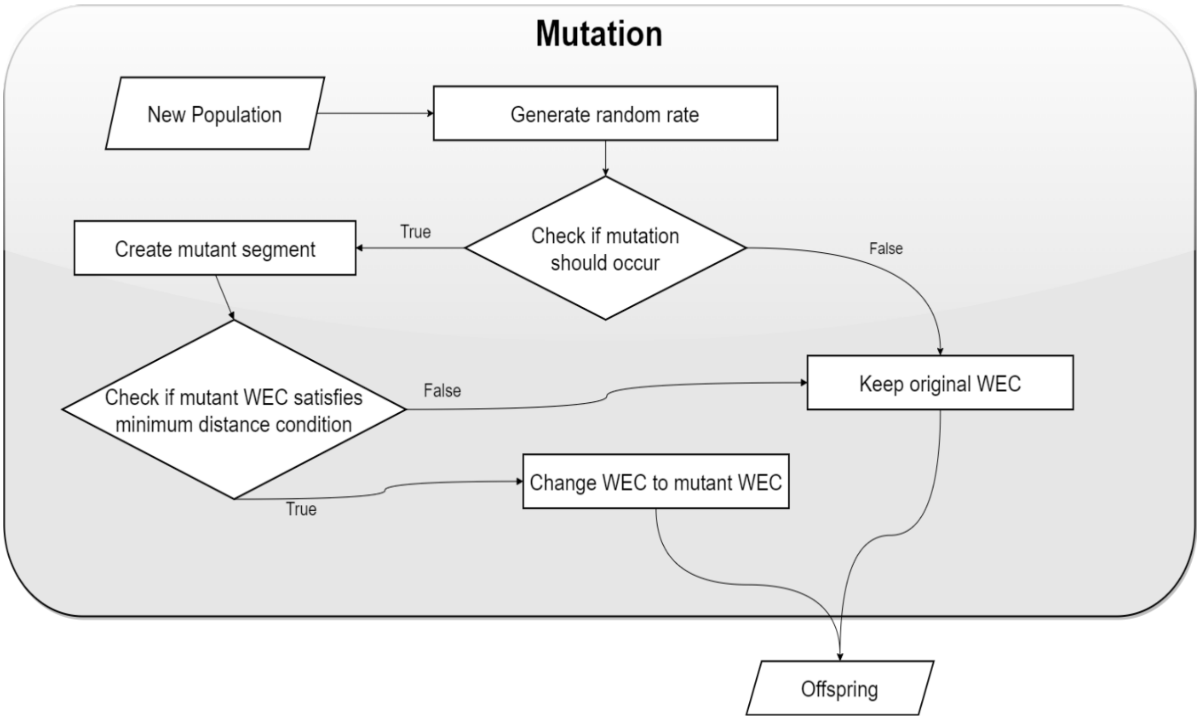

Figure 26 - Flowcharts of mutation functions inside the genetic algorithm.

To maintain population diversity and prevent duplicates, a check for repeated individuals is done after the crossover operation. This ensures that the newly formed population adheres to the principle of a unique solution space within the GA. Finally, the complete population undergoes mutation, introducing random variations within each WEC (segment) while adhering to the pre–defined layout constraints. This mutation process injects novelty into the population, facilitating the exploration of the solution space.

Generating offspring layouts (children) within a continuous domain presents a challenge due to the minimum distance constraint between individual WECs. This function, illustrated in Figure 27, addresses this challenge by randomly selecting a WEC from either parent layout. The selected WEC's position is then evaluated to ensure it adheres to the minimum distance requirement from previously placed WECs in the child layout.

However, this approach can potentially lead to deadlocks where the remaining WECs cannot be positioned within the constraints. To mitigate this, a limit is set on the number of placement attempts for each WEC. If this limit is reached without a successful placement, the reproduction process restarts. This mechanism ensures that even if the parents are highly similar, a valid child layout satisfying the minimum distance restriction will eventually be generated.

There are two possible ways that an individual from previous generations survives to the next one. The first one is that it belongs to the elite of that generation, which assures that the best individuals of the generation are not lost in the reproduction process. The second one is when the crossover does not occur, *i.e.*, the rate of occurrence of that matting is lower than the crossover rate predefined. In this case, the best parents are repeated in the next generation after a chain of checks to ensure no individual repetition in the offspring.

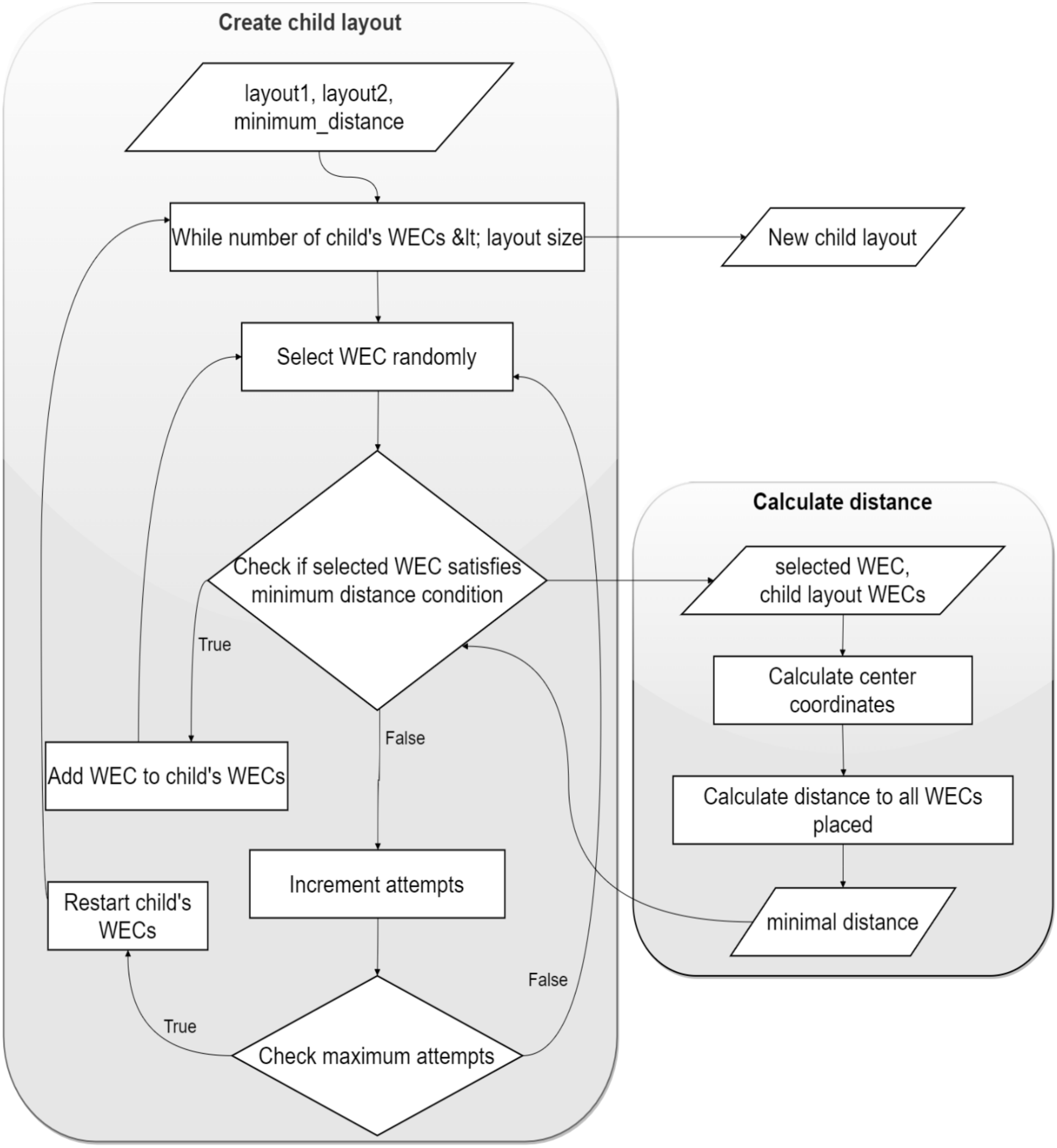

Figure 27 – Flowcharts of the function to create a new (child) layout simulating reproduction between two previous generation layouts (parents).

While the value of each fitness is important to determine the chances of individual survival, there is no guarantee that the ones with the higher fitness values will survive or the ones with the smaller values will perish, because of the non–deterministic nature of the method [213]. Given that, it could occur that some individuals with low fitness value genes might prove to be useful when recombined in new chromosomes, which is a low probability “second chance”, offered by the process flexibility that would be impossible in a more deterministic setting [213].

3.4.1. Optimization Problem Definition

The optimization problem in this study is designed to maximize the WLA index in each generation, as presented in [63] and developed in Section 4.2, which will optimize the *q-factor* and the HRA globally. For demonstration purposes, in this study equal weights (p=s) were assigned to ensure a balanced contribution from both factors and specific weights to optimize for maximum power absorption (p=1) and maximum shield protection (s=1), to verify the data in a single objective. Additionally, a definition of weights using economic parameters was employed in CASE I (section 5.3.1).

The algorithm adjusts the positions of the WECs to find the optimal layout. The position of the WECs is constrained by sector bounds or a polygon, where WECs are limited to this deployment. The selection of the crossover rate and population size was driven by their influence on the required number of SWAN simulations for each layout. Given the computationally intensive nature of multiple SWAN simulations, it was imperative to carefully consider these parameters to strike a balance between solution quality and computational cost.

To optimize the trade–off between exploration and exploitation within the solution space while minimizing the computational burden imposed by the several simulations, the crossover rate (70% and 95%) and population size (25 and 50 arrays) were varied. Additionally, to keep a proportionality and an integer number, the elite size varied with the population size, 12% for cases with 25 layouts and 10% for cases with 50 layouts. This approach allowed to efficiently explore a diverse range of solutions (while ensuring feasibility) and apply them to other arrangements with more WECs (28, 84, 100, 150 and 200) and larger spacing between WECs (5D and 7D).

The termination criteria were defined based on the stability of the main parameters (*q-factor* and HRA), with a tolerance of 10^{-4}. This means that the optimization process terminates after 20 consecutive generations without changes in the *q-factor* and HRA exceeding this threshold.

The arrangement of simulation parameters for model sensitivity analysis, including crossover rate, elite size, number of WECs, number of layouts, and minimal spacing between WECs, is detailed in Table 5 – Simulation Setup. These configurations were designed to test the algorithm under different scenarios and evaluate its robustness and performance in optimizing WEC layouts. The subsequent simulations applied the GA configuration S1, which presents the best results in the analysis.

3.5. Simulations

The simulations are designed to evaluate the proposed framework, ensuring accurate representation of energy extraction and wave field interactions. Therefore, to accommodate a wide range of deployment scenarios, two different obstacle placement methods were employed: a sector–based approach for offshore, shielded deployments, and a random placement approach for nearshore, restricted areas.

In the sector–based approach, WECs are arranged along a circular arc, with their orientation perpendicular to the radius, changing the orientation in the 2D plane. This configuration provides shielding to a specific area. In the nearshore approach, WECs are randomly placed within a defined area, facing the predominant wave direction.

The following sections provide a detailed explanation of the methodologies used to evaluate the performance of individual devices, perform a sensitivity analysis, incorporate economic parameters into the WLA function, and apply the framework to coastal zone case studies.

3.5.1. Single device

The performance assessment of individual WECs is crucial for analyzing the overall performance of a WEC farm. While the rated power of a WEC represents its theoretical maximum power absorption under ideal conditions, real–world performance is often significantly lower due to various factors such as wave conditions and device limitations. To accurately evaluate WEC performance in specific sea states or a range of sea states, simulations of individual WECs are necessary.

One key parameter in WEC farm optimization is the *q-factor*, which quantifies the efficiency of energy extraction from the wave field. To accurately estimate the *q-factor*, it is essential to model the power absorption of individual WECs with sufficient precision. In SNL–SWAN, the power absorption of a WEC is influenced not only by wave height, period, and direction but also by the number of grid lines it intersects. Previous studies suggest that at least 5–10 grid line intersections are required to ensure accurate results. To meet this requirement, the grid resolution in this study was refined to achieve more than 10 intersections per WEC.

To determine the performance of individual WECs in each deployment scenario, two simulation methods were used. For offshore, co–located WECs, an arc method was employed, where WECs were placed at 0.5–degree intervals along the arc and simulated for all sea states. For nearshore WECs, a random method was used, where WECs were randomly placed within the defined area and simulated for all sea states. In both cases, the average power absorption from all simulations was used to represent the performance of a single WEC.

3.5.2. Model sensitivity analysis

3.5.2.1. Case study site

The case–study site is located offshore Viana do Castelo (Northern Portugal), where the offshore farm of WindFloat Atlantic project is located. This wind farm is composed of three floating wind turbines with a total installed capacity of 25 MW, and is located between 17 to 19 km from the coast of Viana do Castelo, where water depths can reach 100 m [73]. The wind farm positioning area is 4.77 km^2, and the protection area is 11.25 km^2 [273]. Figure 28, presents the location of WindFloat park and Table 3 the vertices' coordinates of the protection area and the wind turbines (WFA) [274].

This research work builds upon previous work [63] (section 4.2), which introduced the evaluation parameters HRA, *q-factor* and the WLA index. In this scenario, the importance of shield protection (s) and energy production (p) was considered the same. The WEC used was CECO described in section 3.5.2.2.

Table 3 – Coordinates (WGS84) of the protection area vertices and the wind turbines [274].

Vertex	Latitude (º)	Longitude (º)
A	–9.0875989	41.697497
B	–9.0335472	41.697934
C	–9.0332331	41.675428
D	–9.0872658	41.674992
WFA3	–9.0501671	41.686668
WFA1	–9.0574999	41.686501
WFA2	–9.0646667	41.686501

Unlike the previous work, which employed fixed layouts for the WECs, this study utilizes a continuous domain for WEC placement. This approach allows for greater flexibility, as WEC locations can be freely optimized within the designated area, adhering only to minimum distance constraint between WECs. To initiate the optimization process, the initial layout was generated by randomly placing WECs within the allowable domain. Figure 29 depicts one such initial layout alongside the selected placement area.

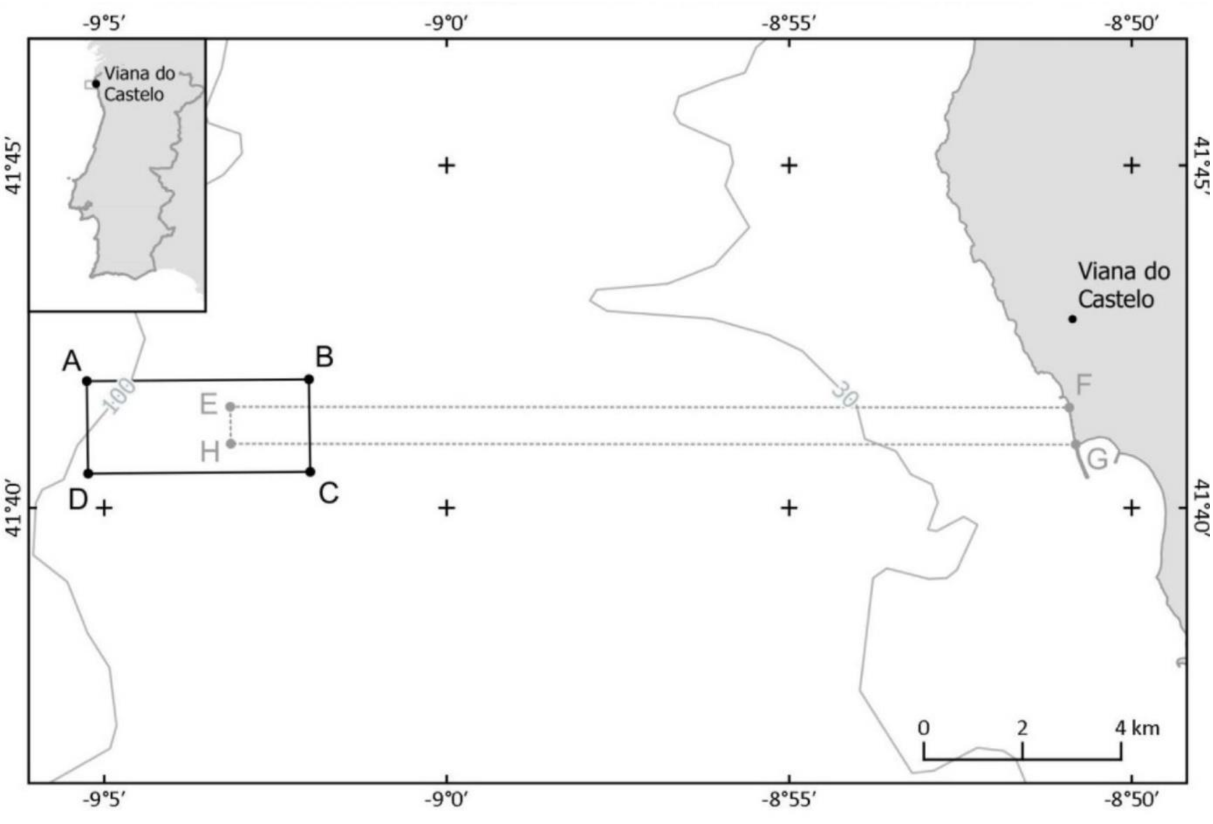

Figure 28 – Location of the WindFloat Atlantic farm. ABCD are the vertices of the protection area and FEGH the submarine cable area [273].

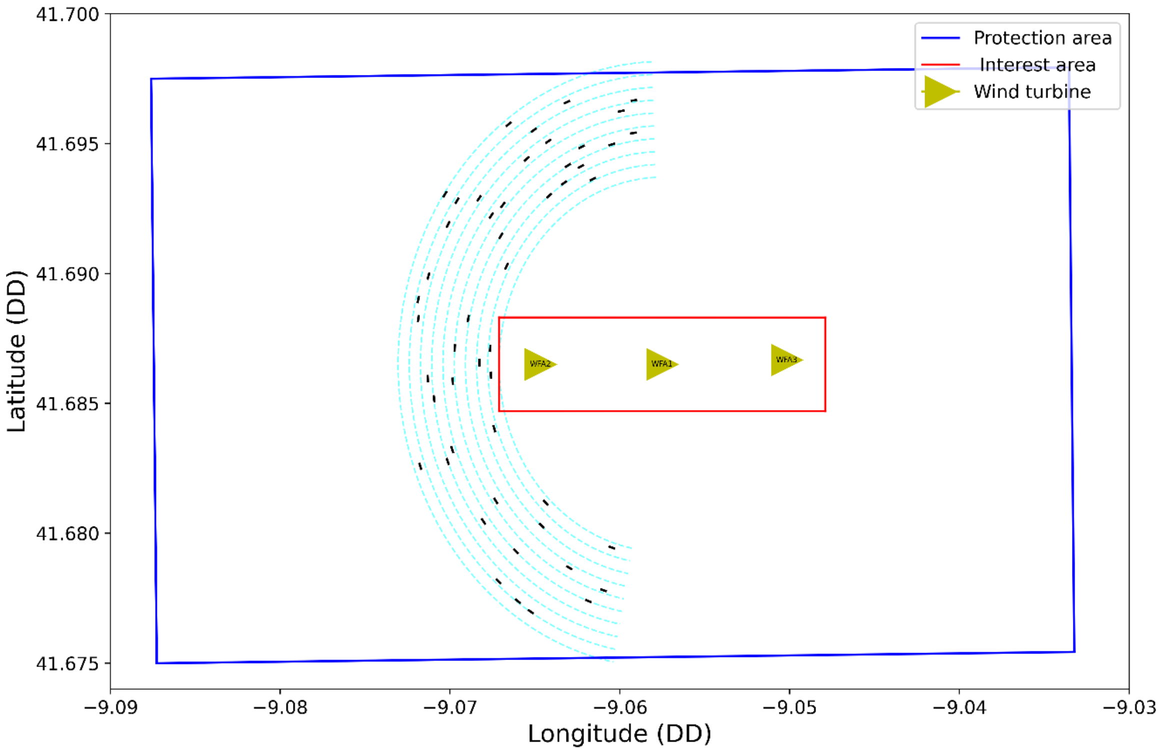

Figure 29 – Protection area (dark blue), WEC farm possible area (light blue), area of interest (red), and wind turbines (yellow).

3.5.2.2. Wave Energy Converter and bathymetry

In this study, the floating version of CECO [275–277] device was used as a case study for capturing wave energy. CECO is a point absorber WEC that utilizes a sloped power take–off (PTO) system [276], allowing it to capture the vertical and horizontal force components of ocean waves [278,279]. The main elements of CECO consist of two lateral mobile modules (LMMs) connected by a frame of tubular elements. In its current design, CECO uses a rack and pinion system to convert the absorbed energy into electricity [275]. Figure 30 illustrates a scheme of the CECO concept and its working principle.

Research over the last eight years has been conducted to optimize the original CECO design. Changes such as the shape and mass of the LMMs have been made to improve the hydrodynamic response of the device and increase its power absorption for a wider range of wave conditions [280]. The PTO damping [281] and inclination [282] have also been found to play a significant role in the device's response. These variables can be adjusted to match the resonance condition for the most frequent and energetic sea states, which improves CECO's power absorption.

CECO also offers high flexibility in terms of installation. The original design, for nearshore shallow waters, was based on a bottom-fixed support structure. However, a floating alternative for deeper locations was designed and optimized for the wave conditions of the Portuguese coast, based on a tension leg platform with a star–shape mooring system. This configuration offers the best results in terms of energy production and mooring loads [277]. In this study, the floating version of CECO defined by Giannini *et al*. (2020) is used as the case study. For the SNL–SWAN, the relevant design characteristics are the width (22m overall), and the power matrix.

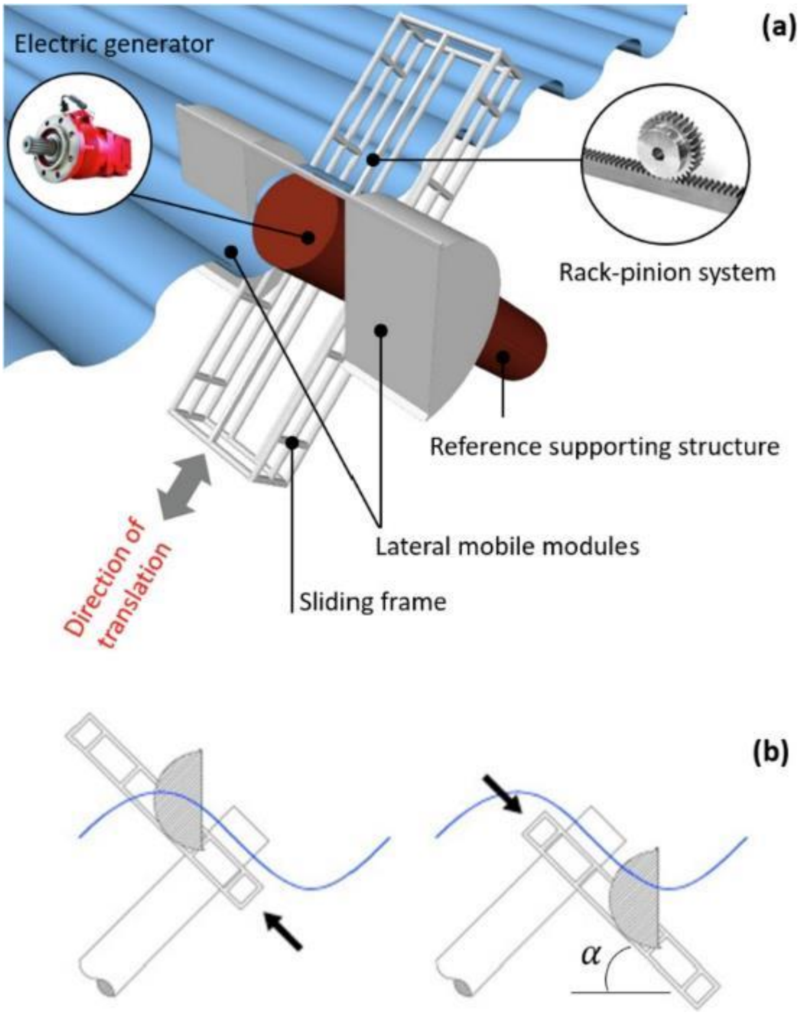

Figure 30 – CECO concept (a) and its working principle under wave action (b) [275].

Table 4 summarizes the principal features of CECO. Since, there has not been many studies done on the impacts of CECO offshore parks, this study uses the results of Ramos *et al*. (2022a), which was done at the same site, as starting point. The authors proposed an arrangement of CECO WECs placed on a curvilinear alignment facing the prevailing wave direction (NW or 315°).

As mentioned before, the SNL–SWAN model uses the WEC power matrix to establish the transmission coefficient. Therefore, the power matrix of CECO [283] was used as an input to the model and is presented in Figure 31.

In SNL–SWAN, a WEC is treated as a line of WEC–wide extension, and the device is considered by the model only where it crosses the grid. Hence the grid must be small enough to catch the WEC line as much as possible. To achieve good accuracy in simulating the WEC with reasonable use of processing time, a grid of 5.5x5.5m was created, which is 1/4 of the WEC size and guarantees at least the crossing of 5 grid cells. The whole extension of the grid covers an area of 6.6x4.4km (1200x800 cells) centered in the WindFloat Atlantic Park.

Table 4 – Principal features of the CECO WEC.

Parameter	Value
PTO inclination angle (°)	30
LMM inclination (°)	45
LMM length (m)	9.52
LMM width (m)	6
LMM maximum stroke (m)	15
LMM mass (ton)	288
Overall width (m)	22
PTO rated power (kW)	500

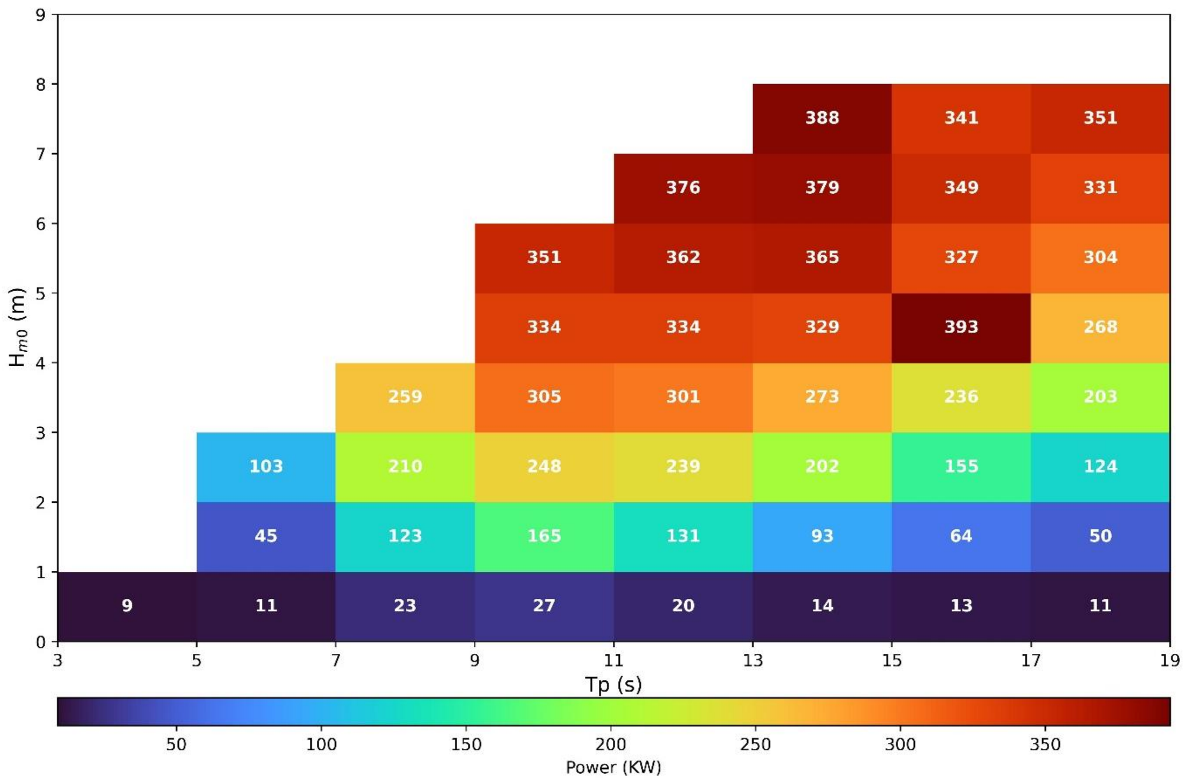

Figure 31 – Power matrix for CECO that shows the average power output by sea state [Adapted from 175]**.**

The bathymetry data were obtained from the datasets of GEBCO (The General Bathymetric Chart of the Oceans), which operates under the joint support of the International Hydrographic Organization (IHO) and the Intergovernmental Oceanographic Commission (IOC) of UNESCO.

3.5.2.3. Simulation setup

The crossover rate and the population size have a significant influence on the model computational time. Therefore, the used approach commenced with a series of simulations where these parameters were systematically varied. Then, upon identifying the optimal configuration, further simulations were conducted to assess the method's efficacy across a broader spectrum, encompassing a larger array of devices and increased inter–device spacing.

Table 5 provides a comprehensive overview of the simulation setups employed in this investigation, detailing the average new layouts generated (referred to as "children") and the corresponding number of simulations needed by each variation of the GA parameters. The "efficiency" of each simulation iteration was quantified by computing the average execution time across its generational iterations, compared against the baseline established by the fastest simulation, which was S1.

Table 5 – Simulation Setup.

SIM	WECs	Layouts	Min Dist.	Elite	Crossover Rate	Children /Generation	Simulations /Generation	Max Gen.
S1	50	25	2.5D	0.12	0.70	15.4	123.2	500
S2	50	25	2.5D	0.12	0.95	20.9	167.2	260
S3	50	50	2.5D	0.10	0.70	31.5	252.0	150
S4	50	50	2.5D	0.10	0.95	42.75	342.0	120
S5	100	25	2.5D	0.12	0.70	15.4	123.2	200
S6	200	25	2.5D	0.12	0.70	15.4	123.2	200
S7	50	25	5D	0.12	0.70	15.4	123.2	125
S8	50	25	7D	0.12	0.70	15.4	123.2	125

As will be more comprehensively elaborated in section 5.1.2, simulation S1 was not only the fastest (by generation) but also presented the best results. Hence, the simulations denoted as S5 to S8 aimed at elucidating the method's scalability to accommodate a larger number of WECs and increased inter–WEC spacings, using as basis S1 configuration. This configuration entailed a crossover rate set at 70%, a population size consisting of 25 individuals (farm layouts), and an elite rate of 12% (equivalent to 3 individuals). Notably, the average efficiencies observed in these subsequent simulations deviated by less than 1% from that of the benchmark S1 simulation.

The simulations were executed on the FEUP cluster, which comprises multiple nodes, each possessing distinct CPU processing capacities. To ensure equitable comparison, the number of generations for each simulation was estimated to achieve at least the computational execution time equivalent of 100 generations of the slowest simulation (S4), which was about 4 days. It is noteworthy that, to maintain consistent runtime conditions, all simulations were executed utilizing 24 cores on an AMD EPYC 7443 processor for a minimum of 10 generations. Consequently, owing to its superior performance, the S1 simulation was extended to 500 generations to optimize the layout of the WEC farm layout.

3.5.2.4. Verification Study

A comparative study was conducted to validate the performance and accuracy of the proposed optimization algorithm. Three simulations were selected (S1, S5 and S6) to obtain results with different numbers of WECs (50, 100, and 200). The study compares optimization results obtained using the dual–objective function (WLA) against those obtained with single–objective functions focused exclusively on maximizing the power production (*q-factor*) and the shield protection factor (HRA). This comparison aims to highlight the importance and effectiveness of the dual–objective approach.

Additionally, the accuracy of the algorithm is evaluated by rerunning the selected cases and comparing the optimized layouts with those presented in the first simulation (original run). To evaluate the positional discrepancies between the rerun optimized layouts and the original simulation, the RMSE was employed as a quantitative metric. The calculation methodology comprised two key steps.

First, to find the optimal pairing of WEC positions, the Kuhn–Munkres algorithm was utilized to establish the optimal correspondence between the WECs in the original and rerun layouts. This method minimizes the total positional distance across all WECs, ensuring an objective and globally optimal pairing. Once the optimal pairs were identified, the RMSE was calculated to the distances between the paired WECs. This approach captures the magnitude of the average positional error in meters, providing a comprehensive measure of the layout deviations between simulations. Additionally, two other parameters were evaluated, the distance between the centroids of each WEC array and the number of WECs with a distance from the pair higher than the WEC width, to evaluate the precision.

This methodology ensures a rigorous and systematic assessment of the optimization algorithm's consistency. The RMSE serves as a robust indicator of the accuracy of the rerun layouts compared to the original simulation, reflecting the algorithm's capability to reproduce optimal configurations under varying conditions.

Considering the computational costs, all simulations performed for verification were executed with a termination criterion of 200 generations and compared to the results of the original simulation at the same generation.

3.5.3. Wave farm Layout based on economic parameters

The methodology, location, device configurations, and algorithmic parameters used in this analysis replicate those from simulation S1 in the sensitivity analysis, as this case demonstrated the most favorable results. In previous scenarios, the weights applied in the objective function were either equal or designed to prioritize power absorption or shield protection, without explicitly incorporating the economic advantages inherent to each parameter.

Typically, the LCoE index is utilized to analyze the economic aspects of WEC farms. However, as LCoE includes several fixed parameters unaffected by WEC positioning or variations with negligible influence relative to the benefits derived from increased power absorption and enhanced accessibility, it was deemed unnecessary to explicitly incorporate all LCoE factors in this case. Instead, the influence of two primary parameters, the HRA and the *q-factor*, was prioritized to define the weights in the objective function.

The valuation of both objectives was grounded in existing economic references. The guaranteed price per kilowatt–hour (kWh) from the WindFloat Atlantic project, as determined by the Portuguese government (0.1552 €/kWh), was used as a proxy for revenue from wave energy production. Meanwhile, the average waiting hour cost for Operations & Maintenance (O&M) in offshore wind farms (300 €/h) provided an estimate for accessibility–related costs. While these values are not directly applicable to WEC farms due to the absence of established wave energy incentives, they serve as reasonable approximations. This approach considers that both wind and wave energy operations share similar thresholds for O&M activities, particularly regarding vessel operations.

Using these values as a reference, the optimal layout of 50 WECs, identified from simulation S1, achieved estimated annual savings of approximately €746,000 and a revenue of around €9 million. It is important to emphasize that this revenue does not represent the total income generated by the farms, as it excludes the comprehensive costs associated with the entire power production chain. The revenue associated with power production, driven by the *q-factor*, was calculated using the following formula:

$$\boldsymbol{Rev = q\text{-}factor \times N_{WECs} \times P_{WEC} \times GP} \tag{44}$$

where, Rev represents the revenue, N_{WECs} the number of WECs in the array, P_{WEC} the power output of a single WEC, and the GP the guarantee price, which is a fixed remuneration rate.

The valuation of HRA was derived from the savings related to the increase in accessibility, defined as the time that the significant wave height (H_s) was reduced to values below 1.5 m, which is the typical threshold for safe sea operations. The savings derived from the improvement in accessibility was linked to reductions in waiting time and the cost of keep the maintenance crew waiting on land, as follows:

$$\boldsymbol{WS = \frac{Ac_{wec} - Ac_0}{Ac_0} * WC} \tag{45}$$

where the WS represents the savings of lower waiting time, Ac_0 the baseline scenario (without WECs) access time to the wind farm, Ac_{wec} the scenario with the WEC farm, WC the waiting time cost.

This relationship was established by applying a matrix of wave height reductions to the dataset, quantifying the accessibility improvements attributable to specific layouts, and translating these into annual waiting time reductions.

Using data from previous simulations involving 50 WECs (S1, S2, S3, S4, S7, and S8), the relationships between the *q-factor* and HRA were analyzed (Figure 32), revealing a strong linear correlation with a Pearson correlation coefficient of 0.92. However, this correlation is notably biased, as the layouts were optimized to simultaneously maximize both factors. To address this, valuations for each objective were obtained through linear regression, as shown in Figure 33 and Figure 34. The resulting representative curves illustrate the relationships between each objective and the corresponding economic benefit.

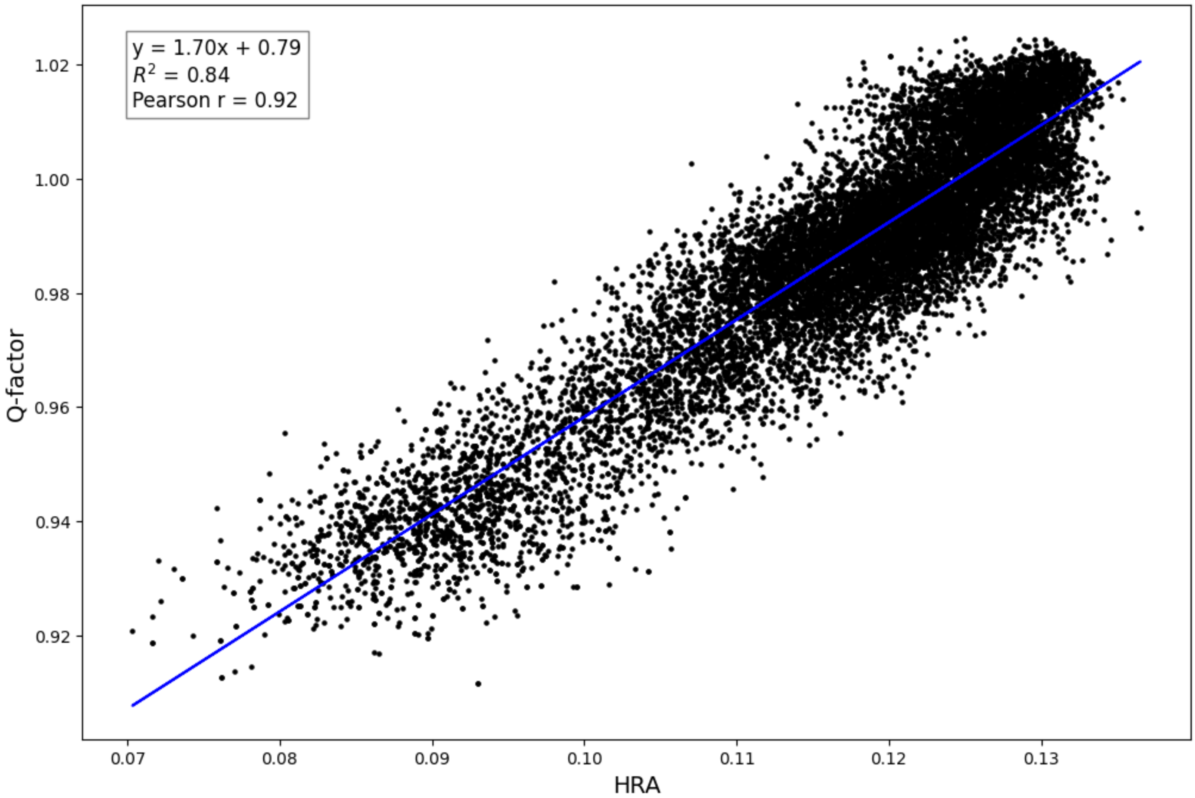

Figure 32 – Relationship between *q-factor* and HRA of layouts analyzed in optimization simulations S1,

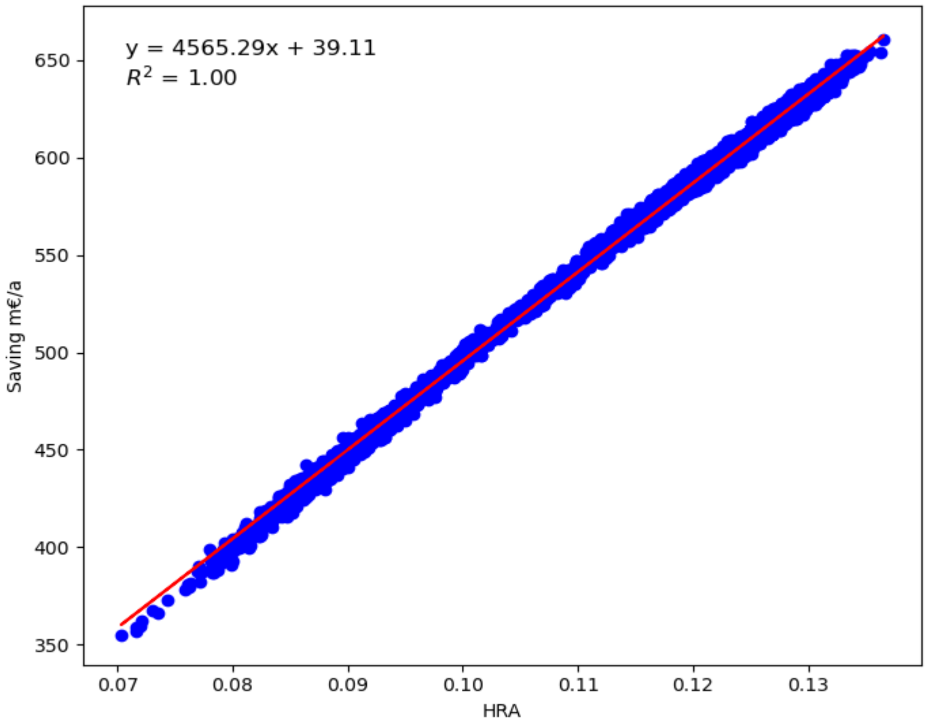

Figure 33 – Relationship between HRA and savings related to increase in the accessibility of the farm.

S2, S3, S4, S7 and S8.

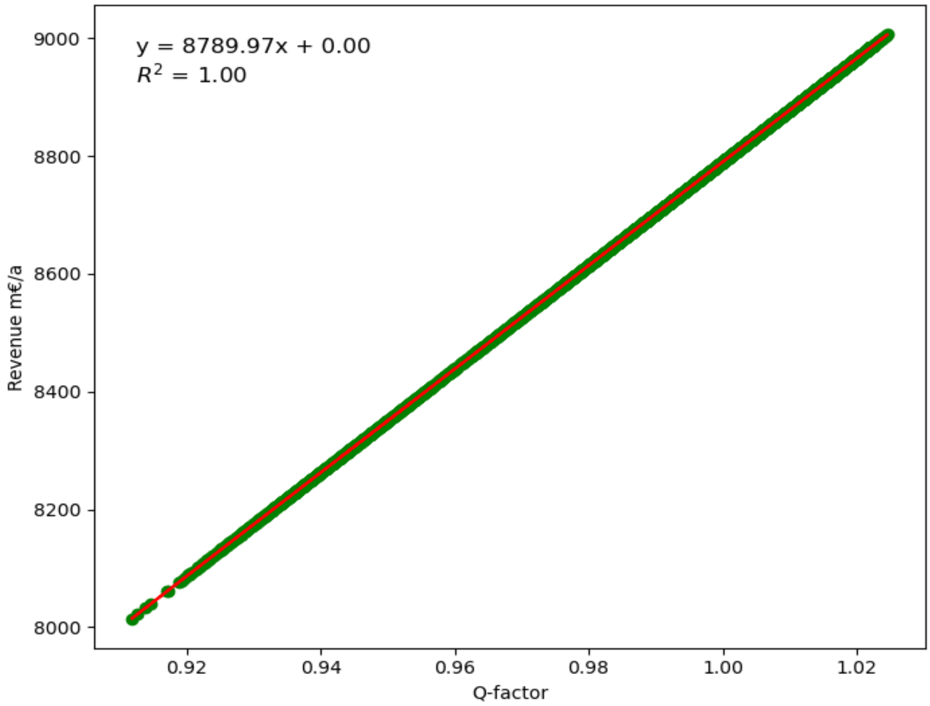

Figure 34 – Relationship between the *q-factor* and the revenue provided by the commercialization of the electric energy produced.

Given that both revenue and savings were evaluated based on full-time annual operations, the process of determining the weights for the objective function began with analyzing the rates of change (or gradients) of the financial valuation curves for each objective. These curves represent the relationship between the specific objective (such as power production or accessibility improvements) and its corresponding economic benefit.

To quantify the gradients, the first derivative of each curve was calculated. The derivative in this context measures the rate of change of the economic benefit with respect to the objective's improvement. Since the relationships between the objectives and their financial outcomes were linear, the derivative simplifies to the coefficient of linear term (m) of each curve.

The next step involved determining the relative contributions of each objective to the overall financial benefit. The gradient of the curve for each objective serves as an indicator of its economic impact. To balance these contributions, the gradients were normalized by calculating their proportions relative to the total gradient (sum of the gradients of all objectives). The weights were then assigned as:

$$\boldsymbol{p} = \frac{\boldsymbol{m_2}}{\boldsymbol{m_1} + \boldsymbol{m_2}} = \mathbf{0.6582}, \qquad \boldsymbol{s} = \frac{\boldsymbol{m_1}}{\boldsymbol{m_1} + \boldsymbol{m_2}} = \mathbf{0.3418} \tag{46}$$

This method ensures that the weights reflect the relative importance of each objective to the overall financial outcome, providing a balanced and economically rational basis for optimization. By constraining the sum of the weights to equal 1, the methodology maintains consistency in the distribution of influence across the objectives while aligning with their economic significance.

3.5.4. Wave farm optimization for coastal zone (nearshore)

This section outlines the methodology used for optimizing WEC farms in nearshore coastal zones. Two distinct Portuguese case sites, Esposende and Aguçadoura, were selected to demonstrate the applicability of the proposed framework. The optimization aims to address two main objectives:

i. Enhancing coastal protection by mitigating erosion and flooding;

ii. Minimizing environmental impact on the shoreline.

Both case sites were selected due to their vulnerability to coastal hazards [284–288], such as erosion and flooding, and the availability of prior studies (Clemente *et al*. [289] for Esposende and Santiago *et al*. [290] for Aguçadoura). These studies serve as benchmarks to compare the effectiveness of the optimization algorithm. Figure 35 shows the localization of the study areas referencing to Esposende, Aguçadoura and Viana do Castelo as reference of the offshore case.

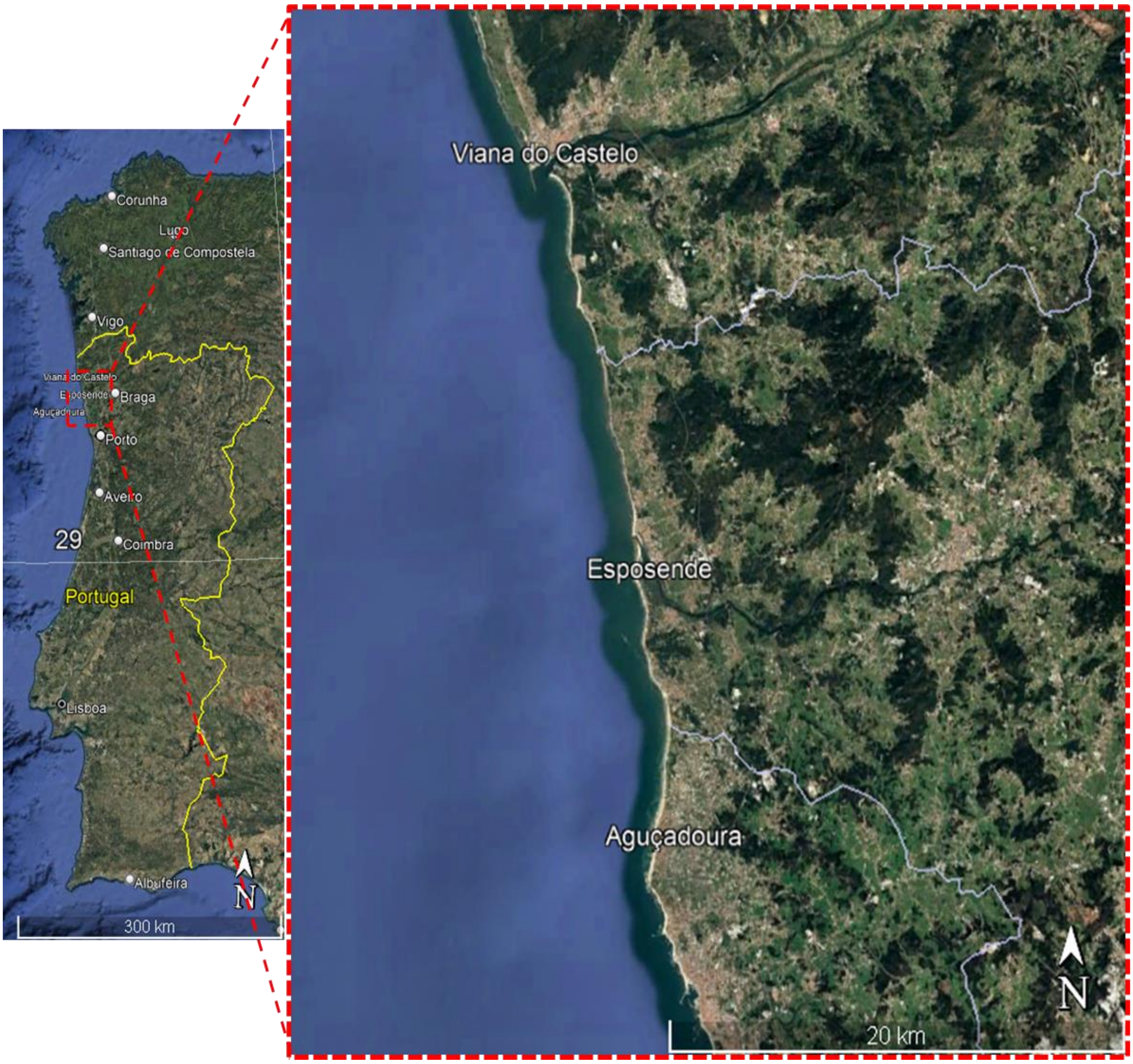

Figure 35 – Localization of the study case, in Esposende, Portugal. Referencing important adjacent areas. Adapted from google earth.

The expected outcomes are the identification of optimized WEC configurations and layouts for coastal protection and reduced environmental impact, the demonstration of the AI framework's ability to outperform existing fixed–layout approaches, and the quantification of wave height reduction, erosion mitigation, and farm efficiency for both study sites.

3.5.4.1. Case Study Sites

3.5.4.1.1. Esposende (Ofir–Fão Beach)

The study area is situated at the mouth of the Cávado River and its estuary (41°32'20.92"N; 8°47'31.65"W), along the coast of Esposende, in the Braga district, Portugal (Figure 35). The river mouth is bounded to the north by a breakwater and to the south by the Ofir sandspit, a sandy formation approximately 2100 m long that separates the river from the sea. This serves as a critical natural defense for Esposende against coastal erosion and wave action, although its morphology is highly variable due to the interplay of marine and fluvial dynamics.

Figure 36 hatched area highlights the risk of flooding and Figure 37 highlights this risk of erosion, emphasizing the urgent need for coastal protection.

Figure 36 – Flood risk areas in Esposende. Adapted from IH portal [291].

The Ofir sandspit and adjacent coastal structures, including a dyke and a groyne, play key roles in managing shoreline evolution. However, these structures are increasingly vulnerable to marine environmental actions which result, for instance, in crest height reductions of the sandspit and frequent overtopping, especially during high tides. Extreme weather events exacerbate this, allowing waves to penetrate the estuary and cause flooding in urban areas. Notably, the Program for Coastal Zones [285] identifies annual erosion rates at Ofir-Fão beach of 1.85–1.95 m, projecting a coastline retreat of approximately 100 m by 2050. This corresponds to the Level I Coastal Erosion Safeguard Zone, posing significant risks to people and property. Additionally, flood risks are concentrated on Ofir–Fão beach, identified as a medium flood risk area for a 100-year return period.

Figure 37 – Erosion risk areas in Esposende. Adapted from POC [285].

The Esposende nearshore, part of the Natura 2000 Network (Littoral North Natural Park) [292], includes protected habitats such as rocky outcrops and biogenic reefs. The area is under pressure from coastal erosion, tourism, and fishing activities, with the latter concentrated within 3 nautical miles of the coast. Despite these challenges, Clemente *et al*. [289] proposed a WEC farm deployment area that balances environmental protection with operational feasibility.

The proposal accounts for geomorphology, dredging sites, sedimentary areas, protected habitats, and suspended sediment flow, alongside seabed characteristics, depth constraints, and marine space conflicts. The selected site adheres to the operational depth range of WEC technology and avoids sensitive areas such as shoreline reefs, Western biogenic reefs, touristic beaches, and sand and gravel deposits. Positioned near the 20–meter depth contour, the farm minimizes visual impact due to its submergence. Its orientation, aligned with prevailing NW–W wave directions, attenuates wave energy leeward of the farm, creating a wake effect that benefits the river mouth and Ofir sandspit, promoting safer conditions for coastal activities. The polygon delineating the proposed deployment area is illustrated in Figure 38.

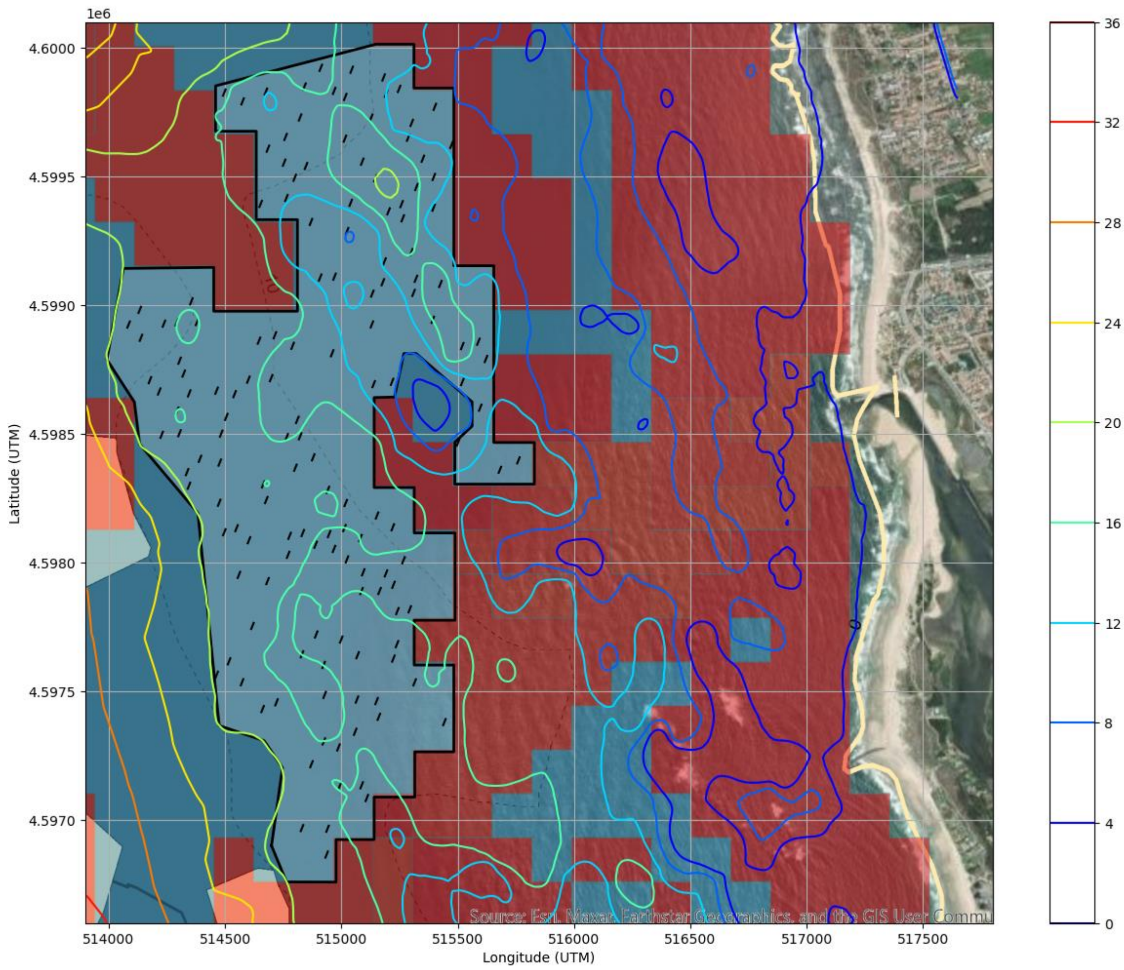

Figure 38 – The Esposende WEC farm deployment area is outlined in black. The WECs are represented by small lines inside this area. Red regions indicate vulnerable habitat areas, while the pastel shading extending from the Cávado River mouth through the red zone represents the suspended sediment flow. The seabed contours are color–coded according to the accompanying color bar. This figure has been adapted from the DGRM geoportal [287] and the IH infographic [291].

3.5.4.1.2. Aguçadoura

The Aguçadoura test site, established in 2001, is a grid–connected facility for maritime renewable energy testing located approximately 5.5 km offshore from Póvoa de Varzim in northern Portugal. This site is internationally recognized as a pioneering location for developing and demonstrating WEC technologies. Spanning an area of approximately 3.0 km² in water depths ranging from 40 to 60 m, it benefits from the energetic wave climate of the Atlantic Ocean, making it ideal for evaluating and optimizing maritime renewable energy devices. Figure 39 presents the local bathymetry and the delimitation of the test site in Aguçadoura by DGRM [293].

Since its inception, the Aguçadoura test site has hosted the testing of some devices: the Archimedes Wave Swing (AWS), tested as part of early advancements in wave energy technology; the Pelamis Wave Power P1 machines, deployed as the world's first commercial–scale wave energy farm, the Aguçadoura Wave Farm, in 2008; the WindFloat 1 Prototype, a floating offshore wind energy device developed by Principle Power; and more recently the CorPower Ocean C4, currently being tested as part of the Hi–Wave5 project.

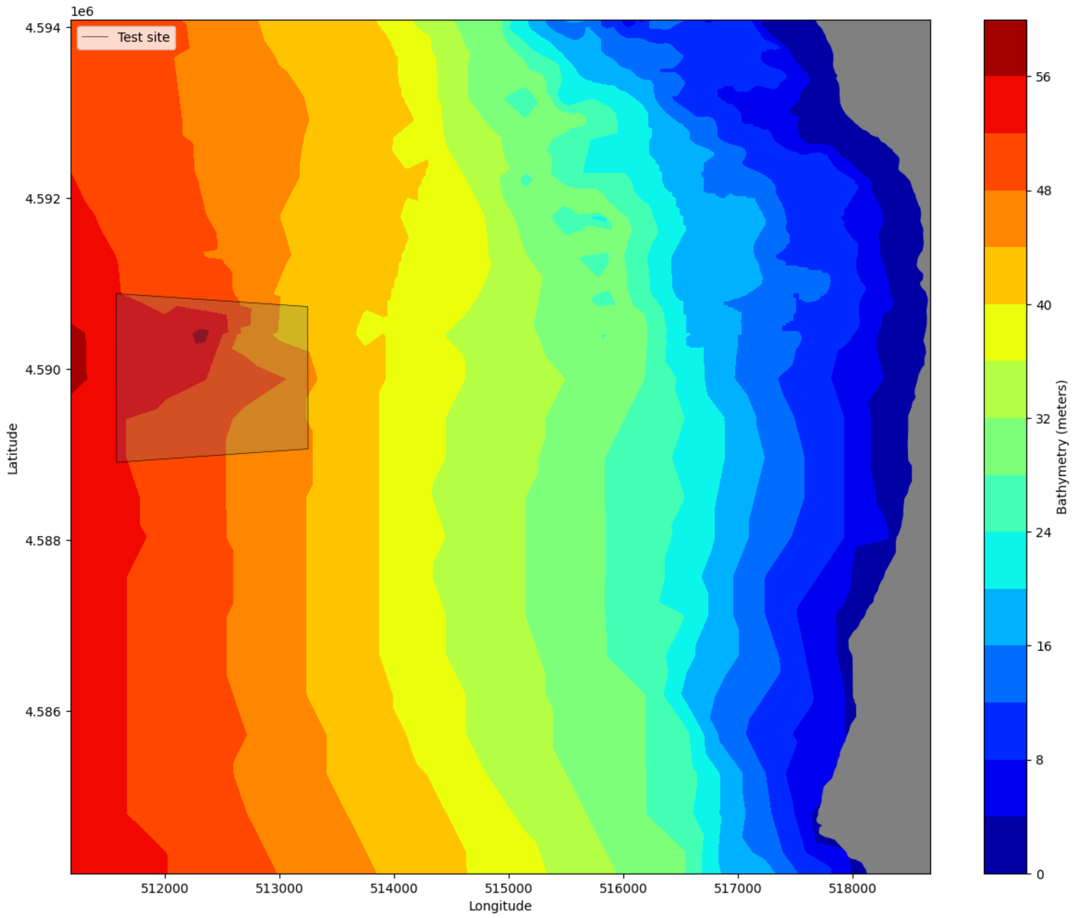

Figure 39 – Bathymetry of the region of the Aguçadoura test site. The grey shadow is the test site.

The HiWave–5 project [294] has deployed a full–scale C4 WEC prototype at Aguçadoura, Portugal (41.4306°N, −8.7861°E), within a 750 × 500 m² test site at depths of 35–50 m. The project capitalizes on the region's robust wave energy resources and existing grid infrastructure. The C4 device, measuring 9 × 18 m and weighing 60 tons, is designed to produce five times more energy per ton than previous technologies. The pilot demonstration aims to validate the technology, achieving market viability and enabling pre–commercial wave farms [290].

Aguçadoura's infrastructure includes a 3 MW export cable for grid integration, supporting the testing of full–scale or partial–scale wave energy devices and floating solar technologies. The site is currently undergoing infrastructure upgrades, including the installation of a three–input subsea hub to accommodate multiple device connections. In addition to wave energy devices, the site also serves as a testing ground for robotic systems, aquaculture structures, and ocean monitoring and cleaning technologies.

Coastal areas near Aguçadoura, such as Apúlia to the north and Ribeira da Barranha to the south, are of interest due to their environmental vulnerability. While these areas generally face low flooding and erosion risks, more significant threats are observed further north in Ramalha, where erosion rates range from 0.65 to 2.35 m per year, and overtopping risks are severe near the Alto River mouth. By 2050, coastline retreat in this region is projected to reach 65 to 125 m. The hatched area in Figure 40 highlights the risk of flooding and in Figure 41 highlights this risk of erosion, emphasizing the urgent need for coastal protection.

Figure 40 – Flood risk for Aguçadoura area. Adapted from IH portal [291].

Figure 41 – Erosion risk for Aguçadoura shoreline. Adapted from POC [285].

Although Aguçadoura experiences relatively low erosion rates, overtopping remains a concern, particularly near Ribeira da Barranha. These vulnerabilities highlight the importance of integrating coastal dynamics into energy development planning to mitigate potential environmental impacts.

The Aguçadoura test site exemplifies Portugal's commitment to advancing its blue economy by fostering sustainable use of marine resources. Managed by WavEC and INESC TEC, the facility continues to evolve in response to technological developments and the needs of developers. Its role as a real–world testing environment has enabled collaborations between academic institutions, technology developers, and government organizations.

By providing a controlled yet dynamic testing ground, Aguçadoura supports the development of innovative technologies that contribute to global renewable energy goals. The site's strategic location and robust infrastructure reinforce its position as a cornerstone in the advancement of maritime renewable energy technologies.

3.5.4.2. Wave Energy Converters

3.5.4.2.1. Oscillating Wave Surge Converter

An oscillating wave surge converter (OWSC) is a type of WEC designed to extract energy from the surge motion of water particles near the surface in response to incoming waves. These devices typically operate in nearshore environments, where wave energy is concentrated due to the shallower depths and the increased influence of wave surges. The OWSC is characterized by its large, flap-like structure that is anchored to the seabed. The bottom-fixed oscillating flap (B–OF) is typically positioned perpendicular to the wave direction. Figure 42 illustrate the concept of a B–OF OWSC [296].

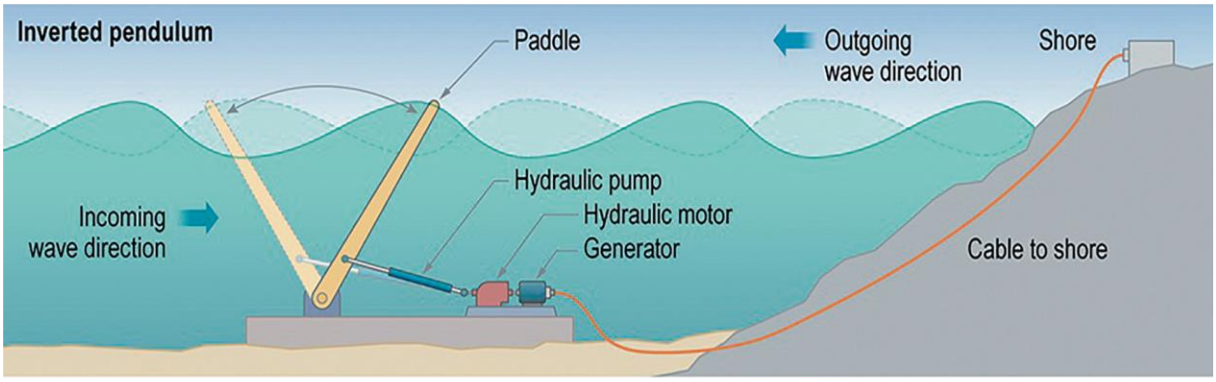

Figure 42 – Representation of the B–OF OWSC concept. Adapted from [296].

The WaveRoller® is a B–OF OWSC developed by the Finnish company AW–Energy [295]. It represents a high Technology Readiness Level (TRL) WEC designed to harness ocean wave energy efficiently in nearshore environments. Operating in water depths of 8 to 20 m, the WaveRoller® is typically deployed between 0.3 and 2 km from the shoreline, making it ideal for shallow to intermediate–depth coastal areas where horizontal water particle motion predominates.

As waves pass over the panel, the surge motion of water particles induces a back–and–forth oscillatory movement. This motion is captured by the panel and converted into electricity through a Power Take–Off (PTO) system, which comprises hydraulic cylinders, a hydraulic motor, and an electric generator. The panel motion pressurizes hydraulic fluid in a closed, hermetically sealed hydraulic circuit, eliminating the risk of environmental contamination. The pressurized fluid powers a hydraulic motor that drives an electricity generator, and the generated electricity is transmitted to the grid via subsea cables.

The WaveRoller® has undergone rigorous testing and multiple stages of development, including prototype evaluations and commercial pilot projects. A notable full–scale deployment off the coast of Peniche, Portugal, demonstrated its capability to produce consistent power output under real ocean conditions. These trials, complemented by numerical studies such as those utilizing the SNL–SWAN model [299,300], have provided valuable insights for optimizing the device's performance.

A single WaveRoller® unit, including one panel and PTO system, has a rated power capacity ranging from 350 kW to 1 MW, with an estimated capacity factor of 25% to 50%, depending on the wave conditions at the deployment site. The device can be deployed as standalone units or in modular arrays to meet varying energy demands. Each panel spans the water column from the seabed to the surface, enabling the device to absorb the wave energy. Its modular design ensures scalability and adaptability to site-specific conditions.

While the WaveRoller® shows immense potential, it faces challenges common to marine energy technologies. These include high initial capital costs, the need for further efficiency optimization, and logistical complexities associated with installation and maintenance in harsh offshore environments. Additionally, issues like corrosion, biofouling, and resilience to extreme weather events require ongoing innovation. Nevertheless, the WaveRoller® exemplifies the promise of wave energy technologies in advancing renewable energy solutions for a sustainable future.

For this study was considered, as done in literature [297,298] a generic B-OF of 3.332 MW. A visual representation and power matrix are provided in Figure 43 . The B-OF is 26 m wide parallel to the wave front, 2 m thick and 16 m high, 14 m of which for the paddle. Table 6 summarizes the principal features of the OWSC B–OF used.

Table 6 – Principal features of the WaveRoller®.

Parameter	Value
Length (m)	2
Overall width (m)	26
Operation Depth (m)	8–20
Total Height (m)	16
Paddle Height (m)	14
PTO rated power (MW)	3.332

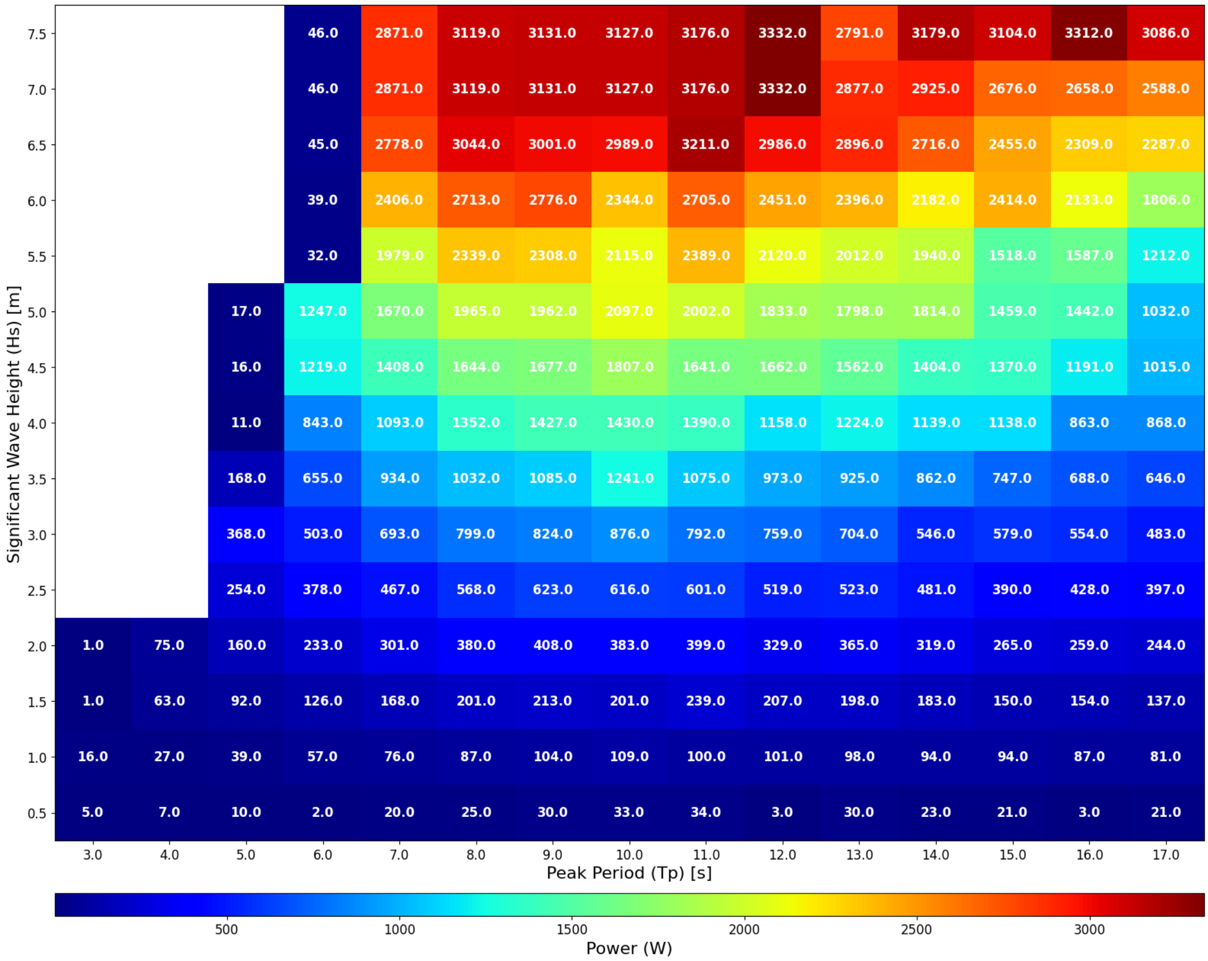

Figure 43 – Power matrix (KW) of a B–OF of 3.3 MW.

3.5.4.2.2. Point absorber - Corpower WEC Stage 4 (C4)

The machine that is simulated at the Aguçadoura test site corresponds to the one developed in the HiWave–5 project [294], from CorPower [301], Figure 45. The HiWave–5 initiative seeks to demonstrate a fully integrated WEC system at a commercial scale through five stages (Figure 44), the Stage 4, involving dry and ocean testing of a single full–scale device was the last one completed, and Stage 5 is intended to focus on the ocean demonstration of a pilot array with three devices [290]. This project aims to achieve a Technology Readiness Level (TRL) 8 by 2025.

The power matrix provided by CorPower (Figure 46) is used in the SNL–SWAN simulation of the C4 WEC unit. This matrix expresses the power absorption of the C4 estimated to be achieved in 2030 and is derived from computer simulations. These simulations account for conversion chain losses (*e.g.*, downtime, array interaction, electrical farm losses, and auxiliary consumption), but exclude external system losses. Array-related losses, which include grid losses and auxiliary consumption, represent about 9.2%, with projections to decrease to 9.1% by 2040 [290].

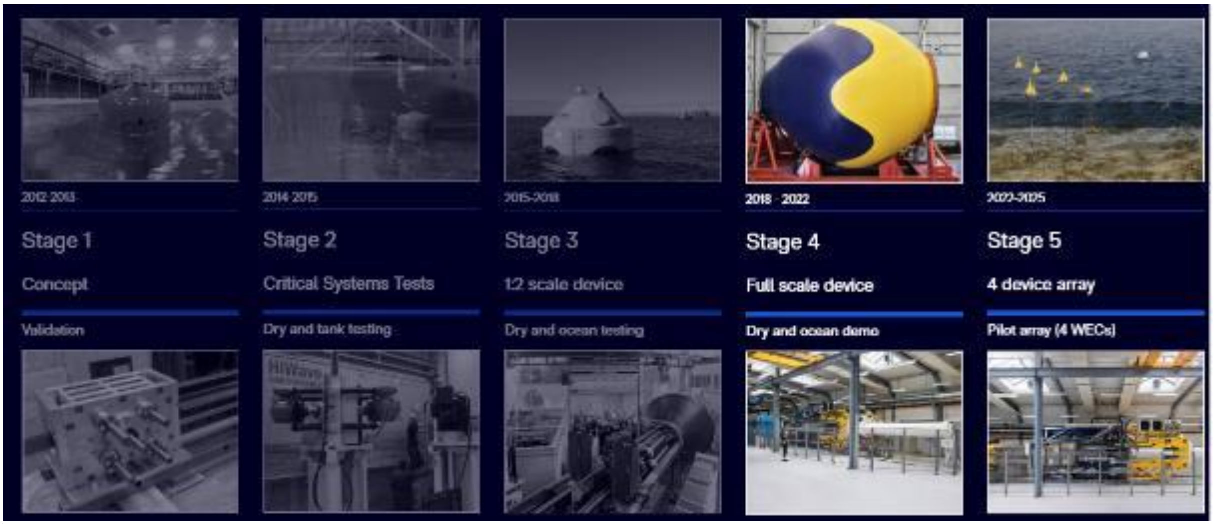

Figure 44 – Programed stages of development according to Corpower. Adapted from [294].

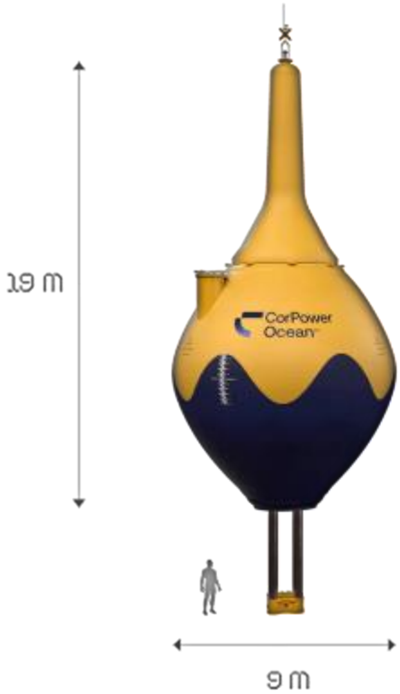

Figure 45 – Corpower C4 WEC used in the Hiwave–5 project. Adapted from [294].

The C4 WEC is a point absorber–type device, consisting of a buoy tethered to the seabed via a tensioned mooring line. It oscillates in resonance with incoming waves to amplify energy capture, a capability made possible through CorPower's proprietary WaveSpring phase control technology. This system allows the device to generate equal amounts of energy during upward and downward movements, while also enabling detuning for enhanced survivability during storms. The device operates optimally in water depths of 30–100 m, with possibilities for deployment at depths exceeding 1,000 m. Its mooring system is designed to accommodate tidal variations of up to 7 m.

The buoy, constructed from composite fiberglass using filament winding, minimizes viscous losses and ensures the Power Take–Off (PTO) system is protected from the marine environment. The PTO includes a rack, gearbox, horizontal axis, flywheels, and generators. The rack–and–gearbox mechanism converts the relative motion of the buoy into rotational energy, which is subsequently transformed into electricity.

The Corpower C4 WEC is distinguished by its WaveSpring phase control mechanism located at the buoy's top. This gas–spring system dynamically adjusts pressure and alignment to enhance energy capture, while also providing protection during extreme wave conditions by detuning the device. The pre–tension system pulls the buoy downwards and upwards according to wave swells.

The C4 enters a transparent mode during storms, minimizing its interaction with wave energy to preserve its structural integrity. Additionally, C4 features the development of the Wet Kit, comprising the WEC along with the Hull, Shroud, Mooring rod, and Tidal regulator. The Hull, an innovative product in this project, is a sandwich structure made from composite fiberglass material produced by filament winding. This design effectively protects the PTO from the harsh marine environment [301].

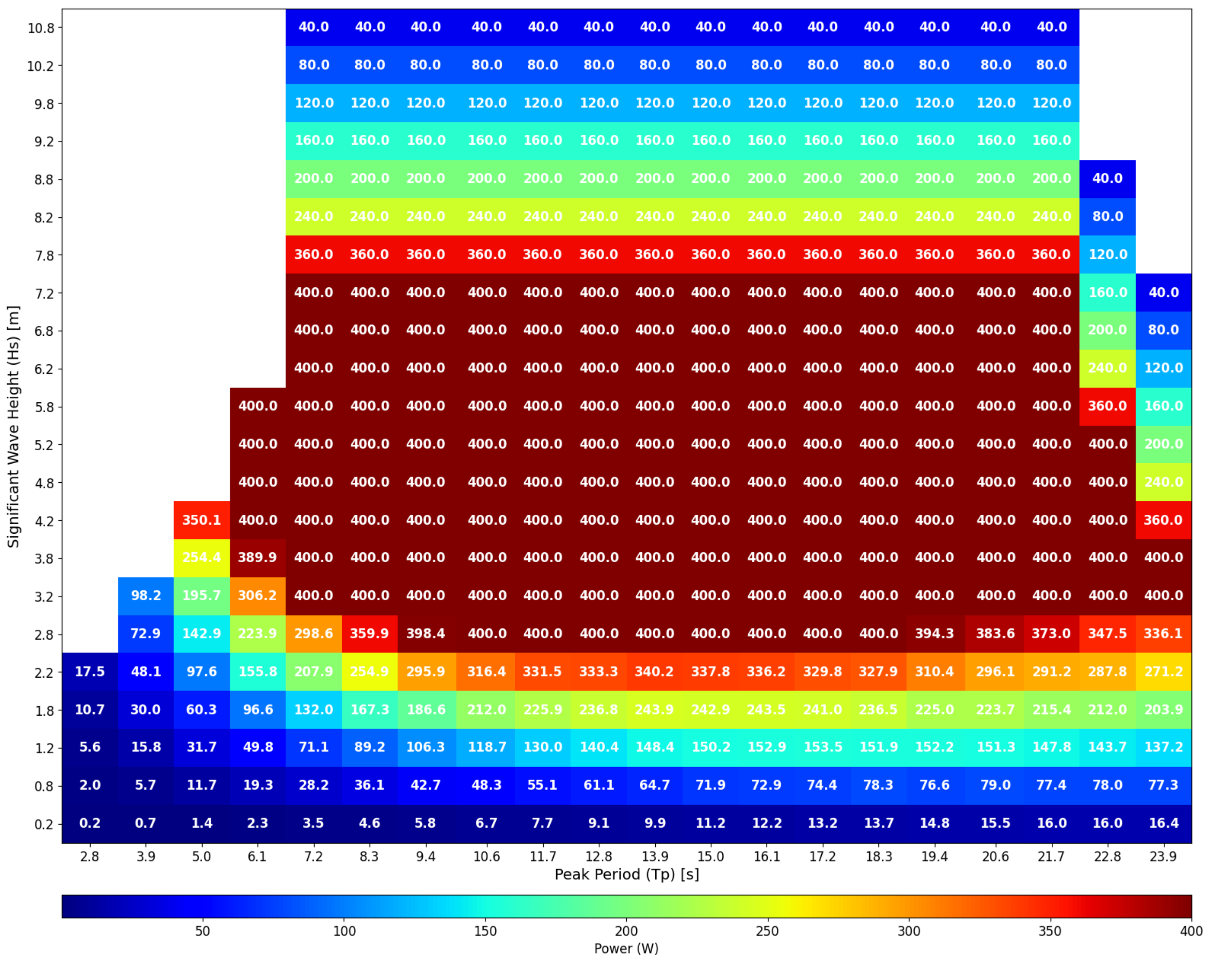

Figure 46 – Power matrix Corpower C4 WEC, adapted from [290].

The WEC has lower visual impact, since the floaters extends less than 10 m above sea level, facilitating acceptance from local communities. The modular design facilitates efficient industrial rollout and supports local supply chains for construction, installation, and maintenance. Moreover, with a power density of 15 MW/km², the wave farm can offer 3 to 5 times more energy output per ocean area than typical offshore wind farms.

3.5.4.3. Simulation Scenarios

The scenarios for enhancing coastal protection in order to mitigate erosion and overtopping risks and for minimizing environmental impact on the shoreline will be simulated at both case sites, each one designed to address specific coastal management objectives:

In the first scenario (enhancing coastal protection), the primary objective is to increase coastal protection by optimizing the deployment of WECs to reduce erosion and mitigate overtopping risks. Simulations will focus on maximizing wave energy dissipation within predefined coastal AOIs. The aim is to identify the most effective layouts and configurations of WECs that enhance energy dissipation in critical areas, thereby contributing to improved coastal stability and reduced vulnerability to extreme wave events. The analysis will examine the relationship between the energy capture capabilities of the devices and the extent to which they can reduce wave energy reaching the shore, with particular attention to reduce the risk of erosion and flooding.

The second scenario, (minimizing environmental impact on the shoreline) aims to minimize the environmental impact of wave energy extraction along the shoreline. In this case, the layouts of WECs will be optimized to avoid areas where coastal protection is unnecessary, ensuring that wave energy is only harvested from regions where it can provide the most benefit. The goal is to maintain the natural integrity of the coastline by preventing unnecessary energy extraction in areas where it could disrupt the local ecosystems or interfere with coastal processes. Simulations will identify optimal configurations that minimize ecological disturbances while still achieving effective wave energy capture in the areas where it is most needed.

To address the unique challenges at each site, specific considerations will be made forboth coastal zones. In Esposende, the area of interest is smaller than the WEC deployment zone and specifically targets vulnerable coastal segments that are mostly at risk of erosion and overtopping. In addition, the deployment zone is located relatively close to the shoreline, and the space between the area of interest and the deployment polygon is minimal. This spatial arrangement requires a highly targeted approach to deployment, ensuring that WECs are positioned strategically to protect the most vulnerable parts of the coastline while avoiding unnecessary interference with other coastal processes.

In contrast, Aguçadoura presents a different set of challenges. The deployment zone is located further from the coastline, which offers greater flexibility in terms of layout optimization. In this case, the focus will be on reducing the overall environmental impact of wave energy extraction, while also considering two distinct areas of interest: one to the north and one to the south of the deployment zone. These areas will be evaluated for their suitability in terms of wave energy capture, and the potential effects on local ecosystems and coastal dynamics will be carefully considered. The greater distance between the deployment zone and the shoreline in Aguçadoura allows for a more dispersed configuration of WECs, reducing the potential for direct impact on the shoreline and allowing for a more gradual transition in wave energy dissipation.

In both sites, the simulations will incorporate a detailed understanding of the local hydrodynamic conditions, coastal topography, and environmental sensitivities to ensure that the wave energy solutions are both effective and sustainable. The outcome of these simulations will provide valuable insights into how wave energy can be harnessed in a way that balances the need for coastal protection with environmental preservation.

3.5.4.4. Optimization Methodology

The methodology builds on prior fixed–layout studies [289,290] while introducing an optimization framework for flexible WEC farm positioning. The approach comprises several key steps to enhance the adaptability and efficiency of WEC farm deployment.

For the Esposende case, representative sea states mirror those used by Clemente *et al*. [289], as both methodologies were developed concurrently. While the present study utilized Python libraries, Clemente *et al*. relied on the IBM® SPSS® Statistics software and did not perform the comprehensive data analysis, cleaning, and parameterization achieved in this research. The adoption of identical sea states facilitates higher fidelity in comparative analyses between the studies. In contrast, for the Aguçadoura case, the approach differed. Santiago *et al*. [290] employed wave data from the Leixões buoy over a 15–day period of high–energy waves. Here, the sensitivity analysis framework applied k–means clustering to identify representative sea states, using data from the ERA5 reanalysis dataset [302] for the period 2001–2017.

The AI–based optimization algorithm was designed to achieve two primary objectives concerning the impact on the wave climate. First, it aimed to maximize coastal protection by evaluating WEC–induced reductions in significant wave height and energy dissipation near the shore, thereby increasing the HRA index. Second, it sought to minimize environmental impact by quantifying energy extraction efficiency while maintaining ecosystem stability, leading to a reduction in the HRA index.

The SWAN simulations employed rectangular grids with a resolution of 3x3 m to ensure sufficient interaction between grid cells and WECs. The optimization scenarios presented distinct challenges, particularly in the second scenario, where minimizing environmental impact required careful delineation of the AOI. This was especially critical in Case II (Aguçadoura), where the deployment zone was situated far from the coast. To address these challenges, multiple AOI configurations were tested:

i. Target AOI: A single area located in front of the deployment zone, targeting specific regions;
ii. General AOI: A single area accounting for extreme wave directions;
iii. U–form AOI: A triple–area configuration surrounding the deployment zone.

This methodology underscores the potential of flexible WEC farm positioning to balance energy extraction with environmental considerations and coastal protection.

4

PARAMETERS PRE–OPTIMIZATION

This chapter aims to present a discussion of the results of the firsts steps of the framework for optimizing a wave energy farm, including choice of numerical model, definition of objective–function and representative sea states.

The research works already carried out allowed to publish two review papers, one on optimization techniques for WEC farms [3], and other on optimization algorithms applied to wave climate and energy resource [272]. Part of the review works can be seen in section 2.5. Also, the work introducing a multi–objective decision tool for both production and protection of the wind farm, presented mostly in section 4.2, was published in [63]. The findings and methodologies detailed in sections 3.3, 3.4, 3.5.1, 3.5.2, 4.3, and 5.1 were published in [4].

4.1.Phase–averaging x phase–resolving models

This section presents the development of the first objective of this investigation, which aims to evaluate different wave propagation models, phase–averaging and phase–resolving types, to assess the impact of WEC arrays on wave climate and nearshore sediment transport. The literature review on this topic is presented in section 2.4.3 – Modeling the WEC park effect, where different models were analyzed for their applicability to the investigation's objective. The selected models for further analysis are the SNL–SWAN and the SWASH.

To simulate current or sediment transport, SNL–SWAN needs to be coupled with other model, as stated in section 2.4.3, while SWASH already incorporates this feature. The one–way coupling between SWAN and SWASH is already implemented in the SWASH source code, eliminating the need for additional development.

Preliminary studies with the SNL–SWAN model have been conducted, focusing on co–located offshore energy farms and analyzing their impact on wave climate. The objective was to investigate the potential effects of an array of WECs on the leeward wave propagation and its synergies with the already installed WindFloat Atlantic wind farm located offshore Viana do Castelo, in the Northern Coast of Portugal, which has a very strong wave resource [74]. Furthermore, this study aims to establish a multi–objective function to examine and choose between WECs arrays, and is presented in more detail in chapter 4.1.

The SWASH model was executed under similar conditions as the SNL–SWAN model to facilitate a comprehensive comparison between the two. By running both models with the most similar possible input parameters, a thorough assessment of their performance and agreement can be conducted. This comparative analysis allows for an evaluation of the capabilities and limitations of each model, aiding in the understanding of their respective strengths and areas for improvement.

When applying a spectrum as the boundary condition in SWASH, it is important to be aware of the evanescent modes. These modes exhibit exponential decay away from the boundary where the spectrum is imposed and are not observable within the model. The presence of evanescent waves is inherent to the underlying equations of the model and their generation is determined by the dispersive characteristics of these equations. Hence, the lowest wave period to be considered in SWASH is given by,

$$\boldsymbol{T_{cf}} = \frac{\boldsymbol{2\pi}}{\boldsymbol{\omega_{cf}}} = \frac{\boldsymbol{2\pi}}{\boldsymbol{2K\sqrt{\frac{g}{d}}}} \tag{47}$$

where ω_{cf} is the cut–off frequency, K the number of layers, g the gravity acceleration and d the water depth. Assuming a uniform water depth of 95 m at the wavemaker boundary a significant wave height of 2.5 m and a peak period of 12 s, Table 7 was created to analyze the number of layers to be used.

Table 7 – Cut–off frequency, f_{cf}, and lowest period, T_{cf}, as a function of the number of layers.

Layers	ω_{cf} (rd/s)	T_{cf} (s)	f_{cf} (Hz)	Evanescence modes (%)
1	0.64	9.78	0.10	71
2	1.29	4.89	0.20	22
3	1.93	3.26	0.31	**~0**

Increasing the number of layers significantly escalates the computational effort. With each additional layer, the number of grid nodes increases, and the computation between layers becomes more computationally demanding. This presents a challenge in striking a balance between the computational efficiency and the desired level of accuracy when simulating wave behavior in deep–water conditions using the SWASH model. Hence, considering the wave data at the location, the same used by Ramos [283], and data from Table 7, two and three layers were used.

Furthermore, when comparing the computational efficiency between the SNL–SWAN model and the SWASH model with three layers, significant disparities in the simulation times were observed. The simulations were carried out with an Intel® Core™ i7–9700 CPU @3.00GHz computer, and a background scenario, without obstacles. The wave parameters were: significant wave height of 2.5 m, peak period of 12 s and wave direction of 285º.

SNL–SWAN model completed the simulation in approximately 4 minutes, running with 1 core. On the other hand, the SWASH model, running in parallel with 8 cores and with three–layer configuration, took more than 17 days and 13 hours to finish, showing a stark difference in computation time of about 6317 times under these conditions.

Despite the significant computational effort invested in the SWASH simulation, the results did not yield satisfactory values. Notably, an unexpected reduction in significant wave height was observed from the expected 2.5 m to an average of 1.6 m. Figure 47 presents the free surface elevation over time for the 3 WindFloat Atlantic wind turbines (WFA).

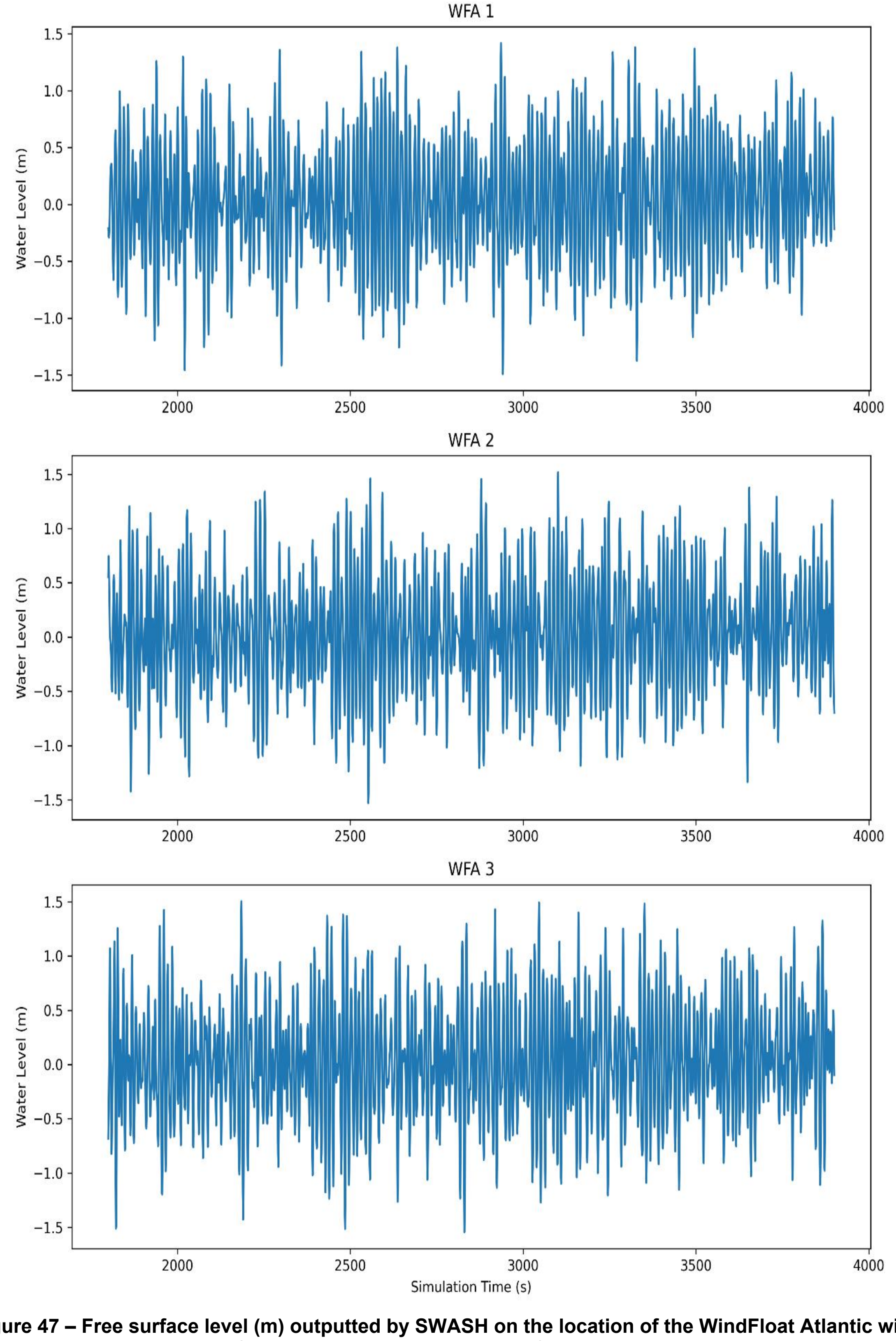

Figure 47 – Free surface level (m) outputted by SWASH on the location of the WindFloat Atlantic wind turbines for wave boundary conditions of H_s=2.5m and T_p=12s.

In conclusion, the comparative analysis of the SNL–SWAN and SWASH models underscores the pivotal role of computational efficiency in selecting the appropriate wave propagation model for analyzing the far-field effects of WEC arrays. While both models have their respective strengths, the high computational demand of SWASH, renders it impractical for extensive parametric studies or real-world applications requiring iterative simulations. Furthermore, the SWASH results exhibited inconsistencies, such as the unexpected reduction in significant wave height, highlighting challenges in achieving reliable outputs under deep-water conditions with high-resolution configurations.

In contrast, the SNL–SWAN model demonstrated remarkable computational efficiency while maintaining satisfactory accuracy for far-field wave propagation analysis [303,304]. This balance between performance and reliability positions SNL–SWAN as the preferred model for this investigation. It enables robust analysis of the far-field effects without the prohibitive computational costs associated with SWASH, ensuring the feasibility of addressing multi-objective optimization challenges and large-scale assessments efficiently.

4.2.Definition of the multi–objective function

The main objective of this thesis is optimizing the layout of the WEC farm, positioning the WECs to maximize energy extraction and the downstream park effect. However, in order to achieve this objective, the definition of the multi–objective function is crucial to set the parameters of the optimization.

In this approach, the first step is to simulate, numerically, different layout schemes, varying the quantity and position of the devices. The model used for this purpose was the SNL–SWAN due to its capacity to represent the WEC. The scenario of a co–located wind–wave offshore park was selected based on its significance and the characteristic of being situated in deep waters, where the impact of the bottom effect and sediment transport can be considered negligible.

The wave characteristics in the study area were derived from the SIMAR datasets, which are managed by the Spanish Port Authority (Puertos del Estado). SIMAR provides hourly re–analysis data for wind and wave conditions in the North Atlantic and the Mediterranean Sea, with a spatial resolution of 0.25° × 0.25°. These datasets are generated through a comprehensive numerical modeling approach that incorporates atmospheric, sea level, and wave conditions [283]. For the specific location of interest, hourly wave data was extracted from the SIMAR dataset, spanning from 1 January 1960 to 15 September 2021. This extensive data set enables a high level of accuracy and reliability.

By utilizing this extensive dataset, accurate and detailed information regarding the sea conditions could be obtained, enabling a thorough understanding of the wave characteristics and their variability over an extended time period. Figure 48 presents the occurrence of wave direction over the year on site, and the probability dispersion of the mean directions.

To properly evaluate the effectiveness of the wave farm layout in terms of shield protection and power absorption, some constraints were imposed on the simulations to restrict the variables to be analyzed.

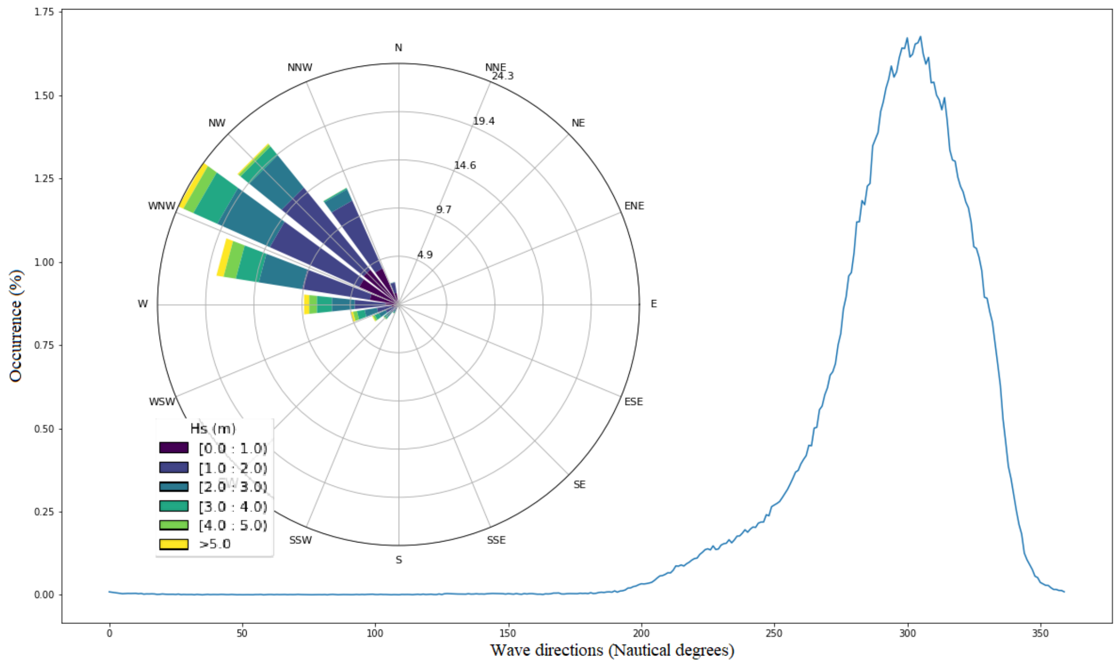

Figure 48 – Occurrences of wave directions over a year on site and the wave rose diagram indicating the direction and the wave height incidence.

These constraints were applied both to the WEC farm layout and environmental conditions. Additionally, a local wave scatter diagram was extracted from data, Figure 49 and Figure 50, characterizing the sea states in terms of mean wave direction (θ_m), significant wave heights (H_S), peak wave period (T_p) and hours of occurrence (O).

The data was evaluated to determine how many simulations were required to depict the major sea conditions. Using computer resources, simulation time, and prior knowledge of the data and location, the 92 most frequent sea states were chosen (Table 8), accounting for 80% of the data. Although not specifically chosen by the author, the selected sea states entirely contained the five major directions, namely WNW, NW, W, NNW, and WSW, as shown in Figure 48.

In this study, the floating version of CECO [275–277] device was used as a case study for capturing wave energy. CECO is a point absorber WEC that utilizes a sloped power take–off (PTO) system [276], allowing it to capture both the vertical and horizontal force components of ocean waves [278,279]. The main elements of CECO consist of two lateral mobile modules (LMMs) connected by a frame of tubular elements. In its current design, CECO uses a rack and pinion system to convert the absorbed energy into electricity [275].

The CECO's design is still under development and continues to evolve as research progresses. Since, there has not been much studies done on the impacts of CECO farms, this study uses the results of Ramos [283], which was done at the same site, as a starting point. The authors proposed an arrangement of CECOs placed on a curvilinear alignment facing the prevailing wave direction (NW or 315°).

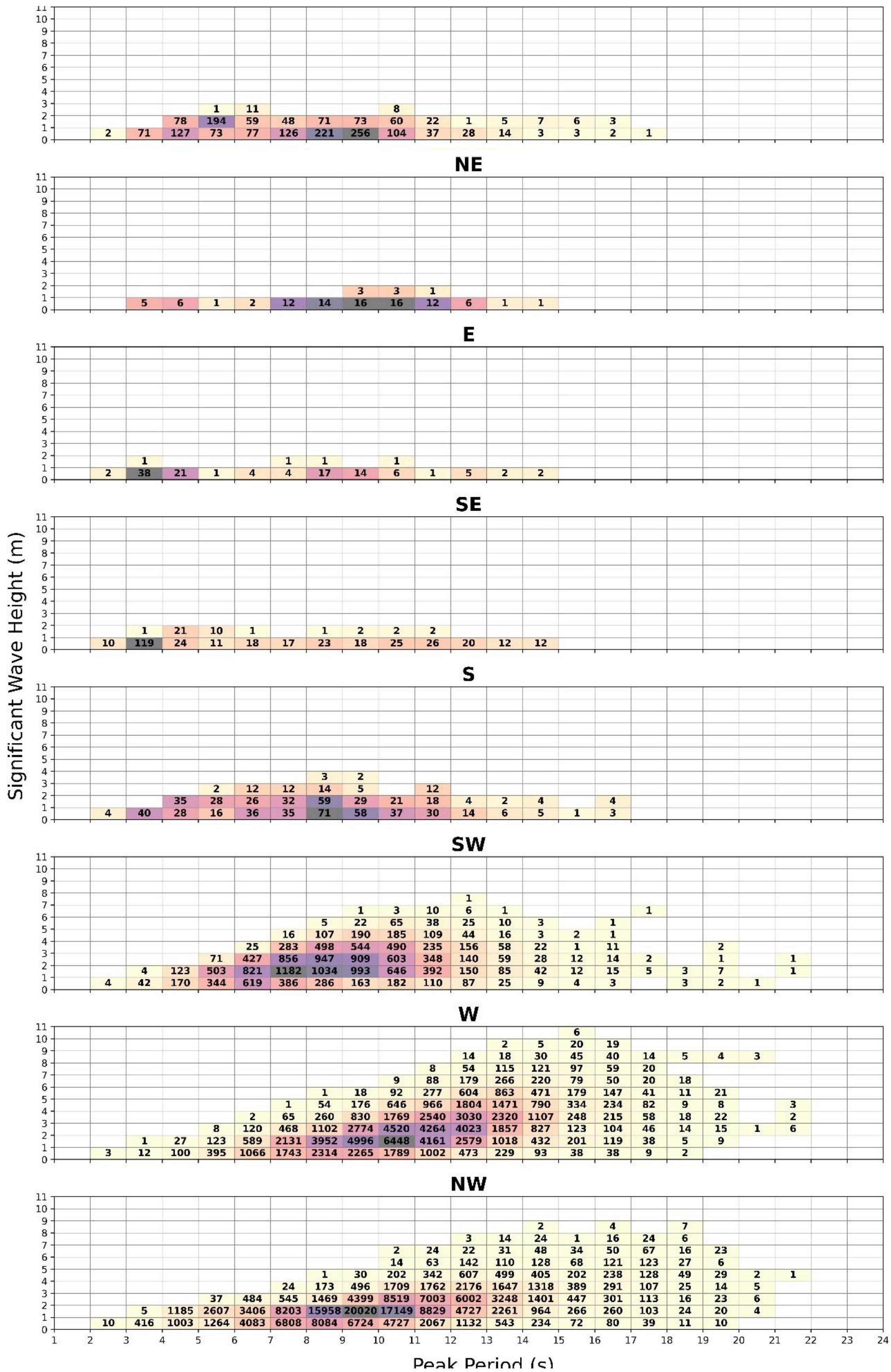

Figure 49 – Wave occurrence Matrix in directions N, NE, E, SE, S, SW, W, NW.

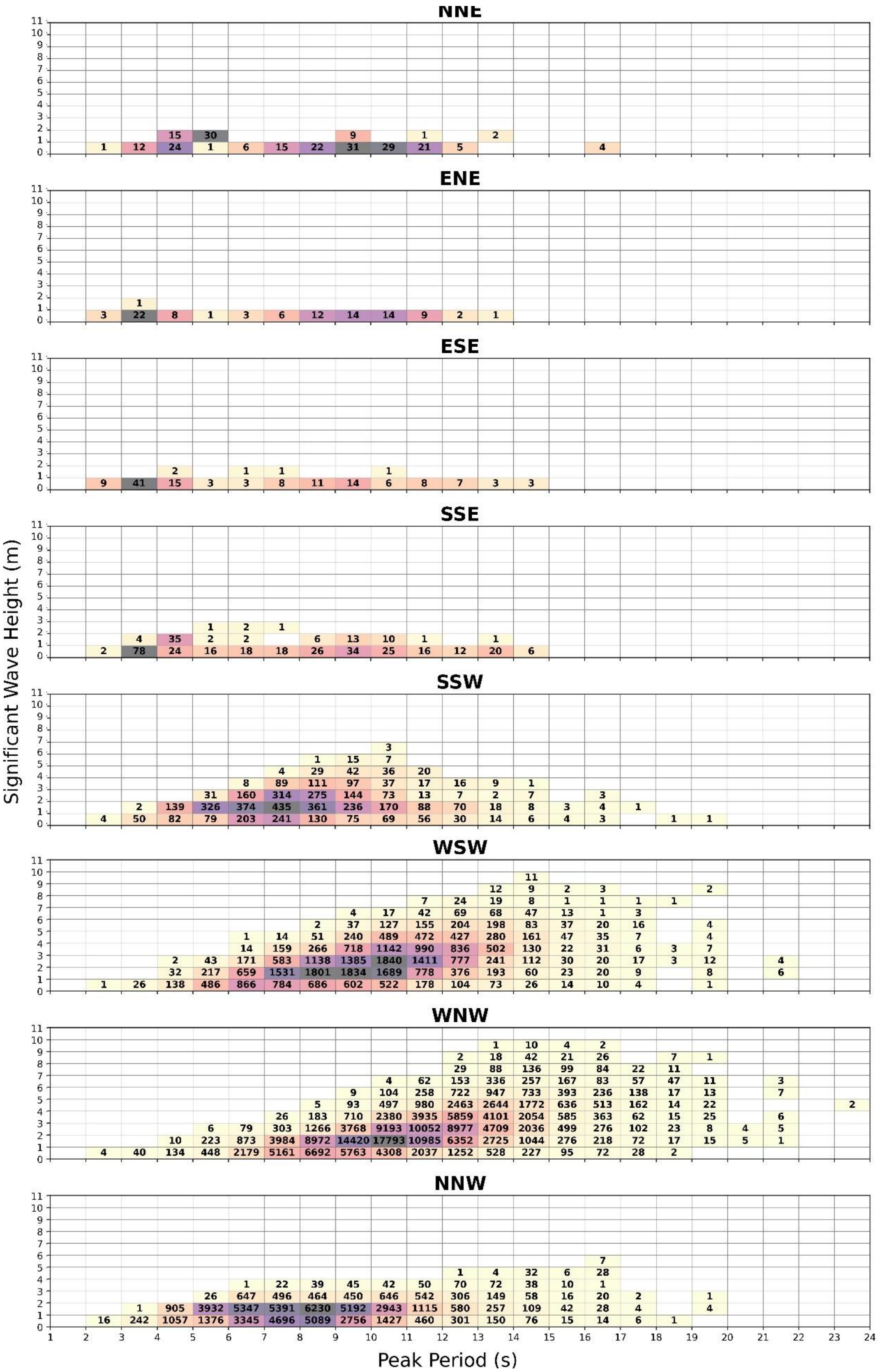

Figure 50 – Wave occurrence Matrix in directions NNE, ENE, ESE, SSE, WSW, WNW, NNW.

Table 8 – Sea states simulated.

Hs	Tp	θm		rate	day/year	Hs	Tp	θm		rate	day/year
1.5	9.5	315	NW	3.71%	14	2.5	9.5	292.5	WNW	0.70%	3
1.5	10.5	292.5	WNW	3.30%	12	1.5	6.5	315	NW	0.63%	2
1.5	10.5	315	NW	3.18%	12	0.5	6.5	337.5	NNW	0.62%	2
1.5	8.5	315	NW	2.96%	11	2.5	13.5	315	NW	0.60%	2
1.5	9.5	292.5	WNW	2.67%	10	3.5	12.5	270	W	0.56%	2
1.5	11.5	292.5	WNW	2.04%	7	1.5	10.5	337.5	NNW	0.55%	2
2.5	11.5	292.5	WNW	1.86%	7	2.5	9.5	270	W	0.51%	2
2.5	10.5	292.5	WNW	1.70%	6	0.5	9.5	337.5	NNW	0.51%	2
2.5	12.5	292.5	WNW	1.66%	6	1.5	13.5	292.5	WNW	0.51%	2
1.5	8.5	292.5	WNW	1.66%	6	4.5	13.5	292.5	WNW	0.49%	2
1.5	11.5	315	NW	1.64%	6	1.5	5.5	315	NW	0.48%	2
2.5	10.5	315	NW	1.58%	6	1.5	12.5	270	W	0.48%	2
1.5	7.5	315	NW	1.52%	6	3.5	11.5	270	W	0.47%	2
0.5	8.5	315	NW	1.50%	5	4.5	12.5	292.5	WNW	0.46%	2
2.5	11.5	315	NW	1.30%	5	3.5	10.5	292.5	WNW	0.44%	2
0.5	7.5	315	NW	1.26%	5	3.5	13.5	270	W	0.43%	2
0.5	9.5	315	NW	1.25%	5	0.5	8.5	270	W	0.43%	2
0.5	8.5	292.5	WNW	1.24%	5	0.5	9.5	270	W	0.42%	2
1.5	10.5	270	W	1.20%	4	1.5	13.5	315	NW	0.42%	2
1.5	12.5	292.5	WNW	1.18%	4	0.5	6.5	292.5	WNW	0.40%	1
1.5	8.5	337.5	NNW	1.16%	4	3.5	12.5	315	NW	0.40%	1
2.5	12.5	315	NW	1.11%	4	1.5	7.5	270	W	0.40%	1
3.5	12.5	292.5	WNW	1.09%	4	0.5	11.5	315	NW	0.38%	1
0.5	9.5	292.5	WNW	1.07%	4	3.5	14.5	292.5	WNW	0.38%	1
1.5	7.5	337.5	NNW	1.00%	4	0.5	11.5	292.5	WNW	0.38%	1
1.5	6.5	337.5	NNW	0.99%	4	2.5	14.5	292.5	WNW	0.38%	1
1.5	9.5	337.5	NNW	0.96%	4	2.5	13.5	270	W	0.34%	1
0.5	7.5	292.5	WNW	0.96%	3	2.5	10.5	247.5	WSW	0.34%	1
0.5	8.5	337.5	NNW	0.94%	3	1.5	9.5	247.5	WSW	0.34%	1
1.5	9.5	270	W	0.93%	3	4.5	12.5	270	W	0.33%	1
1.5	12.5	315	NW	0.88%	3	1.5	8.5	247.5	WSW	0.33%	1
0.5	10.5	315	NW	0.88%	3	0.5	10.5	270	W	0.33%	1
2.5	13.5	292.5	WNW	0.87%	3	4.5	14.5	292.5	WNW	0.33%	1
0.5	7.5	337.5	NNW	0.87%	3	3.5	10.5	270	W	0.33%	1
2.5	10.5	270	W	0.84%	3	3.5	11.5	315	NW	0.33%	1
2.5	9.5	315	NW	0.82%	3	0.5	7.5	270	W	0.32%	1
0.5	10.5	292.5	WNW	0.80%	3	3.5	10.5	315	NW	0.32%	1
2.5	11.5	270	W	0.79%	3	1.5	10.5	247.5	WSW	0.31%	1
1.5	11.5	270	W	0.77%	3	3.5	13.5	315	NW	0.31%	1
3.5	13.5	292.5	WNW	0.76%	3	1.5	7.5	247.5	WSW	0.28%	1
0.5	6.5	315	NW	0.76%	3	4.5	13.5	270	W	0.27%	1
2.5	12.5	270	W	0.75%	3	2.5	8.5	315	NW	0.27%	1
1.5	7.5	292.5	WNW	0.74%	3	0.5	10.5	337.5	NNW	0.26%	1
1.5	8.5	270	W	0.73%	3	2.5	11.5	247.5	WSW	0.26%	1
3.5	11.5	292.5	WNW	0.73%	3	2.5	14.5	315	NW	0.26%	1
1.5	5.5	337.5	NNW	0.73%	3	2.5	9.5	247.5	WSW	0.26%	1

To standardize the layout and facilitate comparisons between arrays, WEC farm designs (Figure 51) followed some restrictions:

- An arc of 60º was considered, based on the incoming wave directions at site;
- Minimal distance from a WindFloat turbine of 200m, based on pre–tests that showed that the reduction of H_S was higher closer to the array;
- Installed power of wave farm similar to the wind farm, about 25MW. Hence, the total number of CECO units used was 50;
- Separations distance between WECs of 2.5D and 5D. This parameter has a great influence on both the amount of energy extracted and transmitted through the park. Based on the literature, larger distances increase the wave power absorption but reduce the shield effect.

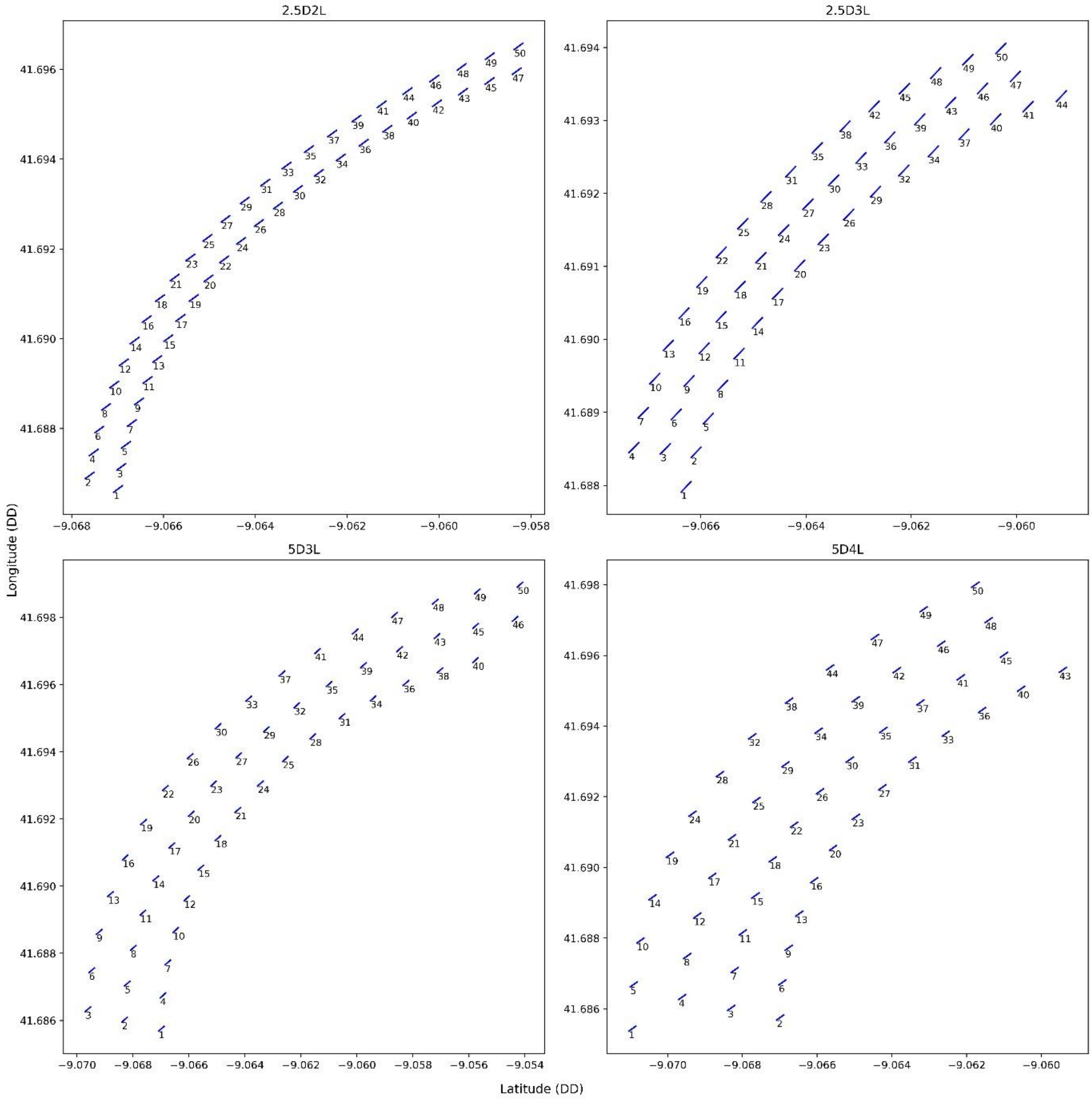

Figure 51 – Layouts used and the corresponding reference number.

The CECO's design is still under development and continues to evolve as research progresses. Since, there has not been much studies done on the impacts of CECO farms, this study uses the results of Ramos [283], which was done at the same site, as a starting point. The authors proposed an arrangement of CECOs placed on a curvilinear alignment facing the prevailing wave direction (NW or 315°).

In the SNL–SWAN model, a WEC is treated as a line of WEC–wide extension, and the device is taken into account by the model only where it crosses the grid. Hence the grid must be small enough to catch the WEC line as much as possible. To achieve good accuracy in simulating the WEC with reasonable use of processing time, a grid of 5.5x5.5m was created, which is 1/4 of WEC size and guarantees at least the crossing of 5 grid cells. The whole extension of the grid covers an area of 6.6x4.4km (1200x800 cells) centered in the WindFloat park.

The bathymetry data were obtained from the datasets of GEBCO (The General Bathymetric Chart of the Oceans), which operates under the joint support of the International Hydrographic Organization (IHO) and the Intergovernmental Oceanographic Commission (IOC) of UNESCO.

The study focuses on evaluating the effectiveness of WEC parks as a buffer solution to waves and to identify the best layout for energy production, considering an offshore floating wind farm. To evaluate the wave height reduction achieved an index for significant wave height reduction in the area of interest (HRA) was established based on Astariz's work [23]. The HRA assesses the H_S reduction within the wind farm area and is calculated using Equation (48). Additionally, the *q-factor* is used to evaluate the efficiency of the wave energy farm, and it is calculated using equation (49), using the power absorption output of SNL–SWAN.

$$\boldsymbol{HRA = \frac{100}{n}\sum_{i}^{n}\frac{Hs_i - Hs_{wec_i}}{Hs_i}} \tag{48}$$

$$\boldsymbol{q - factor = \frac{P_{array}}{\sum P_{wec}}} \tag{49}$$

where the index i is a calculation node (grid node), n the total number of nodes, Hs_i the incident significant wave height on the i^{th} node in the baseline scenario (without WECs), and Hs_{wec_i} the incident significant wave height on the i^{th} node with co–located WECs. P_{array} is the maximum power that may be absorbed by the array and P_{wec} the summation of the maximum power that may be absorbed by each single isolated WEC in the array.

To evaluate the different layout options, a new index called the Wave Energy Park Layout Assessment Index (WLA) was developed. The WLA index browses between the available options and selects the best option, given the stakeholder interests, and it is calculated using Equation (50). The WLA index takes into account the importance of power absorption and the shield effect in selecting the best option.

Moreover, the WLA index normalizes all the values of HRA and *q-factor* and returns a value between zero and one, where one is the best available choice between the options. The index considers the importance of power absorption and the shielding effect.

$$\boldsymbol{WLA} = \boldsymbol{p} * \boldsymbol{N}(\boldsymbol{q} - \boldsymbol{factor}) + \boldsymbol{s} * \boldsymbol{N}(\boldsymbol{HRA}) \tag{50}$$

The parameter p ($p = 1 - s$) is the importance of power absorption to the choice, and s is the shield effect importance.

The rescaling normalization technique, also known as min–max normalization, involves transforming a numeric variable's values to a new range (typically between 0 and 1) by subtracting the minimum value of the variable and dividing by the range of the variable. The formula for min–max normalization is:

$$\boldsymbol{N}(\boldsymbol{x}) = \frac{\boldsymbol{x} - \mathbf{min}(\boldsymbol{x})}{\mathbf{max}(\boldsymbol{x}) - \mathbf{min}(\boldsymbol{x})} \tag{51}$$

where $N(x)$ is the normalized value of x, min (x) is the minimum value of x, and max (x) is the maximum value of x.

The numerical study tested 4 array layouts, each one for 92 different wave directions, covering 76% of annual occurrences, to evaluate the influence of the arrangement, namely the spacing between WECs and between the lines of the array, in the power absorption and in the reduction of the wave height in the wind farm area.

4.2.1. Power absorption of the WEC farm

The absorbed power from each simulation was extracted from the output of the model, including simulations with a single WEC in various positions within the array. Next, the average absorbed power of each simulation and each layout was calculated, weighted according to the probabilities of occurrence of each sea state, presented in Table 8. This allowed the calculation of the mean power absorption and *q-factor* for each layout presented in Table 9.

Table 9 – Results of absorbed power and *q-factor* for each layout.

Layout	WEC mean power absorbed (kW)	Layout mean power absorbed (MW)	Power absorbed/ Power incident (%)	Mean *q-factor*
2.5D2L	70.57	3.53	15.84	0.88
2.5D3L	66.18	3.31	14.18	0.82
5D3L	71.82	3.59	15.77	0.90
5D4L	73.17	3.66	15.83	0.91

The available wave energy flux, or wave power per unit length of wave front (Wm^{-1}), is commonly evaluated in deep waters using the linear wave theory and is formulated in terms of significant wave height (H_s) and wave energy period (T_e). However, the available database provides the peak wave period (T_p) instead of the wave energy period. To address this, T_e can be derived from T_p by employing a calibration coefficient (α).

In this study, a standard JONSWAP spectrum with a peak enhancement parameter (γ) set to 3.3 was adopted, which results in a calibration coefficient of 0.9. Subsequently, the incident power (P_i) can be estimated by multiplying the wave energy flux obtained from the database by the length of the WECs (D) in the array.

$$\boldsymbol{P_i} = \frac{\boldsymbol{\rho\, g^2 \alpha\, T_p\, H_s}^2}{\boldsymbol{64\pi}} * (\boldsymbol{D}) \tag{52}$$

It is clear the higher power absorption capacity of 5D layouts, corroborating the importance of distancing in the power output optimization, nonetheless analyzing the power absorption regarding the wave direction (Table 10) it is possible to see that the positioning of the array plays an important role in the layout optimization.

Table 10 – Mean layout power absorption by mean wave direction.

Wave direction (θ_m)	**Occurrence Frequency (%)**	**Wave Energy Frequency (%)**	**Layout mean power absorbed (MW)**				**Power absorbed/Power incident (%)**			
			2.5D2L	2.5D3L	5D3L	5D4L	2.5D2L	2.5D3L	5D3L	5D4L
WSW	5.53	5.03	0.13	0.12	0.14	0.15	0.66	0.59	0.71	0.73
W	15.22	29.28	0.80	0.75	0.82	0.84	2.72	2.42	2.78	2.85
WNW	32.21	40.08	1.57	1.48	1.60	1.63	6.13	5.50	6.08	6.17
NW	31.78	23.47	0.94	0.88	0.95	0.96	5.51	4.92	5.38	5.27
NNW	10.64	2.15	0.08	0.07	0.08	0.08	0.82	0.75	0.82	0.81

As expected, layouts with higher spacing between WECs performed better. However, it was expected that the addition of rows of WECs would result in a decrease of the mean energy extraction due to the lower energy harvesting by the back rows, but this was not observed in the 5D arrays. This could be justified by the complex interactions between waves and the device, generating areas of constructive and areas of destructive interference.

Figure 52 presents the mean power absorption output for each WEC. In all cases, the southernmost WECs present the best results for energy extraction, regardless of the row it is in. This could be explained by the higher occurrence of incoming waves from those directions, which expose these WECs to more energetic waves.

In general, the devices in the north performed worse than the south ones, which can be explained as almost 75% of incident energy is from the southmost directions (WSW, W and WNW). However, it is possible to see WECs with lower performance among others with higher performance. These results can be explained by the destructive interaction caused by reflected waves from the backlines and is an opportunity to further improve the performance of the layout by changing the location of the lower performance devices.

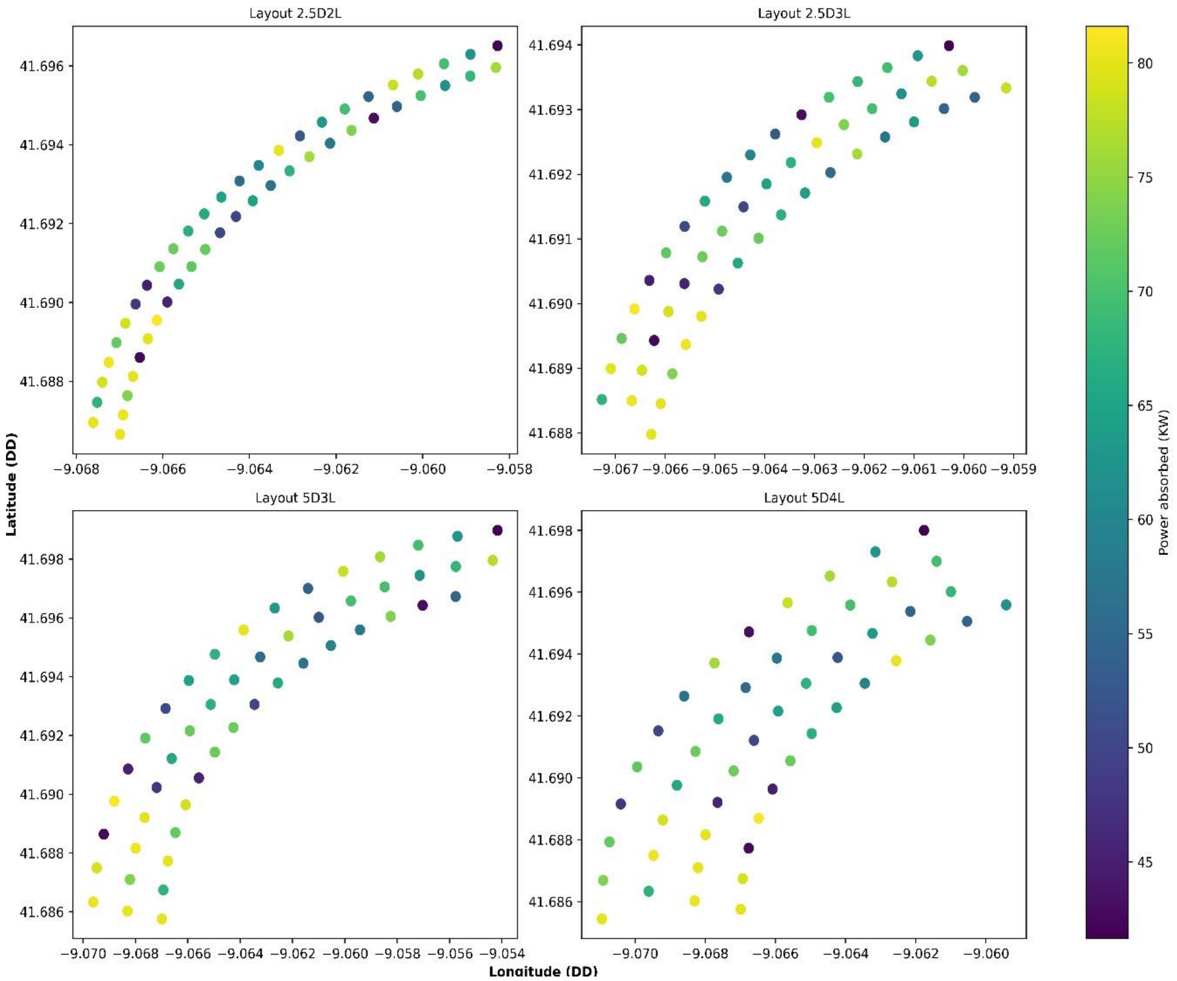

Figure 52 – Mean power absorption output by each WEC.

4.2.2. Impact on wave climate

All simulations present a zone with a higher decrease in H_S right after the devices, as can be seen in Figure 53. Although some impact of the arrays could be sensed for kilometers downstream spreading both longitudinally and transversely, the area of higher reduction forms a cone–shaped shadow in the lee of the array, which is clearer to see in arrays with 2.5D, where the reduction of H_S is higher than for the 5D layouts arrays.

The results by layout, averaging all simulations, provide information on which layout performed better globally. It is possible to observe, as expected, that the layouts with less spacing (2.5D) present higher and more uniform H_S reductions, but the area with the higher H_S reduction is smaller. The 2.5D3L array presents the highest reduction in the lee of the array. However, since the number of WECs is fixed, the array length is smaller than the others, consequently this layout suffers from the "short blanket dilemma", as the wind turbines cannot be positioned all together inside the optimal reduction zone.

A quantitative analysis is required to fully understand the shield effects. For this, the HRA index was calculated for each simulation, and the results were concatenated in reduction matrices, Figure 54 and

Figure 55 and for 2.5D layouts, and Figure 56 and Figure 57 for 5D layouts, regarding the layout and the wave direction. In other words, 20 different reduction matrices were created for specific scenarios of layout and wave direction.

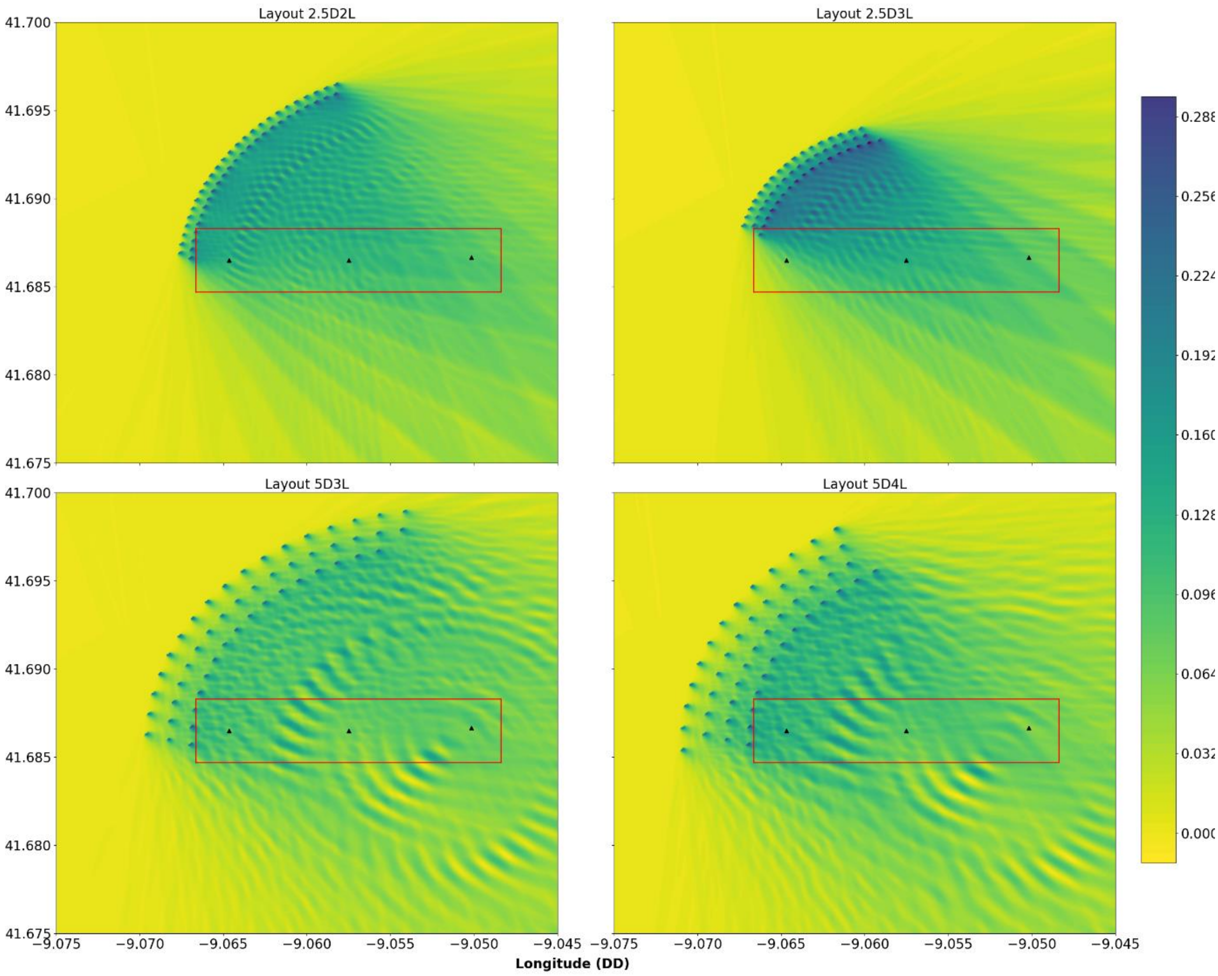

Figure 53 – Mean wave height reduction for different arrays.

Having the reduction matrices, it was possible to expand the results to all wave condition inside the same direction category by a linear interpolation. Table 11 presents the HRA indexes for each layout and direction.

The results show that the arrays with smaller WEC spacings and more lines have a higher shield effect. Comparing the arrays with the same number of lines, the array with 2.5D presents an HRA about 37% higher than the one with twice that spacing. Additionally, it shows that the decrease in spacing between WECs could provide a better shielding performance than the increase in the number of rows, as the 2 rows 2.5D performed better than the 4 rows 5D, for this specific scenario.

The better performance of the 2.5D layouts is clearer, while the number of lines has a lesser impact on shield performance. It is possible to see variations of performance for the same spacing between WECs, although, in the major cases the arrays with more lines performed better. Considering that all layouts have the same number of devices, the number of lines should be chosen with cautions, as it reduces the length of the arc.

The results of HRA can also be quantified by the impact on the extension of weather windows for operation and maintenance (O&M) of offshore wind farms, which represents a significant portion of the total lifetime costs of the installation [305]. Access to turbines is crucial in reducing these costs [306], with workboats being the most cost–effective access system, limited by a significant wave height of 1.5 m [62,307]. Thus, the extension of weather windows for O&M can result in a reduction in the overall project cost of energy.

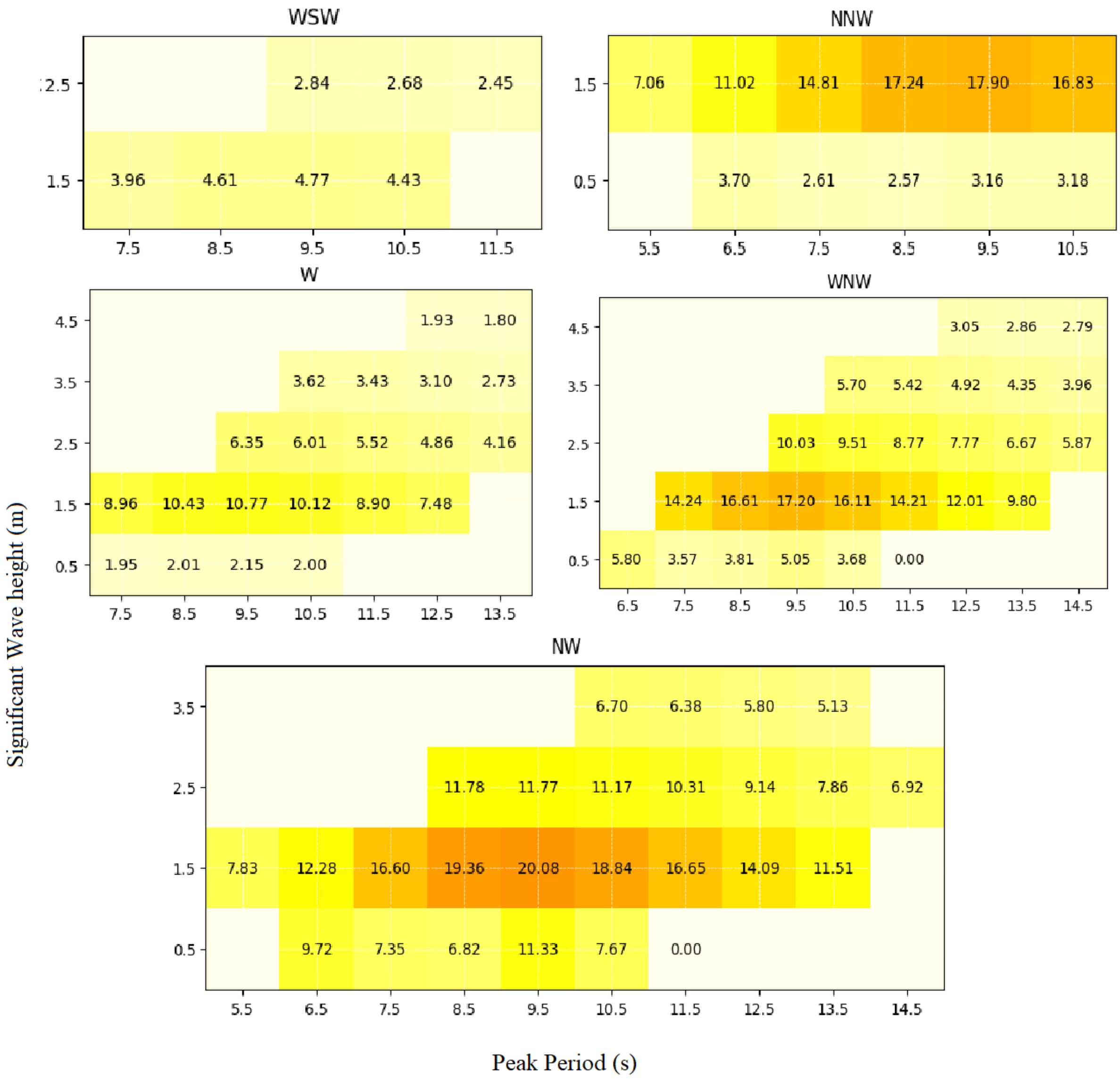

Figure 54 – Reduction matrices for 2.5D2L layout by mean wave direction. The reduction obtained for each bin is in percentage in the center of the bin and the colors represent the reduction.

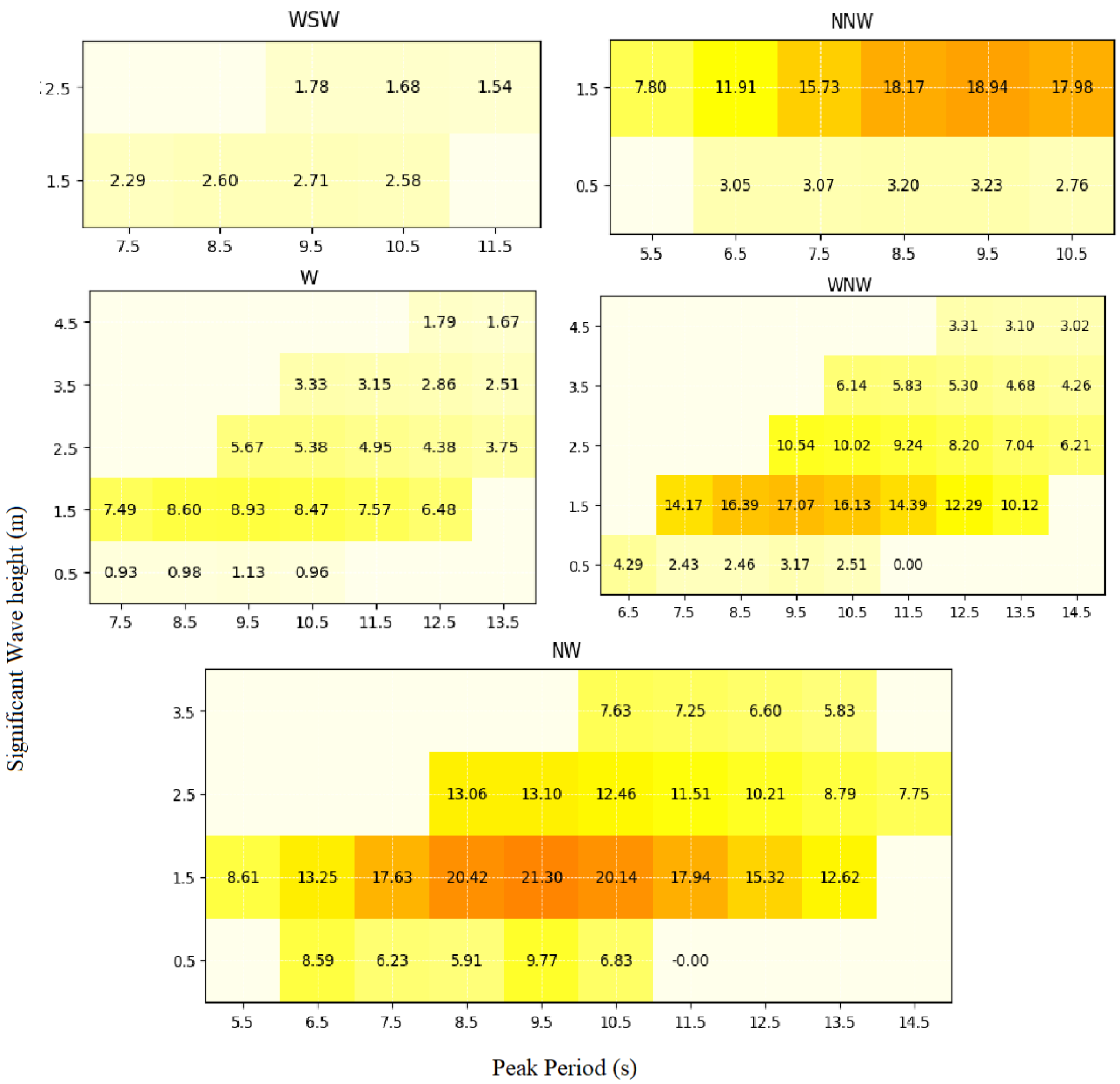

Figure 55 – Reduction matrices for 2.5D3L layout by mean wave direction. The reduction obtained for each bin is in percentage in the center of the bin and the colors represent the reduction.

Finally, an analysis was conducted to assess the impact of the wave farm layout on the operational limit of workboats (H_s< 1.5m). For this purpose, a total of 539313 valid hours were analyzed from January 1st, 1960 to September 15th, 2021. Out of these, the wave height (H_s) was over the threshold of 1.5 m for 296558 times, representing almost 55% of the valid period. By analyzing the layouts, an increase in the accessibility timeframe was achieved (as seen in Table 12). The results showed that the best scenario was obtained by the 2.5D3L layout, which resulted in a 22.3% increase in annual accessibility to the turbines, which represents more than 1944 hours added to the annual weather window.

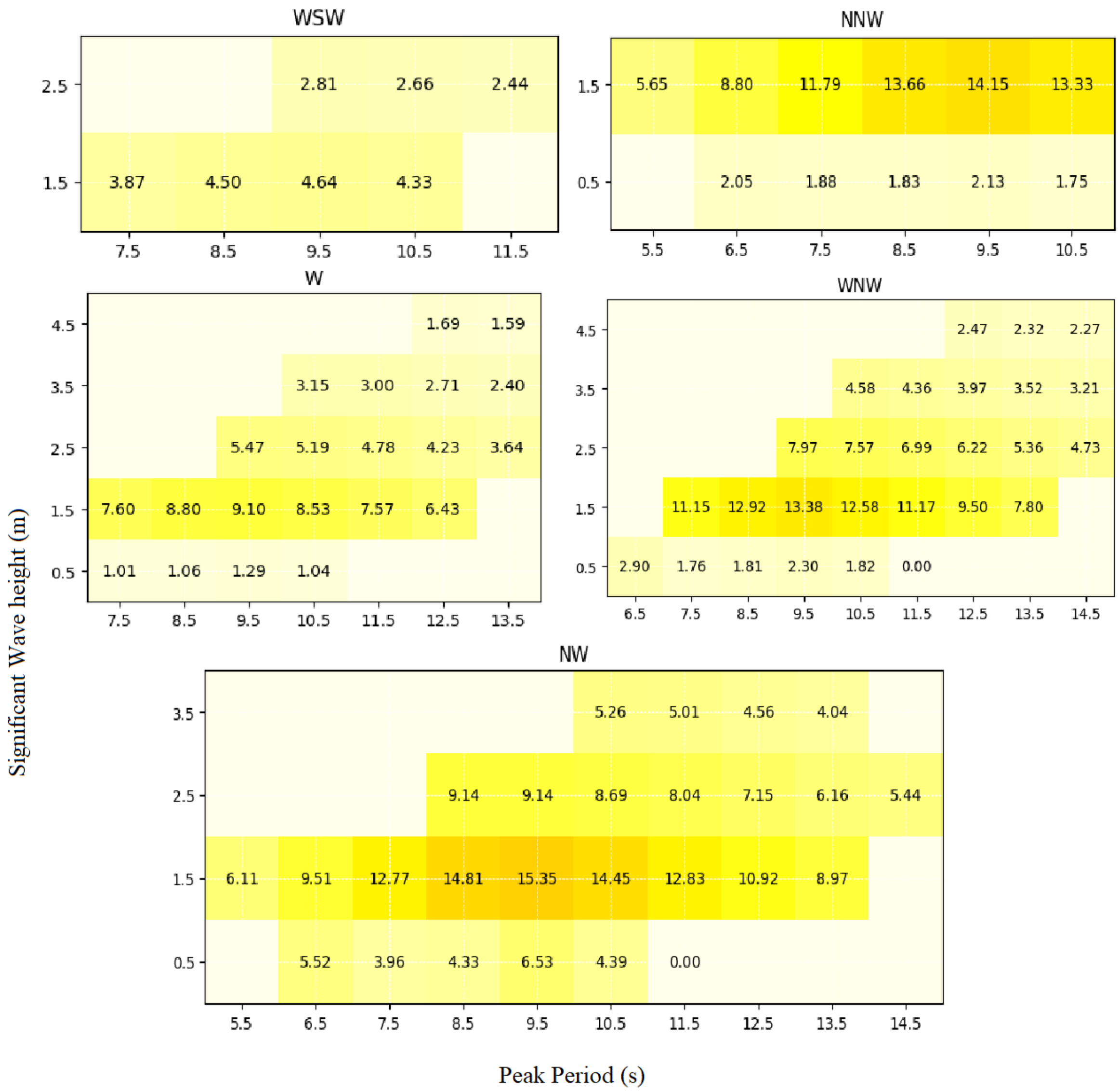

Figure 56 – Reduction matrices for 5D3L layout by mean wave direction. The reduction obtained for each bin is in percentage in the center of the bin and the colors represent the reduction.

Table 11 – Wave Height reduction in the AOI calculated by the interpolation of all main directions data.

Layout	θ_m	HRA (%)	Mean HRA (%)	Layout	θ_m	HRA (%)	Mean HRA (%)
25D2L	WSW	2,92	9,03	**5D3L**	WSW	2,88	7,03
	W	4,92			W	4,16	
	WNW	8,76			WNW	6,79	
	NW	12,04			NW	9,09	
	NNW	9,92			NNW	7,82	
25D3L	WSW	1,70	8,95	**5D4L**	WSW	3,70	7,99
	W	4,11			W	5,31	
	WNW	8,60			WNW	8,27	
	NW	12,42			NW	9,87	
	NNW	10,31			NNW	7,56	

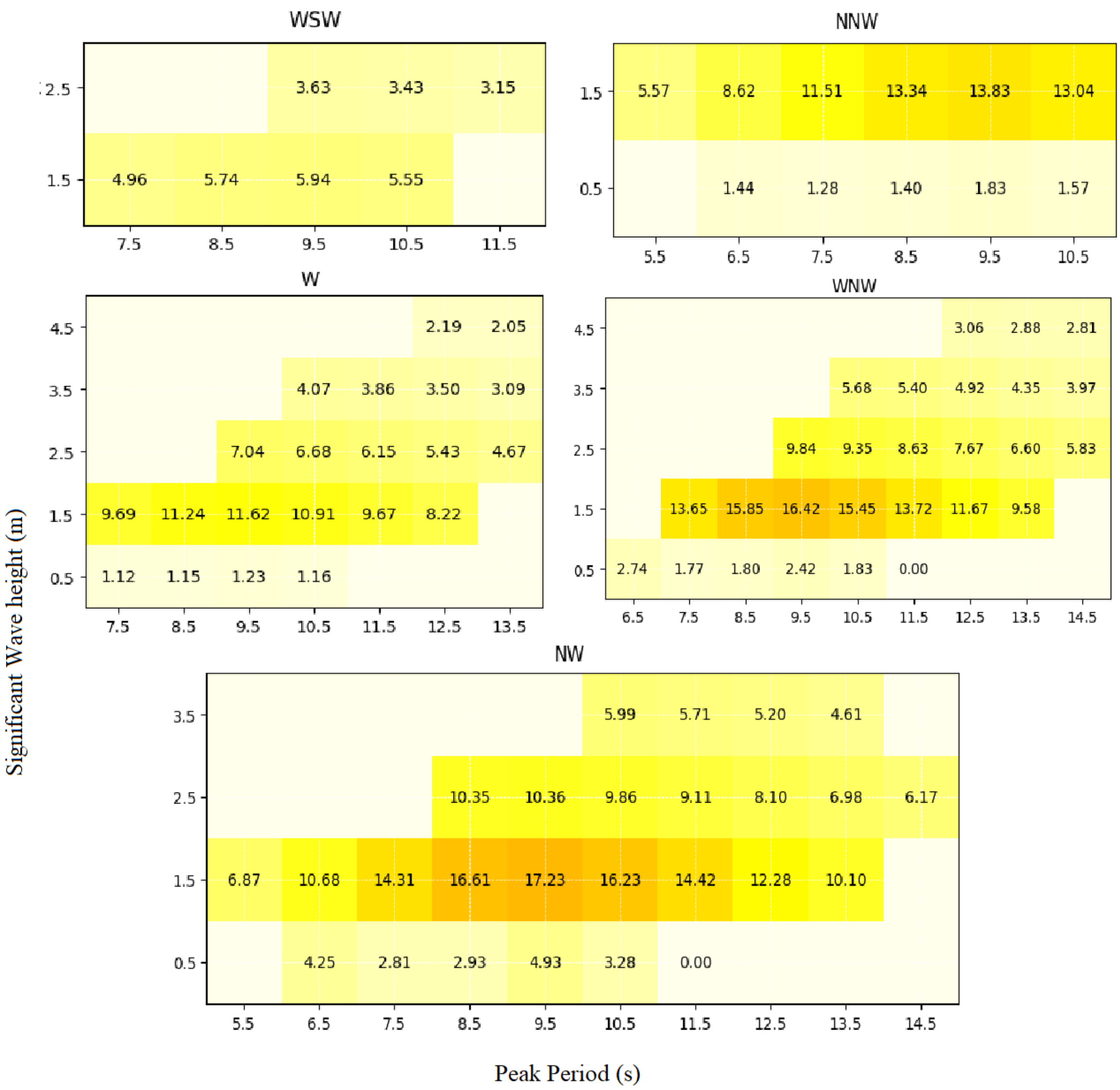

Figure 57 – Reduction matrices for 5D4L layout by mean wave direction. The reduction obtained for each bin is in percentage in the center of the bin and the colors represent the reduction

Table 12 – Accessibility time for the wind farm standalone and the co–located park layouts.

Layout	θ_m	Time gain (%)	Mean gain (%)	h/year	Layout	θ_m	Time gain (%)	Mean gain (%)	h/year
25D2L	WSW	3,1	22,2%	1944	**5D3L**	WSW	2,9	17,8%	1561
	W	6,8				W	5,9		
	WNW	15,1				WNW	11,9		
	NW	27,9				NW	22,1		
	NNW	47,8				NNW	39,5		
25D3L	WSW	1,8	22,3%	1957	**5D4L**	WSW	3,6	20,4%	1788
	W	5,7				W	7,5		
	WNW	15,0				WNW	14,7		
	NW	29,3				NW	24,5		
	NNW	49,4				NNW	38,9		

4.2.3. Power absorption and shield effect combined

The optimization of the wave farm layout is a multi–objective task, and two of the most important parameters when performing an optimization for a co–located situation is the power production and the impact on the wave heights. Both parameters could be analyzed by indexes that summarize their relative performance, with *q-factor* for power production and HRA for shield effect. However, they do not follow the same trend for the different arrangements, as increasing the number of lines is beneficial for shielding but decreases the power production, and the opposite occurs regarding spacing between devices. Hence, finding the optimal solution in this situation is not seeking the best solution of any of the parameters, but understanding the implementation objectives and finding a best fit solution.

To analyze both indexes simultaneously and create a new one combining information from the two, first, they were normalized and rescaled to make the comparison between them feasible. Additionally, as the definition of optimal parameters or situations is not the scope of this study, a Parametric Plotting method was carried out to understand the tradeoffs between parameters. The results can be seen in Figure 58 where the shield protection factor (HRA) varies with the relevance, s, from 0 to 100%.

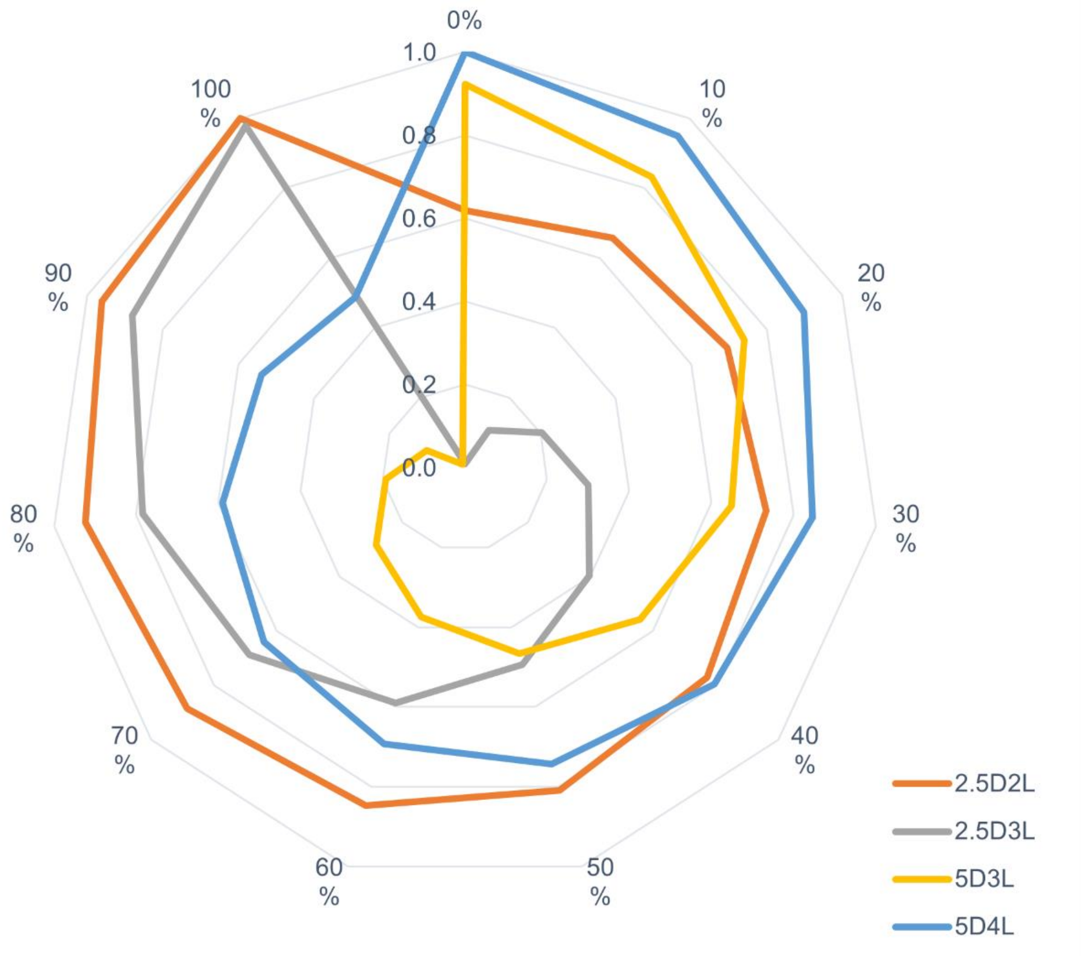

Figure 58 – Comparison between layouts response for the parametric plotting of the shield protection parameter.

Some layouts are less dependent on the variations of s and p parameters, like the 2.5D2L, or could be highly sensitive to them, like the 2.5D3L and 5D3L. Less variation in the parametric plotting means that the layout outputs change more slowly over the scenarios, leading to a less complex or smoother index curve. It indicates that the relationship between the variables is more predictable or stable, and less subject to rapid changes or fluctuations. In other words, less variation in the parameter results in a simpler and more predictable pattern in the layout graph, which makes it more reliable in extrapolation situations.

Figure 58 presents clearly when one layout imposes itself on the other. Looking into it, is possible to observe that 5D4L presents the best results until a shield relevance of 40% and 2.5D2L is the best option for shield relevance above 50%. Likewise, here is observable that the 2.5D2L is the most balanced array layout, with a coefficient of variation of about 15%, while the other was 22% (5D4L), and 62% (2.5D3L and 5D3L).

Even having all parameters, it is still needed a decision maker to choose between possible layouts for the co–located wave–wind offshore energy park, considering the relevance of power production and shield protection. The present study goes beyond a mere exhaustive analysis, its primary objective is to propose a comprehensive strategy and approach for the analysis and decision–making process regarding the optimal positioning of converter arrays, by addressing the complex challenge of maximizing the benefits for both wave and wind resources.

In conclusion, this study provides a valuable contribution to the field of wave energy farms by exploring the effectiveness of WEC farms to serve as shield protection or a buffer solution to waves. The study utilized SNL–SWAN, a widely–used numerical model for simulating wave energy farms, to evaluate the effectiveness of different layouts for energy production and wave reduction.

One of the strengths of this study is the creation of a new index, the Wave Energy Park Layout Assessment Index (WLA), which combines the *q-factor* and the HRA index to provide a comprehensive evaluation of different layout options. This index can be a useful tool for stakeholders to evaluate and compare different layouts based on their priorities for power absorption and shield protection.

Overall, this study provides a valuable framework for understanding the concepts of SNL–SWAN, the necessary inputs, and the possible outputs for layout optimization of a wave energy farm. The WLA index approach can be applied to other wave energy farm scenarios, providing a useful tool for stakeholders to make informed decisions about the optimal layout for their specific objectives.

This study enabled the accomplishment of some crucial steps to achieve the objective of a layout optimization with the genetic algorithm:

- Creation of an automatic routine that generates inputs and runs the SNL–SWAN model for any desired scenario, including layouts and sea states;
- Creation of the fitness equation, based on WLA, to compare each result and perform the selection.

The next step in this research involves developing a method to reduce the number of sea states without losing their representativeness. This is essential because the current model requires a large number of simulations for each layout (one individual of the population) in each sea state, which means that adding one sea state would increase the simulations by about 5000 times or 14 days, assuming SNL–SWAN running in series and the same computational power as described in this section.

4.3.Representative sea states using machine learning

While the method used to define the simulation parameters in section 4.1 was good to represent the sea states and the incoming wave energy, it used 90 different sea states, which is unfeasible in an evolutionary algorithm that use several iterations.

The efficiency of the GA model in WEC farm optimization is highly dependent on the number of sea states considered. Since GA simulations require evaluating each population member (layout) under all sea states across generations, the computational cost increases significantly with additional sea states. For instance, in a scenario with 50 individuals, a 95% crossover rate, and 100 generations, adding just one sea state would result in over a 4000–fold increase in simulations (Scenario S4, see Table 5). This exponential growth can become a major bottleneck, especially considering the vast amount of data (nearly 600,000 entries in the co–located case). Nevertheless, the unsupervised learning techniques effectively deal with massive volumes of data [262].

As stated previously, the number of sea states significantly increases the computational cost (scaling with population size and generations). Hence, this study prioritizes data reduction through statistical analysis and cleaning techniques avoiding losing data quality and representativeness.

4.3.1. Offshore co–located cases in Viana do Castelo

The wave characteristics in the study area were the same as section 4.2 derived from the SIMAR datasets. Table 13 presents additional important parameters.

Table 13 – Statistical description of data parameters.

	H_s (m)	T_p (s)	Θ_m (°)
Mean	1.9	10.2	295
Standard Deviation (std)	1.2	2.4	30
Minimum	0.1	2.4	0
Quantile 25%	1.1	8.5	281
Quantile 50%	1.6	10.1	299
Quantile 75%	2.5	11.8	315
Maximum	10.4	23.6	359

Figure 59 shows the normal distribution of the wave parameters, highlighting the mean and one and two standard deviations (std). As can be seen also in the wave rose (Figure 48), almost all directions are concentrated between incident angles of 225°(WNW) and 327° (NNW). In fact, 99.5% of all data are between 194 and 357 nautical degrees. Additionally, the significant wave height (H_S) and the peak wave period (T_P) in the less frequent directions have lower values. The means of these parameters are above half of the values for the most frequent directions, and they do not exhibit similar peaks of high values. Figure 60 presents a heatmap of H_s distribution over time, where it is possible to see gaps in the data and a seasonal variation, with lower H_s during summertime.

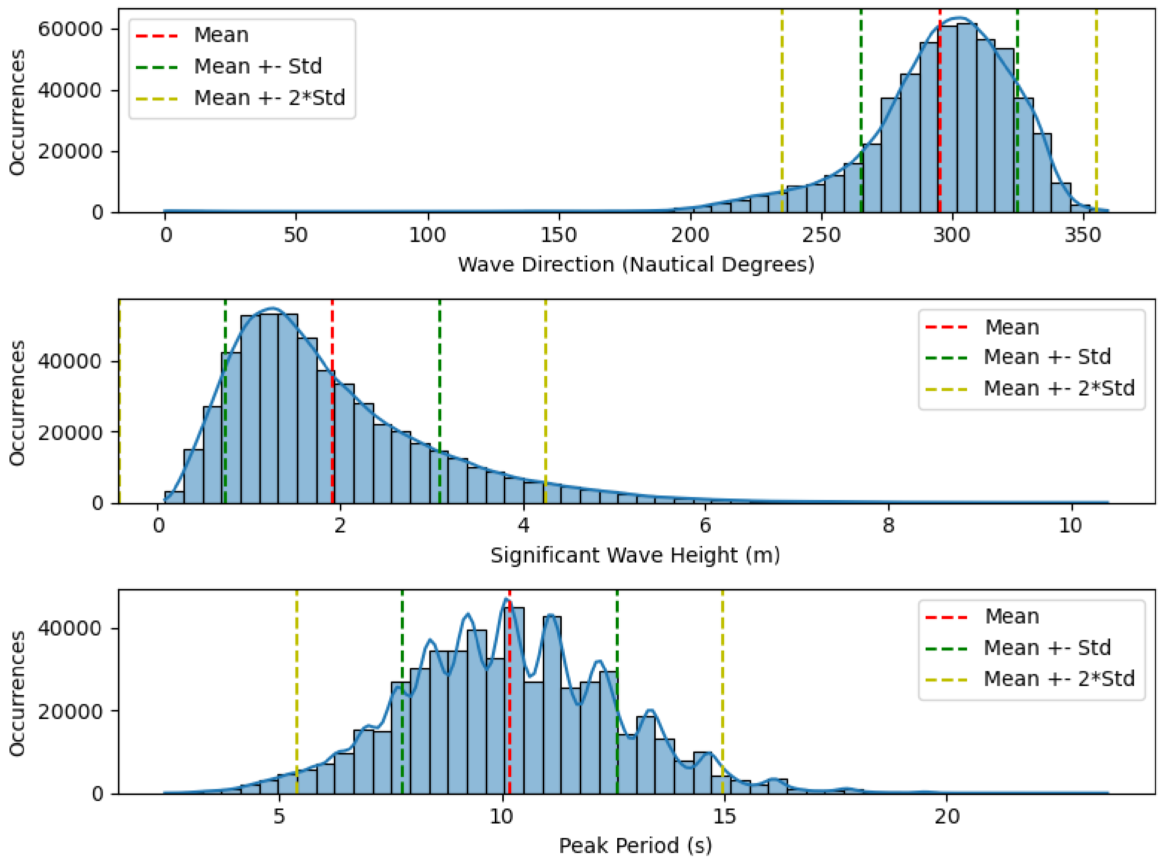

Figure 59 – Normal distribution of the wave parameters.

Significant wave height and wave period exhibit a relationship during wave propagation and attenuation. The relationship between H_s and T_p can generally be expressed as $T_p = \xi * (H_s)^\tau$ [308]. Several researchers have proposed empirical relationships between H_s and T_p for various locations [308–315]. In this study, the relationship between H_s and T_p (Figure 61) is estimated using observed data, and the values of ξ and τ are determined through curve fitting and a nonlinear least squares method,

$$T_p = 9.04 \times {H_s}^{0.23} \tag{53}$$

After the first analysis of the data, some trials were done with different clustering methods and different data cleaning. The methods applied were Kmean, Gaussian Mixture models (GMM) and Variational Bayesian Gausian Mixture models (VBGMM), with the whole dataset and normalized parameters, following the procedure of Camus [262], to equalize the scales.

The three clustering methods presented similar results for the whole dataset (Figure 62), and for filtering extreme values (Figure 63), the quantiles 2.5% and 97.5% were used. Furthermore, filtering all parameters equally by a top percentile (95th or 99th) yielded similar results, with a slight increase in the directional distribution of clusters. However, there is a significant loss in H_s and T_p data. On the other hand, it is possible to observe that more than 99% of all incident wave energy is concentrated in directions between 213° and 338°, as shown in Figure 64, that presents the cumulative distribution of wave power over wave directions.

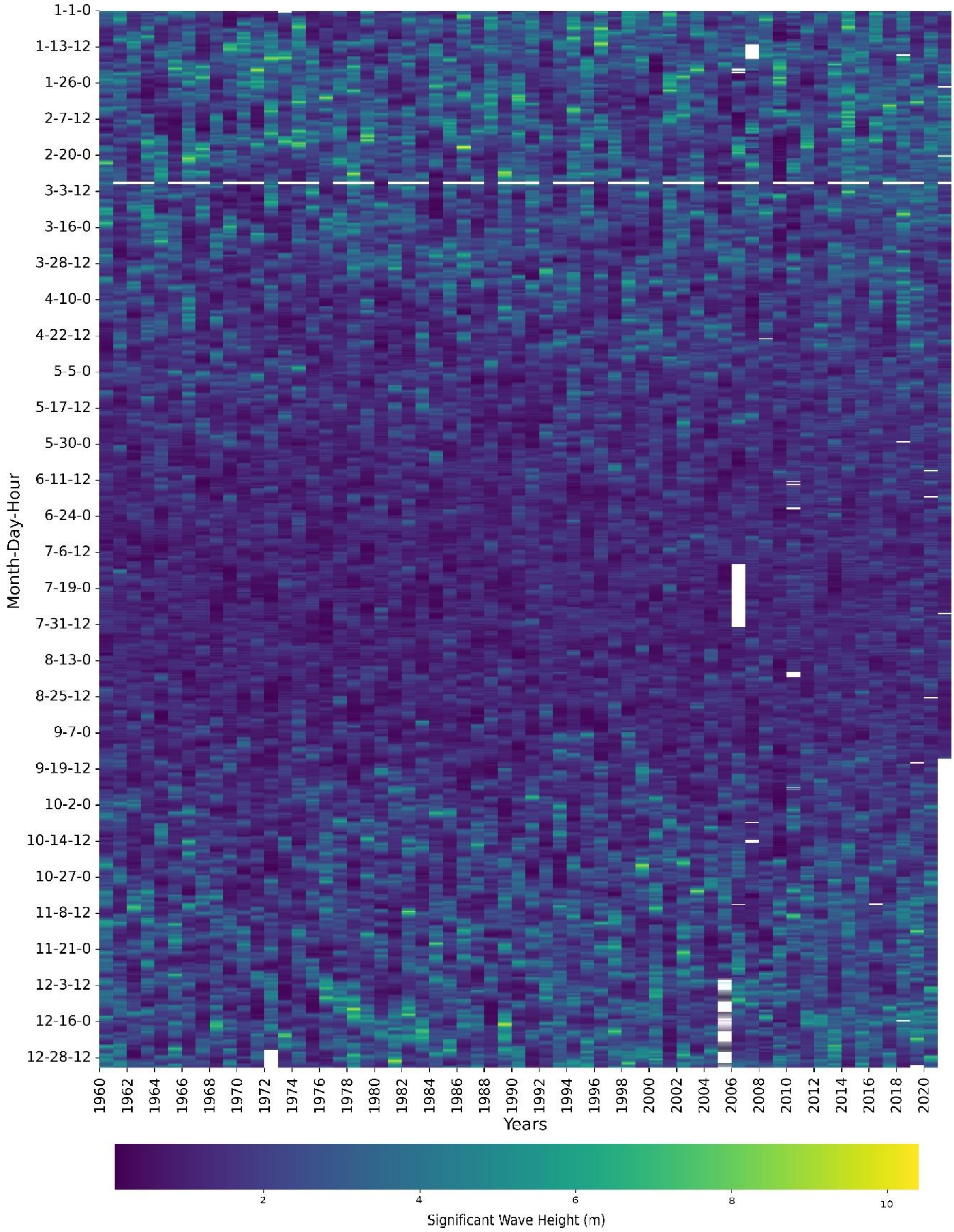

Figure 60 – Heatmap of the significant wave height over time.

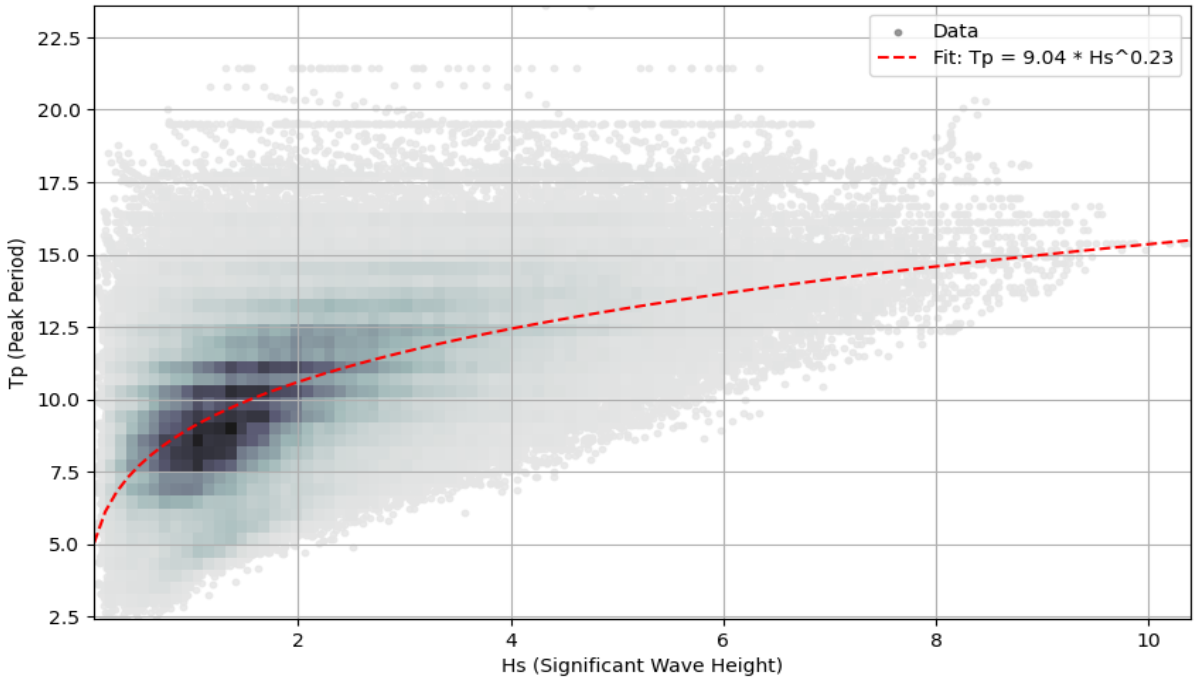

Figure 61 – Correlation between Significant Wave Height (H_s) and Peak Period (T_p), where each data point represents the original values color–coded by data density. The fitted curve indicates the best–fit relationship between H_S and T_p.

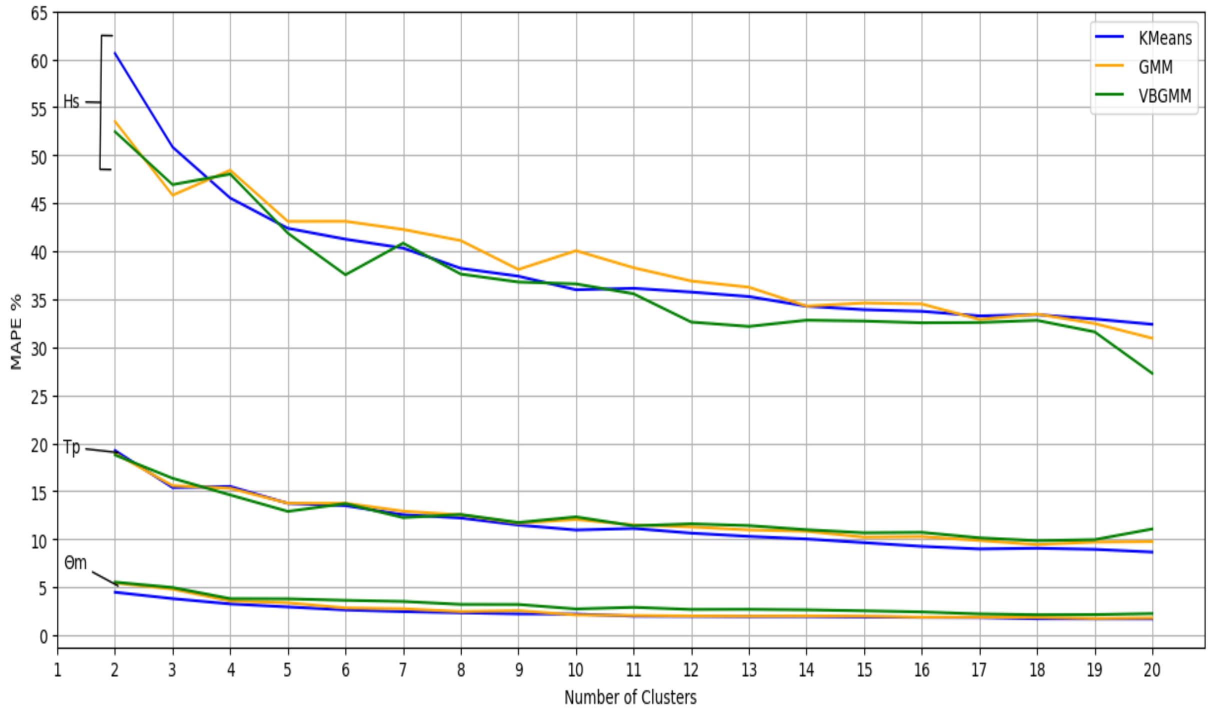

Figure 62 – Mean absolute percentage error (MAPE) for different numbers of clusters and different methods: k–means, Gaussian mixture models (GMM) and variational Bayesian Gaussian mixture models (VBGMM).

In the context of this work, WEC farms have the primary goal of harvesting wave energy and protecting the wind farm or the shoreline from high waves. Therefore, the WEC farm does not have to be optimized for all directions, in other words, it will not enclose the wind farm or consider the income wave direction from the shoreline. Additionally, the WECs do not operate in extreme conditions and the intention is to estimate the optimal solution to the layout of the farm, that will operate thought several years.

Therefore, the wave direction can be concentrated within an angular range (126° sector), regarding incident wave energy. This range size is particularly important because traditional distance metrics, like the Euclidean distance used in k–means clustering, do not handle angular distances well. For instance, they might calculate the distance between 10° and 350° as 340° instead of the correct 20°, which is essential for circular distance considerations. This highlights the need for specialized methods or adjustments in clustering algorithms to handle circular distance calculations effectively.

To ensure the required accuracy, it was evaluated the goodness of fit was evaluated using the RMSE and the coefficient of determination (R^2) for the relationship between H_s and T_p. The overall data analysis yielded an RMSE of 1.96 and an R^2 of 0.33. Specifically, for the quantile reduction, the RMSE was 1.12, and the R^2 was 0.80, indicating a strong level of representativeness and robustness in the reduction process.

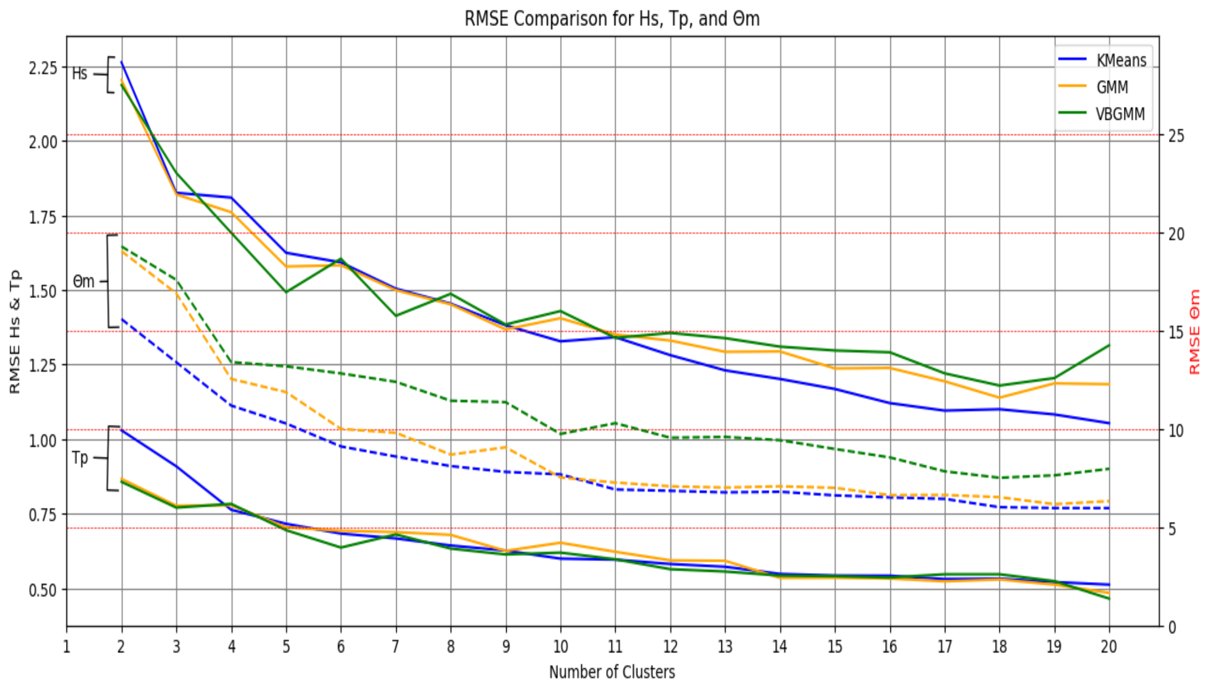

Figure 63 – Root Mean Square Error (RMSE) for different numbers of clusters and different methods: K–means, Gaussian mixture models (GMM) and variational Bayesian Gaussian mixture models (VBGMM).

Upon implementing a cleaning over the directions, keeping only a 126° sector between 213° and 338°, the data was subjected to clustering once more, to power representativeness (φ_p) of each cluster amount. Figure 65 shows the outcomes of the cluster's representativeness map up to 20 clusters. Notably, the partition in 8 clusters is the lowest partition where the rate of power efficiency surpasses 90%. Hence, it was determined that 8 clusters were the minimum number required to effectively represent the sea states.

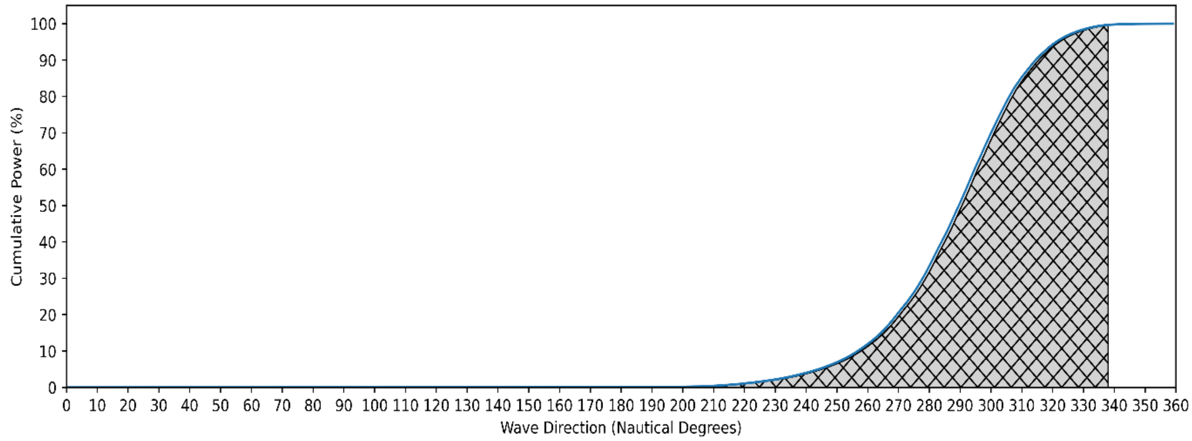

Figure 64 – Cumulative incident wave energy distribution by wave direction.

Figure 67 shows the data obtained by the directional filtering, clustered by the k–means. The centroids of each cluster represent the wave parameters that were pursued (shown in Figure 67).

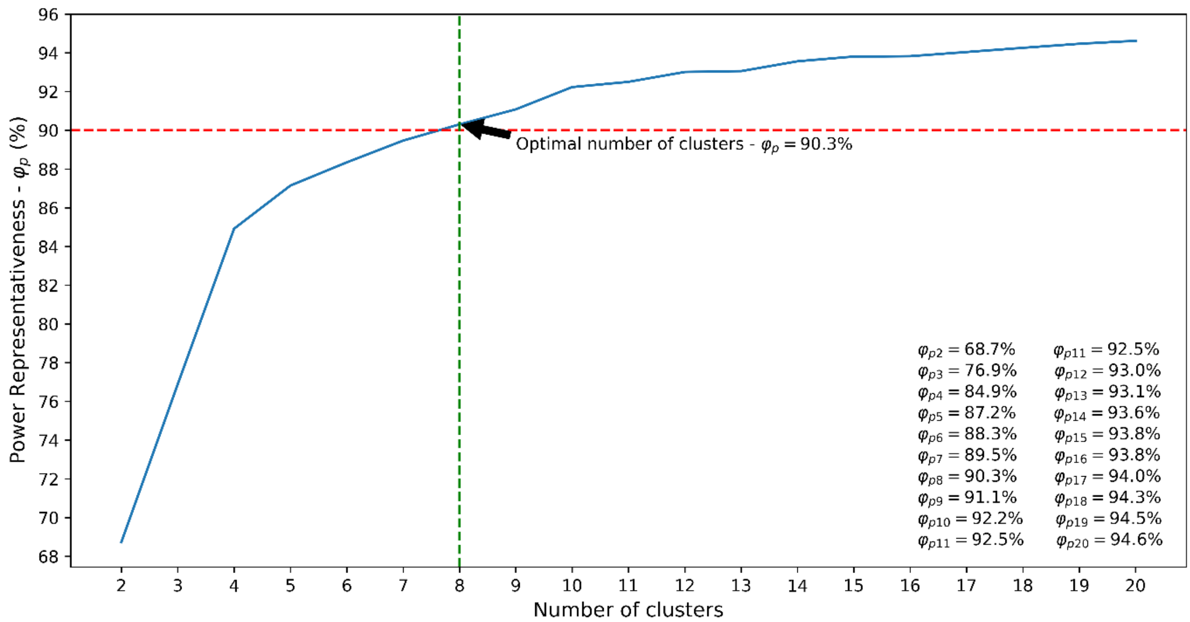

Figure 65 – K–means clustering wave power efficiency up to 20 clusters.

An automated search was conducted within the dataset, assessing MAPE of each sea state in relation to the hourly mean of each parameter. This analysis aimed to locate the optimal temporal positioning throughout the year for these sea states. The findings demonstrate that selected sea states effectively encapsulate the seasonal variations across the entire annual cycle (Figure 68).

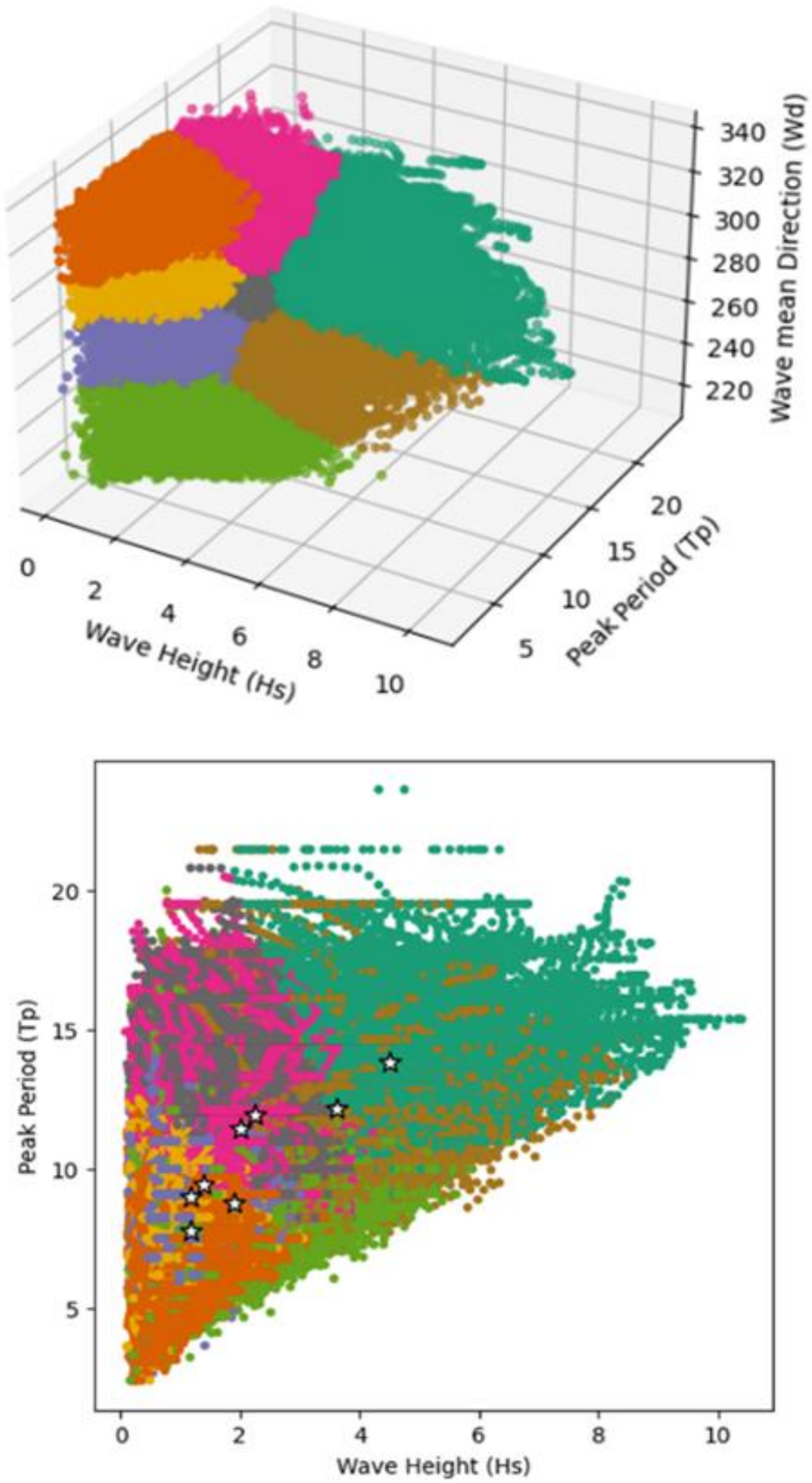

Figure 66 – 3D and Xy plan view of the clusters obtained by k–means. Each color represents one cluster and the white stars the centroids.

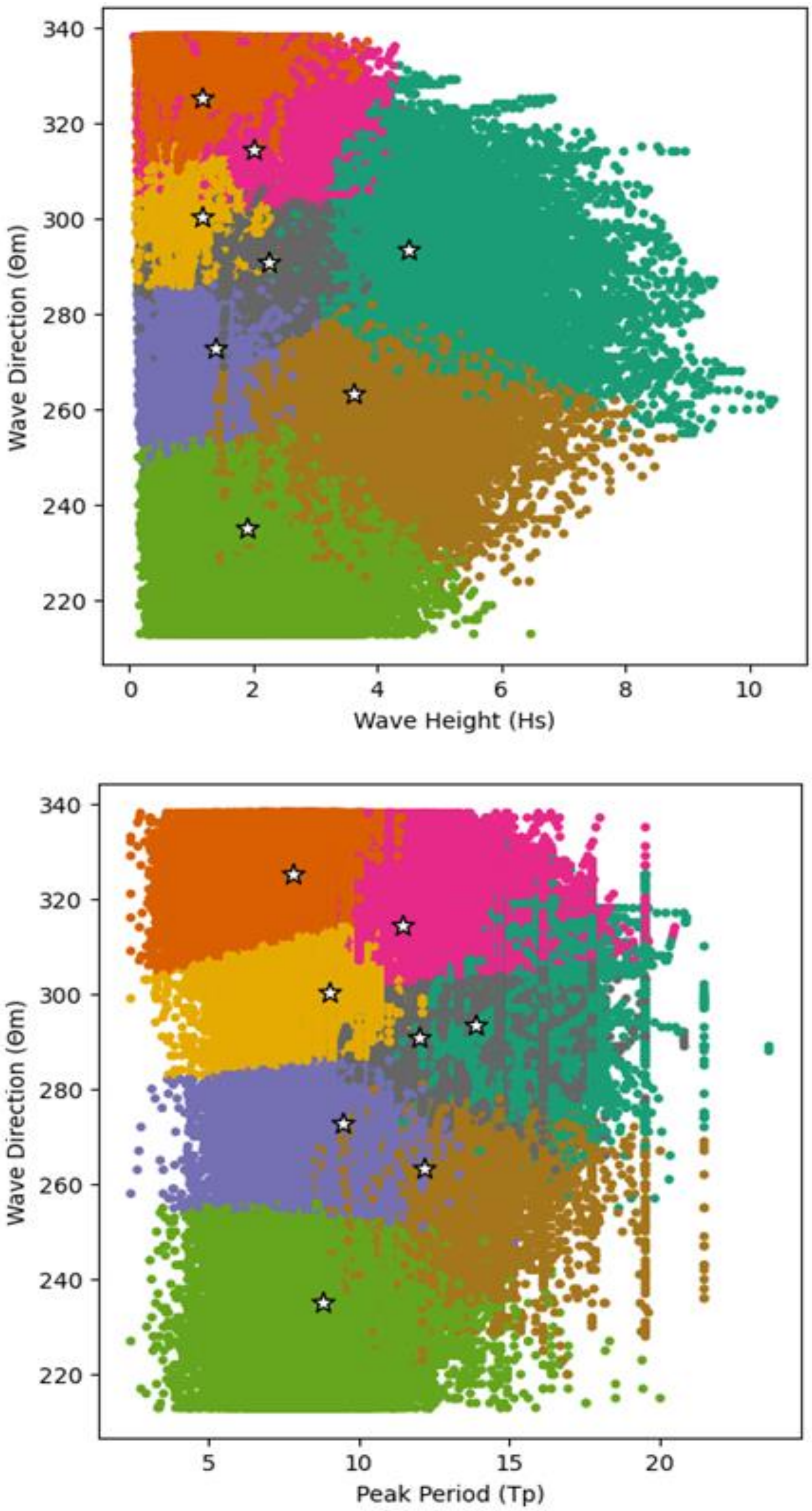

Figure 67 – View of plans Xz and YZ of clusters obtained by k–means. Each color represents one cluster and the white stars the centroids.

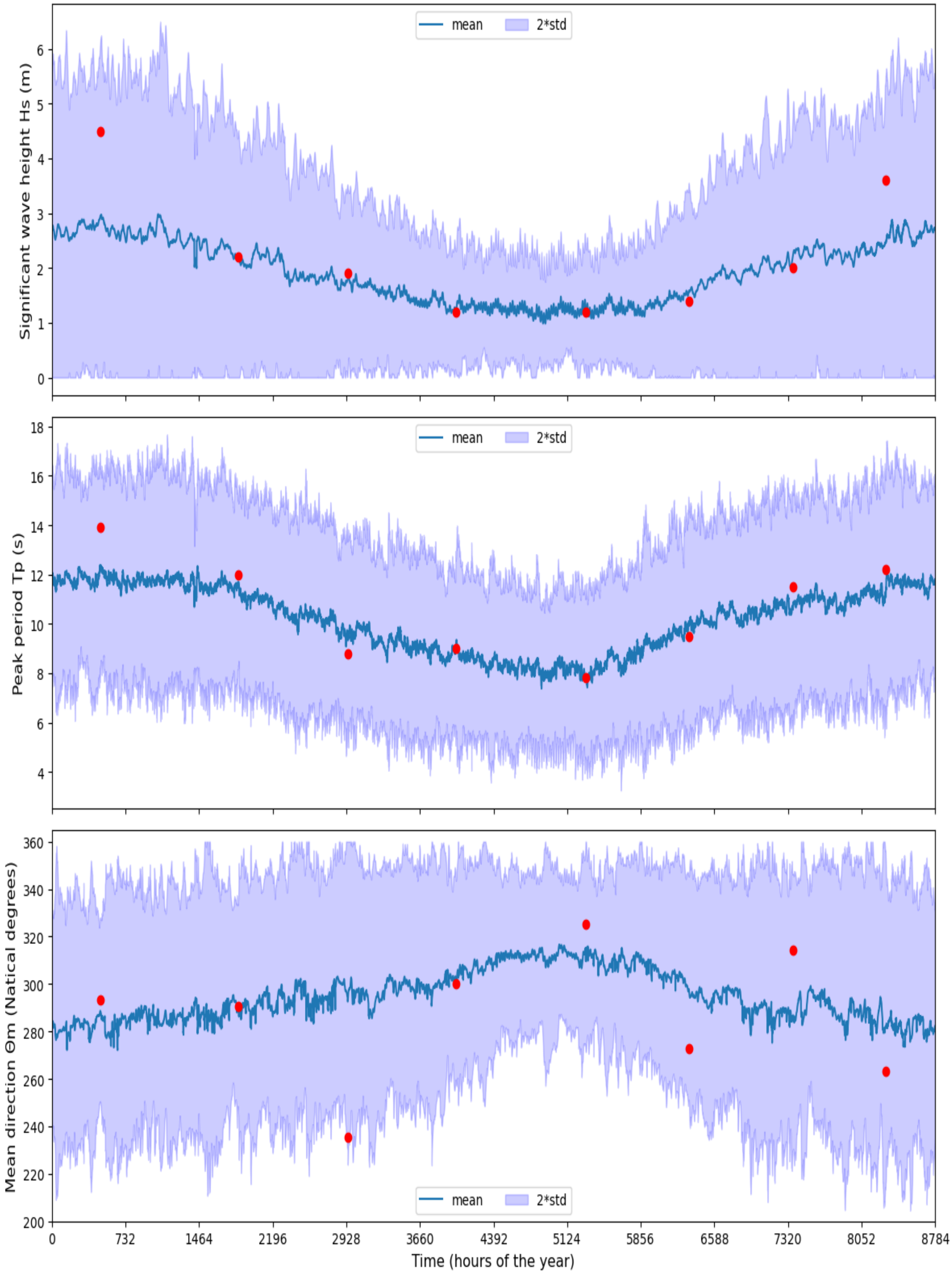

Figure 68 – Fit of the chosen sea states compared with hourly mean parameters. Blue line is the hourly mean and the purple shadow the standard deviation multiplied by 2, which represent approximately 95% of data.

Table 14 – Wave parameters achieved with k–means.

Cluster	H_s (m)	T_p (s)	Θ_m (°)
0	1.2	7.8	325.5
1	1.2	9.1	301.5
2	1.3	9.4	274.7
3	1.9	8.8	235.7
4	2.1	11.6	314.1
5	2.3	12	290.7
6	3.5	12	262.7
7	4.6	13.9	292.2

4.3.2. Nearshore Esposende

The representative sea states used for Esposende case replicates the obtained by Clemente *et al*. [289]. Figure 69 and Table 15 illustrate and present the results of k–means clustering and the definition of the sea states applied.

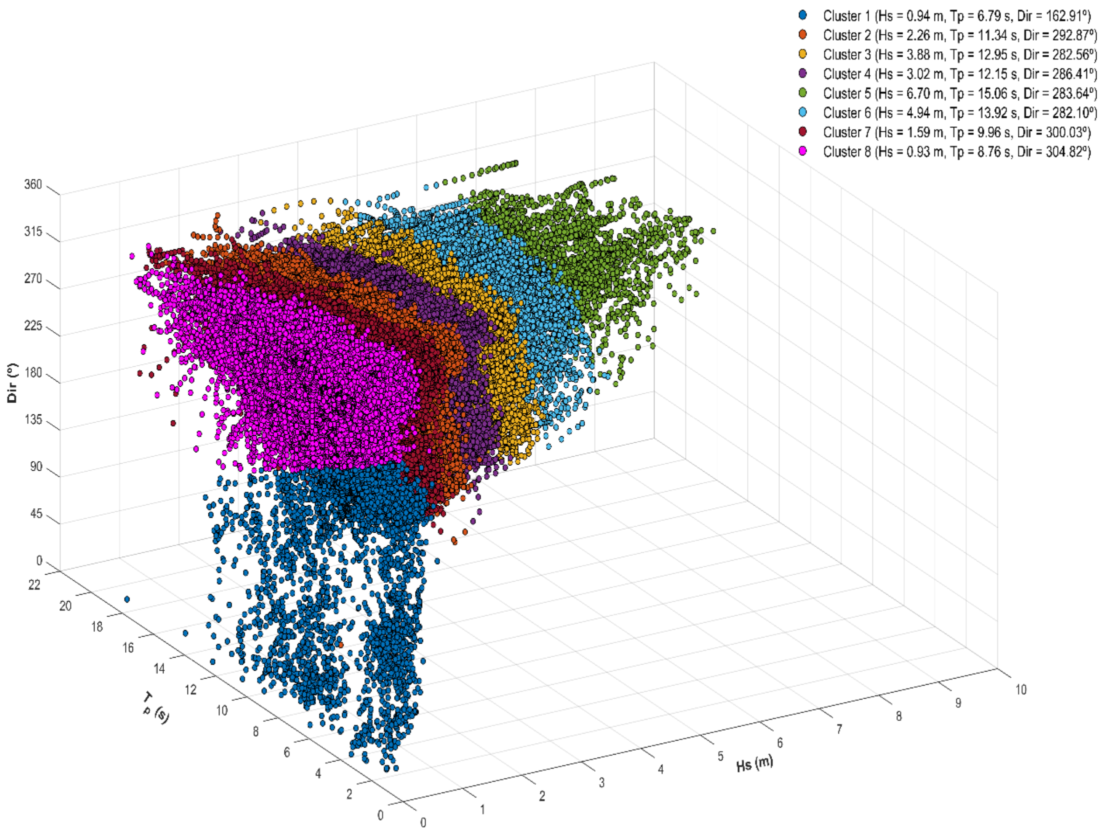

Figure 69 – Selected clusters for definition of representative sea states of Clemente *et al* [289].

Table 15 – Representative sea states of Esposende case study.

Sea State	Hs (m)	Tp (s)	Θm (°)
0	0.94	6.79	162.91
1	2.26	11.34	292.87
2	3.88	12.95	282.56
3	3.02	12.15	286.41
4	6.7	15.06	283.64
5	4.94	13.92	282.1
6	1.59	9.96	300.03
7	0.93	8.76	304.82

4.3.3. Nearshore Aguçadoura

The Aguçadoura test site is located further to the south and at a greater distance from the SIMAR data utilized in Viana do Castelo (section 4.3.1). Therefore, the ocean wave time series for the European coast, produced on behalf of the Copernicus Climate Change Service [316] is employed to demonstrate the applicability of the methodology using open–source data. Although, this dataset presents a time series of the coastal wave climate from 1976 to 2100 using historical data (1976 to 2005), ERA5 reanalysis data (2001 to 2017) and two IPCC climate projections RCP 8.5 (2040 to 2100) and RCP 4.5 (2070 to 2100) [317], to have consistency only the ERA5 [302] reanalysis data from 2001 to 2017 were employed.

ERA5 is the fifth generation of the ECMWF (European Centre for Medium–Range Weather Forecasts) reanalysis, covering global climate and weather data from the past eight decades. It provides hourly estimates for a wide range of atmospheric, ocean–wave, and land–surface variables, including wind speed, temperature, and humidity. The ERA5 dataset is presented on a regular latitude–longitude grid with a resolution of 0.5º. Figure 70 presents the data points of the ERA5 reanalysis across the Iberian Peninsula, with a zoomed–in view of the Aguçadoura test site location and the surrounding points, highlighting the data point used as reference.

The wave characteristics exhibit similarities to those observed in the preceding analysis, with wave directions predominantly originating from the north–west quadrant. This directional trend is illustrated in the wave rose provided in Figure 71, which visually represents the frequency distribution of wave directions and wave heights for the analyzed dataset.

In addition to the directional analysis, Table 16 provides a comprehensive summary of key parameters relevant to characterize the wave climate. These parameters include metrics such as the significant wave height (H_s), peak wave period (T_p), and mean wave direction (Θ_m), which are critical for understanding the overall wave dynamics in the study area.

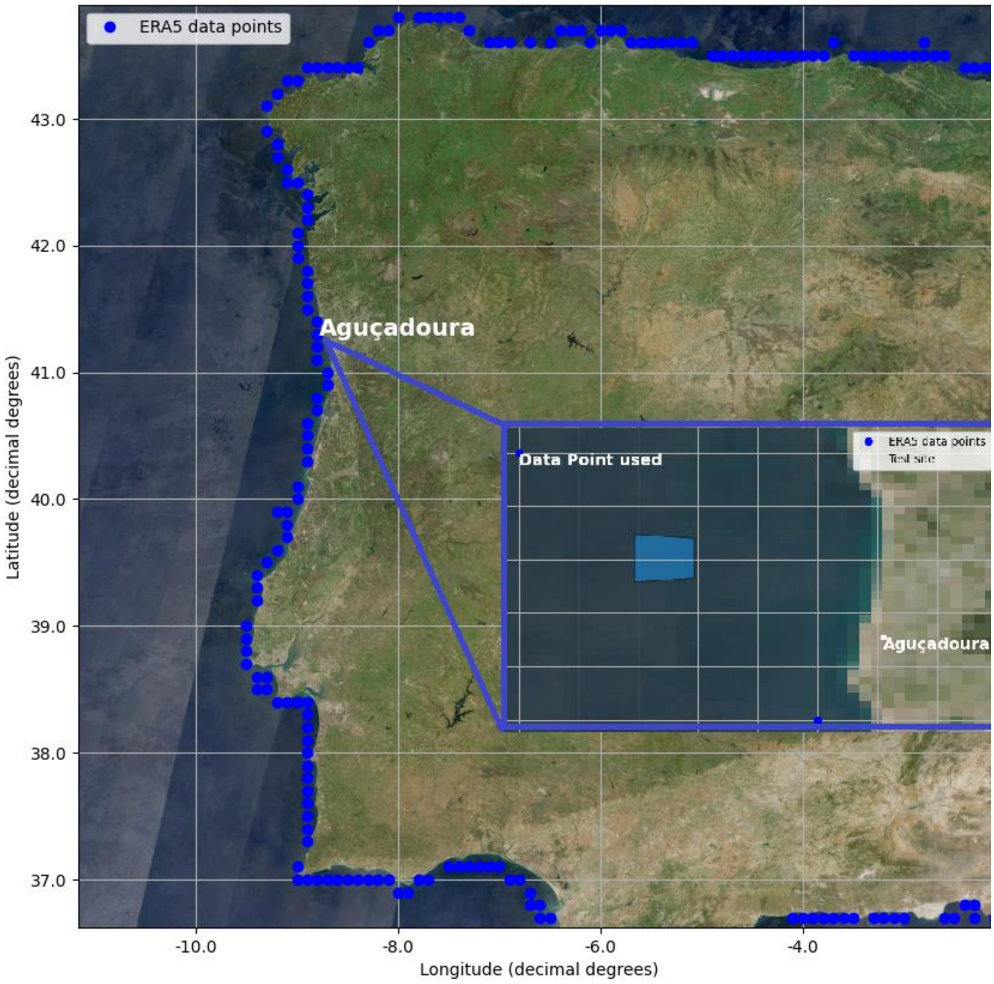

Figure 70 – ERA5 data along the Iberian Peninsula with a zoom–in at Aguçadoura test site.

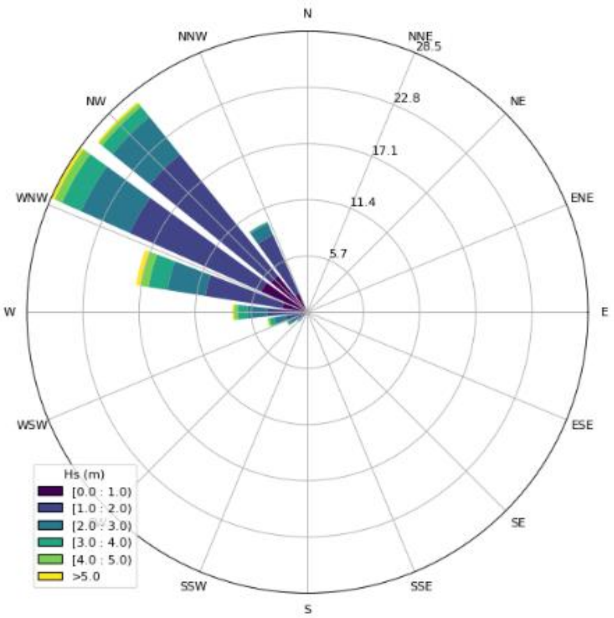

Figure 71 – Wave rose diagram indicating the directions and the wave heights for Aguçadoura in the period of 2001 to 2017 using the ERA5 reanalysis data.

Table 16 – Statistical description of Aguçadoura data parameters.

	H_s (m)	T_p (s)	Θ_m (°)
Mean	1.83	11.1	297.6
Standard Deviation (std)	0.99	2.4	24.3
Minimum	0.24	3.4	0.40
Quantile 25%	1.15	9.3	286.4
Quantile 50%	1.58	11.0	301.4
Quantile 75%	2.24	12.7	314.0
Maximum	8.20	22.2	359.7

Further analysis reveals that 99.1% of the total wave energy is concentrated within a directional range spanning from 224° (west–southwest) to 335° (north–northwest), as depicted in Figure 72. This range accounts for 98.32% of the observed wave data, indicating a high level of directional consistency in the wave climate. Moreover, it is noteworthy that significant wave height (H_s) and peak wave period (T_p) are lower in the less frequent wave directions, reflecting reduced energy conditions in these areas.

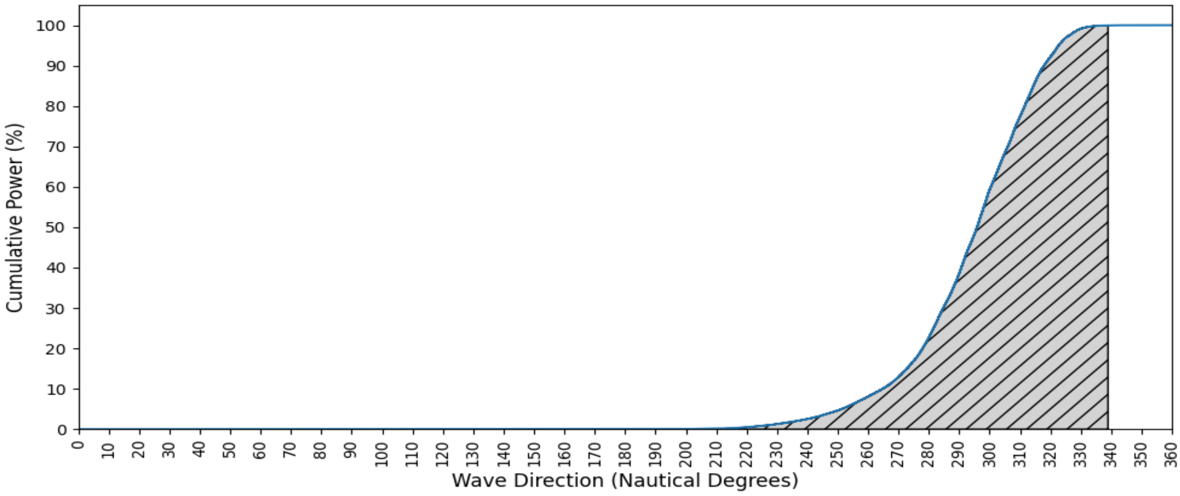

Figure 72 – Cumulative wave power curve for Aguçadoura.

Figure 73 illustrates the normal distribution of wave parameters, emphasizing the mean and the range encompassing one to three standard deviations (std). This visualization aids in understanding the variability of wave characteristics within the dataset. Based on the occurrence of wave directions, it is possible to determine the predominant wave direction using a Gaussian fit, which identifies a dominant direction of 308 nautical degrees.

Seasonal variations in wave characteristics are further explored in Figure 74, which presents a heatmap of H_s distribution over time. The heatmap highlights distinct seasonal patterns, with lower H_s values observed during the summer months, indicating a reduction in wave energy during this period. These findings provide valuable insights into the temporal and directional dynamics of the wave climate, contributing to a more nuanced understanding of the site's marine environment.

Following the implementation of a directional filtering process, wherein only data within the 111° sector between 225° and 335° was retained, the dataset was subjected to a clustering analysis to assess the power representativeness (φ_p) of each cluster configuration. The results of this analysis are presented in Figure 75, which depicts the representativeness map for up to 20 clusters. Notably, it was observed that a partition into 6 clusters represents the minimum configuration for which the representativeness of the clusters in terms of wave power exceeds 90%. Consequently, it was determined that a minimum of six clusters is required to effectively characterize the sea states within the specified directional range.

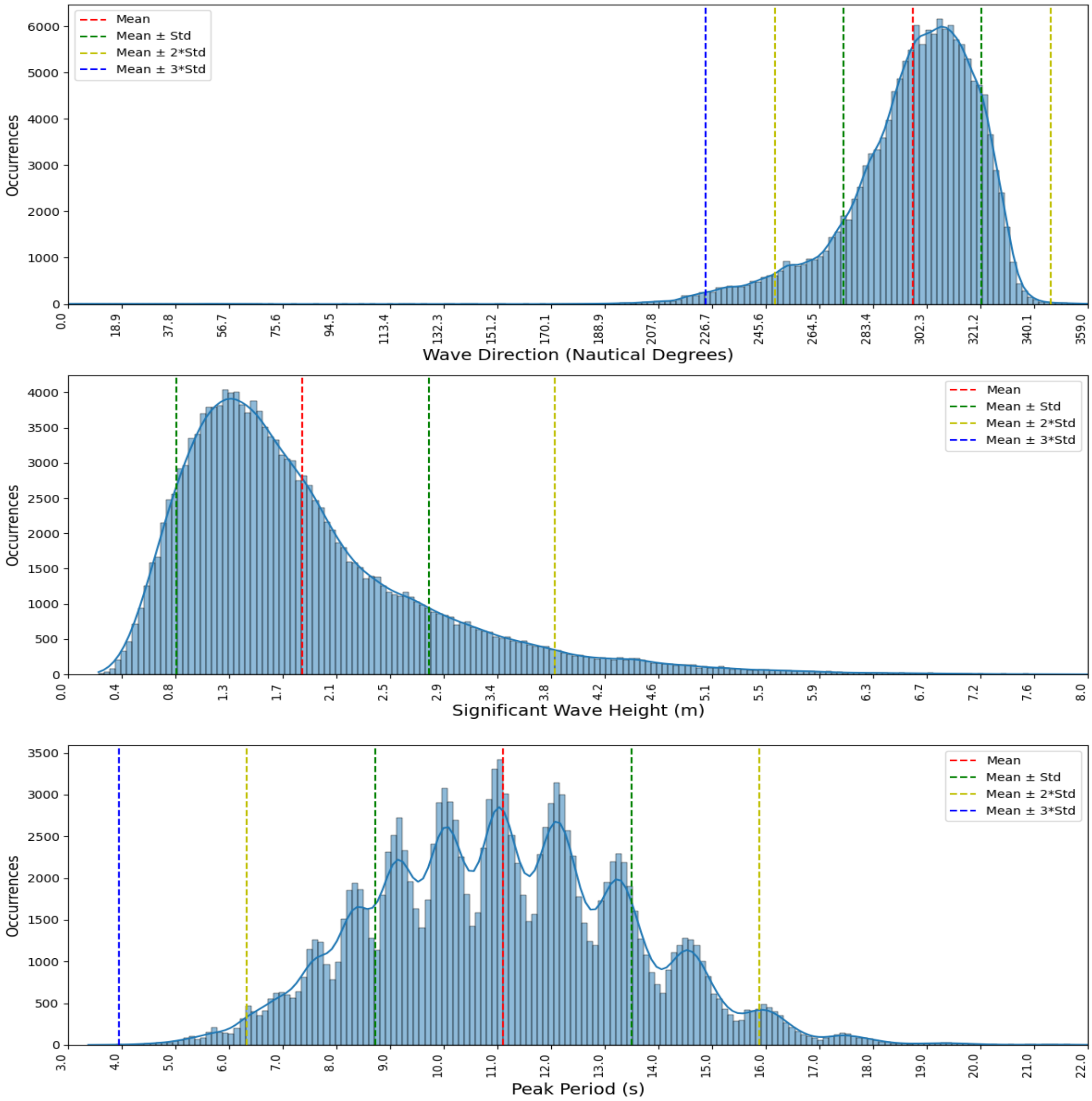

Figure 73 – Normal distribution of wave parameters for Aguçadoura.

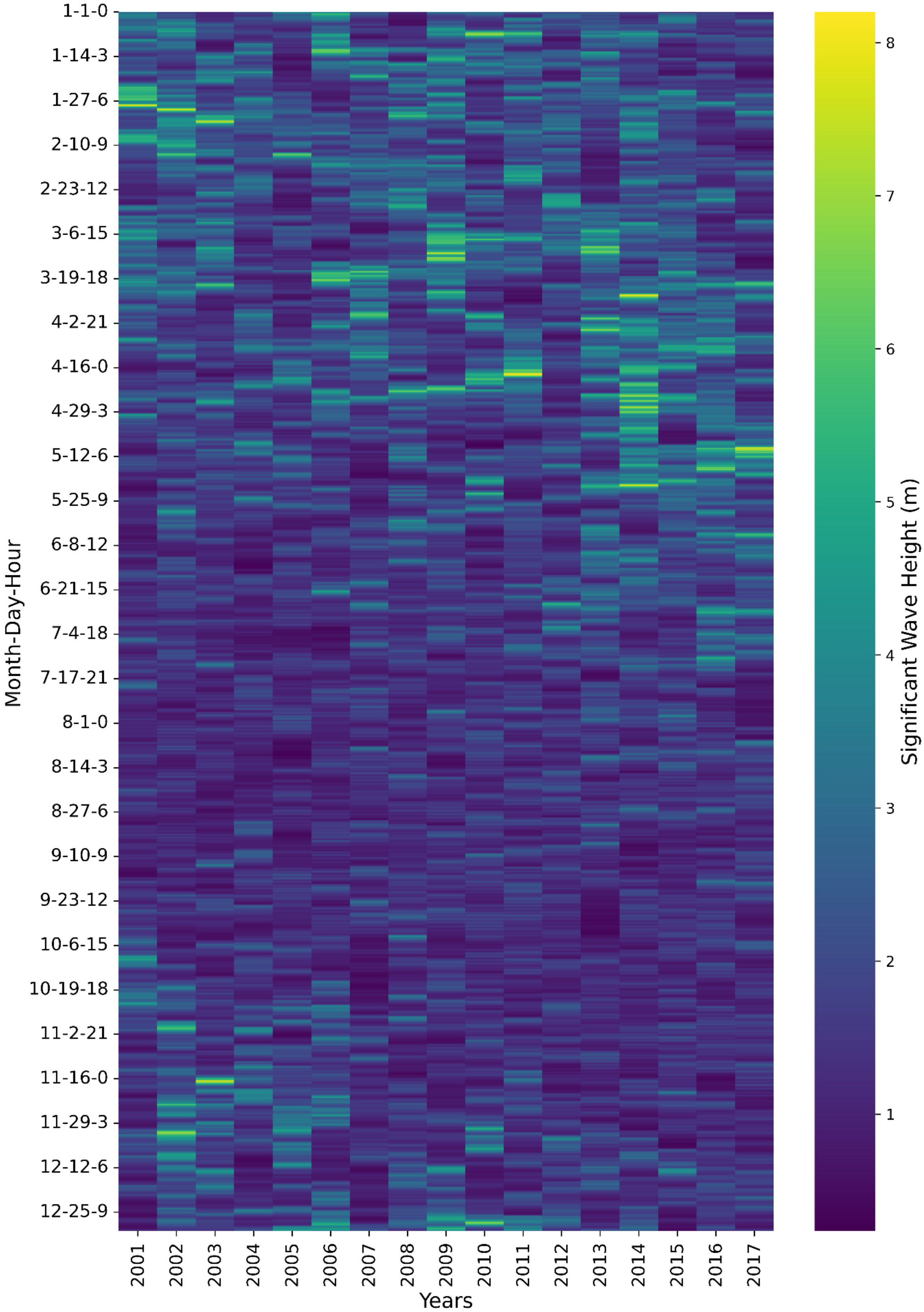

Figure 74 – Heatmap of the significant wave height from 2001 to 2017 from ERA5.

Figure 76 and Figure 77 provide additional insights into the dataset following directional filtering and subsequent k–means clustering. These figures allow to visualize the clustered data, with each cluster's centroid representing a distinct set of wave parameters. The corresponding wave parameters for each cluster centroid are detailed in Table 17, offering a comprehensive summary of the key characteristics of the clustered sea states.

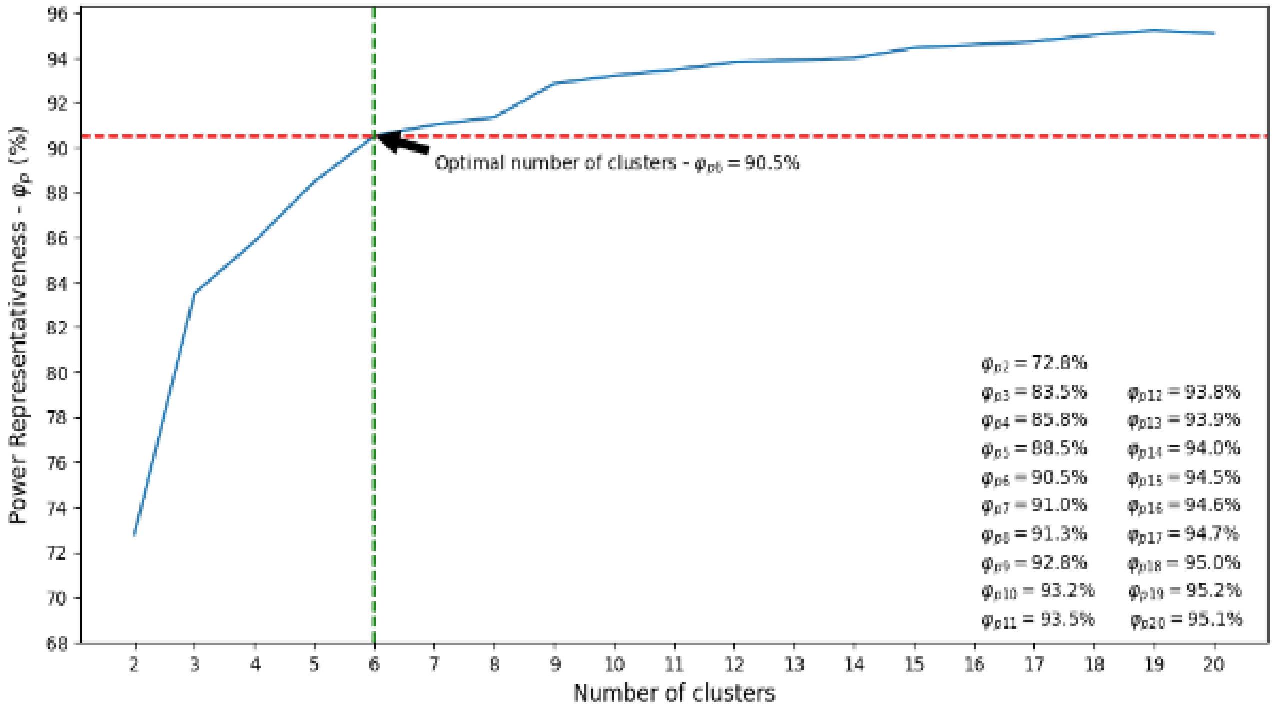

Figure 75 – K–means clustering wave power efficiency up to 20 clusters for Aguçadoura.

Table 17 – Wave parameters achieved with k–means.

Cluster	H_s (m)	T_p (s)	Θ_m (°)
0	2.0	12.7	312.0
1	1.2	8.9	318.6
2	2.0	10.0	252.2
3	1.2	9.9	293.9
4	2.2	13.0	284.5
5	4.2	14.4	293.1

To establish a correlation between the obtained sea states and wave data throughout a representative year, the automated MAPE search for each sea state relative to the hourly mean of each wave parameter was used to determine the optimal temporal positioning of the sea states within the annual cycle.

By aligning the sea states with the wave data, it was possible to identify patterns that correspond to seasonal variations. This approach effectively demonstrated the relationship between the sea states and the distinct seasonal characteristics of wave behavior, providing valuable insights into the temporal distribution and representativeness of the clustered wave conditions over the course of a year.

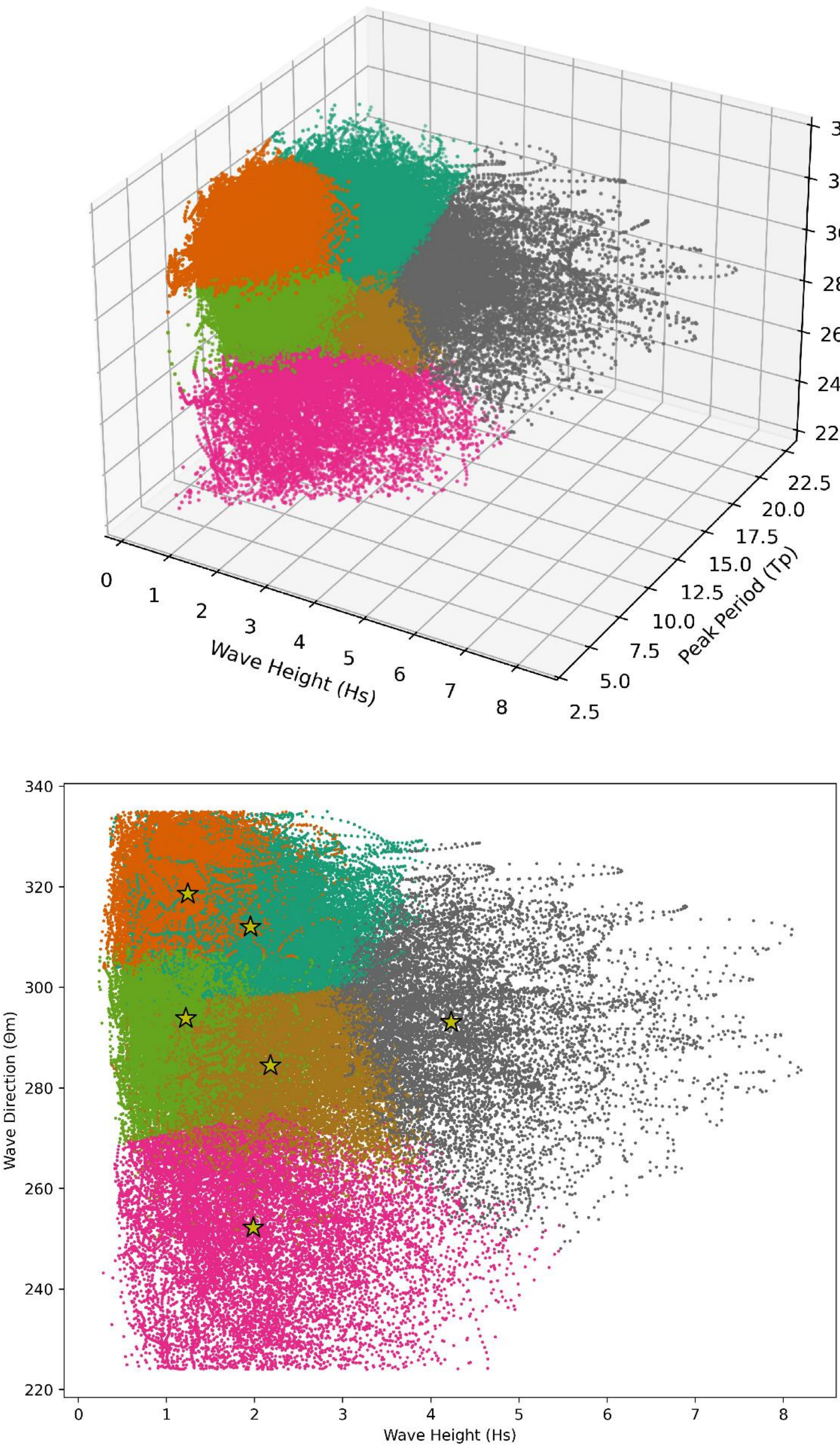

Figure 76 – 3D and θ_m x H_s view plane of the clusters obtained by k–means. Each color represents one cluster and the yellow stars the centroids sea states for Aguçadoura.

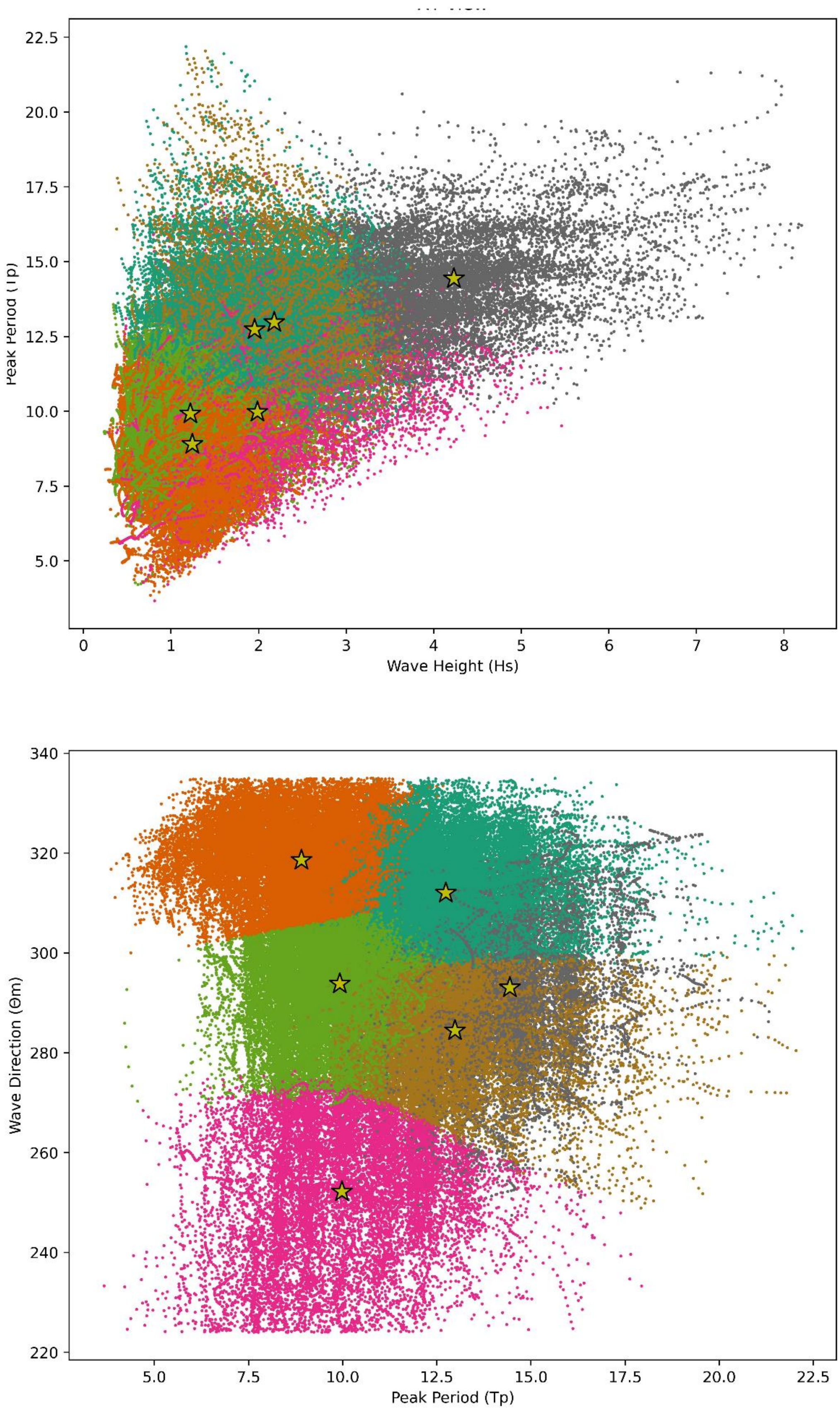

Figure 77 – T_p x H_s and θ_m x T_p view planes of the clusters obtained by k–means. Each color represents one cluster and the yellow stars the centroids sea states for Aguçadoura.

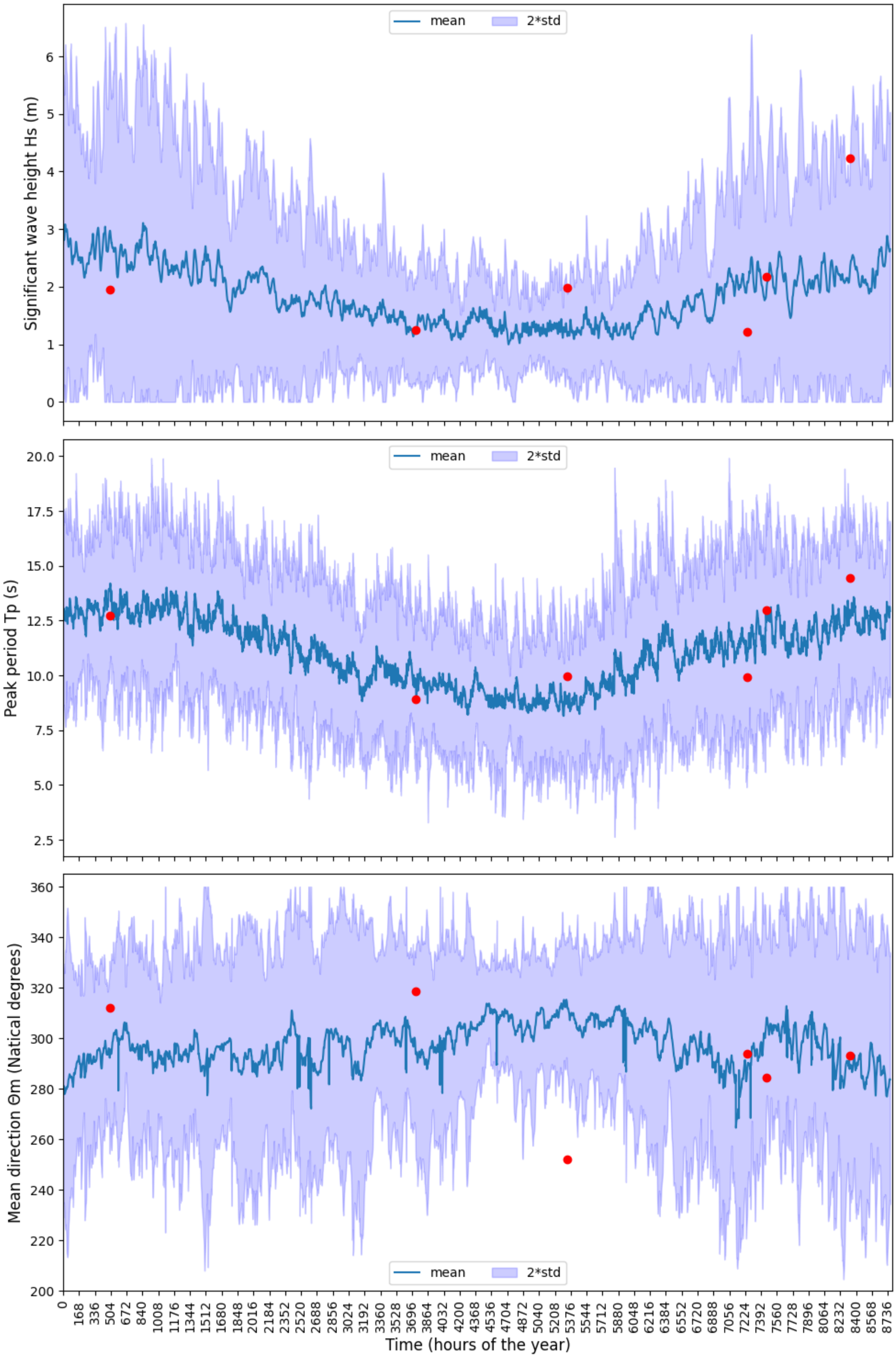

Figure 78 – Hourly mean fit of the chosen sea states for Aguçadoura. Blue line is the hourly mean and the purple shadow twice the standard deviation, which represents approximately 95% of data.

5

LAYOUT OPTIMIZATION WITH GENETIC ALGORITHM

5.1.Sensitivity analysis and definition of GA parameters

5.1.1. Definition of single WEC power absorption

The definition of power absorption of a single WEC is important to estimate the *q-factor*, which is the most used parameter for the optimization of wave energy farms. Since using the rated power of the device overestimates the power output, two different methods were used to estimate the average power absorption of a single WEC: positioning of the WEC randomly a thousand times in the domain, and in an arc path with each WEC at every 0.5º. As the average of the arc method returned a higher single WEC absorption, this method was used to estimate the *q-factor* of the layouts. The statistics of the arc method are displayed in Table 18.

Table 18 – Statistics of the single WEC simulations using the distribution in arc.

Parameter	Value (kW)
mean	129.3
std	9.6
min	104.6
25%	120.6
50%	130.3
75%	135.3
max	149.3

5.1.2. Results of the wave farm layout optimization

The study initially focused on optimizing the parameters of the GA, contrasting the runtime efficiency and the evolution of results for HRA, *q-factor*, and WLA across generations and execution time. Table 19 the outcomes derived from using 24 cores within the AMD EPYC 7443 node. It delineates the average execution time for 1 and 100 generations, estimates the equivalent generations attainable within a four–day timeframe, and provides the runtime efficiency of each simulation.

The evolution of the results is presented in Figure 79 for the HRA and *q-factor*, and in Figure 80 for the WLA, offering comparisons across generation and execution time. Upon individual examination, all simulations (presented in Table 5) exhibit remarkably similar trends across generations, with S4 showing marginally superior results compared to the others.

Table 19 – Results of S1, S2, S3 and S4 simulations regarding the average execution time.

SIM	Average generations time (min)	100 generations time (days)	Generations in 4 days	Run time efficiency
S1	18.5	1.3	308	1
S2	25.1	1.7	227	1.36
S3	37.8	2.6	150	2.05
S4	51.3	3.6	111	2.78

In comparing simulations S1 to S4 using the WLA index (Figure 80), it becomes evident that, by generations, S4 notably distinguishes itself from the others. This outcome was anticipated, given the utilization of a 95% crossover rate and a larger population, both of which contribute to a more favorable environment for the emergence of novel and superior individuals. However, it is crucial to acknowledge that the assessment of farm layouts depends on SWAN simulations, and expanding both parameters leads to an increase in the number of simulations and, subsequently, the execution time. Consequently, the optimal adjustment for the algorithm must be carefully weighed against execution time constraints. In this context, simulation S1, the swiftest among them, unequivocally demonstrates superior results with the best balance between HRA and *q-factor* from the initial hours of simulation.

Figure 79 shows the results of the simulations considering the execution time of 100 generations of S4, which is 86 hours. The data show that as it is a multi–objective optimization, and both parameters are equally balanced, the best result for one parameter will not always return the best output. As an example, in Table 20 the results of WLA for S3 after 86 h are better than for S2 and S4, although S2 has a higher *q-factor* and S4 has a higher HRA than S3.

Table 20 – Results of simulations S1, S2, S3 and S4 considering an execution time equivalent of 100 generations of S4 (86h).

Simulation	Generations	HRA (%)	*q-factor*
S1	279	13.21	1.008
S2	205	12.28	1.010
S3	136	12.44	1.007
S4	100	12.93	0.999

Having established the S1 configuration as the optimal choice, simulations S5 to S8 were subsequently conducted to gauge the algorithm's performance across other variants. These included variations in the number of WECs and in the minimal distance between them. By exploring these additional factors, it was aimed to comprehensively assess the adaptability and efficacy of the GA in accommodating different parameters crucial to the design and optimization of WEC farm layouts.

All simulations performed showed a distinct evolutionary trajectory, even when sharing identical array parameters. The individual progressions across generations are visually depicted in Figure 81 and Figure 82, where a simultaneous moving average, with a window of 5 values for both objectives (HRA and *q-*

factor), is presented for all simulations, and provides an interesting visualization of the trade–offs between the objectives.

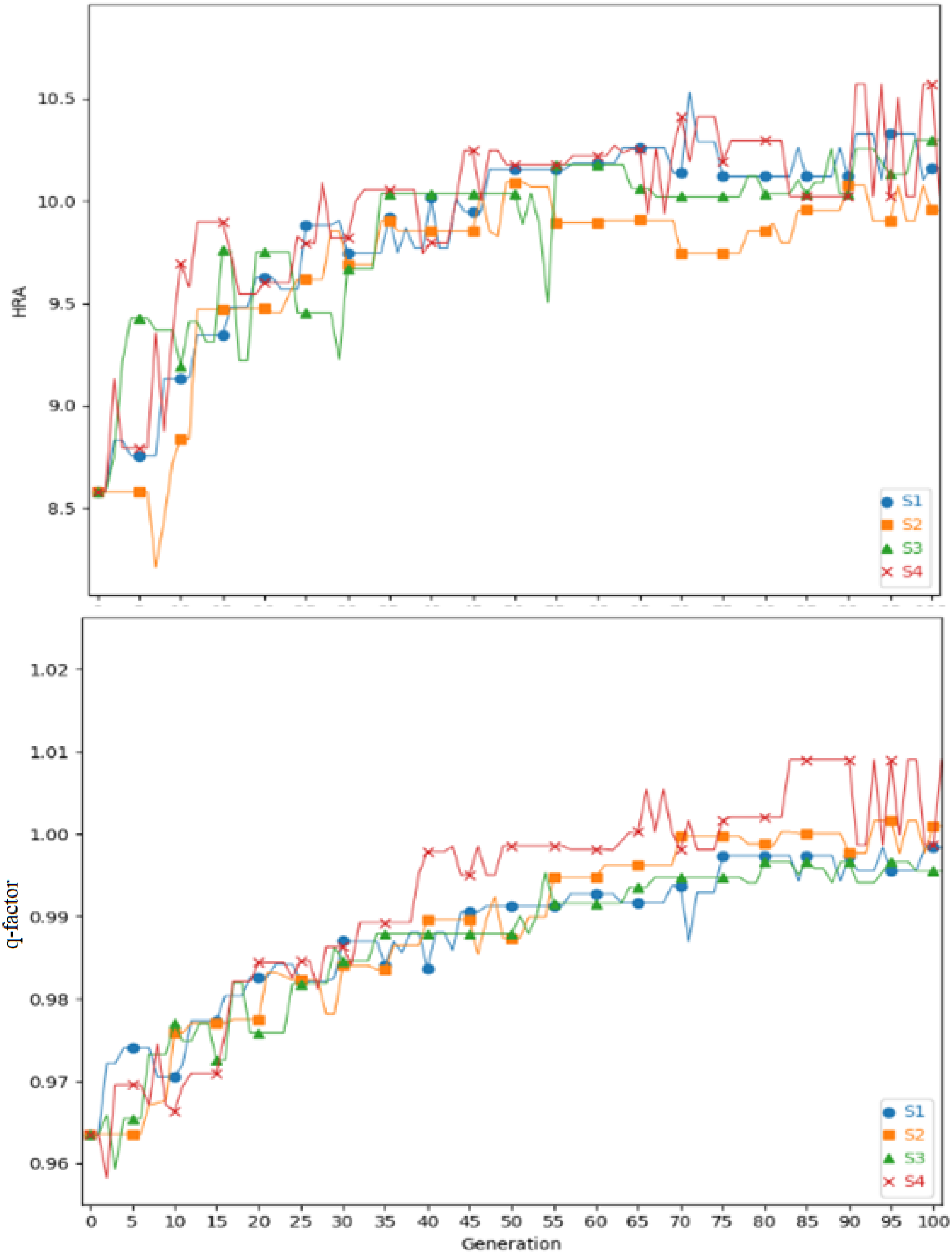

Figure 79 – Evolution of the parameters HRA (upper) and *q-factor* (lower) of simulations S1 to S4 through 100 generations.

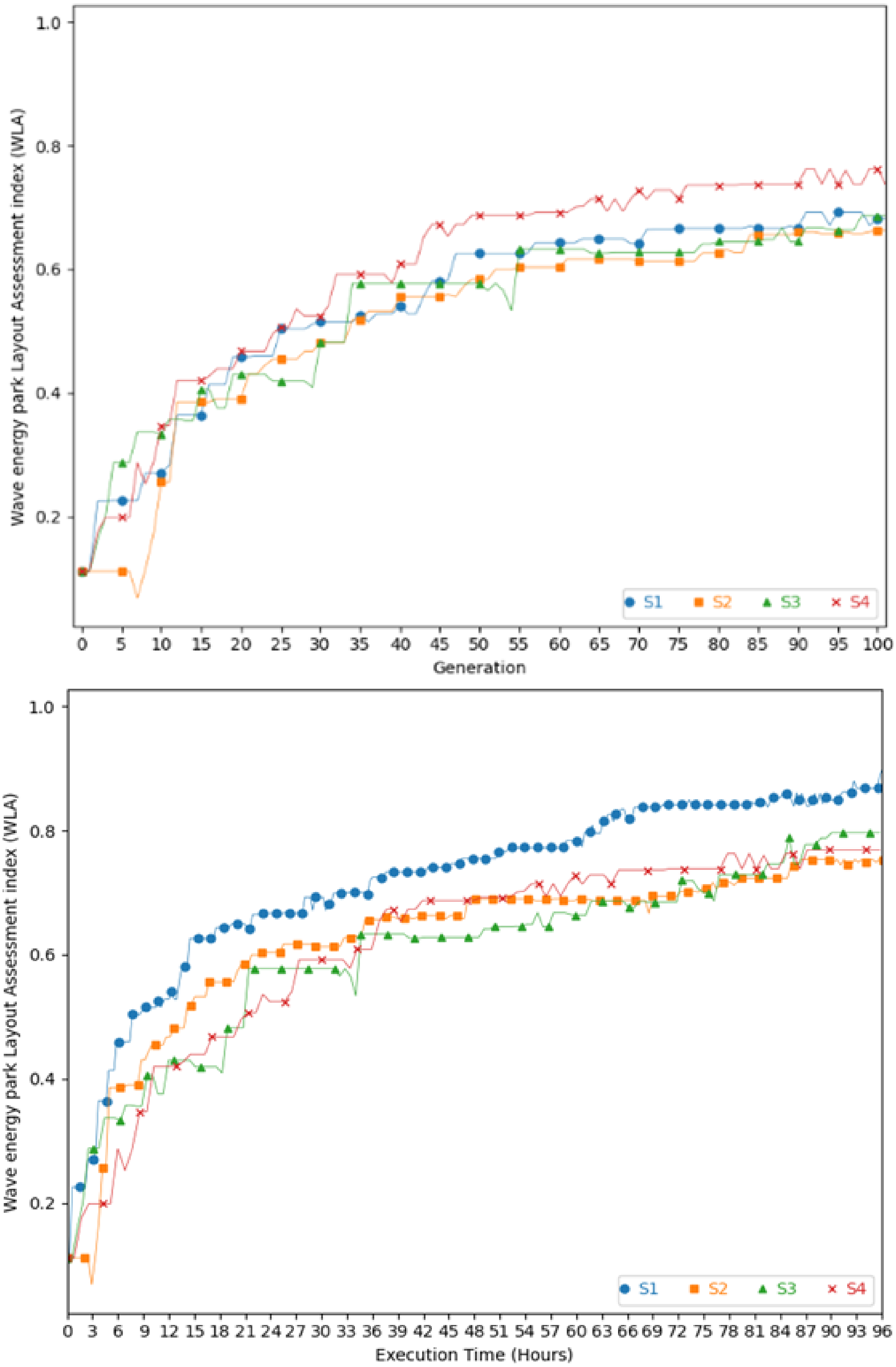

Figure 80 – Wave energy park Layout Assessment index (WLA) evolution of simulations S1 to S4, comparing the result by generation and the execution time.

Furthermore, Figure 83 and Figure 84 offer insight into the optimized final WEC farm design for each variation. Despite all simulations showcasing a heightened density of WECs strategically positioned to harness the most energetic sea states, the path to achieving these outcomes varied significantly, resulting in diverse final configurations. These graphical representations underscore the nuanced and multifaceted nature of the optimization process, highlighting the unique pathways each simulation traverses to attain its final objective.

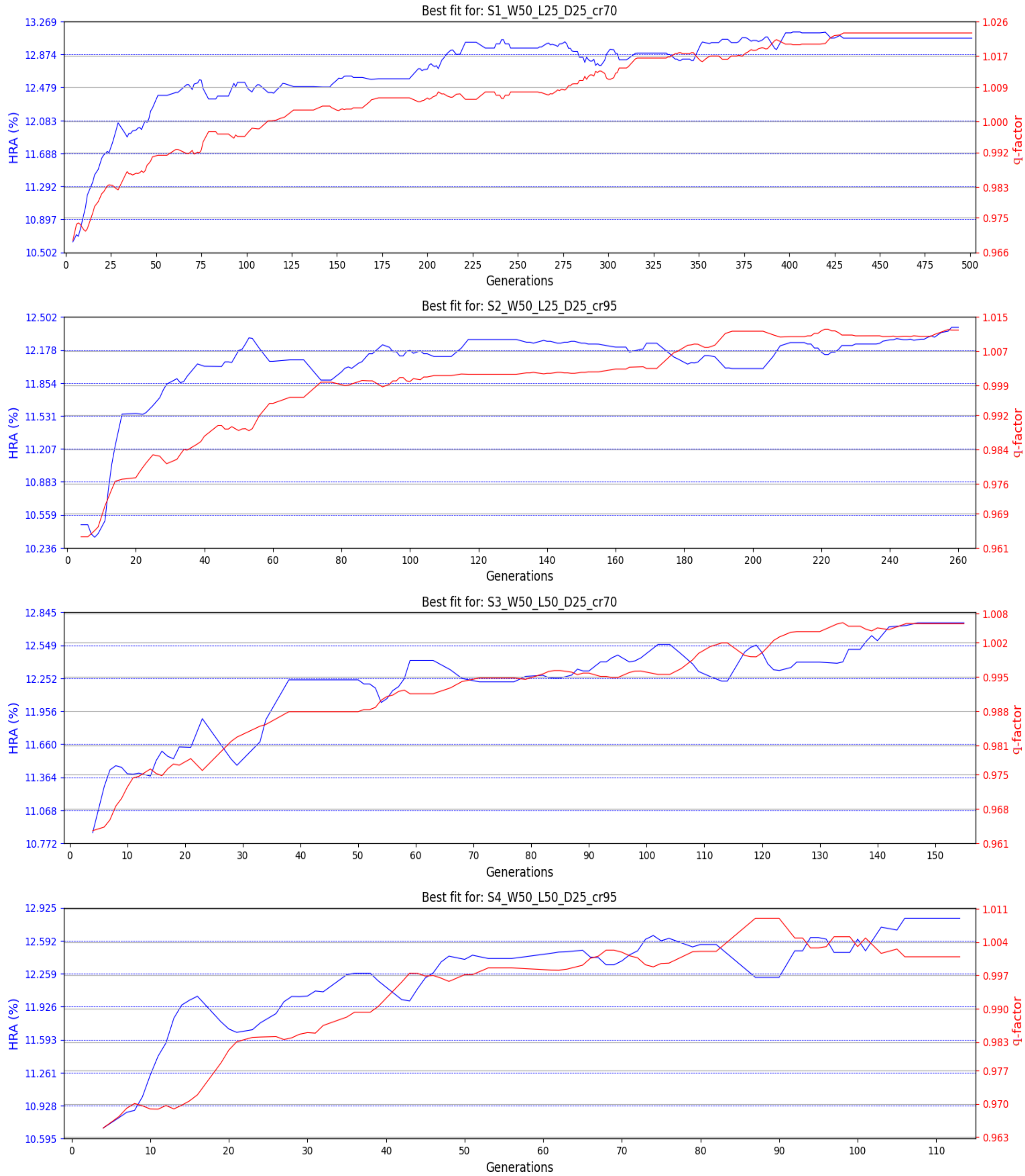

Figure 81 – Comparison of the evolution of the HRA and *q-factor* parameters for S1 to S4 simulations.

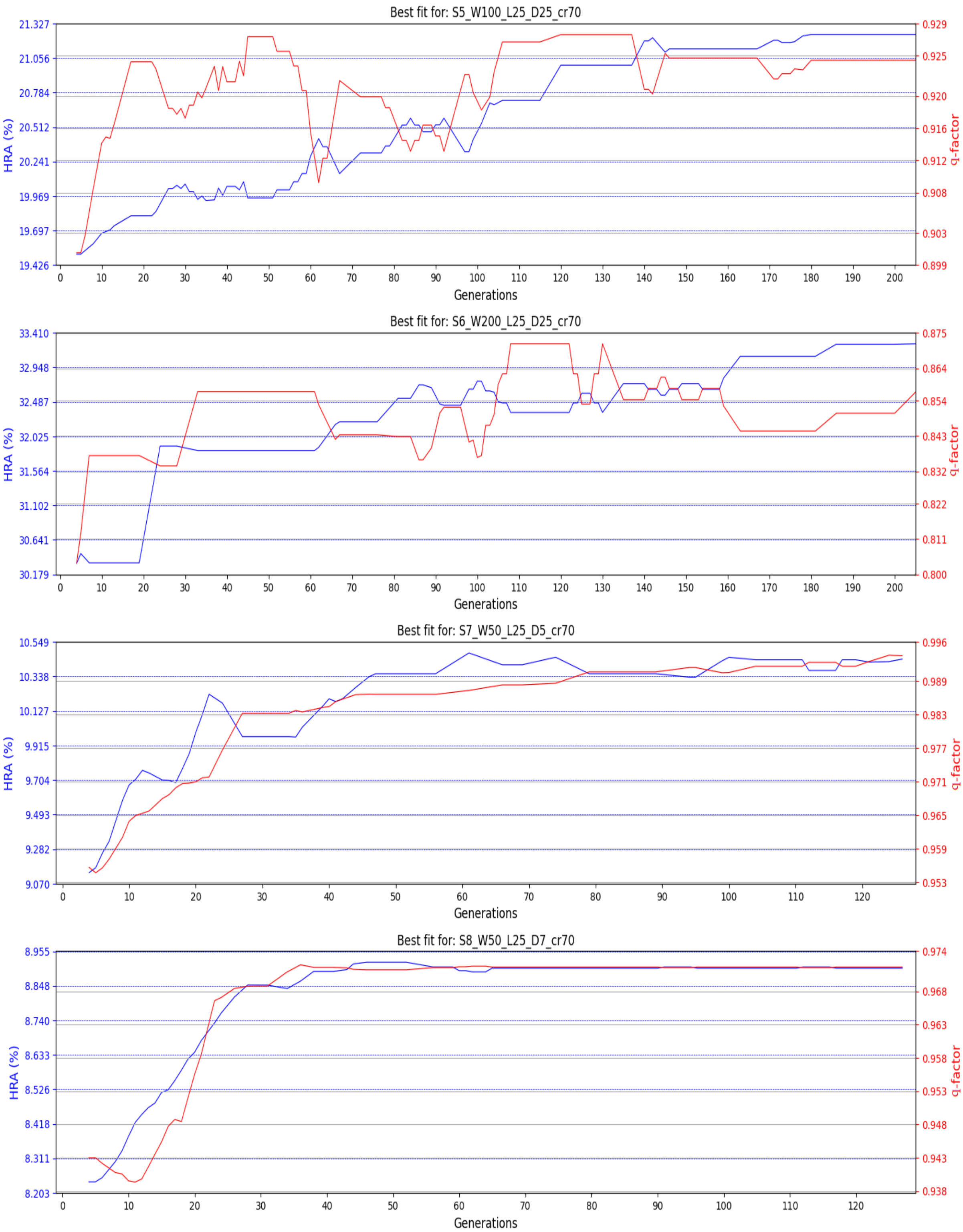

Figure 82 – Comparison of the evolution of the HRA and *q-factor* parameters for S5 to S8 simulations.

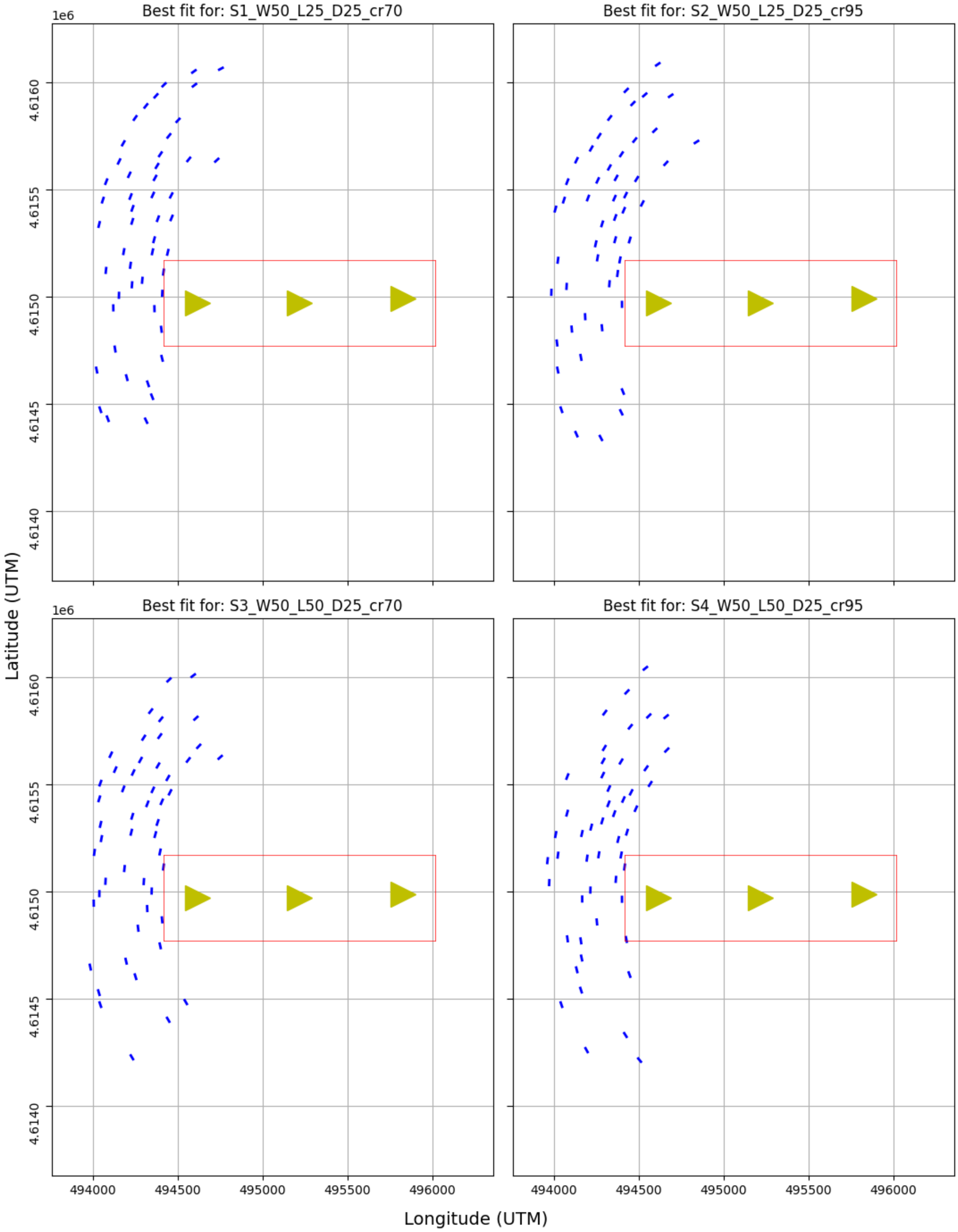

Figure 83 – Best fit layout for S1 to S4 simulations. The blue lines represent the WECs, the yellow triangles the wind turbines of the WindFloat Atlantic and the red rectangle the interest area.

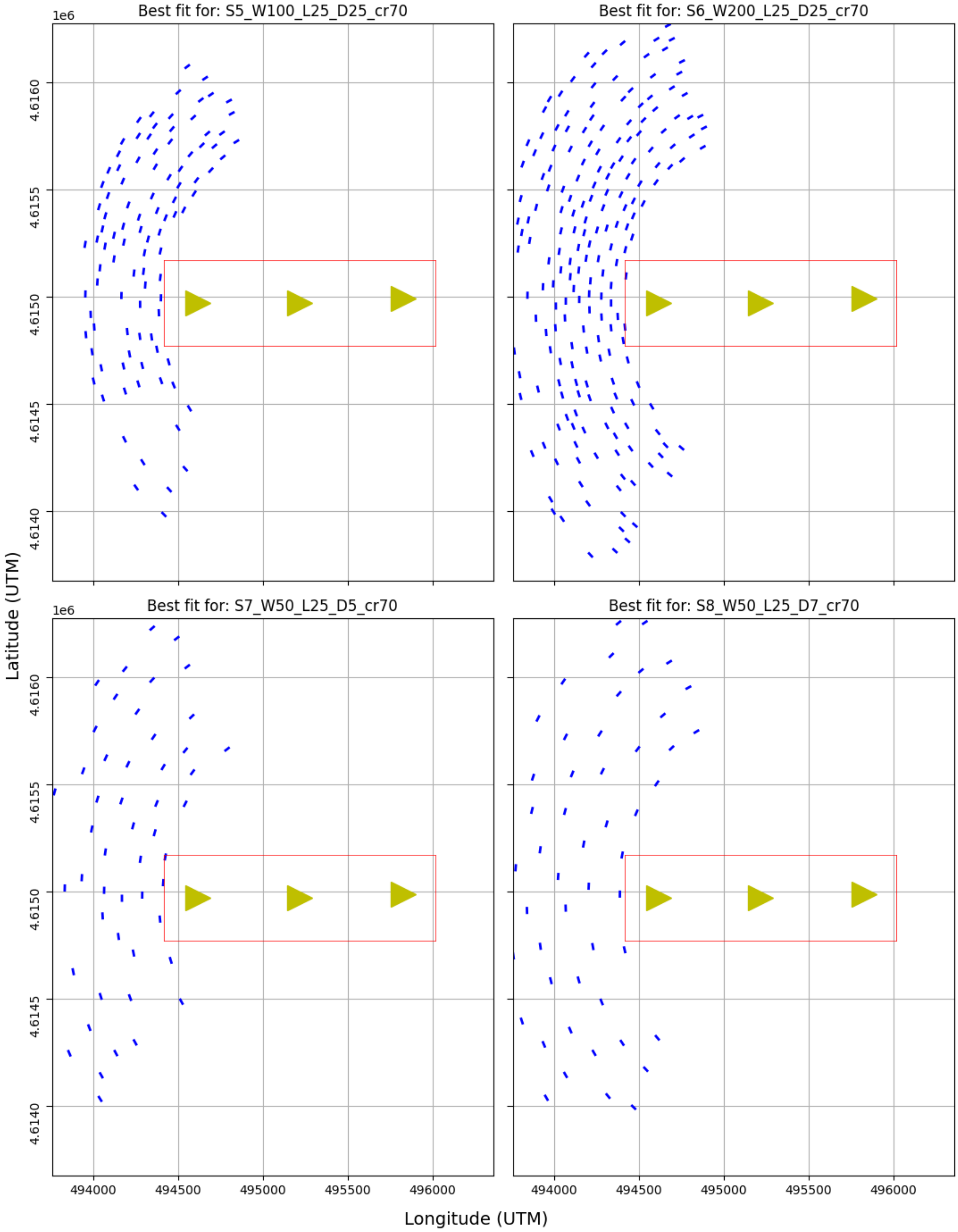

Figure 84 – Best fit layout for S5 to S8 simulations. The blue lines represent the WECs, the yellow triangles the wind turbines of the WindFloat Atlantic and the red rectangle the interest area.

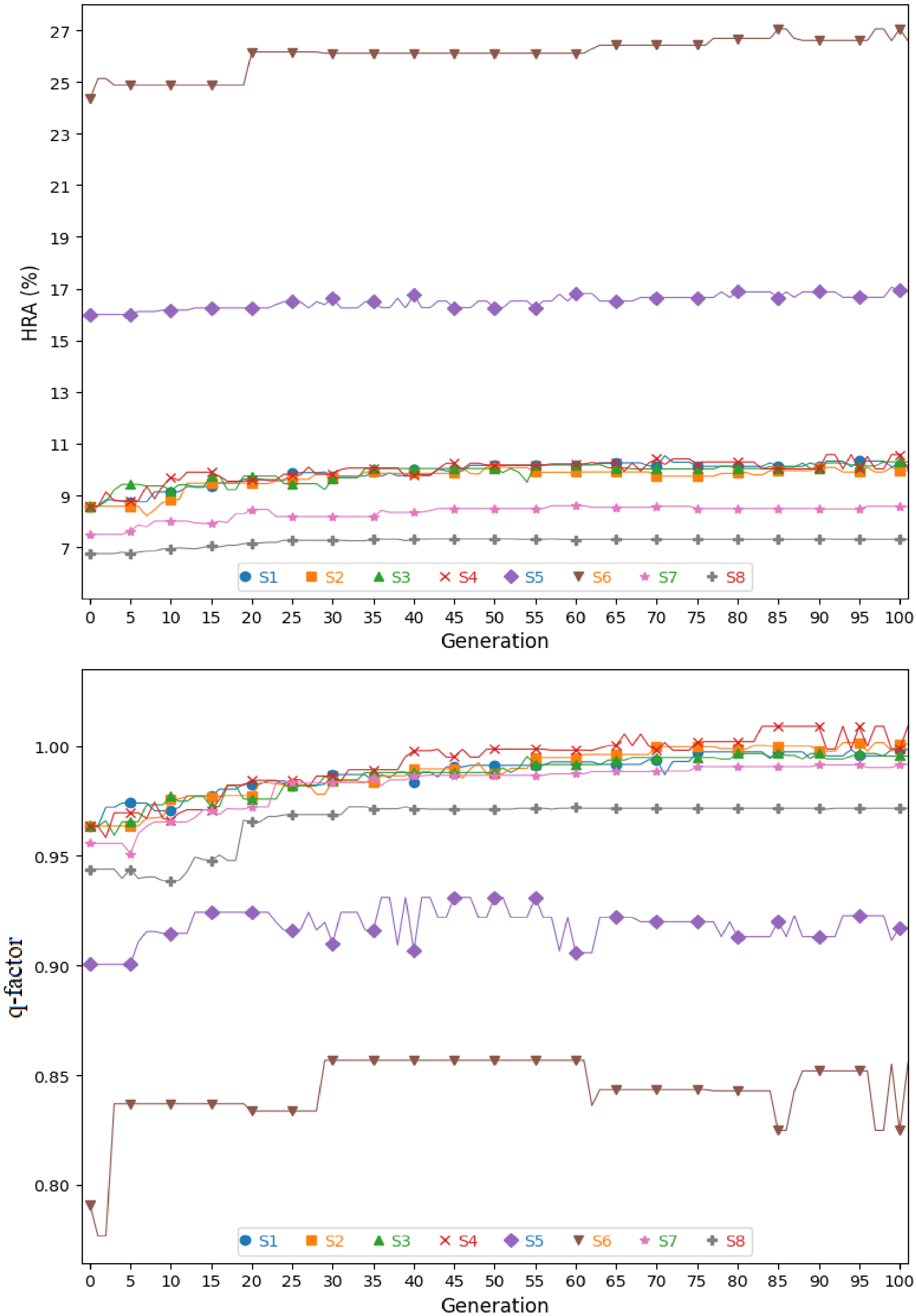

Figure 85 – Evolution of the parameters HRA and *q-factor* of all simulations through 100 generations.

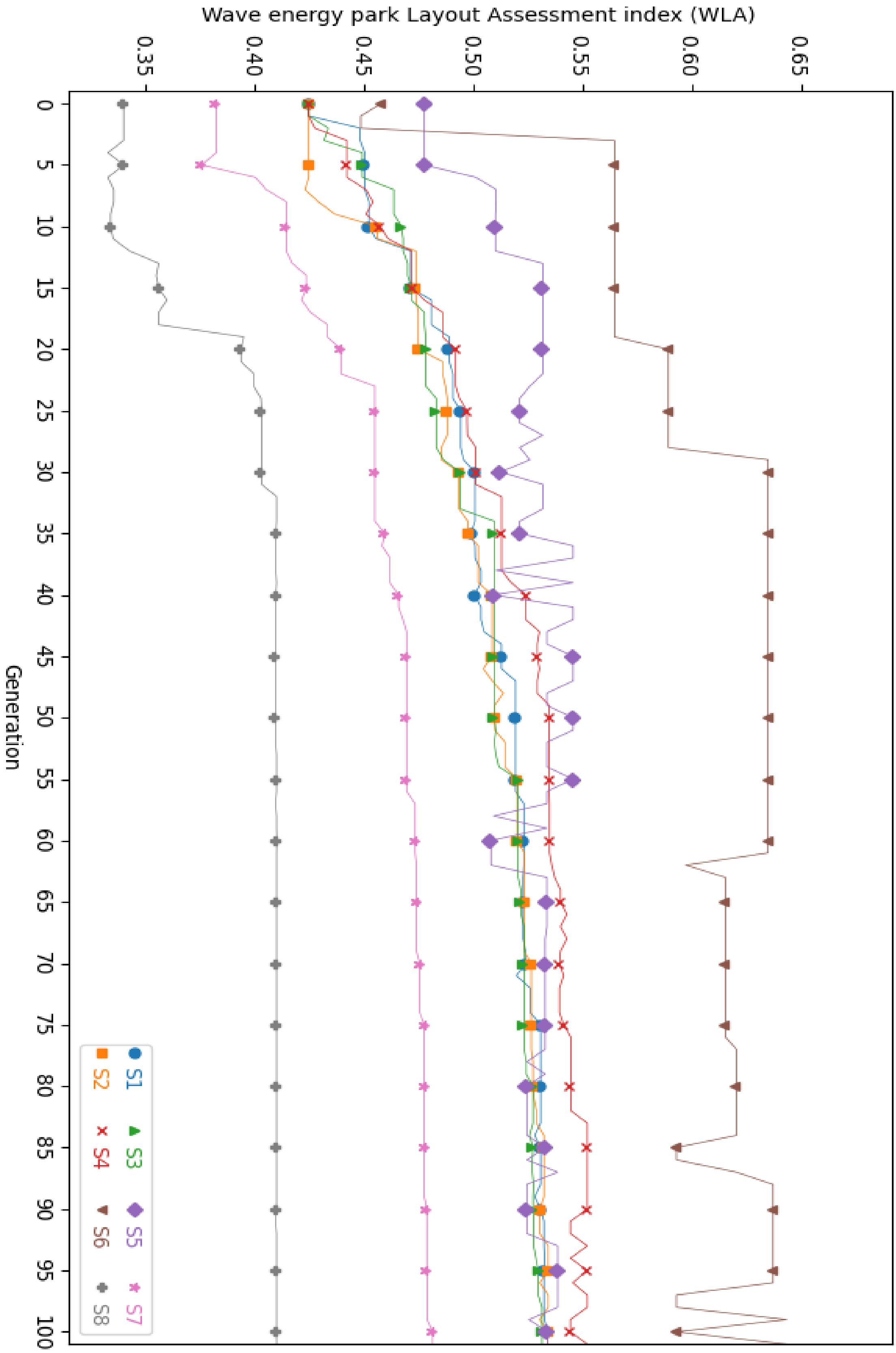

Figure 86 – Wave energy park Layout Assessment index (WLA) evolution of all simulations comparing the result by generation and the execution time.

In the analysis of the different arrangement's inputs and restrictions, the evolution of all simulations was plotted considering the values of HRA and *q-factor*, in Figure 85, and of WLA, in Figure 86. The dynamic nature of the WLA requires recalculating it after every generation, as the data is normalized. To ensure consistency across simulations, the WLA for all scenarios was calculated using the global maximum and minimum values derived from simulations S1 to S4 (in Figure 85) and simulations S1 to S8 (in Figure 86). This approach facilitates a standardized comparison across different simulation runs, allowing for a comprehensive evaluation of the optimization process's performance and effectiveness.

The exceptionally high HRA value in the 200 WECs layout (S6) resulted in a significantly larger WLA, effectively compensating for its lower *q-factor*. However, it is crucial to acknowledge the challenges posed by area restriction issues arising from either an excessive number of WECs or a wide inter–WEC spacing. These constraints constitute formidable obstacles within the optimization framework, as they can limit the development of the algorithm, causing premature convergence evidenced by horizontal curves. This underscores the complex interplay between the layout optimization objectives and the physical constraints inherent in the wave energy conversion domain.

To gain more insights on the array efficiency relative to the number of devices, the Capture Width Ratio (CWR) was also analyzed, which is a widely used metric for evaluating the hydrodynamic efficiency of a WEC. It represents the proportion of wave energy absorbed by the device relative to the energy flux available within its characteristic length. This efficiency is expressed as a ratio of the power absorbed by the WEC to the product of the wave energy flux per unit width and the characteristic width of the device.

The characteristic width, D, is often defined as the physical width of the WEC that is perpendicular to the wave front. In this study, D corresponds to the overall width of the CECO. The CWR can be expressed as:

$$CWR = \frac{P_{abs}}{J.\mathrm{D}} \tag{54}$$

where P_{abs} is the power captured by the WEC, and J the wave energy flux per meter of wave front. Unlike absolute measures of absorbed energy, the CWR offers a dimensionless perspective on the performance of a device. By normalizing energy capture relative to the device's size, it becomes easier to compare different WECs, regardless of their physical dimensions or operational scales. This makes the CWR particularly useful for benchmarking and performance optimization.

Table 21 presents the final outcomes of each simulation. Although comparisons among simulations S1 to S4 are not feasible due to the different execution times and generation counts, it is pertinent to note that comparisons between S5 to S6 and S7 to S8 are viable, as these simulations are variations of the same parameter and feature identical generation counts. Additionally, and in accordance with the findings presented in [63], the accessibility for the operation and maintenance of the wind farm emerges as a critical parameter for analyzing the efficiency of wave height reduction. Consequently, this parameter has been duly incorporated into Table 21 for a comprehensive analysis.

In contrast with the findings detailed in section 4.2 [63], which share the same inputs as this study and entailed the positioning of 4 WEC farms in a customized arc arrangement, simulation S1 exhibited notable superiority. Specifically, in comparison to the best layout identified in section 4.2 [63], simulation S1 showed an 87% improvement in absorbed wave power and a 46% enhancement in wave height reduction within the designated area of interest.

Table 21 – Final generation results for best fit layout, and estimated increase in the accessibility of the wind farm for operation and maintenance.

Simulation	Generation	Power absorption (MW)	CWR	*q-factor*	HRA (%)	Accessibility increase (%)
S1	500	6.61	40.25	1.023	13.21	28.4
S2	260	6.54	39.62	1.012	12.52	26.7
S3	150	6.50	33.21	1.006	12.82	27.6
S4	125	6.47	38.96	1.001	12.86	27.8
S5	200	11.95	34.39	0.924	21.08	44.0
S6	200	22.15	30.08	0.857	32.14	69.5
S7	125	6.42	38.90	0.992	10.43	22.2
S8	125	6.28	38.27	0.972	8.92	19.0

The Capture Width Ratio decreases as the number of WECs increases, indicating a trade–off between total energy absorption and individual device efficiency. Simulations with fewer WECs, such as S1 (50 WECs) and S2 (50 WECs), show higher CWR values (40.25 and 39.62), reflecting better energy capture efficiency per device. However, as more WECs are added, like in S5 (100 WECs) and S6 (200 WECs), the CWR drops significantly, despite a higher total power absorption, suggesting that scaling up the number of devices reduces their relative efficiency. This trend highlights the balance between optimizing the number of devices and maximizing energy capture efficiency.

As the S1 simulation demonstrated superior performance, extending it to 500 generations allowed for a detailed analysis of its behavior. Figure 87 shows a notable initial improvement in both parameters, followed by a gradual enhancement in *q-factor* over the subsequent generations, while HRA remains relatively stable after 300 generations. This pattern highlights the inherent trade-offs between parameters, notably observed in the best layout curve, where new individuals with higher *q-factor* exhibit lower HRA than the previous best fit, and *vice versa*.

Moreover, it is noteworthy that not only the best fit individual or the elite evolve. Instead, the entire population experiences an increase in values, indicating a collective trend toward achieving optimal results. While the population range maintains the potential to circumvent local optima, the ongoing evolution of individuals across successive generations suggests a continual exploration of the solution space, thus mitigating the risk of convergence towards suboptimal solutions.

Interestingly, the best fit individual remained unchanged in the last 50 generations, despite sporadic instances of improved HRA and *q-factor* in other individuals. This suggests the possibility of a superior fit individual, albeit with diminishing probability as the best fit remains unchanged over successive generations.

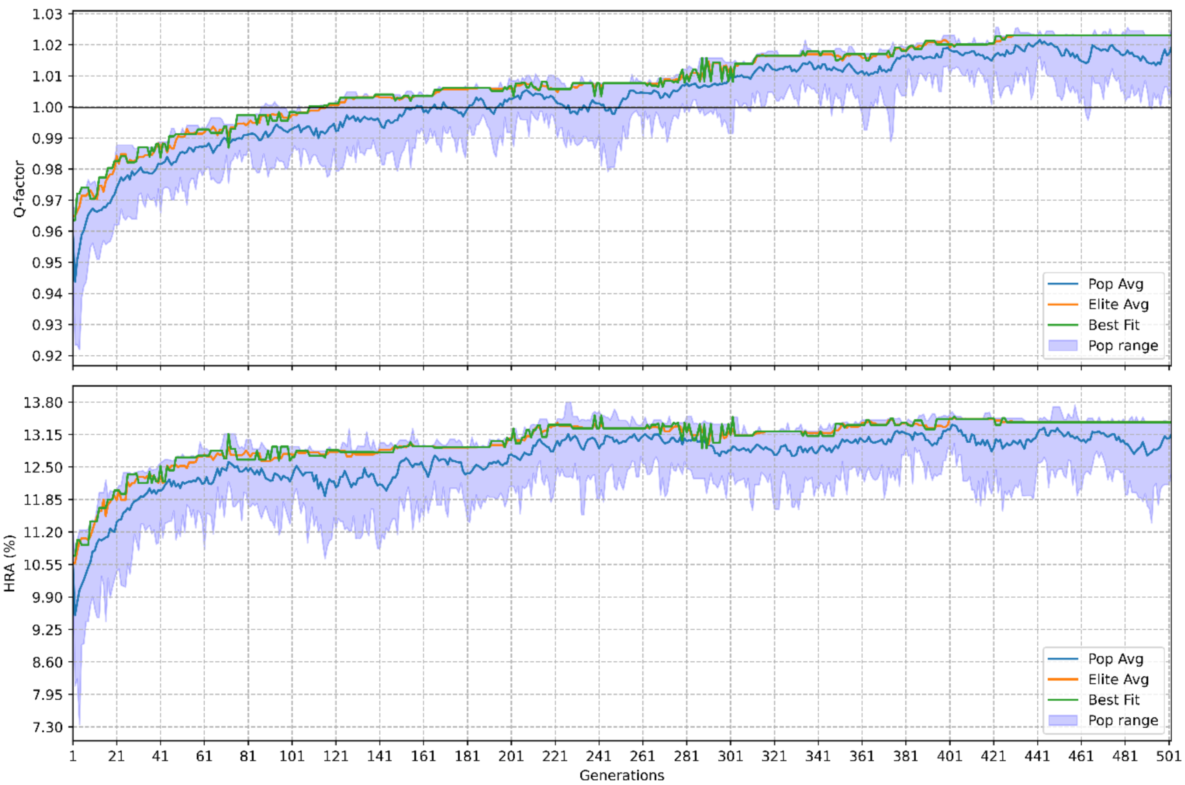

Figure 87 – Evolution of simulation S1 for the HRA and *q-factor* parameters. The purple shadow represents the range of values presented in the population, the green line the best fit layout, the blue line the average of all population and yellow line the average of elite layouts.

5.1.3. Comparative analysis and validation of the optimization algorithm

In the following was performed sensitivity analysis a comparative study replicating simulations with different number of WECs. The outcomes for the 200th generation of configurations S5 and S6 are presented in Table 21, while configuration S1 achieved a power absorption of 6.51 MW and an HRA of 12.86%. A summary of the results for all comparative cases can be found in Table 22.

Table 22 – Results of the verification and validation study. Where Δd is the distance from the first run position.

Sim	Power abs (MW)	Power Error (%)	HRA (%)	HRA Error (%)	Layout RMSE	Pairs (%) Δd >1D	Centroid Δd (m)
S1 rerun	6.53	0.26	12.63	–1.80	112.71	52	16.76
S5 rerun	11.90	–0.47	20.89	–0.91	106.81	57	22.16
S6 rerun	22.17	0.09	32.48	1.04	98.81	44	14.42
S1 max shield	6.22	–4.42	14.53	12.96	225.71	86	51.55
S5 max shield	11.44	–4.28	22.76	7.95	136.52	88	68.36
S6 max shield	21.24	–4.14	33.97	5.68	110.52	88	49.73
S1 max power	6.59	1.20	9.78	–23.97	336.69	90	171.72
S5 max power	12.09	1.14	18.94	–10.14	180.73	91	84.68
S6 max power	22.35	0.88	30.43	–5.32	170.28	93	72.00

To further illustrate the findings, the outcomes of the S1 configuration are highlighted in Figure 88 and Figure 89, which provide an evolutionary comparison of the two optimization runs with equal weights assigned to power absorption and shield protection. Additionally, Figure 90 showcases the layouts of all S1 simulations, including those optimized solely for power absorption and shield protection. These visualizations emphasize the versatility and effectiveness of the proposed optimization algorithm under varying objectives.

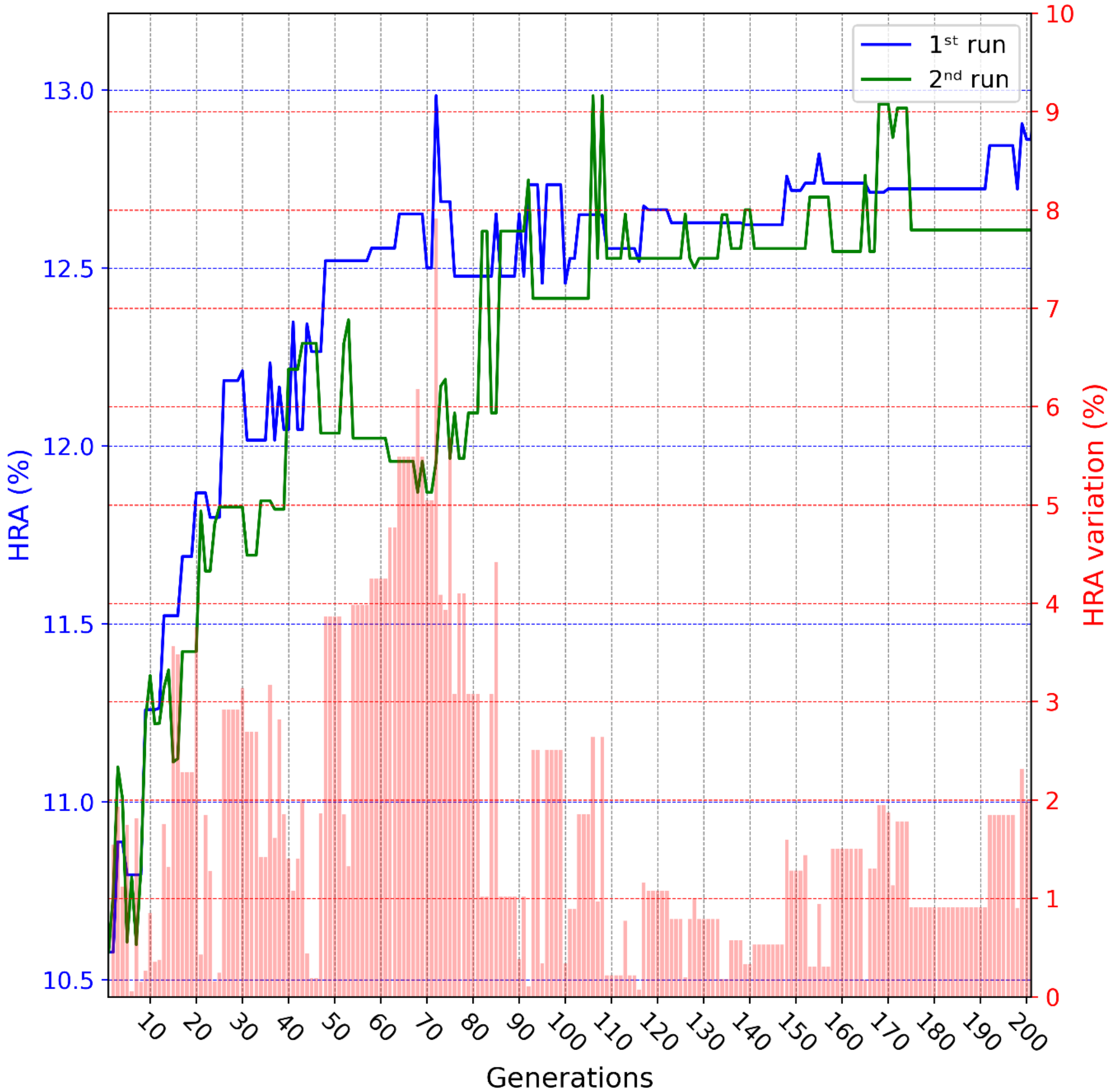

Figure 88 – Comparison of the evolution of the HRA values and their variation for the two simulations with S1 parameters. The blue line represents the evolution of first run, the green line the evolution of second run and the red bars represent the percentual difference between each run.

The second round of simulations with equal weights assigned to shield protection and power absorption produced results that were remarkably similar to the first ones. Approximately half of the WECs were positioned in locations less than one device diameter (<1D) apart, with variations in HRA of less than 2% and power absorption differing by less than 0.5%. Additionally, the RMSE remained stable around

5D across all three simulations of different numbers of WECs. The evolutionary process of the optimization was also highly similar, indicating a strong tendency toward convergence on a global optimum with minimal variation.

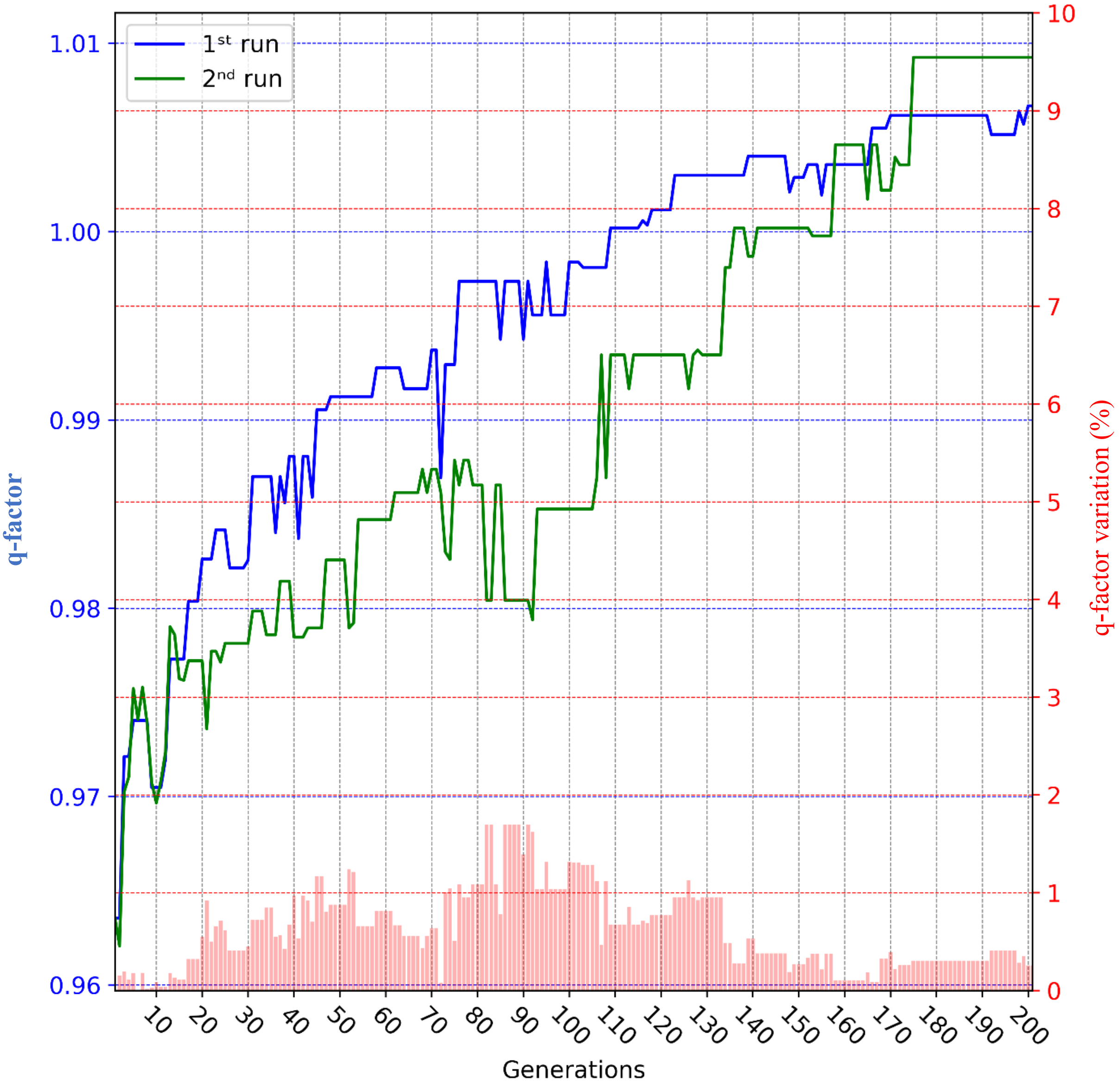

Figure 89 – Comparison of the evolution of the *q-factor* values and their variation for the two simulations with S1 parameters. The blue line represents the evolution of first run, the green line the evolution of second run and the red bars represent the percentual difference between each run.

Notably, the simulations performed for maximizing just one parameter exhibited higher variations in RMSE and centroid positions compared to the rerun simulations, as these focus on a single objective, which causes greater layout variability, with approximately 90% of the devices repositioned. The RMSE was higher for layouts with fewer WECs compared to those with more devices. A plausible explanation is the reduction of available space for positioning in larger layouts, which leads to a more uniform device distribution and minimizes the average positional differences between optimized pairs.

The centroids, which can represent the positioning of a central collecting hub, were highly stable for the rerun simulations, with variations of 1D or less. An exception occurred in the S1 maximum power case, where centroid variation reached 8D due to the focus on maximizing power absorption alone, which led to more distinct optimized positions. Nevertheless, considering the layout domain of approximately 1.3 km², this difference is practically insignificant.

The random nature of the initial generation and the mutation process, which allows WECs to be repositioned anywhere within the domain regardless of previous layouts, supports this global optimization search. This tendency for the simulations to converge toward a common solution is further demonstrated by the evolution of the entire population, as shown in Figure 21, where the population progresses collectively toward an optimal configuration.

These results further corroborate the trend toward an optimal global layout. A plausible explanation for the consistency of results and the similarity in evolutionary paths, even when considering continuous spatial positioning, lies in the random sampling of 500 layouts in the initial generation. This broad exploration minimizes the likelihood of convergence to local optima by effectively distributing the WECs across the entire domain.

For the simulations that aimed to maximize only one parameter in the objective function, the non–prioritized parameter was consistently neglected in the best–fit solutions, never achieving the highest value in the generation and remaining close to the generation average. Conversely, the prioritized parameter was always maximized. This is reflected in Table 10, where reductions in power absorption and HRA are evident for the neglected objectives.

Interestingly, Table 22 also reveals that, even with equal weights, power absorption reaches levels very close to those achieved in simulations exclusively maximizing power. This suggests a potential barrier for this parameter, as the *q-factor* is already close to or exceeds 1. On the other hand, HRA appears to have more room for improvement. Furthermore, small variations in power absorption have a more pronounced impact on shield protection than variations in protection have on power absorption.

Examining Figure 90 and the variations in centroids, it becomes evident that prioritizing one objective significantly influences the spatial arrangement of the layouts. Simulations that prioritize shield protection exhibit a more compact spatial distribution, concentrating the WECs in areas aligned with the predominant wave energy directions and frequencies. Conversely, simulations that prioritize power absorption result in a more dispersed spatial configuration, aimed at minimizing interference between WECs and maximizing wave energy exposure for each device. These findings highlight how the objective function weights influence not only the performance metrics but also the spatial characteristics of the optimal WEC layouts.

These findings emphasize the importance of carefully calibrating the weights of the objective function. Their adjustment should be based on thorough evaluation and may consider a range of economic, social, and environmental factors to reflect stakeholder priorities and optimize outcomes effectively.

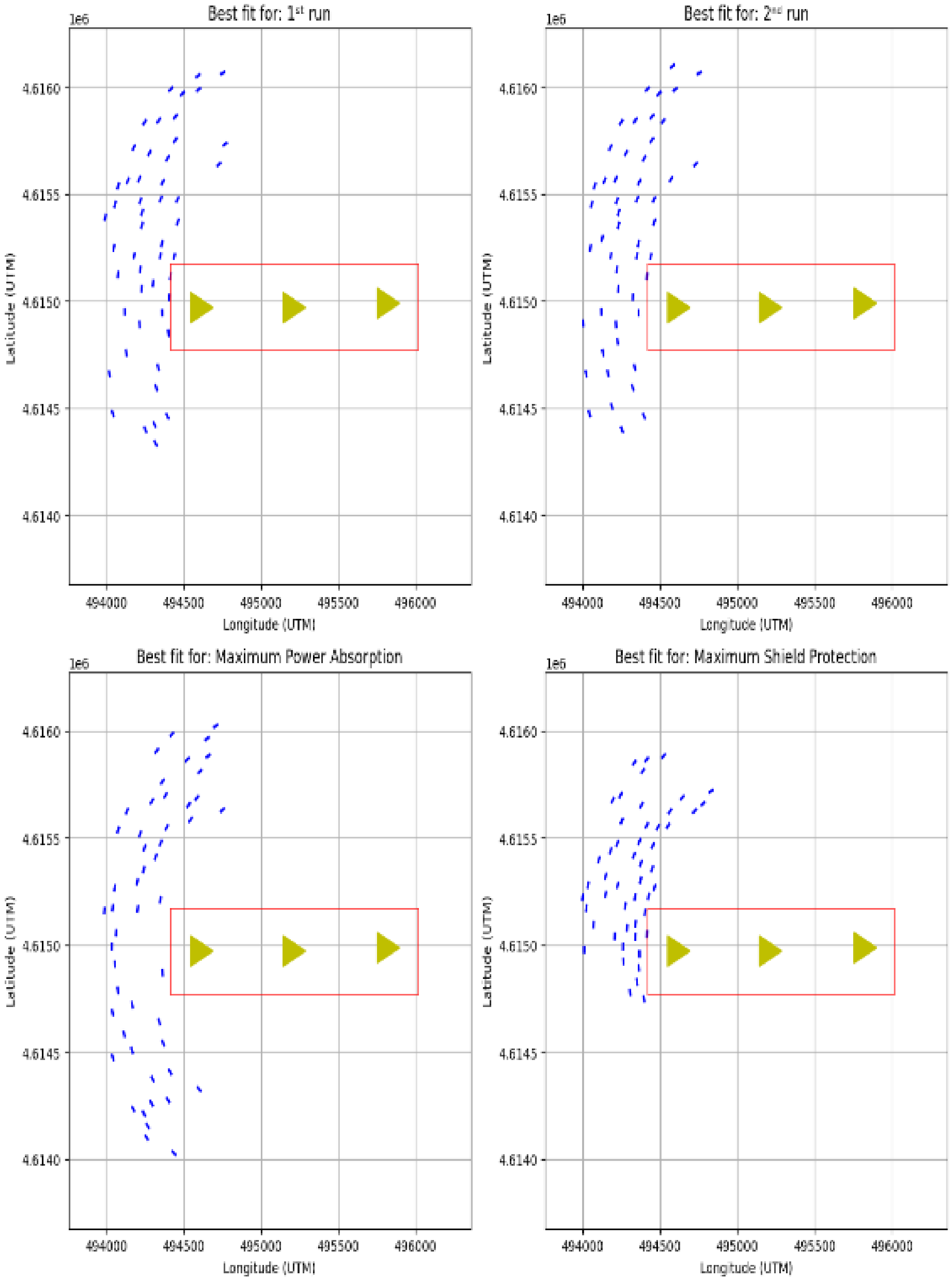

Figure 90 – Best fit layout of generation 200 for each simulation using the S1 parameters. The blue lines represent the WECs, the yellow triangles the wind turbines of the WindFloat Atlantic and the red rectangle the interest area.

5.1.4. Sensitivity analysis conclusions

This study successfully employed a GA to optimize the layout of a WEC farm situated offshore Viana do Castelo, Portugal. The farm's primary objective was to harness wave energy while simultaneously protecting a co–located wind farm from waves, in order to increase the weather windows for operation and maintenance.

The key findings of the study are as follows:

- K–means clustering effectively reduced the number of sea states required for the accurate wave farm simulations while preserving at least 90% of the incoming wave energy. However, it is crucial to acknowledge that k–means clustering utilizes Euclidean distance, which is not well–suited for analyzing data with circular characteristics, such as wave direction. This limitation was overcome by restricting wave directions to a sector lower than 180º. Alternatively, employing specialized distance metrics for circular data representation could be explored in future works;
- The GA configured with a 70% crossover rate, a population size of 25 individuals, and an elite rate of 12% achieved the optimal balance between solution quality and computational efficiency. Importantly, this approach leverages a continuous domain for WEC placement. Unlike traditional grid–based methods that restrict WEC positions to pre–defined locations, the GA allows for a more nuanced and potentially superior optimization by enabling free positioning within the designated area;
- Compared to a previous study with a non–optimized layout design, the proposed GA method yielded a significant improvement in both the absorbed wave power (87% increase) and wave height reduction (46% increase) within the designated area of interest;
- The limitations of the study include the inherent trade–offs between the optimization objectives (HRA and *q-factor*) and the challenges posed by area restrictions due to a large number of WECs or wide inter–device spacing.

In essence, this study demonstrates the effectiveness of the GA in optimizing wave farm layouts for efficient wave energy capture while simultaneously mitigating negative wave impacts on co–located wind farms. The proposed methodology, particularly the utilization of a continuous domain and the versatile SNL–SWAN model, is valuable for advancing the development and implementation of wave farms. The vast range of inputs and outputs allowed by SNL–SWAN model enhances the applicability and comparability of this framework across diverse WEC technologies and environmental conditions.

This finding underscores the nuanced interplay between different performance metrics within multi–objective optimization frameworks. It suggests that achieving the most favorable outcome needs a holistic evaluation of various parameters and their respective trade–offs, rather than focusing solely on individual metrics. Such insights are instrumental in refining optimization strategies and enhancing the effectiveness of WEC layout design processes.

5.2. Economical optimization of an offshore co–located wave farm

The optimization process presented in this section considers the evaluation of objectives as defined in Section 3.5.3, where the weights of the WLA function were assigned values of 0.6582 for power production and 0.3418 for shield protection. In addition, based on the outcomes of the sensitivity analysis, the simulation configuration S1 was applied to the GA parameters to ensure consistency with previous simulations.

As anticipated, the evolution of the layouts (Figure 91 and Figure 92) diverged from the S1 simulation results (Figure 87), with the *q-factor* reaching a value of 1.0 after only 42 generations. Moreover, this simulation achieved a *q-factor* similar to that of the S1 simulation at the 500th generation in approximately 50% of the computational time. While this approach accelerated the optimization process significantly, it should be noted that when compared to simulations that only optimized power production (referred to as "S1 max power" in Section 5.1.3), the current simulation did not reach the maximum potential for power production. This observation suggests that although the optimization strategy effectively improved convergence speed, it did not fully exploit the power production potential in isolation.

However, the goal of the current optimization is not solely to maximize power production. Shield protection, as an additional objective, plays a crucial role in determining the optimal layout. The HRA index, which is central to the shield protection objective, exhibited a more irregular evolution throughout the generations. This irregularity can be attributed to the fact that the weight of HRA is less than half of that of the *q-factor*. Consequently, HRA must undergo significantly larger fluctuations in order to influence the fitness function. This is evident from the several peaks in the HRA curve that did not lead to modifications in the best–fit layout. Notably, towards the end of the simulation, a substantial increase in the HRA led to a slight decrease in the *q-factor* of the best–fit layout, indicating that the interaction between the two objectives can influence the optimization process in complex ways.

Figure 91 illustrates the evolution of the simulation using the weighted parameters for shield protection and power production. The purple shaded area represents the range of values observed across the population, the green line denotes the best–fit layout, the blue line represents the average of all population members, and the yellow line indicates the average of the elite layouts. Figure 92 compares the evolution of the HRA and *q-factor* parameters throughout the optimization process, further highlighting the relationship between these two objectives.

Upon reviewing the results, it becomes evident that tuning the algorithm using the desired weights for power production and shield protection facilitates the achievement of optimal results more quickly than when the optimization is not tuned. Additionally, this approach does not sacrifice layouts that yield favorable results for the less prioritized objective, as is the case when using a single–objective function. The comparison between the single–objective simulation and the current multi–objective optimization reveals that power production reaches a near–threshold level of development, which subsequently limits further improvements. This stage of development then creates space for the HRA to evolve, especially if a layout with high protection appears.

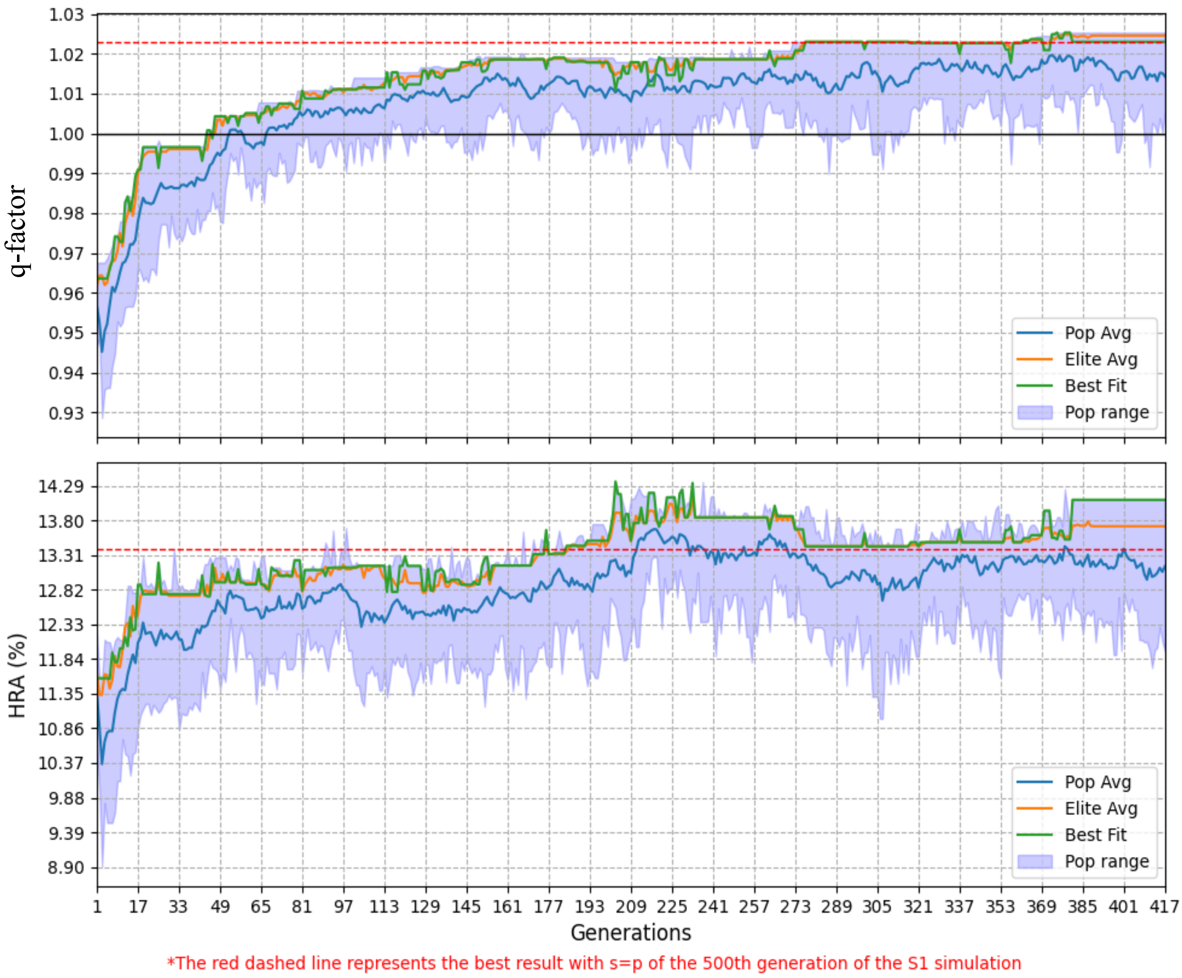

Figure 91 – Evolution of simulation using economical parameters to define the weights of shield protection and power production. The purple shadow represents the range of values presented in the population, the green line the best fit layout, the blue line the average of all population and the yellow line the average of elite layouts.

The simulation reached the termination criterion of 20 consecutive generations without modifications in the objectives at generation 401, at which point the results were nearly identical to those obtained in the S1 simulation. Table 23 presents a comparison between the results of the S1 and economical optimization simulation.

Table 23 – Comparison between results of S1 and economical optimizations.

Simulation	Generation	Power absorption (MW)	*q-factor* (%)	HRA (%)	Accessibility increase (%)
S1	500	6.61	102.3	13.2	28.4
Economical	401	6.61	102.3	13.1	28.3

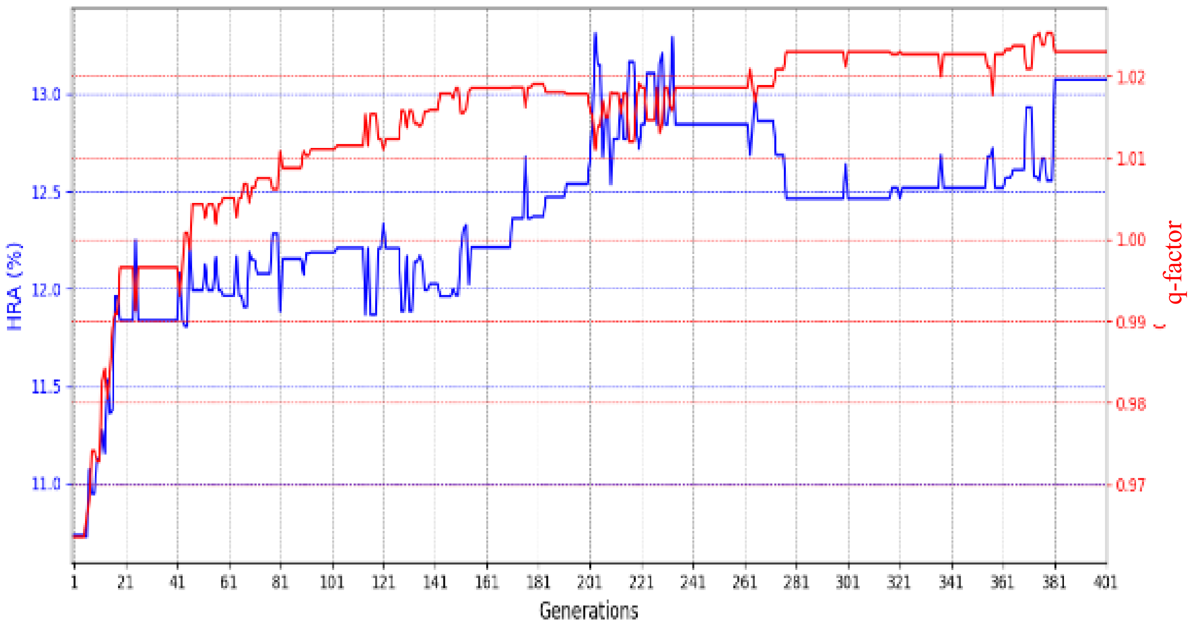

Figure 92 – Comparison of the evolution of the HRA and *q-factor* parameters for economical optimization.

Upon reviewing the results, it becomes evident that tuning the algorithm using the desired weights for power production and shield protection facilitates the achievement of optimal results more quickly than when the optimization is not tuned. Additionally, this approach does not sacrifice layouts that yield favorable results for the less prioritized objective, as is the case when using a single–objective function. The comparison between the single–objective simulation and the current multi–objective optimization reveals that power production reaches a near–threshold level of development, which subsequently limits further improvements. This stage of development then creates space for the HRA to evolve, especially if a layout with high protection appears.

Considering that WEC technologies have not yet reached commercial availability, it is noteworthy that the proposed optimization algorithm can still deliver high–quality results even without the explicit valuation of objectives. This flexibility in the algorithm makes it a valuable tool for accelerating the implementation of wave energy technologies. By providing optimal layouts for specific sites, the algorithm can facilitate the evaluation of the feasibility of wave energy farms, even in the early stages of technology development. This suggests that the proposed methodology can play a pivotal role in advancing the practical deployment of wave energy systems, offering a valuable resource for decision–makers in the energy sector.

5.3.Optimizing nearshore wave farms

The proposed optimization methodology encompasses two principal dimensions: power performance, aimed at maximizing energy production, and environmental considerations, focusing on the impacts generated on the wave climate. In previous scenarios, where wave farms were positioned offshore in deep waters, the wave farms exhibited negligible effects on the seabed and minimal influence on far–

field wave conditions. This observation aligns with findings in existing literature [6]. Consequently, such offshore configurations exerted almost no discernible impact on coastal zones and shorelines. However, when optimizing nearshore wave farms in shallow or intermediate waters, the interaction between WECs and the seabed becomes more pronounced, as are their effects on shoreline dynamics.

In typical studies of coastal morphological evolution, SWAN is often coupled with sediment transport models to provide a comprehensive analysis. However, the variation in wave energy, intrinsically linked to sediment dynamics, can be evaluated using SWAN alone. This allows for an assessment of wave energy reduction along the shoreline, enabling comparative analyses of different wave farm layouts, as outlined in section 2.2.3 of this work. This approach provides a practical yet robust framework for evaluating environmental impacts without necessitating full coupling with sediment transport models in preliminary analyses.

The environmental parameters considered in this study include bathymetry, wave height, wavelength, peak wave period, wave direction, sediment type, currents, and other relevant factors, all contextualized within the geographic and environmental characteristics of the northern coast of Portugal. The configuration of the numerical models is informed by previous studies that successfully applied similar approaches to assess environmental conditions in nearshore systems [171]. Additionally, the methodology incorporates insights from simulations conducted earlier in this research, ensuring methodological consistency and alignment with established practices.

The analysis will quantify alterations in the coastal zone relative to a baseline scenario, providing a detailed evaluation of the potential impacts generated by the proposed nearshore WEC arrays. This evaluation encompasses both beneficial and adverse environmental implications. Positive effects may include enhanced coastal protection and a shielding effect that could benefit human activities, such as aquaculture. Conversely, potential negative impacts, such as localized erosion or sediment redistribution, will also be assessed. These insights aim to provide a balanced understanding of the environmental trade–offs associated with nearshore wave energy extraction.

Throughout the research, the optimization algorithm underwent continuous development and refinement, with specific advancements implemented during its application to nearshore zones following its initial use in offshore co–located areas. Among the new features introduced was the ability to select between maximum or minimum normalization of the HRA index within the WLA function, providing greater flexibility in aligning the optimization objectives with site–specific requirements. Moreover, additional parameters to evaluate the power production performance of the WEC array were incorporated.

Two metrics were analyzed for this purpose: the coefficient of variation of the absorbed power, which quantifies the relative dispersion of power output across the array, and a novel metric termed "Peak–to–Mean" (P2M). The P2M parameter, defined as the difference between the maximum power absorption ($max|P_{wec}|$) and the average power absorption of all WECs ($\bar{P}_{wec}$), normalized by the average, offers insight into the smoothness of the power production within the array.

$$\boldsymbol{P2M} = \frac{\boldsymbol{max}|\boldsymbol{P_{wec}}| - \overline{\boldsymbol{P}}_{\boldsymbol{wec}}}{\overline{\boldsymbol{P}}_{\boldsymbol{wec}}} \tag{55}$$

These parameters are particularly valuable for assessing variations in power output among WECs in different configurations and for comparing the smoothness and stability of energy production across layouts. By evaluating these metrics, the algorithm enhances its capacity to identify optimal designs that balance energy efficiency with operational reliability.

The results for the two Portuguese case sites, Esposende and Aguçadoura, are presented in the following subsections. For both locations, power production was optimized to achieve maximum *q-factor* values, ensuring efficient energy extraction. However, shield protection objectives varied between maximizing the HRA index to enhance coastal protection and minimizing the HRA index to reduce environmental impacts. It is essential to note that while this study focuses on hydrodynamic parameters, the findings aim to support future research and projects targeting wave energy extraction and coastal protection solutions.

5.3.1. CASE I: Esposende – OWSC (Waveroller®)

The Esposende study site is characterized by a designated AOI that is smaller in size compared to the broader deployment zone (Figure 93). The primary goal within this area is to significantly reduce incoming wave energy, thereby contributing to enhanced coastal protection against phenomena such as flooding and erosion. The optimization of WECs in this specific region aims to mitigate the impact of wave energy on the shoreline, offering a strategic solution for addressing coastal vulnerabilities.

Previous simulations conducted by Clemente *et al*. [289] utilized fixed array configurations to analyze the same sea states. These earlier simulations serve as a useful benchmark for comparison with the results of the present study. By contrasting the findings of the current research with those from the previous work, it becomes possible to assess the effectiveness of the dynamic array configurations and their impact on wave energy reduction. This comparative analysis will provide valuable insights into the benefits of flexible, optimized wave farm layouts over traditional static configurations.

Furthermore, to demonstrate the applicability of the proposed algorithm, the layout optimization was performed with the aim of minimizing environmental impact. Specifically, two separate optimization scenarios were considered: one aimed at maximizing the HRA to enhance coastal protection, and the other focused on minimizing the HRA to reduce environmental disruption. These simulations highlight the algorithm's ability to efficiently explore different optimization objectives. The following subsections present the results for both the maximum and minimum HRA scenarios, along with a comparative analysis of these findings in relation to the study conducted by Clemente *et al*.

The optimization for maximizing the HRA terminated after 300 generations, while for minimizing the HRA concluded after 107 generations. Table 24 presents the GA parameters applied for Esposende case study.

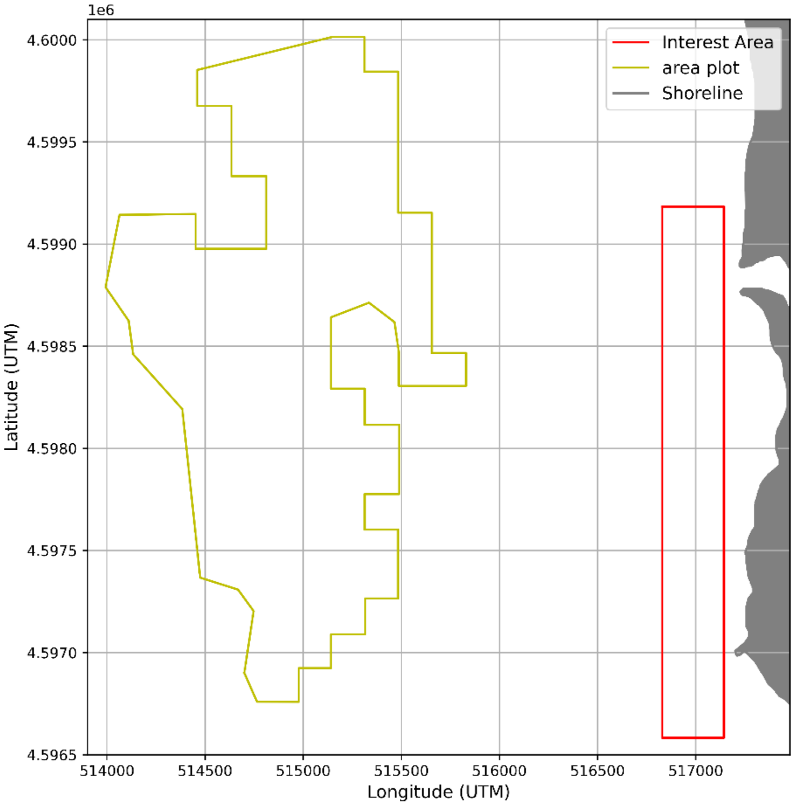

Figure 93 - Esposende deployment area and area of interest (AOI).

Table 24 – Input parameters applied in the GA for Esposende case

Parameter	Value
Initial population	200
Crossover rate	70%
Mutation rate	1%
Population size (layouts)	25
WECs per layout	150
WEC length (D)	26 m
Minimum distance between WECs	1.5 D
Elite size	3
Maximum generations	300
Maximum non–changing generations	20
Convergence tolerance	10–4

5.3.1.1. Maximizing coastal protection (maximizing HRA)

The initial population of 200 arrays provided a diverse foundation for the optimization process, while increasing the velocity of the whole process it decreased the need to simulate all 500 layouts as used for the offshore cases. During the early stages of the simulation, the GA exhibited rapid improvement in the *q-factor* and HRA parameters, with a marked increase observed within the first 30 to 40 generations.

However, after this initial phase of rapid improvement, the optimization process entered a plateau, with only marginal gains in performance achieved in the subsequent generations. Notably, the *q-factor* remained nearly constant throughout this plateau, showing minimal variation as the search space became increasingly refined. In contrast, the HRA exhibited a more challenging evolutionary trajectory, as its progression was intermittently constrained by the stability of the *q-factor*. This is evident from the peaks observed along the optimization process, where the HRA advanced in discrete steps after several generations, often pausing in smaller plateaus before achieving further improvements. These dynamics highlight the interdependence of the two metrics and the complexities of navigating trade–offs within the optimization landscape.

Figure 94 illustrates the progression of the *q-factor* and HRA metrics over the generations, showing the best layout (green line), the average values for the elite layouts (orange line), the average value for all the population (blue line) and the range of values of all population (purple shadow).

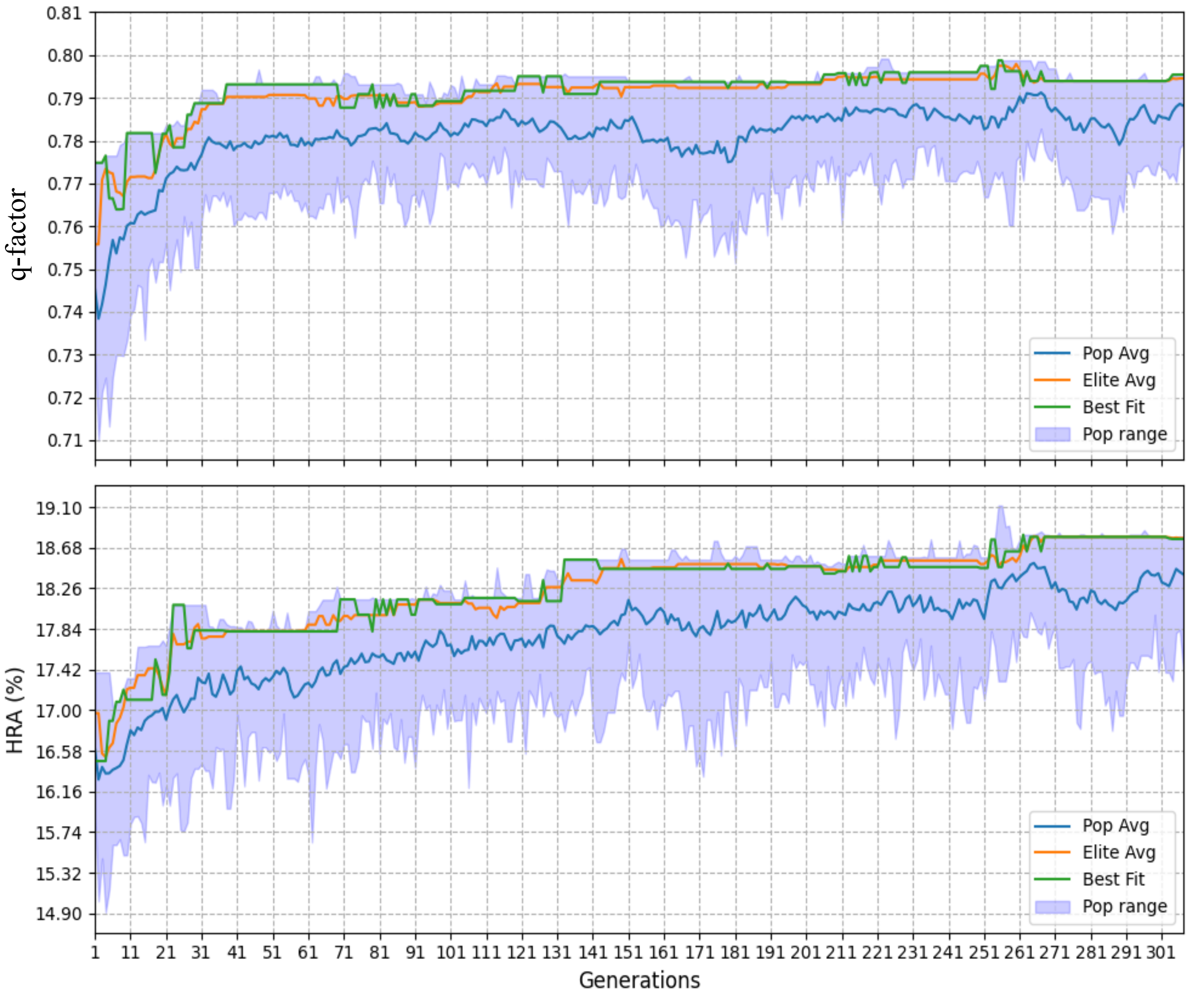

Figure 94 – Evolution of objectives throughout the generations for Esposende coastal protection case. The purple shadow represents the range of values presented in the population, the green line the best fit layout, the blue line the average of all population and the yellow line the average of elite layouts.

It is noteworthy that in multi–objective optimization, achieving a balance between competing objectives is of critical importance. This is evident from the presence of several peaks observed in both parameters, which, despite their potential, their fitness was not enough to include them in the elite layouts. This exclusion occurred because the improvements in one objective came at the expense of the other, resulting in a reduced overall fitness for those layouts. Such trade–offs underscore the challenges inherent in simultaneously optimizing multiple, often conflicting, criteria.

Figure 95 combines the *q-factor* and HRA metrics, providing insights into their simultaneous progression. The *q-factor* and HRA evolved in parallel, showing periodic oscillations that suggest the algorithm was balancing trade–offs between these two objectives. This simultaneous improvement reinforces the interdependence of the metrics and highlights the GA's ability to explore various configurations before converging on layouts with optimal performance for both parameters.

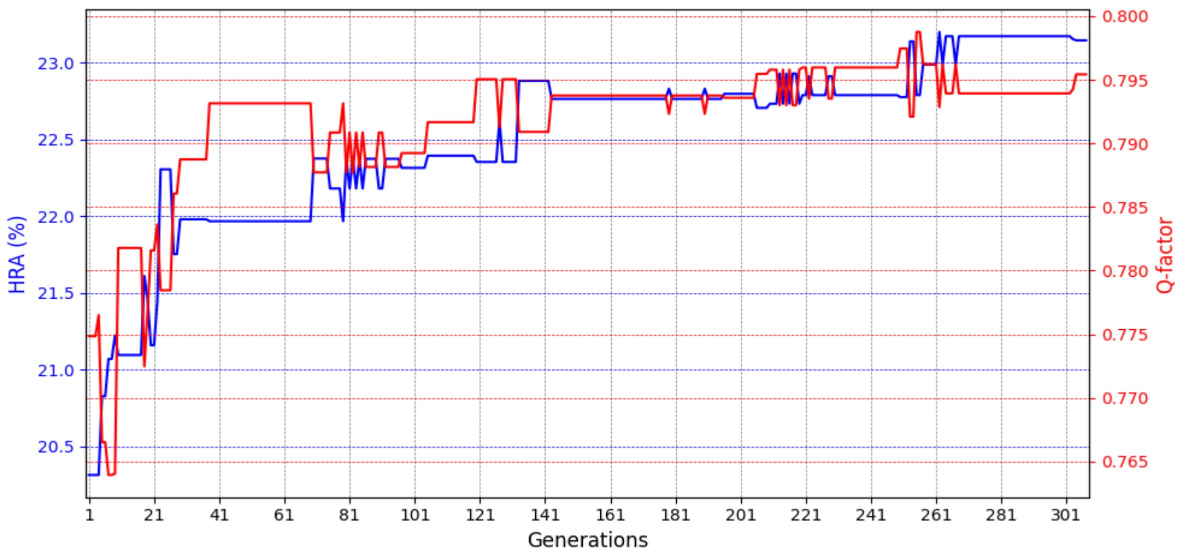

Figure 95 – Comparison of the evolution of *q-factor* and HRA for Esposende coastal protection case.

Figure 96 illustrates the evolution of metrics assessing the distribution of power within the WEC array. In the initial generations, the coefficient of variation was notably high, indicating significant disparities in power absorption among individual WECs. However, as the algorithm progressed, this metric declined, reflecting an improved uniformity in power distribution. Similarly, the Peak–to–Mean (P2M) ratio, which exhibited pronounced peaks during the early generations, diminished over time, signifying a smoother and more balanced energy output across the array.

Although the latter half of the simulation showed limited progress in improving the *q-factor* and HRA, the GA demonstrated its effectiveness in refining the smoothness of the energy production profile. This refinement is particularly evident in the P2M parameter, which highlights a reduction in the gap between peak and average power absorption. The algorithm's ability to enhance the consistency and reliability of energy output underscores its value in generating practical and efficient WEC array configurations. These results indicate that, even under challenging optimization conditions, the GA successfully balances performance metrics with operational smoothness, enhancing the overall viability of the layouts.

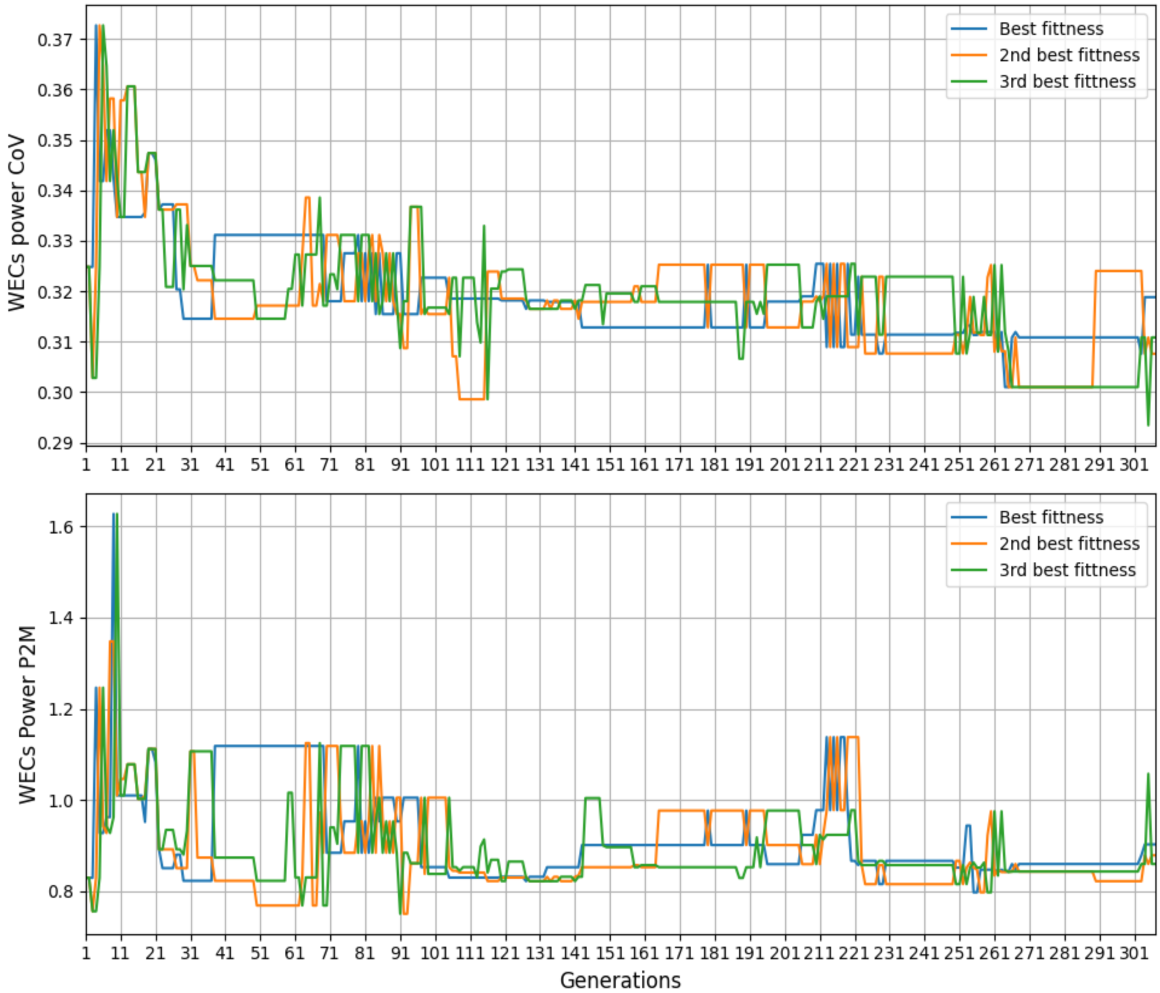

Figure 96 – Evolution of the coefficient of variation and the Peak–to–Mean (P2M) ratio for Esposende coastal protection Case.

Figure 97 illustrates the simulation area, highlighting the deployment region in yellow and the AOI in red. The zoomed–in view of the deployment area provides additional details, showing the restricted zones around each WEC, where a minimum distance must be maintained, as well as the available placement area (in yellow). This visualization demonstrates that the optimization process is not constrained by spatial limitations, as a significant portion of the deployment area remains available for WEC placement.

The layout also indicates that, while the optimization algorithm distributed the WECs effectively across the entire available area, some WECs are still positioned more isolated from others. This spatial separation contributes to a higher variation in power absorption among the WECs, reflected in the values of the smoothness parameters. These observations suggest that there is still potential for further refinement of the layout to enhance the uniformity of power distribution. Nonetheless, the algorithm has demonstrated substantial effectiveness in balancing the distribution of WECs throughout the deployment area, optimizing the use of available space while adhering to the placement constraints.

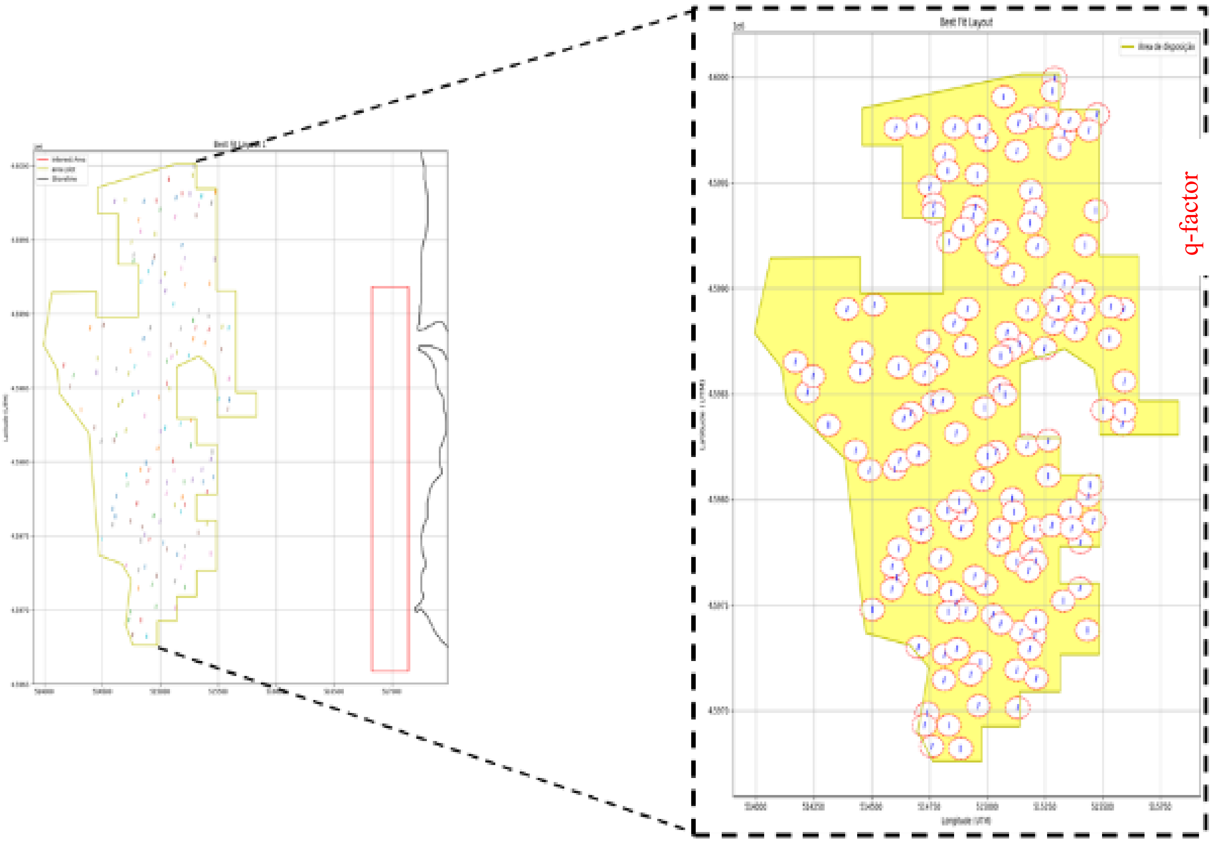

Figure 97 – Best layout configuration for Esposende coastal protection case.

The optimization process demonstrated significant improvements in key performance metrics when compared to previous studies. The best–fit layout achieved a *q-factor* of 0.79, representing a 27% increase over the results reported by Clemente *et al*. Similarly, the best–fit HRA value was about 19%, marking a notable 40% improvement relative to the outcomes of Clemente *et al*. These advancements underscore the algorithm's capacity to identify high–performing layouts under the specified optimization objectives.

5.3.1.2. Minimizing environmental impact (minimizing HRA)

Although it is well known that Esposende, particularly the Ofir breakwater area and Fão beach, faces significant challenges related to erosion and overtopping, and the optimization aiming coastal protection is the most appropriate for this case, an optimization aiming for minimum environmental impact was carried out to demonstrate the algorithm and advance scientific development. This optimization aimed to balance maximum energy production with minimal environmental impact on the coastline, simultaneously maximizing the *q-factor* and minimizing the HRA. Such a demonstration is particularly relevant for the placement of wave energy parks near biologically sensitive and protected areas.

The simulation was terminated after 107 generations, with the best–fit *q-factor* reaching 0.78, a value approximately 25% higher than that reported by Clemente *et al*. Conversely, the best–fit HRA achieved 12%, a reduction of 7% compared to the same reference study. These results indicate that the optimization process successfully balanced the dual objectives of maximizing energy efficiency and minimizing environmental impact. Figure 98 presents the evolution of objectives throughout the generations for Esposende minimal impact case.

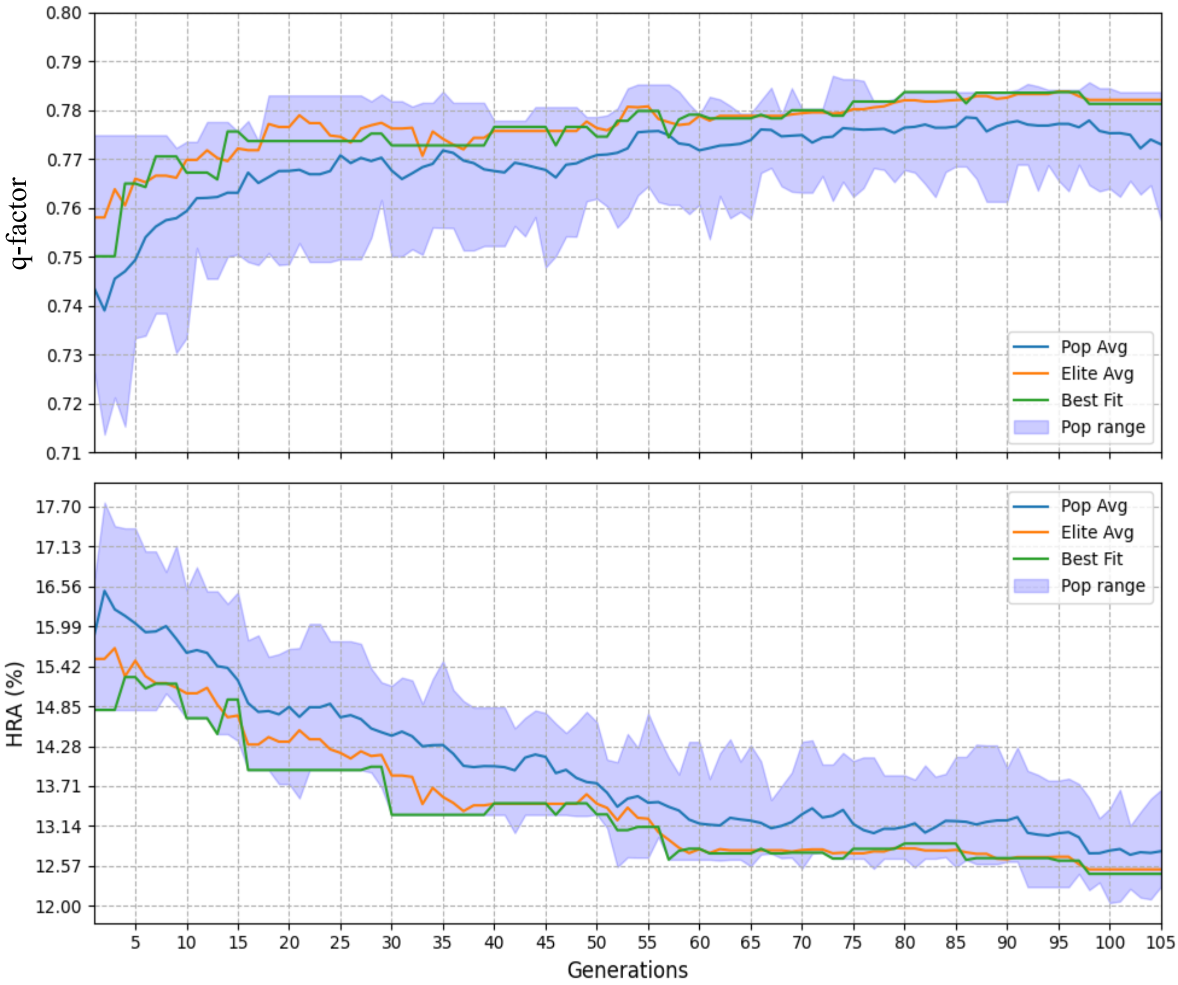

Figure 98 – Evolution of objectives throughout the generations for Esposende minimal impact case. The purple shadow represents the range of values presented in the population, the green line the best fit layout, the blue line the average of all population and the yellow line the average of elite layouts.

The algorithm exhibited a noticeable upward trend in the *q-factor* and a corresponding decline in the HRA, as could be observed in Figure 98, highlighting the ability of the GA to progressively refine solutions that meet both objectives. Notably, the best HRA results were consistently found near the lower end of the population range, contrary to what was observed when the HRA was being maximized. Additionally, the minimization of HRA exhibited greater variability and less stability compared to the maximization cases, despite the curve showing a clear tendency toward convergence. This behavior highlights the complexity of simultaneously optimizing environmental and energy production objectives.

Figure 99 illustrates the CoV and P2M metrics, with high CoV and P2M in the initial populations, and as the optimization progresses, the CoV values steadily decrease for all fitness levels, suggesting that the GA is effectively minimizing the variability in power output across the WECs. However, P2M exhibited significant variability across generations, despite converging to a low value at the end. This suggests that the Peak–to–Mean parameter may not adequately capture the smoothness of the layout distribution when one of the objectives is not aiming for maximization. Consequently, a new parameter that considers both the peak and the minimum power values within the farm could be beneficial for a more comprehensive evaluation of layout smoothness.

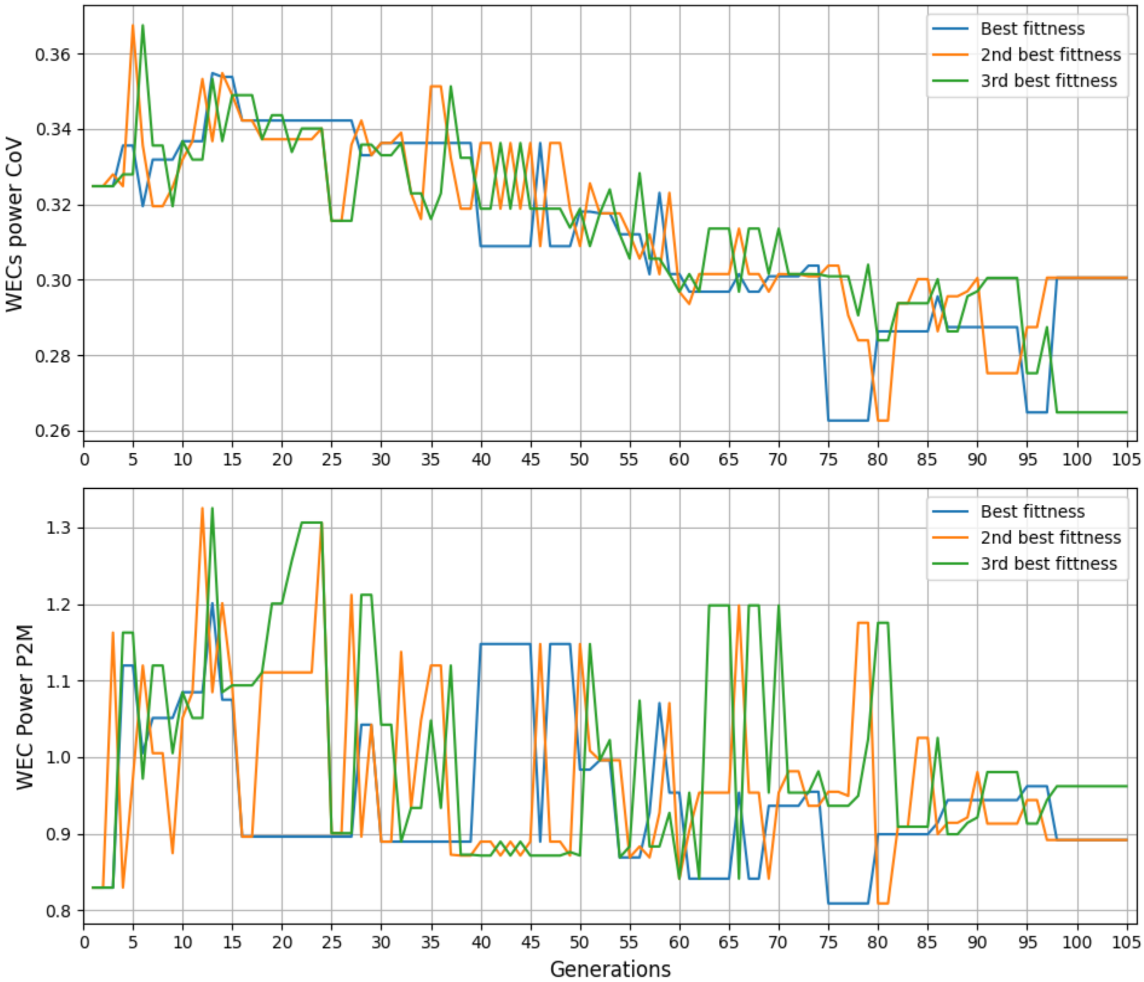

Figure 99 – Evolution of the coefficient of variation and the *Peak–to–Mean* (P2M) ratio for Esposende minimal impact case.

The lower CoV observed in this scenario compared to coastal protection scenarios demonstrates the GA's effectiveness in generating consistent and operationally stable configurations. Figure 100 illustrates the best–fit configuration, revealing a distinct shift in WEC distribution. Unlike coastal protection scenarios where WECs tend to cluster near the shoreline, the optimized layout exhibits an arrangement more distant from the east board. This is expected, as the distance between WECs is a critical parameter influencing their interaction with the wave climate. Notably, two prominent groups of WECs emerge in the north and south, likely driven by the position of the AOI and the dominant wave directions (northwest). The algorithm appears to be strategically positioning the WECs to minimize interference with the most energetic incoming waves, thereby avoiding significant impacts in the vicinity of the AOI. Given the large deployment area and the specific focus on the AOI, the algorithm efficiently distributes WECs across the available space, mitigating environmental impacts by reducing the HRA while simultaneously optimizing energy production.

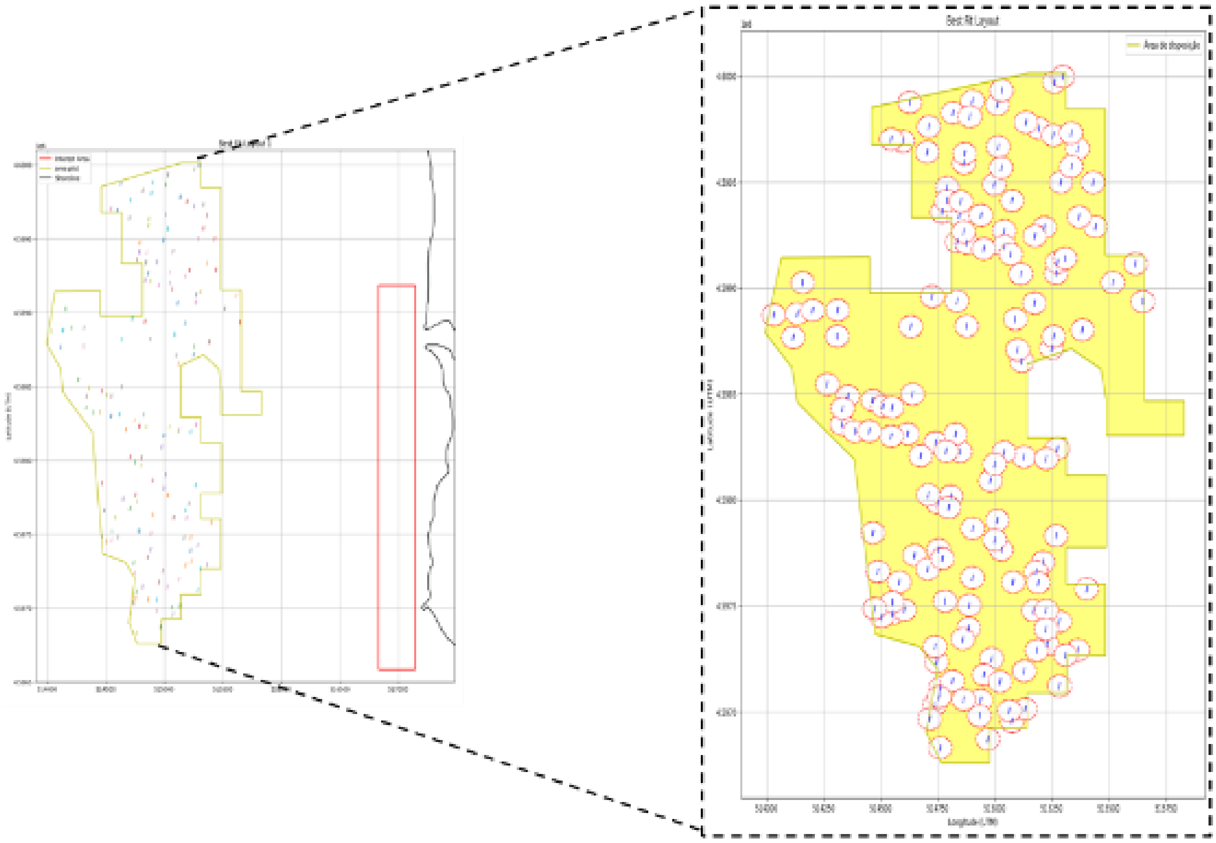

Figure 100 – Best layout configuration for Esposende minimal impact case

5.3.1.3. Comparison with previous studies

This section presents a comparative analysis of the optimized wave farm layouts with a previously published configuration proposed by Clemente *et al*. [289]. The fixed layout used in Clemente *et al*. was reproduced using the same bathymetry, grid and initial boundary conditions as the simulations of the GA optimization. The performance of each scenario is evaluated based on the HRA of the AOI, power generation, using *q-factor*, and a visual analysis of the energy flux reduction in the entire domain. The analysis aims to demonstrate the effectiveness of the GA–based optimization approach in improving wave farm performance and mitigating environmental impacts compared to a pre–defined layout. Figure 101 illustrates the spatial distribution of energy flux reduction for fixed wave farm, whereas Figure 102 and Figure 103 present the same output, but for the farm optimized for coastal protection (shield layout) farm the optimized for minimal impact (low-impact layout), respectively.

The energy flux reduction maps reveal distinct spatial patterns. The fixed scenario exhibits a concentrated area of high energy flux reduction, likely due to the fixed WEC placement. In contrast, the "shield layout" demonstrates a more widespread and extensive area of energy flux reduction, suggesting that the optimization for coastal protection has effectively increased wave energy dissipation over a larger region. The "low-impact layout", while showing a reduction in energy flux, exhibits a less pronounced and more localized impact compared to the "shield layout", as expected due to the optimization objective of minimizing shoreline impact.

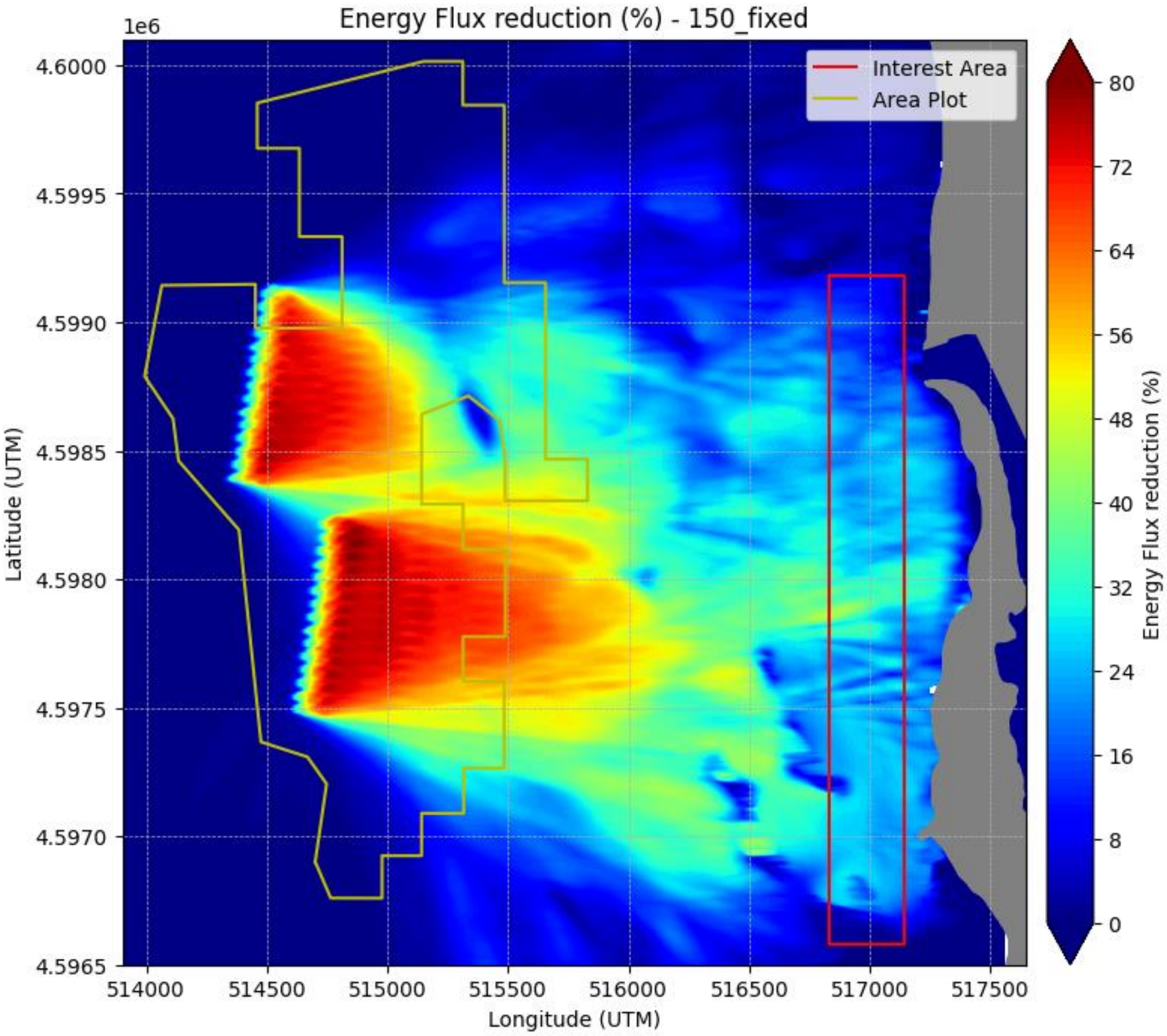

Figure 101 – Wave energy flux reduction (%) of the best wave farm (150 WEC) of Clemente *et al.* [289] **layout.**

Another benefit of the more dispersed layouts (shield and low-impact) compared to the fixed layout is that they may have a lower impact on the benthic community and sediment transport in the vicinity of the wave farm. The concentrated area of high energy reduction in the fixed layout, occurring in relatively shallow waters, can have a more significant impact on the benthic environment and sediment dynamics in that specific region. While the fixed layout may have a lower impact on sediment transport along the shoreline (which is at high risk of erosion), the more dispersed layouts may offer a better balance between energy extraction and potential environmental impacts on the seabed.

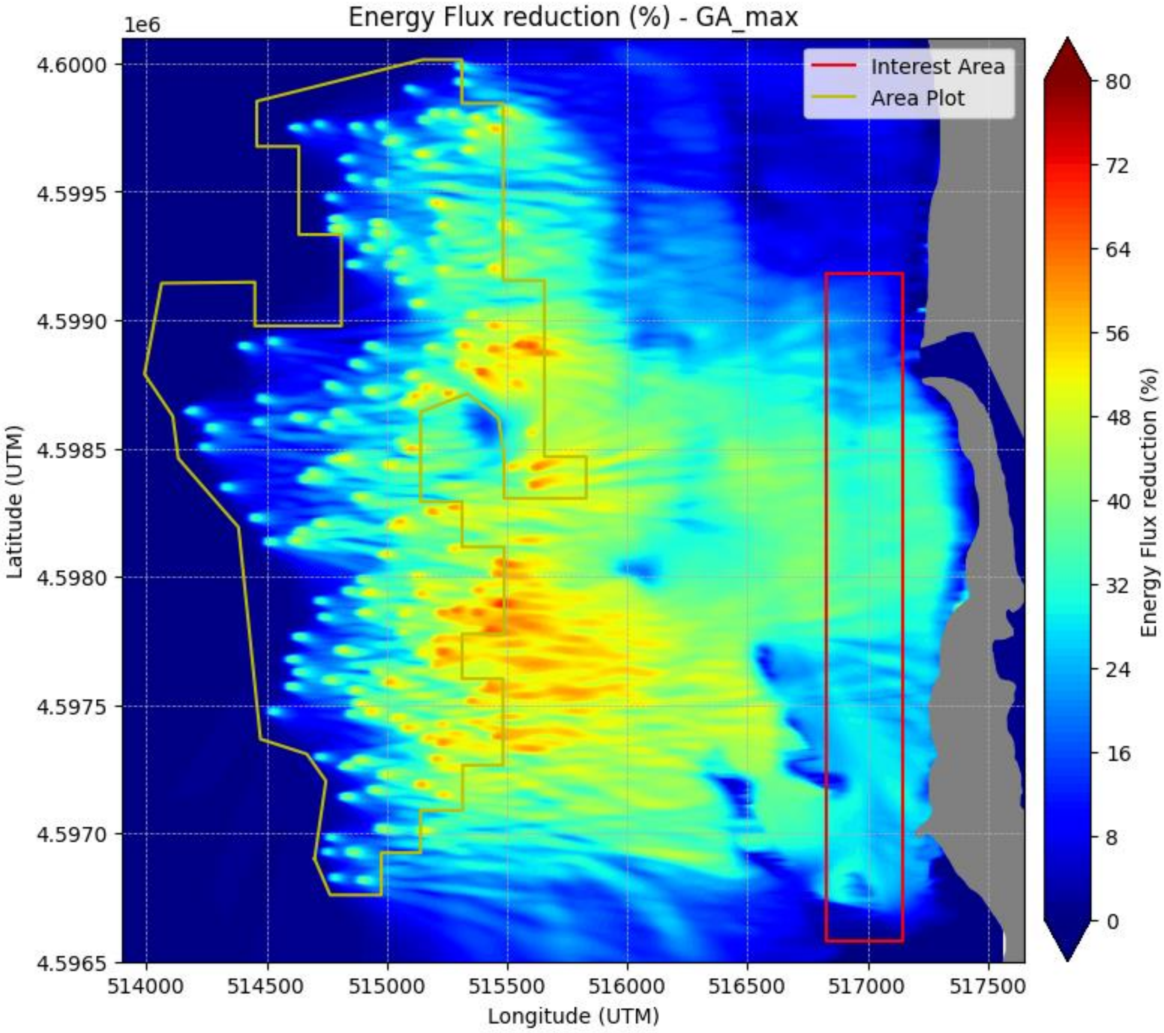

Figure 102 – Wave energy flux reduction (%) of the optimized wave farm for Esposende coastal protection case.

Table 25 summarizes the key performance metrics for each scenario. The "shield layout" exhibits a significantly higher HRA compared to the fixed one, indicating a substantial increase in wave energy dissipation. Conversely, the "low-impact layout" has a lower HRA than the fixed one, as expected, due to the optimization objective of minimizing shoreline impact. In addition, both optimized scenarios demonstrate higher power generation compared to the fixed configuration, suggesting that the optimization process has improved energy extraction efficiency. This improvement in power generation while simultaneously considering HRA demonstrates a more favorable trade–off between energy production and environmental impact in the optimized layouts.

Table 25 – Comparison of optimization objectives for fixed and optimized layouts of Esposende case.

	HRA	HRA variation	Power Absorption (MW)	*q-factor*	Power variation
Fixed	13.4%	–	38.8	0.64	–
Shield	18.8%	39.6%	48.9	0.80	25.9%
Low Impact	12.8%	–7.3%	48.1	0.78	23.6%

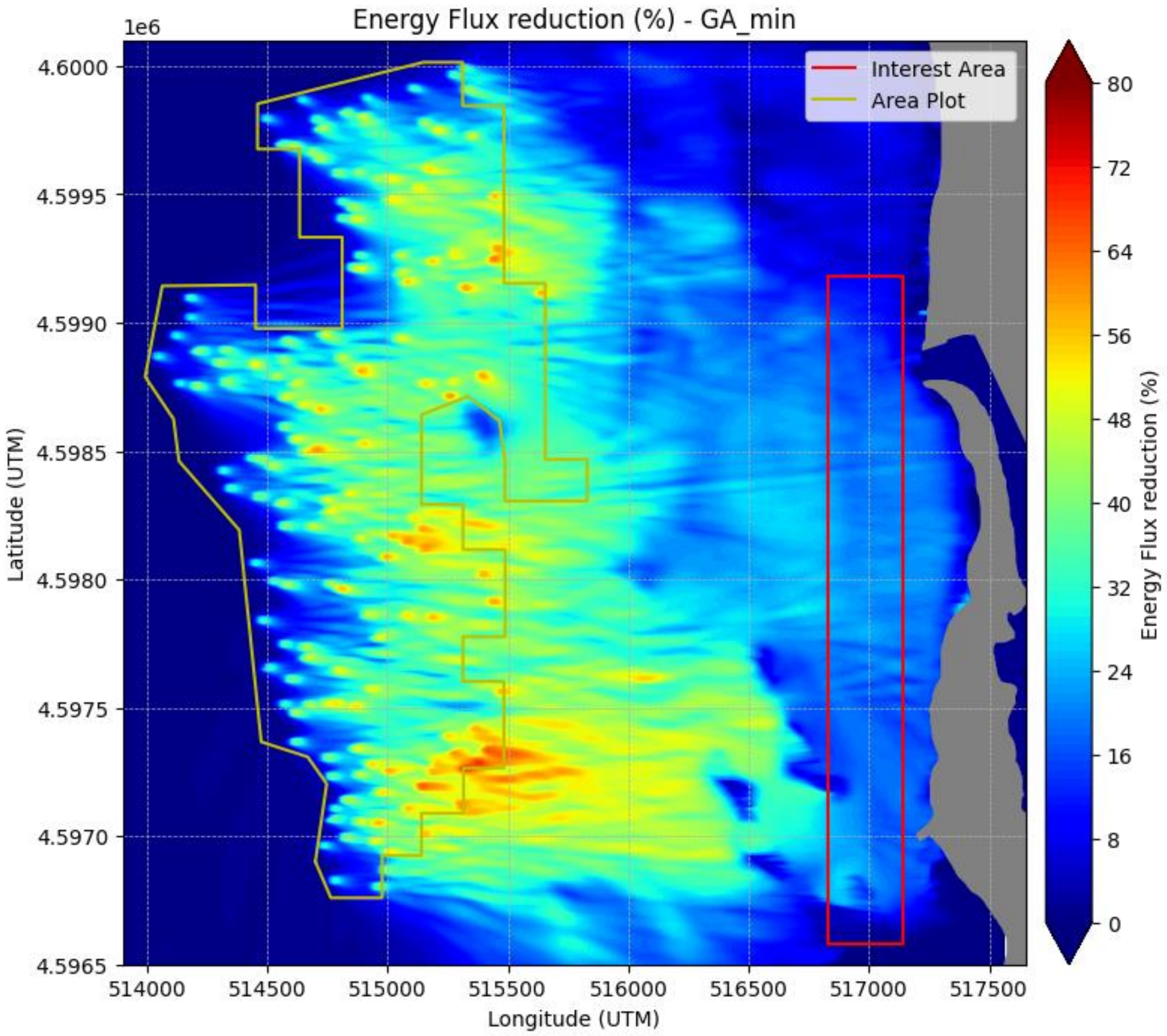

Figure 103 – Wave energy flux reduction (%) of the optimized wave farm for Esposende minimal impact case.

The results demonstrated the algorithm's efficiency in both wave impact scenarios. When applied to reduce incoming wave energy on the coast, the GA decreased wave height in the AOI by nearly 40%, while simultaneously increasing the power absorption of the farm by approximately 26% compared to a fixed layout. In the case of minimizing coastal impact, the GA reduced the impact by about 7%, while increasing power absorption in almost 24%. Visual analysis clearly highlights the distinction between the GA–optimized layouts and the fixed one; although all three configurations show significant wave energy reduction near the shoreline, the GA layouts have a smoother energy reduction, which is an advantage, as peaks of reduction could lead to a worse impact on habitats and sea life.

In conclusion, the GA–optimized configurations exhibit improved performance in terms of energy extraction, environmental impact mitigation, and the balance between these two critical factors, demonstrating the versatility of the GA approach in addressing diverse optimization objectives. These findings highlight the promise of GA–based optimization for the development of efficient and environmentally sustainable wave energy farms.

5.3.2. CASE II: Aguçadoura – Point absorber (C4 CorPower)

Aguçadoura encompasses two areas of particular interest regarding coastal flooding and erosion, situated to the north (Apúlia) and south (Ribeira da Barranha) of the designated deployment zone. Although these areas are identified as being susceptible to some level of risk in terms of flooding and erosion, they do not exhibit a high degree of vulnerability [284–288, 291,292]. As a result, the primary focus of the optimization efforts within this region is not on directly enhancing coastal protection but rather on reducing the overall environmental impact. However, to provide a more comprehensive understanding of the potential effects, simulations focused on coastal defense will also be conducted, enabling a more detailed future analysis of the site's environmental dynamics.

The Aguçadoura test site, located offshore of the northern coast of Portugal, is a pivotal location for testing marine renewable energy technologies, particularly WECs. This site has played an integral role in the development and demonstration of various ocean–based energy solutions. Notably, Aguçadoura features a 3MW export cable for grid connection, which facilitates the testing of wave energy devices at both full scale and reduced scale. The infrastructure at Aguçadoura supports the evaluation of innovative technologies in a real–world marine environment, advancing the understanding of their performance and operational viability.

Although no large–scale WEC farm is currently planned for deployment at Aguçadoura, the testing of devices such as the CorPower units and the associated studies generated through the SAFE WAVE project provide valuable insights into the site's potential. As a consequence of these ongoing studies, the application of the proposed optimization algorithm to this area will serve as a demonstration of its usability for larger, generic longshore areas. This approach offers a general framework for assessing the environmental aspects of wave energy conversion, with a particular focus on the objectives related to minimizing environmental disruption while maximizing efficiency. The insights gained from this case study will contribute to refining the algorithm's application across diverse coastal environments, furthering the understanding of its potential for environmental optimization in marine renewable energy projects.

The simulations conducted in this study utilized the 10 MW and 30 MW configurations designed by CorPower, arranged in an "X" formation with a central hub of 28 WECs per layout. These configurations were selected to facilitate comparison with the study carried out by Santiago *et al*. [290], which analyzed different sea states using a smaller AOI. To extend the analysis, the AOI in this study was expanded further south, encompassing regions not included in Santiago *et al*.'s work [290]. Consequently, new simulations replicating their methodology were performed to establish a baseline for comparison and assess the efficiency of the proposed dynamic layouts relative to conventional "Fixed X" configurations. This approach ensured a comprehensive evaluation of both studies under comparable conditions.

Additionally, simulations were conducted to evaluate the optimization of the layout for both maximum and minimum HRA (significant wave height reduction) with the 10 MW and 30 MW configurations. Initially, these simulations used a large, simple AOI. However, due to the complexity of implementing the minimum HRA objective in areas far from the deployment zone, a new approach was developed. This method involved contouring the AOI around the deployment zone in a "U" shape, allowing for a more practical and efficient simulation of the minimum HRA optimization. This approach was particularly beneficial for addressing the environmental impact in regions distant from the deployment zone, where wave energy interaction is less significant.

In summary, this study not only compares the effectiveness of different layout configurations but also introduces a new method for optimizing the environmental impact, thus enhancing the applicability of the algorithm to large coastal areas. Table 26 presents the GA parameters applied for Esposende.

Table 26 – Input parameters applied in the GA for Aguçadoura case.

Parameter	Value
Initial population	200
Crossover rate	70%
Mutation rate	1%
Population size (layouts)	25
WECs per layout	28/84
WEC length (D)	9 m
Minimum distance between WECs	16.67 D
Elite size	3
Maximum generations	300
Maximum non–changing generations	20
Convergence tolerance	10^{-4}

5.3.2.1. Maximizing coastal protection (maximizing HRA)

For the Aguçadoura case study, two wave farm configurations were considered, as previously proposed by Santiago *et al*. [290]: a 10 MW farm with 28 WECs and a 30 MW farm with 84 WECs. Both configurations were simulated to evaluate their performance and impact. Given that the region includes a coastal hazard risk area spanning the shoreline, the AOI could have been divided into multiple target areas or defined as a single large AOI encompassing all regions. However, due to the significant distance between the test site and the shoreline, smaller, localized AOIs near the coast would fail to accurately represent the variation in HRA, limiting their impact on the optimization process.

To address this challenge, a general AOI was chosen for the simulations. This AOI was strategically positioned approximately midway between the test site and the shoreline, ensuring it was extensive enough to encompass all simulated wave directions incident on the test site. This setup is illustrated in

Figure 104, demonstrating how the AOI was designed to adequately capture the key dynamics relevant to the optimization process.

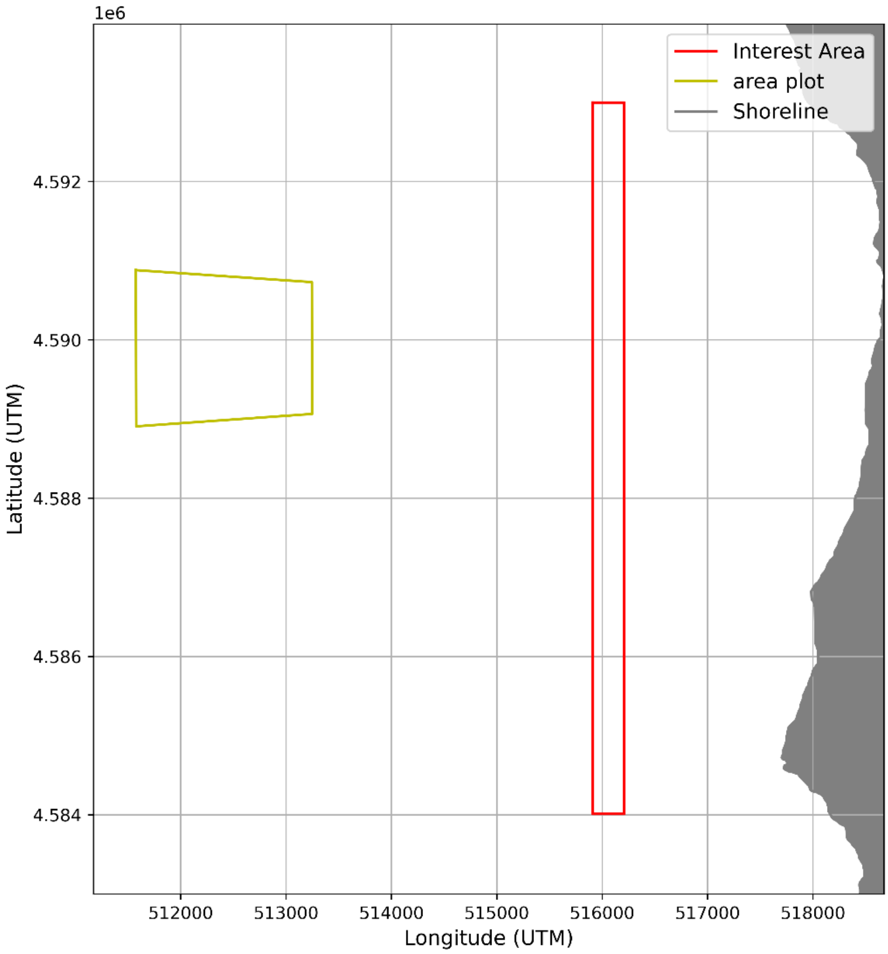

Figure 104 - Aguçadoura deployment area and single general area of interest.

Figure 105 and Figure 106 depict the progression of the *q-factor* and HRA for the 10 MW and 30 MW wave farms, respectively, across generations. These figures present the best layout (green line), the average values of the elite layouts (orange line), the average value for the entire population (blue line), and the range of population values (purple shadow). Compared to other case studies, such as the offshore co–located farm and the Esposende case studies, the evolution curves for the Aguçadoura simulations exhibited smoother behavior, with fewer abrupt peaks and troughs, and faster convergence. Specifically, convergence was achieved after only 70 generations in the coastal protection scenario and 103 generations in the minimal impact scenario.

This rapid convergence can be attributed to the quick rise in the objectives, particularly the *q-factor*, which surpassed the threshold value of 1 early in the process. For the 10 MW farm, this threshold was exceeded even within the initial population. The results indicate that the algorithm efficiently identified promising solutions early on, streamlining the optimization process and reducing the number of iterations required.

The unique characteristics of the AOI in this case also played a role in shaping the results. As the AOI is located at a considerable distance from the deployment area, the HRA values were inherently lower, reducing their order of magnitude from 10^1 to 10^0. This lower scale minimized the impact of HRA on the optimization process, particularly since the tolerance for convergence was set at 10^{-4}. While this setup effectively facilitated convergence, the tolerance can be adjusted as needed to align with stakeholder requirements.

Furthermore, the use of a large AOI influenced the computed HRA values. As the HRA is an index averaging the reduction in wave height across the entire AOI, the large area diluted the influence of the wave farm. For many wave directions, the wave farm's impact was not uniformly felt across the entire AOI, meaning the regions significantly affected by the farm represented only a small percentage of the total area. This effect reduced the overall HRA values, demonstrating how the spatial scale and positioning of the AOI can influence optimization outcomes.

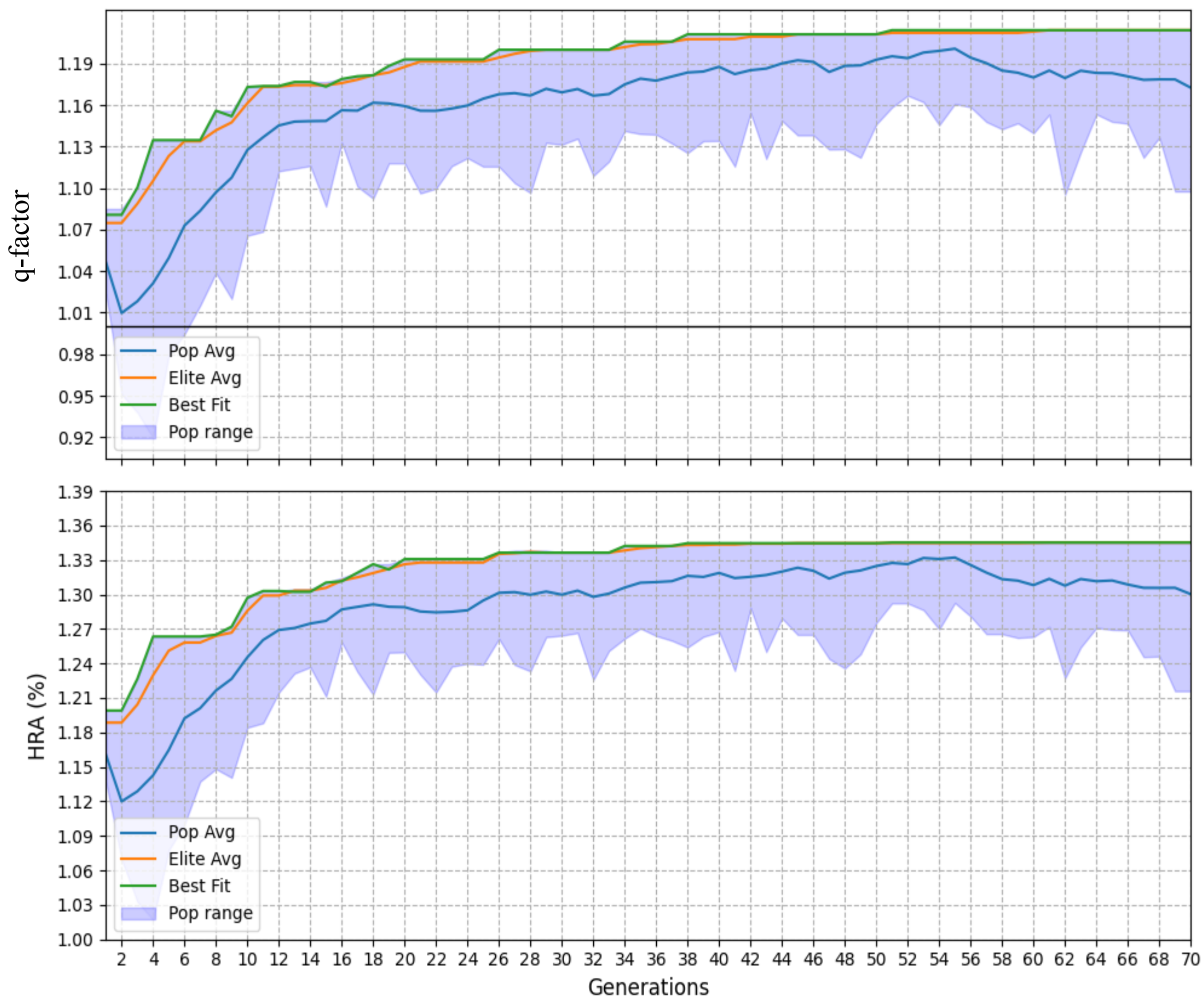

Figure 105 – Evolution of optimization objectives (*q-factor* and HRA) over generations for the 10 MW farm in the Aguçadoura coastal protection case. The purple shadow represents the range of values presented in the population, the green line the best fit layout, the blue line the average of all population and the yellow line the average of elite layouts.

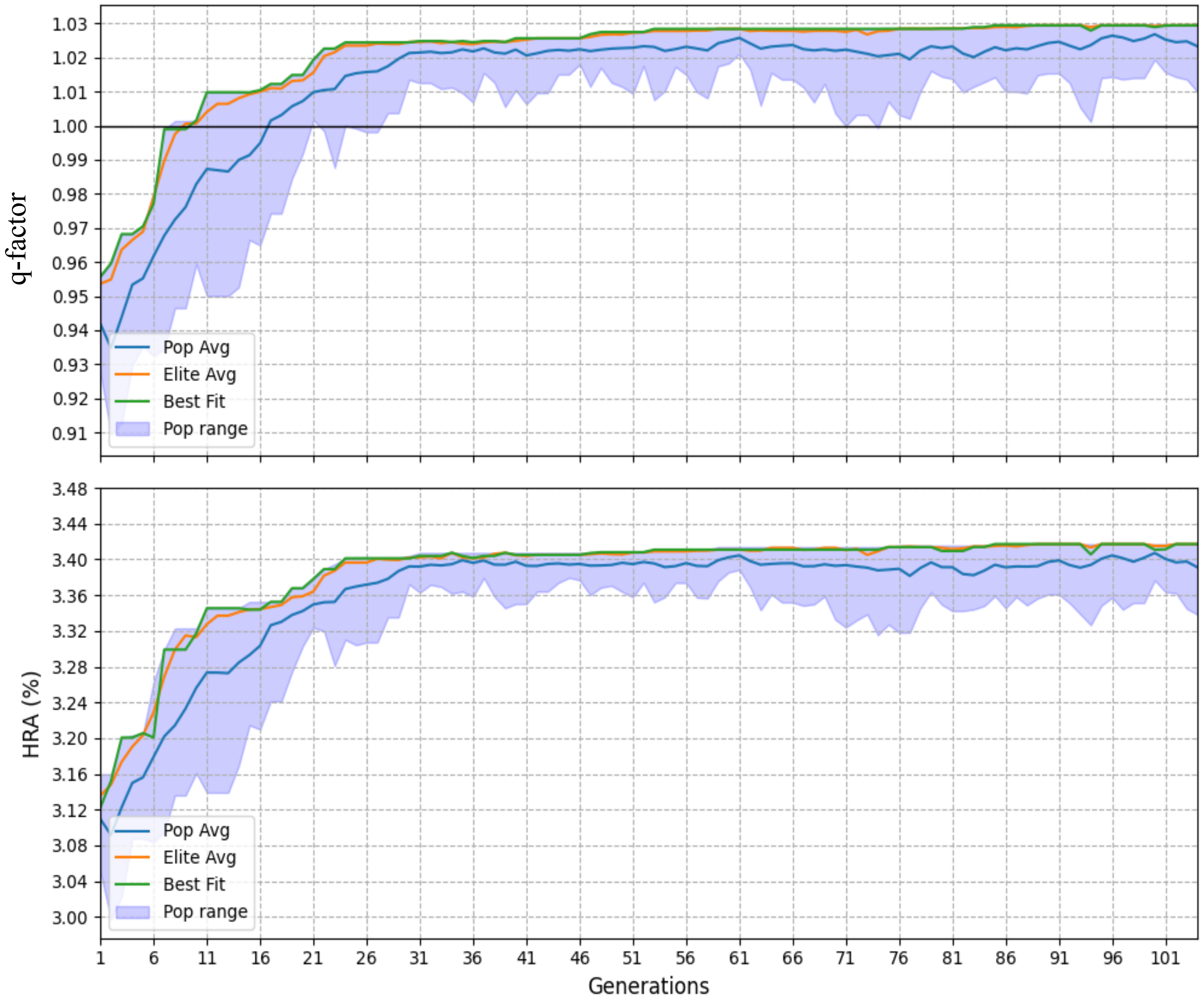

Figure 106 – Evolution of optimization objectives (*q-factor* and HRA) over generations for the 30 MW farm in the Aguçadoura coastal protection case. The purple shadow represents the range of values presented in the population, the green line the best fit layout, the blue line the average of all population and the yellow line the average of elite layouts.

The *q-factor* values were relatively high, with the best 10 MW layout exhibiting an average absorbed power approximately 21% higher than that of a single WEC. A potential explanation lies in the methodology employed to estimate the power output of one WEC. Specifically, this value was derived from the average of 1,000 simulations, wherein a single WEC was randomly positioned within the deployment area. This approach inherently introduces variability owing to the influence of local bathymetry, which alters wave conditions and, consequently, the available energy. Moreover, the position of the WEC and the relative dimensions within the computational grid further influence the absorbed power output, contributing to the observed performance differences.

Figure 107 and Figure 108 illustrate the progression of the distribution parameters "WEC Power CoV" and P2M for the elite layouts of the 10 MW and 30 MW farms, respectively. Additionally, Figure 109 and Figure 110 present the best–fit layouts for each farm. Interestingly, both parameters in both cases exhibited lower values in the initial population, followed by a rise during the early stages of optimization, and eventually stabilized as the generations progressed. This behavior can be attributed to the relatively small deployment area, where the top three arrays among the 200 randomly generated initial layouts featured WECs dispersed across the entire area, leading to very low CoV and P2M values. However, as the optimization process repositioned the WECs to enhance the HRA and *q-factor*, these parameters adjusted to more balanced values.

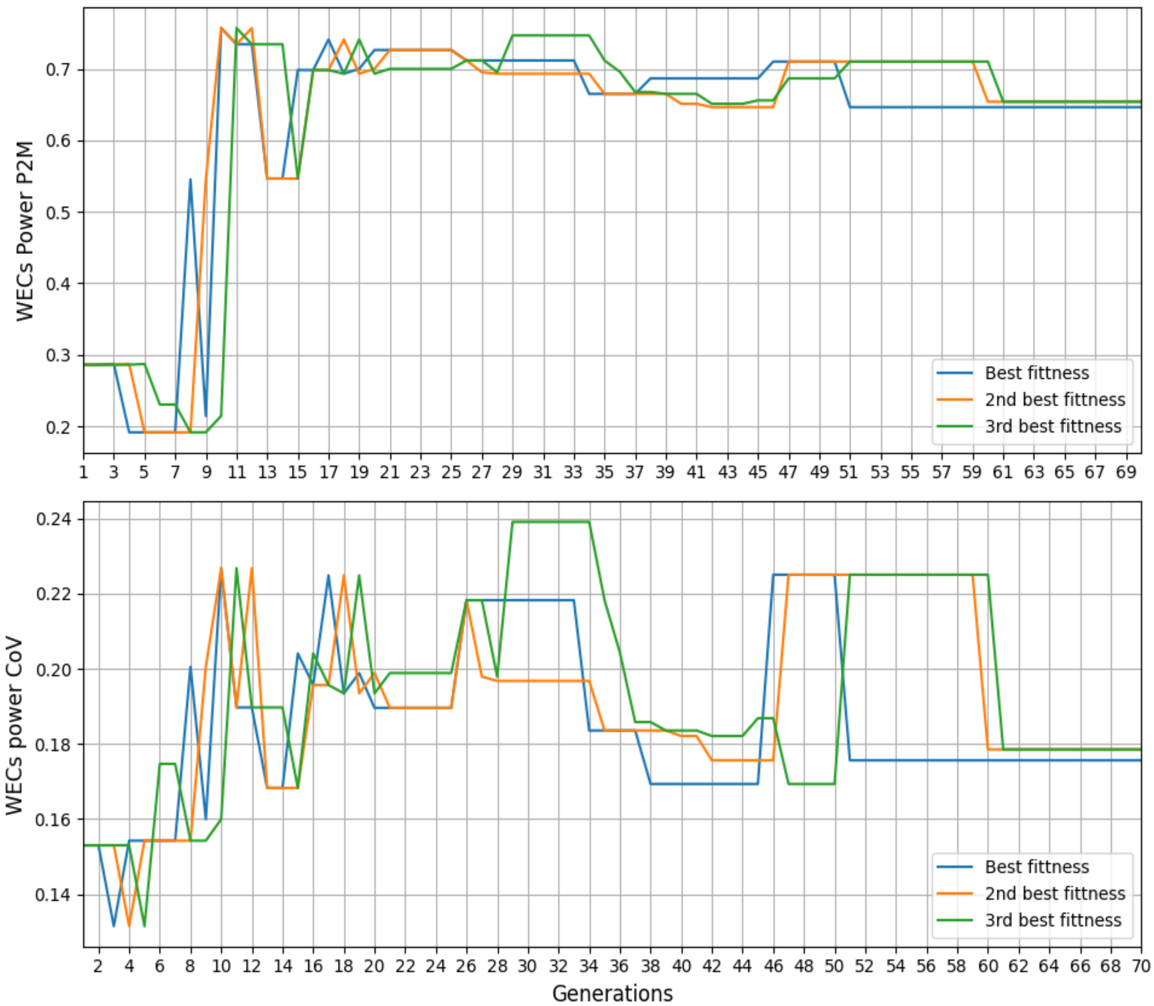

Figure 107 – Evolution of the coefficient of variation and the *Peak–to–Mean* (P2M) ratio for the 10 MW farm in the Aguçadoura coastal protection case.

Despite the initial rise, the final results show that the Aguçadoura case outperformed the Esposende case in terms of CoV and P2M. The 10 MW farm achieved a CoV lower than 0.2 and a P2M lower than 0.7, while the 30 MW farm achieved a CoV lower than 0.25 and a P2M below 1. These lower P2M values suggest that the genetic algorithm optimized the layouts into well–distributed arrays with minimal variations in power absorption among WECs. This indicates an effective balance between energy production and layout uniformity.

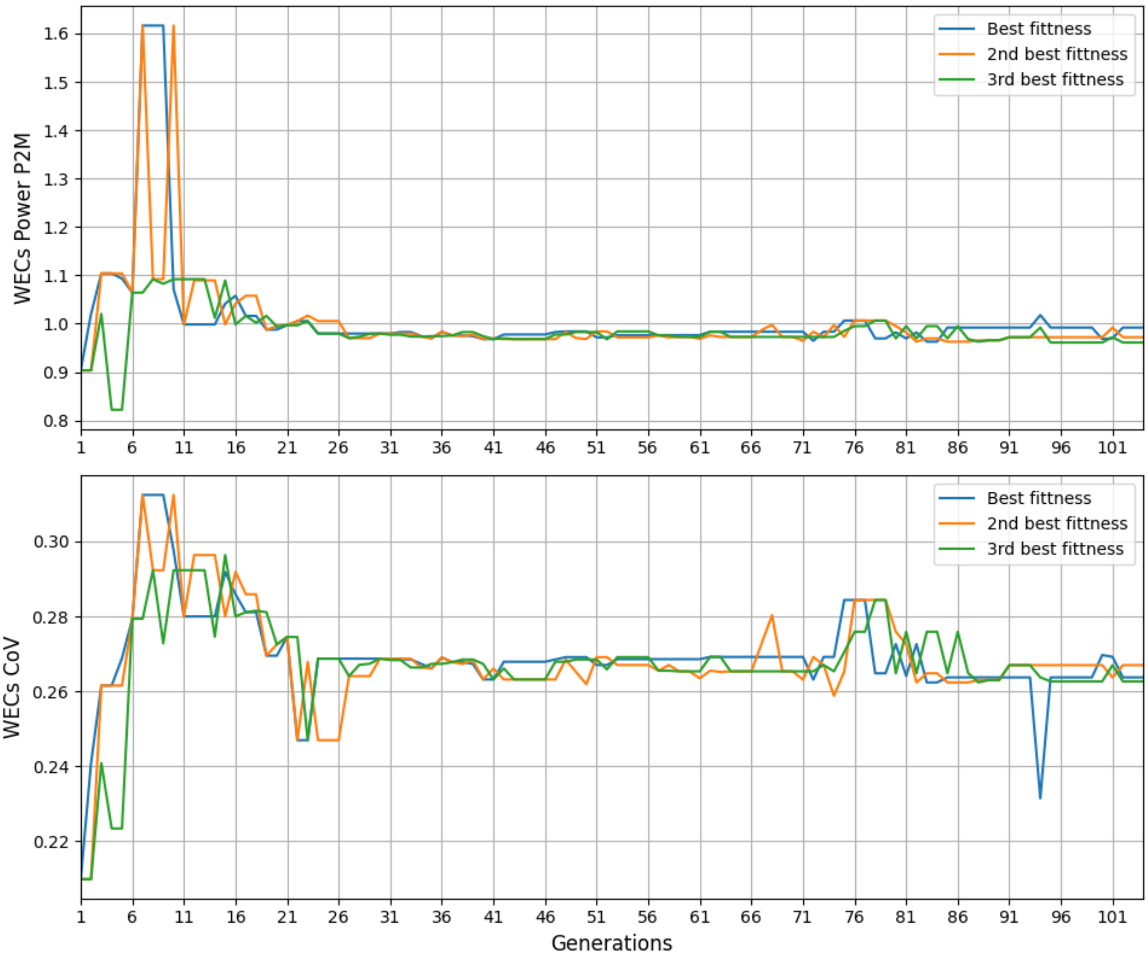

Figure 108 – Evolution of the coefficient of variation and the *Peak–to–Mean* (P2M) ratio for the 30 MW farm in the Aguçadoura coastal protection case.

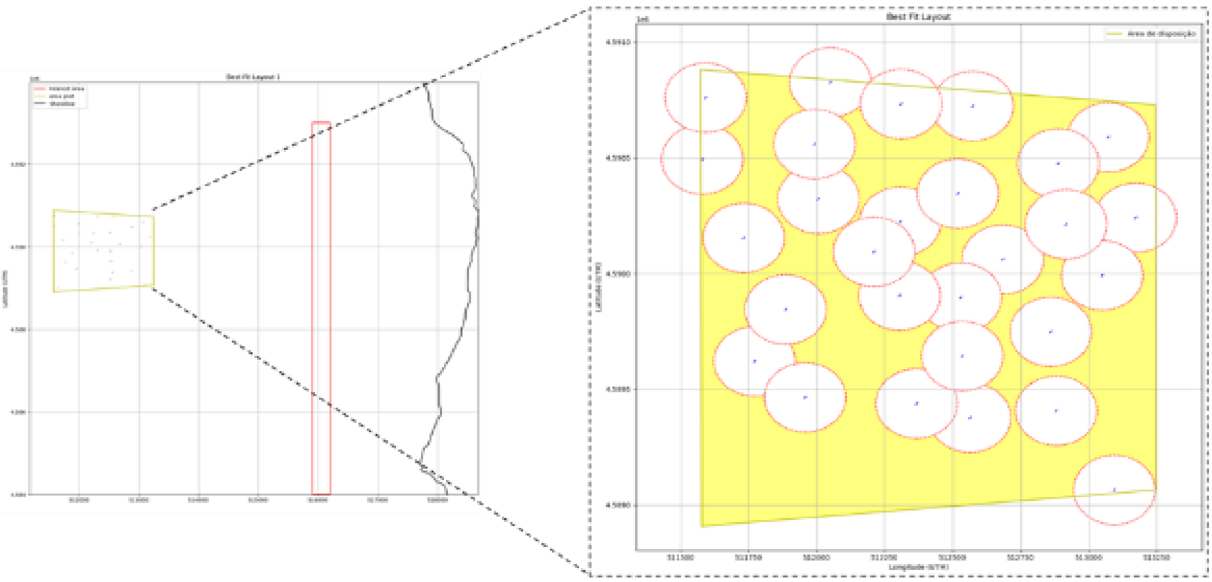

Figure 109 – Best layout configuration for the 10 MW farm in the Aguçadoura coastal protection case.

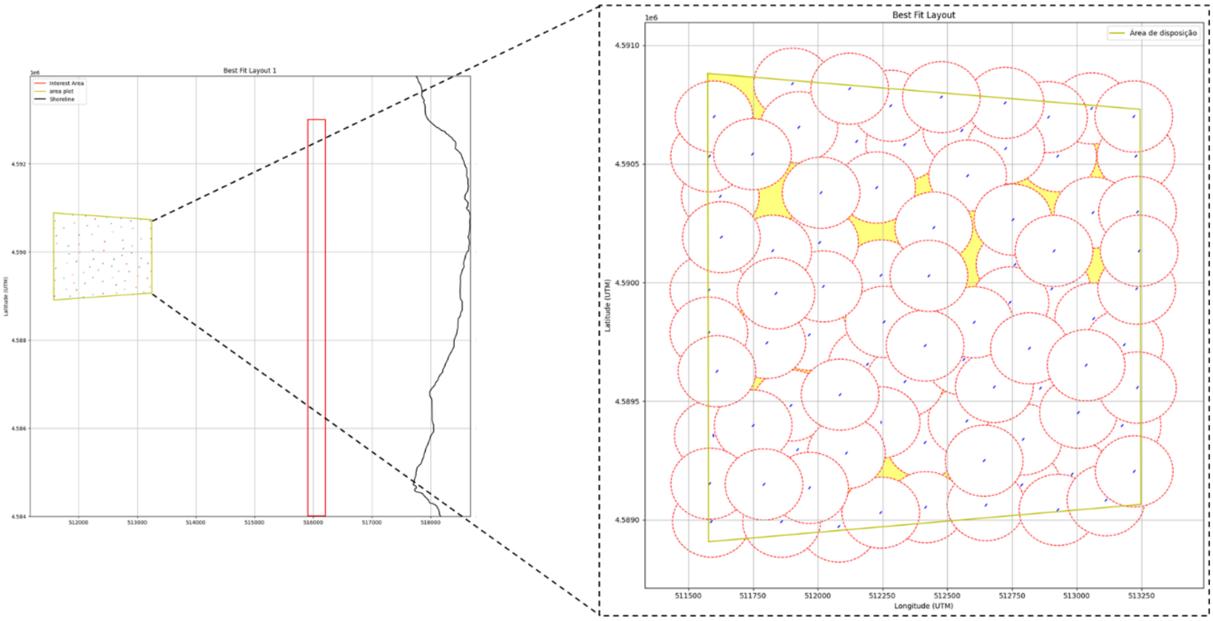

Figure 110 – Best layout configuration for the 30 MW farm in the Aguçadoura coastal protection case.

However, the results for the 30 MW farm were generally less favorable due to the constraints of the small deployment area. Figure 110 clearly illustrates the lack of free space (indicated by yellow regions) for placing additional WECs, leading to tightly packed arrays. This density had a direct impact on performance: while the 10 MW farm achieved a *q-factor* of 1.21, the 30 MW farm reached only 1.03. The easternmost WECs (downstream) in the 30 MW farm experienced significant interference from upstream WECs, further reducing performance. This interference also influenced P2M values, as power absorption became less uniform.

Moreover, the limited space significantly affected environmental impact metrics. The 30 MW farm, with a *q-factor* approximately 15% lower than the 10 MW farm, exhibited an HRA increase of about 153%, rising from 1.35% to 3.42%. The smaller deployment area and higher WEC density amplified the influence of the farm on the surrounding wave field, resulting in greater wave height reductions across the AOI.

The constrained deployment area also contributed to the rapid convergence of the optimization process. With limited space, a high number of WECs, and minimal spacing between them, the search space for the genetic algorithm was effectively reduced, allowing it to identify optimized solutions in fewer generations. This highlights the interplay between deployment area size, WEC density, and the efficiency of the optimization process in achieving balanced layouts.

5.3.2.2. Minimizing environmental impacts (minimizing HRA)

Minimizing the HRA in wave farm design presents a unique set of challenges. Unlike maximizing HRA, where simply concentrating wave energy dissipation within a defined area can achieve the objective, minimizing HRA requires a more nuanced approach. When dealing with a small AOI, minimizing HRA can be relatively straightforward by strategically placing WECs to avoid impacting the specific target area. However, for larger AOIs or when considering the shoreline as a whole, this approach can be less effective. Simply aiming to avoid impact within the delimited AOI may inadvertently shift the impact to areas outside the defined boundary, leading to unintended consequences. The following subsections present the results obtained using different AOI configurations: first, employing a general single AOI for the 10 MW farm, and then introducing a novel "U–form" AOI surrounding the wave farm for both 10 and 30 MW farm deployments.

5.3.2.2.1. General AOI – Single longshore area

This subsection presents the results of the optimization process aimed at maximizing power production while minimizing environmental impact, using the general AOI, previously applied in the coastal protection case. Figure 111 illustrates the evolution of the objective functions, the *q-factor*, and HRA.

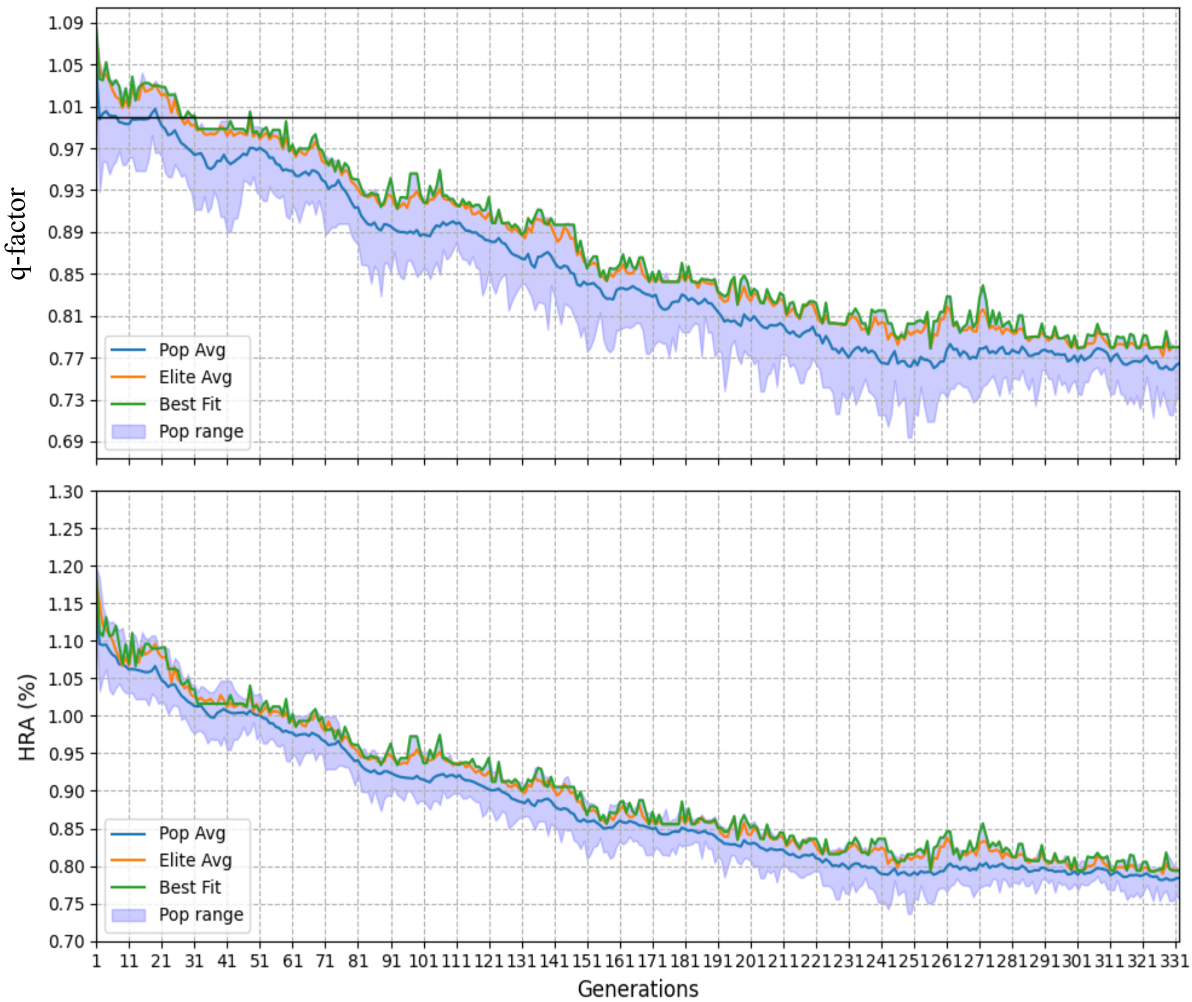

Figure 111 – Evolution of optimization objectives (*q-factor* and HRA) over generations for the 10 MW farm in the Aguçadoura minimal impact case using a general single AOI. The purple shadow represents the range of values presented in the population, the green line the best fit layout, the blue line the average of all population and the yellow line the average of elite layouts.

The optimization exhibited unexpected behavior, with both objectives demonstrating a continuous decrease. This undesirable trend can be attributed to several factors, including the significant distance from the deployment area, the potential to avoid the AOI entirely, and the availability of considerable free space within the deployment area for WEC placement. These factors likely contributed to the observed behavior.

Consequently, the layouts evolved towards an agglomeration in the southern portion of the area, presumably to avoid the defined AOI, as evidenced in Figure 112. This agglomeration resulted in a decrease in both HRA and the *q-factor*, indicating a suboptimal solution. Furthermore, the CoV and P2M values increased, suggesting an uneven distribution of power production due to the concentration of WECs in the lower left corner while others remain sparsely distributed.

These results highlight the limitations of using a single, longshore–oriented AOI for this specific scenario. This approach did not effectively prevent the displacement of the impact caused by the wave farm to adjacent regions, failing to achieve an optimal balance between power production and environmental impact. Therefore, an alternative definition of the AOI is required to address these limitations and guide the optimization process towards more desirable solutions.

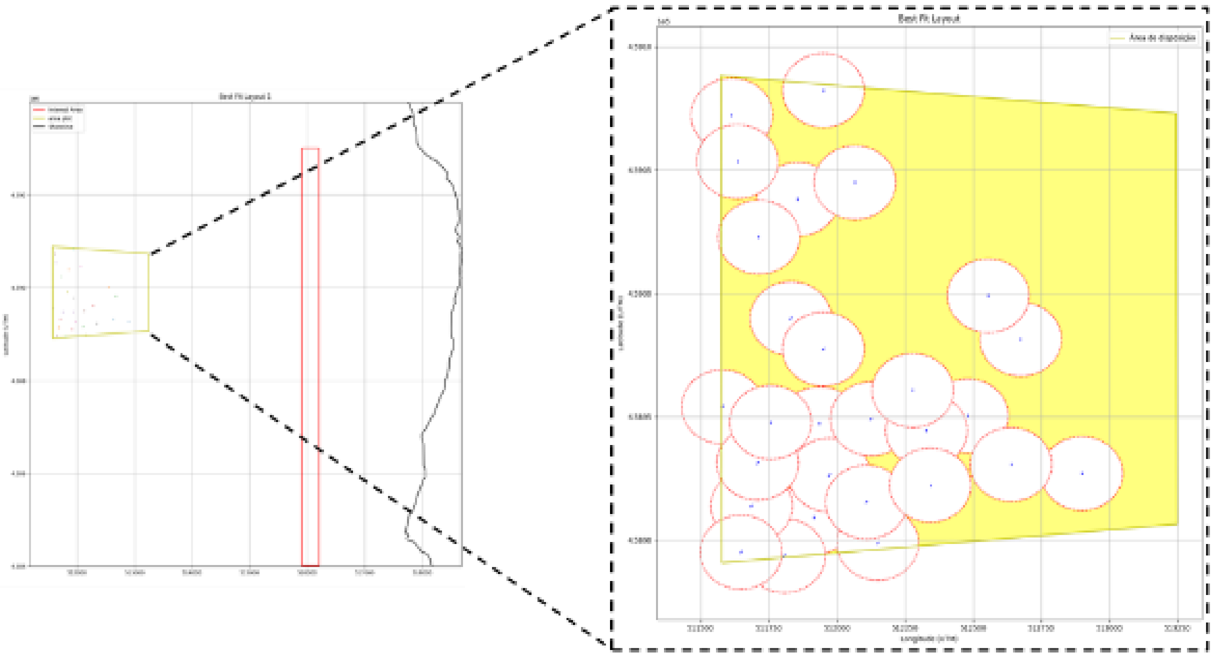

Figure 112 – Best layout configuration for the 10 MW farm in the Aguçadoura minimal impact case using general AOI.

5.3.2.2.2. U–form AOI – Triple area around the wave farm

To achieve the objective of maximizing the *q-factor* while minimizing the HRA for a broad general area distant from the coastline, a U–form AOI was proposed, as illustrated in Figure 113. This configuration was specifically designed to encompass all leeward interference of the wave farm on the wave climate, maintaining a distance of 1 km from the deployment zone.

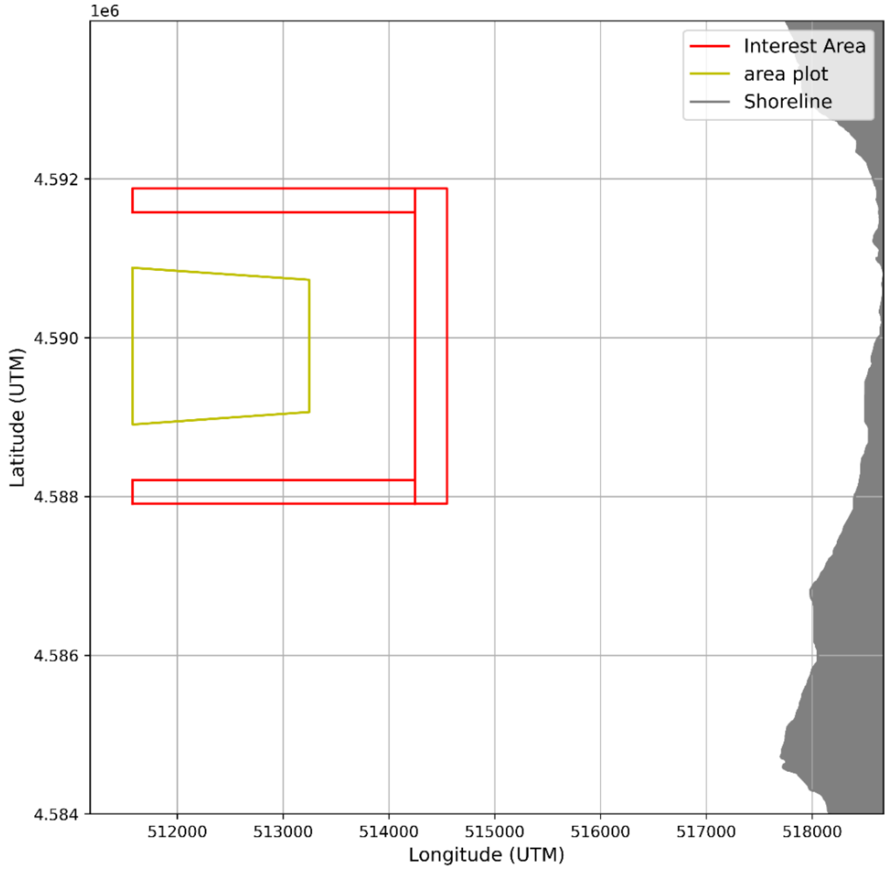

Figure 113 - Aguçadoura deployment area and U-form area of interest (AOI).

As in previous cases, Figure 114 and Figure 115 depict the evolution of the *q-factor* and HRA for the 10 MW and 30 MW wave farms, respectively. In both scenarios, the new AOI demonstrated its effectiveness in guiding the optimization algorithm to achieve a balanced compromise between the objectives.

The simulation for the 10 MW wave farm concluded after 75 generations, while the 30 MW wave farm required 117 generations. Both simulations exhibited rapid improvement in the *q-factor* during the initial generations, stabilizing at near–optimal values with minor fluctuations in subsequent generations. Conversely, the HRA displayed an opposing trend, as expected.

However, an analysis of the population range revealed distinct evolutionary patterns between the two simulations. The 10 MW wave farm exhibited greater variability and a wider range of possibilities, while the 30 MW wave farm converged towards a narrower population range. This difference can be attributed to the spatial constraints of the deployment area, which are significantly more restrictive for the larger 30 MW farm.

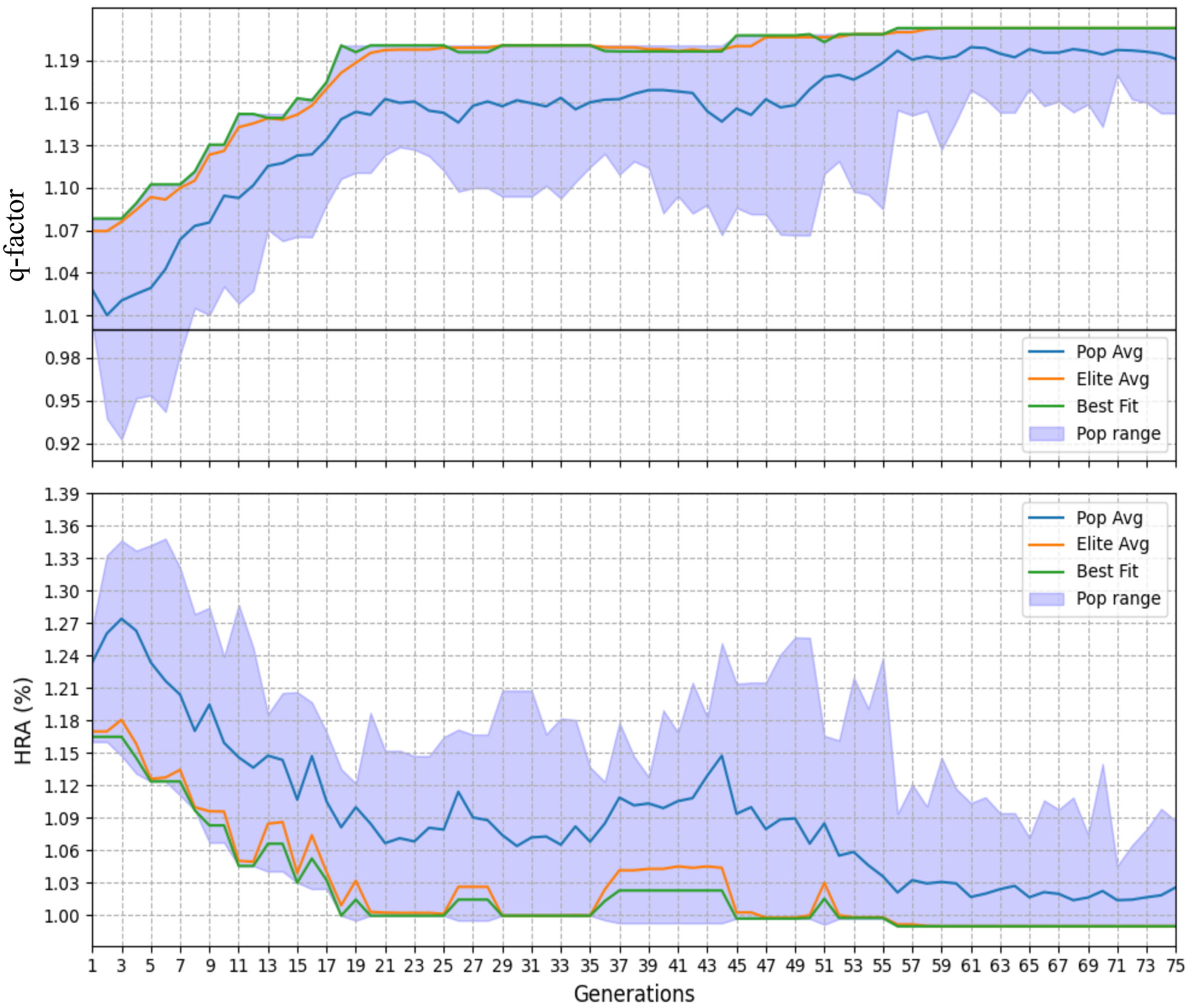

Figure 114 – Evolution of optimization objectives (*q-factor* and HRA) over generations for the 10 MW farm in the Aguçadoura minimal impact case using the U–form AOI. The purple shadow represents the range of values presented in the population, the green line the best fit layout, the blue line the average of all population and the yellow line the average of elite layouts.

Examining the coefficient of variation (CoV) and P2M metrics, presented in Figure 116 and Figure 117, it is evident that these values did not exhibit substantial improvement during the simulations. For the 10 MW farm, this was primarily because these metrics were already low at the outset. Notably, P2M reached a value below 0.5, indicating that the most power–absorbing WECs did not absorb more than 50% of the average power absorbed by all WECs in the park. Due to the small number of WECs, both metrics reflected good results, ensuring smoothness in the park's configuration. Conversely, for the 30 MW farm, the densely packed configuration of WECs resulted in a reduced average power absorption compared to the highest–performing WECs located along the westernmost boundary.

As observed in previous studies, the *q-factor* and HRA exhibited opposing trends: while maximizing separation increased power absorption, it simultaneously decreased the downstream impact on wave height. Consequently, the WLA assumed a high correlation between maximizing the *q-factor* and minimizing HRA. Additionally, similar to the Esposende case, the 10 MW farm converged to comparable *q-factor* values of 1.214 for shield protection and 1.212 for low–impact layouts. However, the HRA displayed some variability, with values of 1.35% for shield protection and 0.99% for the low–impact layout, a difference of approximately 27%.

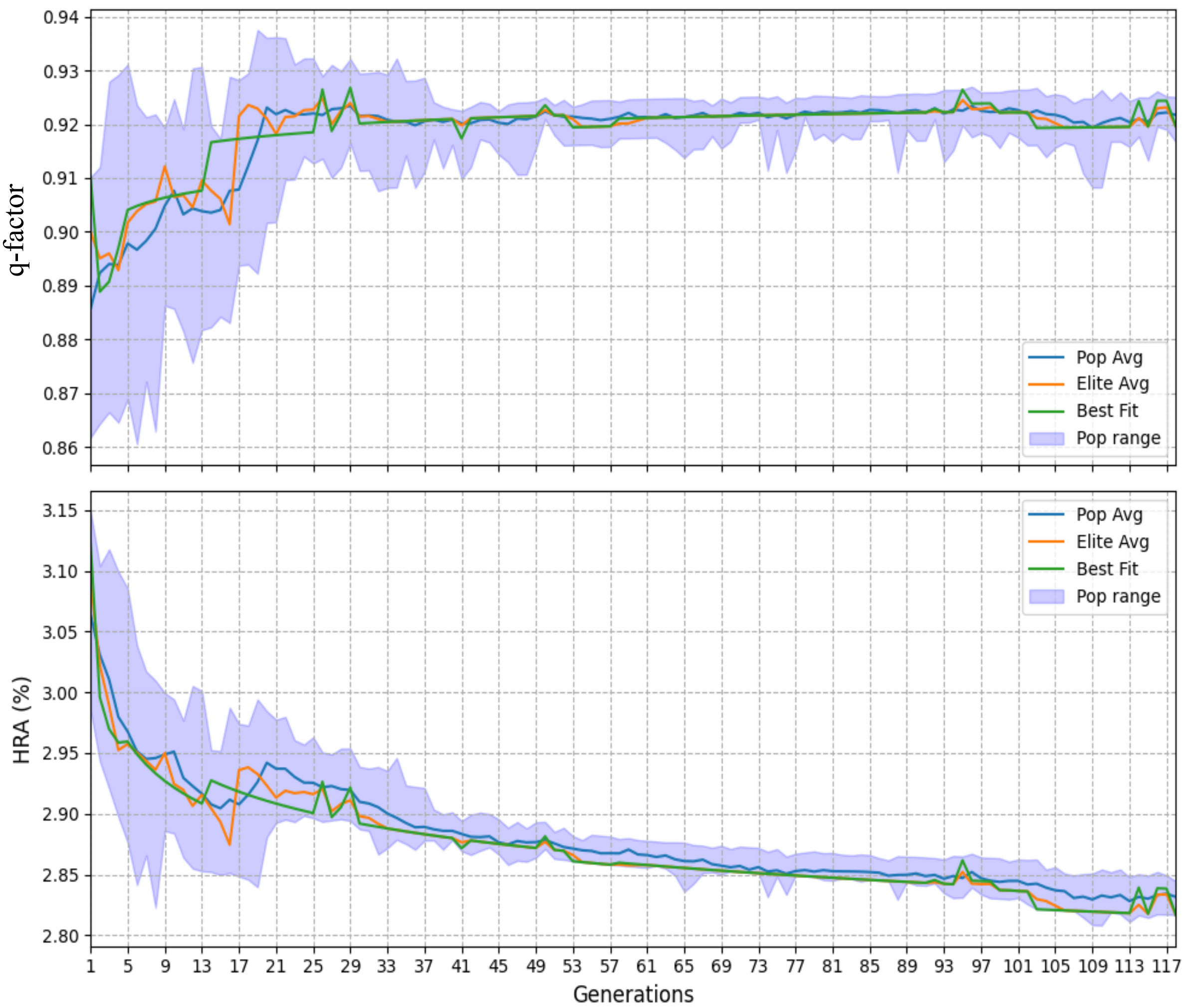

Figure 115 – Evolution of optimization objectives (*q-factor* and HRA) over generations for the 30 MW farm in the Aguçadoura minimal impact case using the U–form AOI. The purple shadow represents the range of values presented in the population, the green line the best fit layout, the blue line the average of all population and the yellow line the average of elite layouts.

For the 30 MW simulation, the CoV and P2M metrics also converged to results similar to those observed in the maximizing power scenario. This outcome is likely attributed to the spatial limitations of the deployment area, which constrained the distribution of WECs. The HRA for shield protection was 3.42% and for low-impact 2.82%, representing a difference of 21%. Similarly, the *q-factor* for shield protection was 1.03, while for low-impact it was 0.95, a difference of 9%. These differences highlight the trade–offs between maximizing wave absorption efficiency and minimizing environmental impact, which become increasingly pronounced in larger farms with more significant spatial constraints.

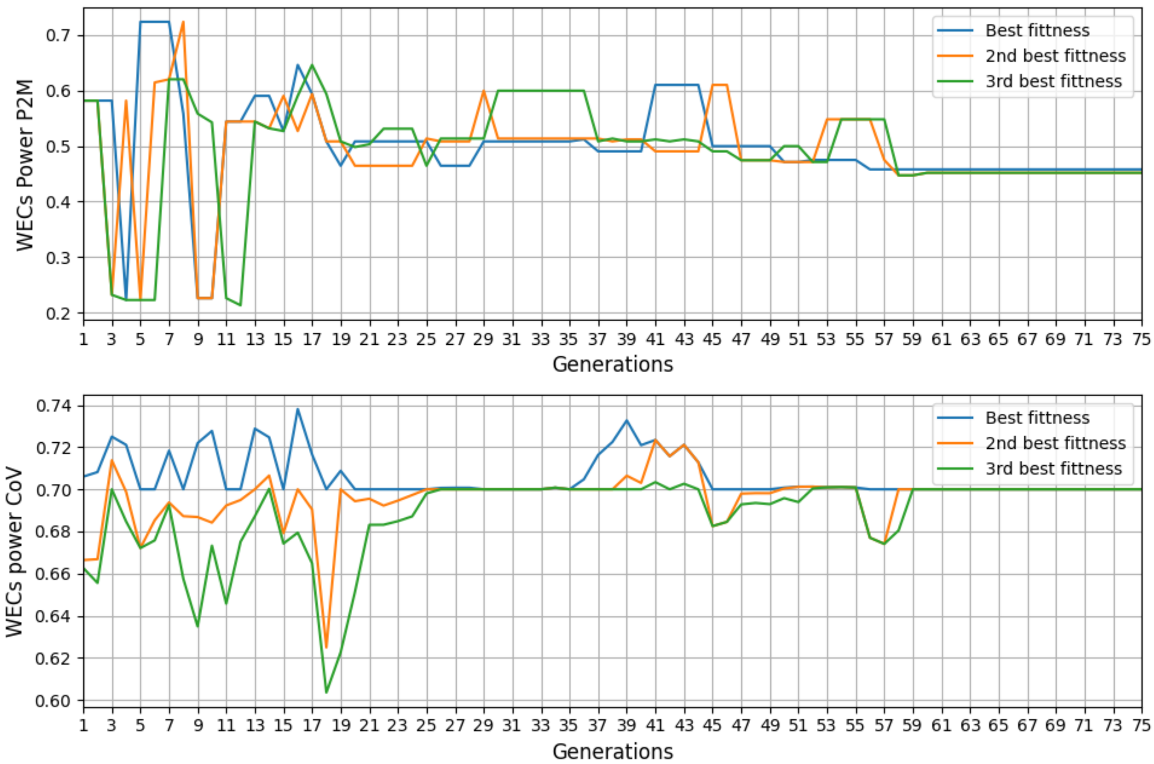

Figure 116 – Evolution of the coefficient of variation and the *Peak–to–Mean* (P2M) ratio for the 10 MW farm in the Aguçadoura minimal impact case using the U–form AOI.

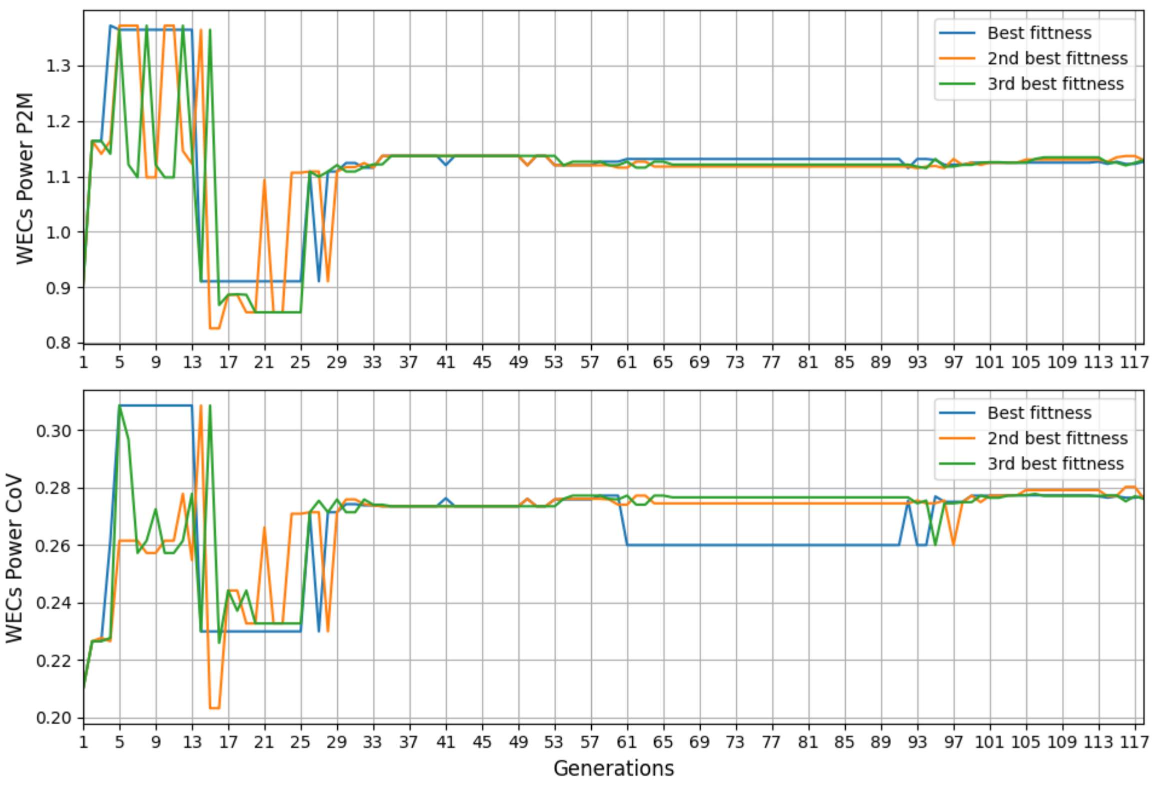

Figure 117 – Evolution of the coefficient of variation and the *Peak–to–Mean* (P2M) ratio for the 30 MW farm in the Aguçadoura minimal impact case using the U–form AOI.

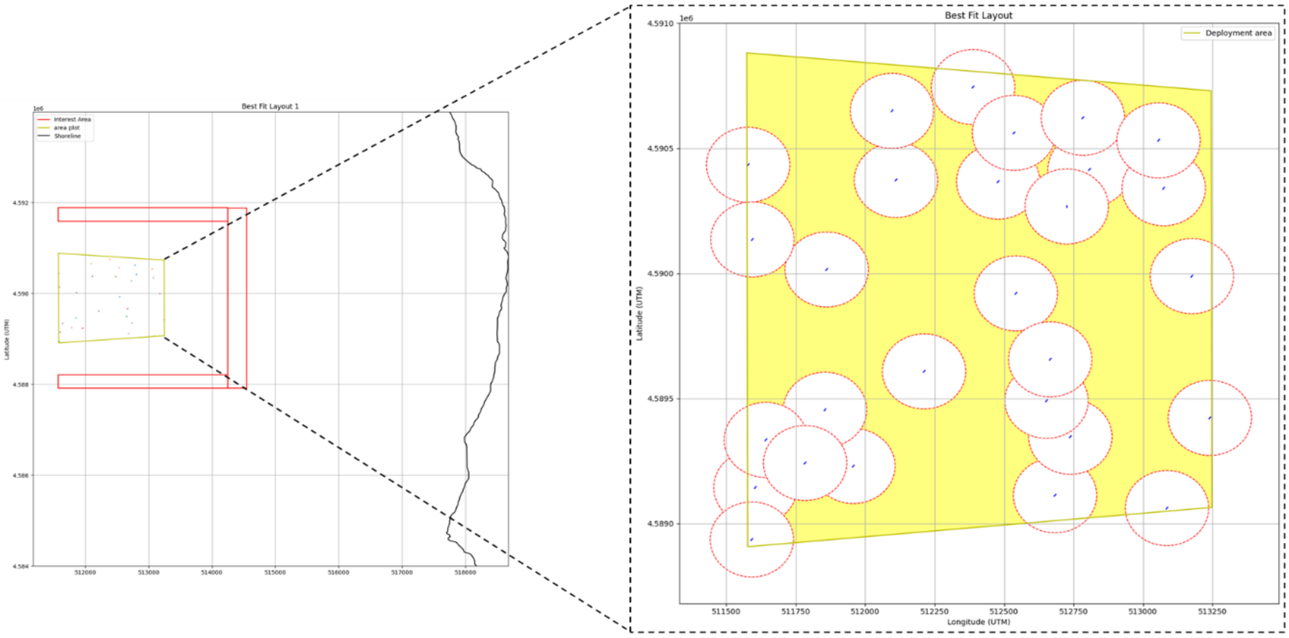

Figure 118 – Best layout configuration for the 10 MW farm in the Aguçadoura minimal impact case using U–form AOI.

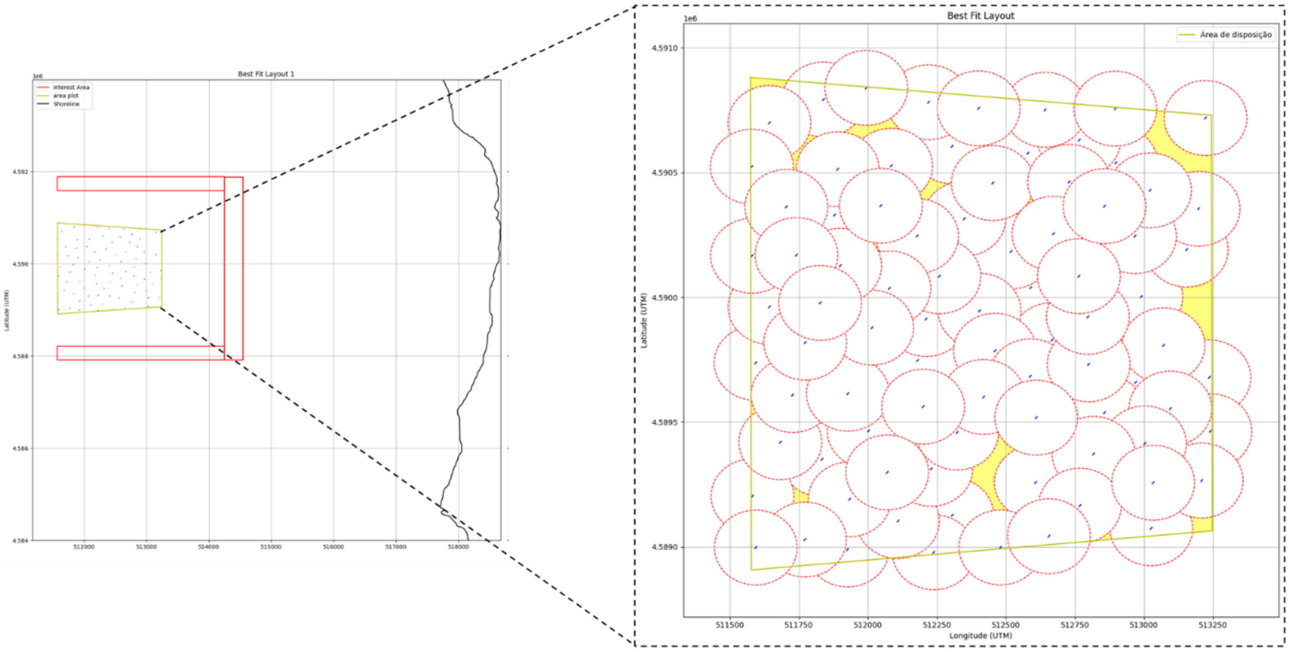

Figure 119 – Best layout configuration for the 30 MW farm in the Aguçadoura minimal impact case using U–form AOI.

These findings underscore the interplay between deployment area constraints, wave farm size, and the optimization algorithm's performance, highlighting the importance of carefully defining the AOI to accommodate the specific characteristics of each scenario.

5.3.2.3. Comparison with previous studies

Santiago *et al*. [290] utilized a computational grid with a 9×9 m cell size. However, this resolution is suboptimal for SNL–SWAN modeling due to the characteristic length of the C4 WEC being 9 m, resulting in each WEC intersecting the grid at only a single point. Ideally, a grid should provide approximately 10 intersections to enhance accuracy and adequately capture the WEC's interaction with the wave field. While the expansive domain size (approximately 10×8 km) limited the reduction of the cell size, this study employed a finer resolution of 3×3 m. Despite the increased computational demand, this resolution significantly improved the accuracy of the simulations compared to the 9×9 m grid. Although some divergence between the results of the two studies is evident, they maintain consistency and exhibit high–fidelity agreement in terms of wave energy flux reduction.

Another key distinction between the studies lies in the input wave data. Santiago *et al*. [290] relied on 15 days of data representing the most energetic sea conditions, derived from the Leixões buoy measurements. In contrast, this study employed representative sea states obtained through k–means clustering of ERA5 data, as detailed in Section 4.3.3. This methodological difference underscores the importance of using diverse datasets to capture a broader spectrum of sea states, ensuring that the simulations are representative of both typical and extreme conditions.

Additionally, the general AOI considered in this study extends significantly farther south compared to that analyzed by Santiago *et al*. [290], encompassing regions not included in their simulations. Consequently, new simulations replicating the methodology of Santiago *et al*. [290] were conducted to enable a direct comparison and assess the efficiency of the optimized layout relative to the regular grid–based positioning of a WEC farm.

Santiago *et al*. [290] analyze and quantify the influence of a WEC farm on the nearshore wave climate using the wave energy flux difference; one of the outcomes is reproduced in Figure 120. The most significant wave energy reductions were observed immediately to the lee of the WEC farm, exceeding 10% within a maximum distance of 250 m, while the shadowing effect diminished gradually, with nearshore energy reductions falling below 2%. The authors suggested that the 10 MW farm in Aguçadoura test site would not significantly affect sediment transport or other nearshore processes.

The replication of the Santiago *et al*. [290] study is illustrated in Figure 121. However, due to the lack of detailed information about their results across the entire domain, combined with differences in the domain size and grid refinement between their study and the present work, only a qualitative comparison was possible to assess the comparability of the outcomes. By examining Figure 121 and Figure 122, similar patterns can be observed. Both studies show the shadowing effect, with a 10% reduction in wave energy immediately to the lee of the WEC farm. Additionally, the lateral spread of the reduction reaches comparable positions along the coast.

In the present work, the finer grid resolution provides greater detail but results are less smoothed compared to ones of the Santiago *et al*. [290] study. Nonetheless, the observed trends confirm a consistent behavior between the two studies, validating the comparability of their findings despite methodological differences. Considering the results obtained in the reproduction, the following subsections present the comparative study between the 10 MW farm and the results obtained using the 30 MW farm.

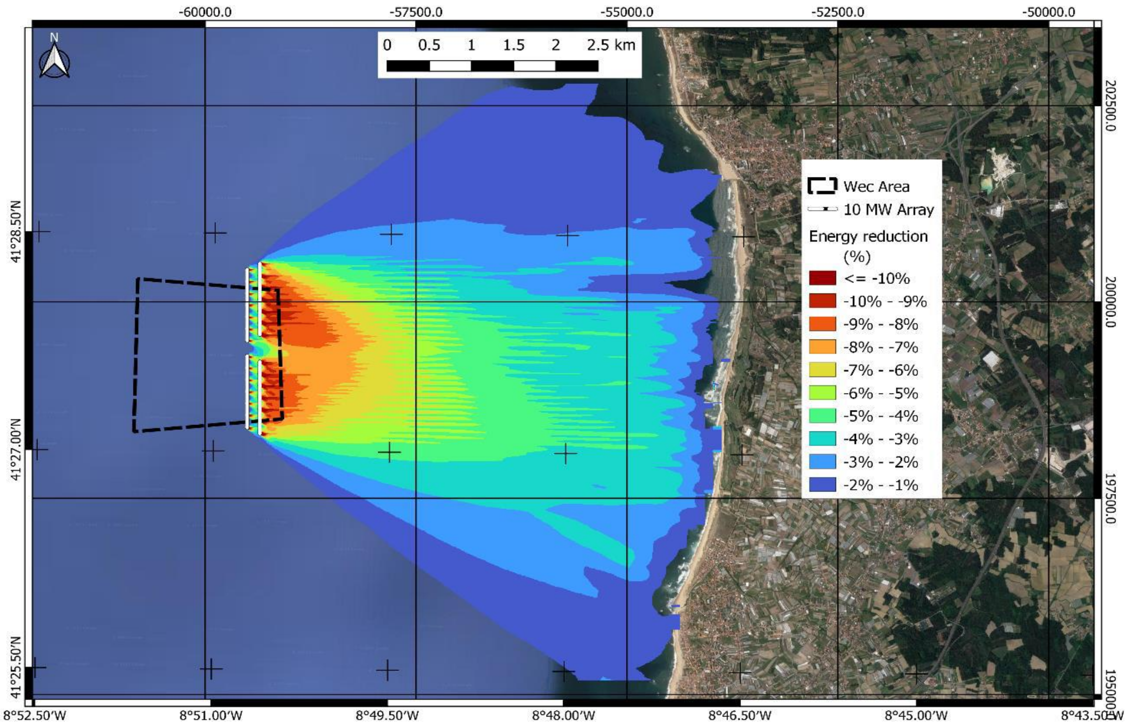

Figure 120 – Wave energy flux reduction of a 10 MW wave farm in Aguçadoura. Reproduced from Santiago *et al.* [290].

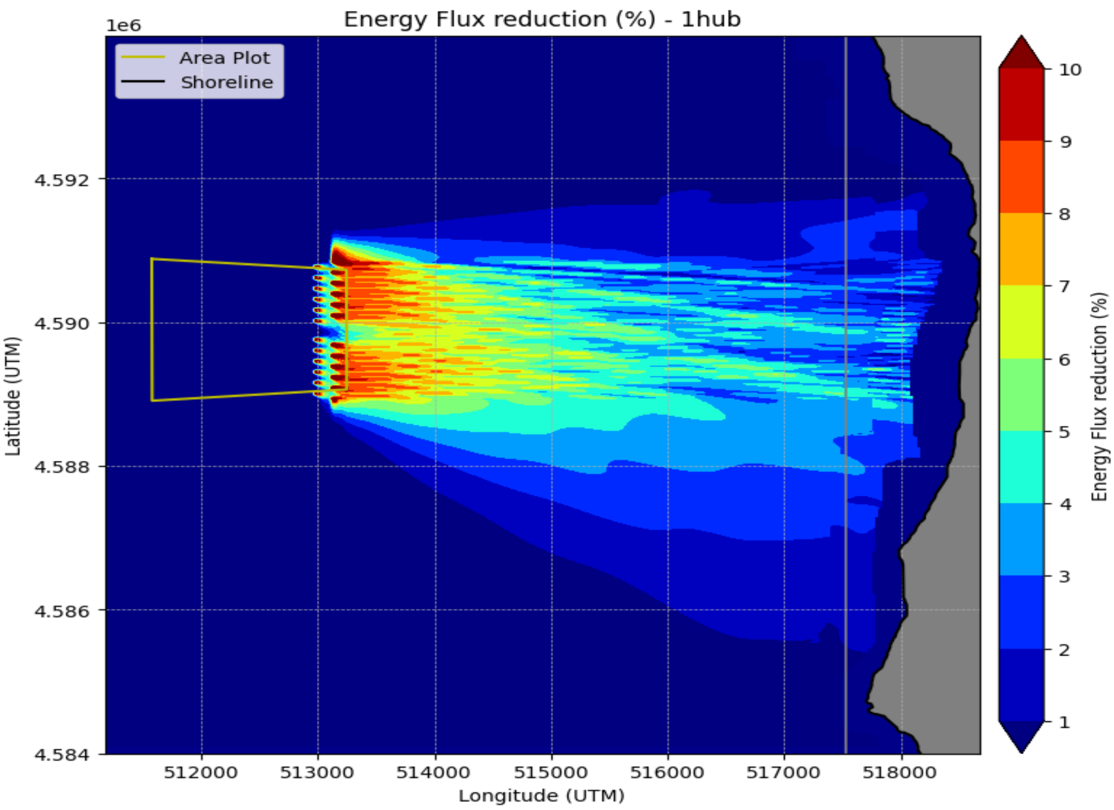

Figure 121 – Reproduction of Santiago *et al* [290] **study, using the domain and inputs of the optimization methodology.**

5.3.2.3.1. 10 MW (28 WECs) wave farm results

In this section, the comparison between the results obtained for three different scenarios for the 10 MW farm is made (Figure 122, Figure 123 and Figure 124) covering the percentual energy flux reduction for the fixed layout, the coastal protection case and the minimal impact case, respectively. All images show the spatial distribution of wave energy flux reduction behind the WEC farm, with a consistent scale ranging from 0% to 15%, enabling a fair qualitative comparison. Figure 121 and Figure 122 present the results of the same simulation, however, it was chosen to be illustrated again in the same scale of colors as the optimized scenarios to provide a smoother and more continuous gradient, facilitating a direct comparison with the optimized layouts.

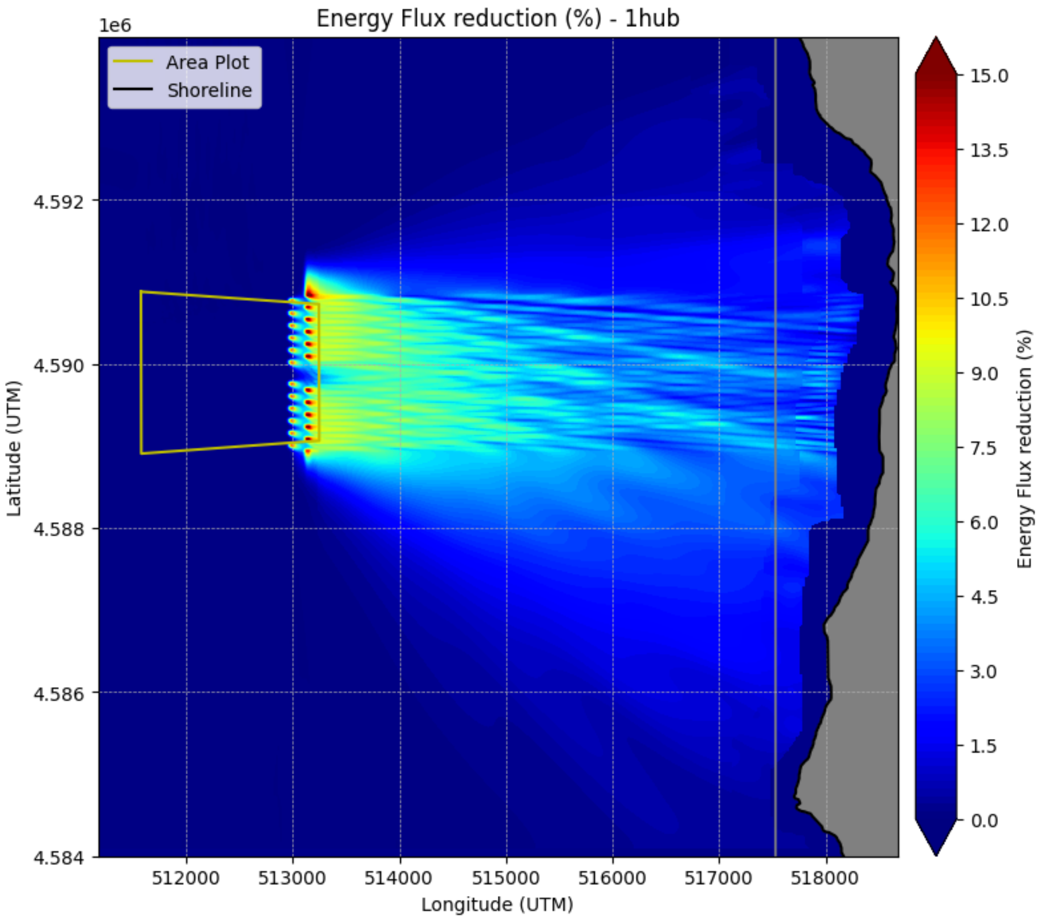

Figure 122 – Wave energy flux reduction (%) of a fixed 10 MW wave farm for Aguçadoura case.

The WEC farm's shadowing effect is clearly visible in all cases, with the energy flux reduction peaking immediately behind the farm and gradually decreasing towards the shore. The energy flux reduction map for the coastal protection optimization (Figure 123) reveals a broader and more dispersed reduction pattern compared to the fixed layout (Figure 122), with peak reduction values higher inside the deployment zone, over 15%, the area of high reduction extends further laterally and covers a larger region behind the WEC farm. This extended lateral spread reaches a greater portion of the shoreline, demonstrating the effectiveness of the coastal protection optimization in maximizing wave energy dissipation over a wider area. This layout appears particularly suitable for enhancing the protection of coastal regions by redistributing wave energy more extensively.

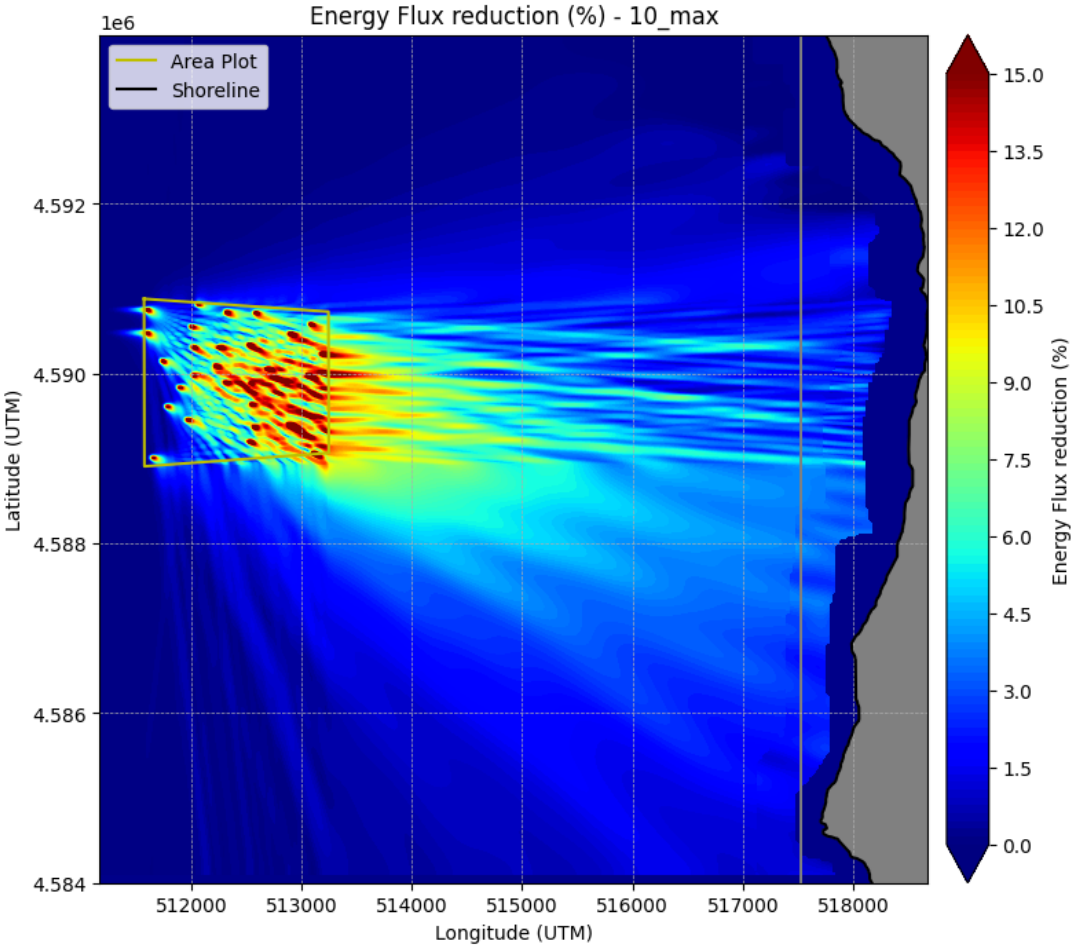

Figure 123 – Wave energy flux reduction (%) of the optimized 10 MW wave farm for Aguçadoura coastal protection case.

In contrast, the minimal impact optimization (Figure 124) shows a more concentrated reduction pattern. The highest reduction areas are equally localized directly behind the WEC farm. However, with a much narrower spread compared to the coastal protection case. The reduction diminishes more rapidly as it approaches the shoreline, resulting in lower values in nearshore areas. This layout is designed to minimize the disruption of natural wave dynamics while maintaining energy absorption efficiency. The sharper gradient observed in this case aligns with the goal of preserving environmental conditions by limiting the spatial extent of wave energy dissipation.

When comparing the three cases, the peak reduction values are consistent across all layouts, exceeding 15% immediately behind the WEC farm. The nearshore reduction is most pronounced in the coastal protection case, indicating enhanced energy dissipation closer to the shore, whereas the minimal impact optimization minimizes this effect to reduce environmental disruption. Each layout aligns with its intended objectives, with coastal protection optimization effectively prioritizing widespread energy dissipation, making it ideal for general shoreline protection, and minimal impact optimization, prioritizing energy absorption efficiency while minimizing environmental disruption.

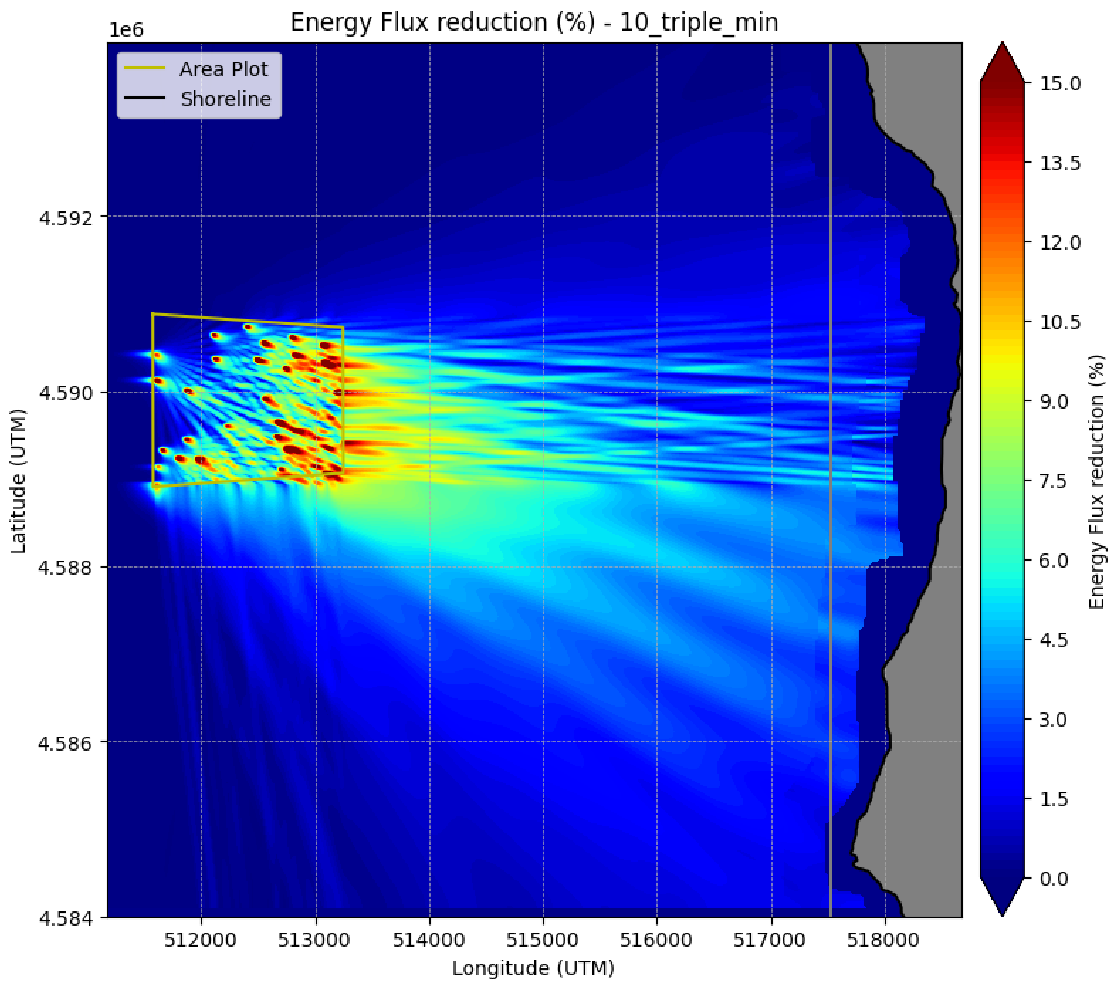

Figure 124 – Wave energy flux reduction (%) of the optimized 10 MW wave farm for Aguçadoura minimal impact case.

The reproduction of Santiago *et al.* [290] study (Figure 121) provides a valuable baseline for validating the methodology and serves as a reference point for comparing the optimized layouts. While the general AOI used in coastal protection optimization differs from the AOI used for minimal impact optimization, it was employed as a metric for quantitative comparison. This AOI, located midway between the WEC farm and the shoreline, ensures consistent evaluation of wave energy reduction and enables meaningful comparisons between scenarios.

Table 27 summarizes the key performance metrics for each configuration. The "shield layout", optimized for coastal protection, demonstrates a significantly higher HRA (1.35%) compared to the fixed layout (1.04%), indicating a notable increase in wave energy dissipation. Conversely, the "low-impact layout" exhibits a slightly lower HRA (0.99%) than the fixed layout, as expected due to its objective of minimizing shoreline impact. Both optimized scenarios outperform the fixed configuration in power absorption, with the shield and low-impact layouts achieving a *q-factor* of 1.21 approximately.

These results highlight the effectiveness of the optimization process in balancing energy production and environmental considerations.

Table 27 – Comparison of optimization objectives for 10 MW farms of Aguçadoura case

	HRA	HRA variation	Power absorption (MW)	*q-factor*	Power variation
Fixed	1.04%	–	3398.00	0.900	–
Shield	1.35%	29.51%	4582.13	1.214	34.85%
Low Impact	0.99%	–4.27%	4576.46	1.212	34.68%

These results demonstrate the algorithm's versatility in meeting distinct optimization objectives. The GA improved the wave height reduction in the AOI by nearly 30% for coastal protection, and achieved a 4% reduction of HRA in the minimal impact scenario, while boosting power absorption by 35% in both scenarios. This balance between energy production and environmental considerations showcases the effectiveness of the GA in improving wave energy farm performance across distinct priorities.

Visual analysis further reinforces the differences between the three configurations. While all scenarios exhibit significant wave energy reduction near the shoreline, the GA–optimized layouts dissipate wave energy more effectively across a broader area. The "shield layout" achieves the greatest lateral spread of energy flux reduction, making it ideal for protecting coastal regions. On the other hand, the "low-impact layout" focuses on minimizing nearshore disruption, concentrating energy reduction immediately behind the farm. Both optimized scenarios demonstrate a more favorable trade–off between energy production and environmental impact when compared to the fixed configuration.

5.3.2.3.2. 30MW (84 WECs) wave farm results

For the hypothetical 30 MW wave farm comprising 84 WECs, the fixed layout was created using three pre–designed "X" arrays deployed aligned and equally spaced at the test site. Figure 125, Figure 126, and Figure 127 depict the percentage energy flux reduction maps generated by the fixed layout, the coastal protection optimized layout, and the minimal impact optimized layout, respectively, with consistently scale up to 30% of reduction.

Table 28 presents the key performance metrics for the three configurations analyzed in the hypothetical 30 MW wave farm. The "shield layout" achieves the highest HRA at 3.42%, representing a significant improvement over the fixed layout's 2.82%. This increase confirms its effectiveness in enhancing wave energy dissipation and fulfilling its objective of coastal protection. In contrast, the "low-impact layout" maintains an HRA nearly identical to the fixed layout (2.82%), demonstrating its focus on minimizing changes to the shoreline. These results align with the distinct goals of each optimized layout, as the "shield layout" prioritizes coastal protection, while the "low-impact layout" aims to reduce interference with natural coastal processes.

In the fixed layout (Figure 125), wave energy reduction is concentrated directly behind the farm, with limited lateral spread towards the shoreline. The uniform dissipation pattern indicates a lack of targeted optimization, resulting in moderate wave energy reduction near the AOI and along the coast.

Table 28 – Comparison of optimization objectives for 30 MW farms of Aguçadoura case.

	HRA	HRA variation	Power absorption (MW)	*q-factor*	Power variation
Fixed	2.82%	–	9591.16	0.847	–
Shield	3.42%	21.36%	11655.15	1.029	21.52%
Low Impact	2.82%	0.04%	10725.12	0.947	11.82%

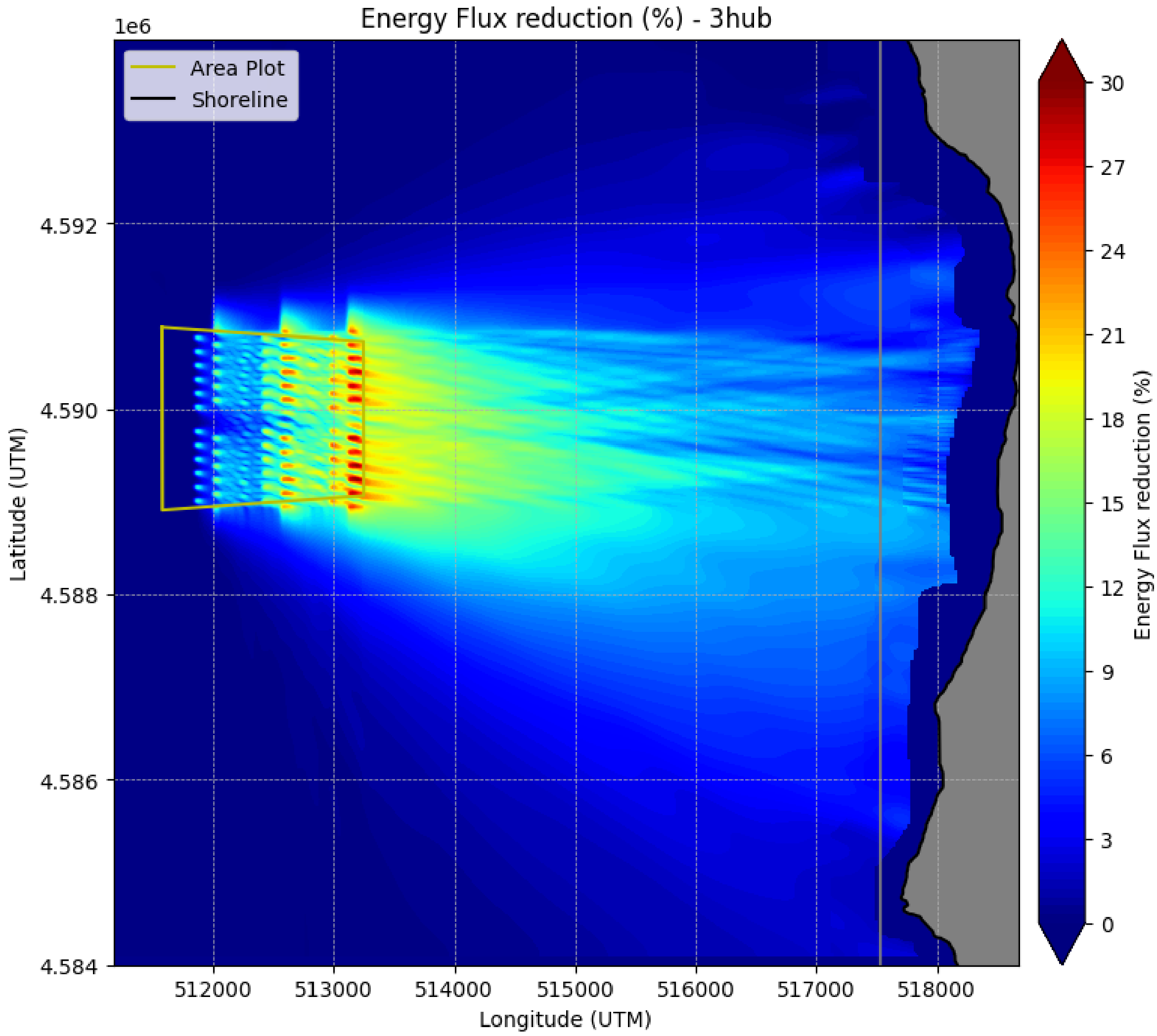

Figure 125 – Wave energy flux reduction (%) of fixed 30 MW wave farm of Aguçadoura case.

The "shield layout" (Figure 126) demonstrates a significant improvement in wave energy dissipation, with a well–defined shadowing effect extending across a broader area. The energy reduction is most pronounced in the lee of the array, peaking over 30% inside and outside the deployment zone. The reduction shadow between 12% and 15% (greenish colors) is wider reaching some points of the coastline, while in the other layouts it stops at the midway approximately, aligning with the objectives.

The "low-impact layout" (Figure 127) maintains a similar HRA in the general AOI as the fixed layout but with a more focused dissipation pattern. The energy flux reduction is distributed in a way that minimizes impact along the shoreline while achieving notable improvements in power absorption. The narrower shadowing effect compared to the "shield layout" reflects its optimization goal of balancing energy extraction with minimal shoreline impact.

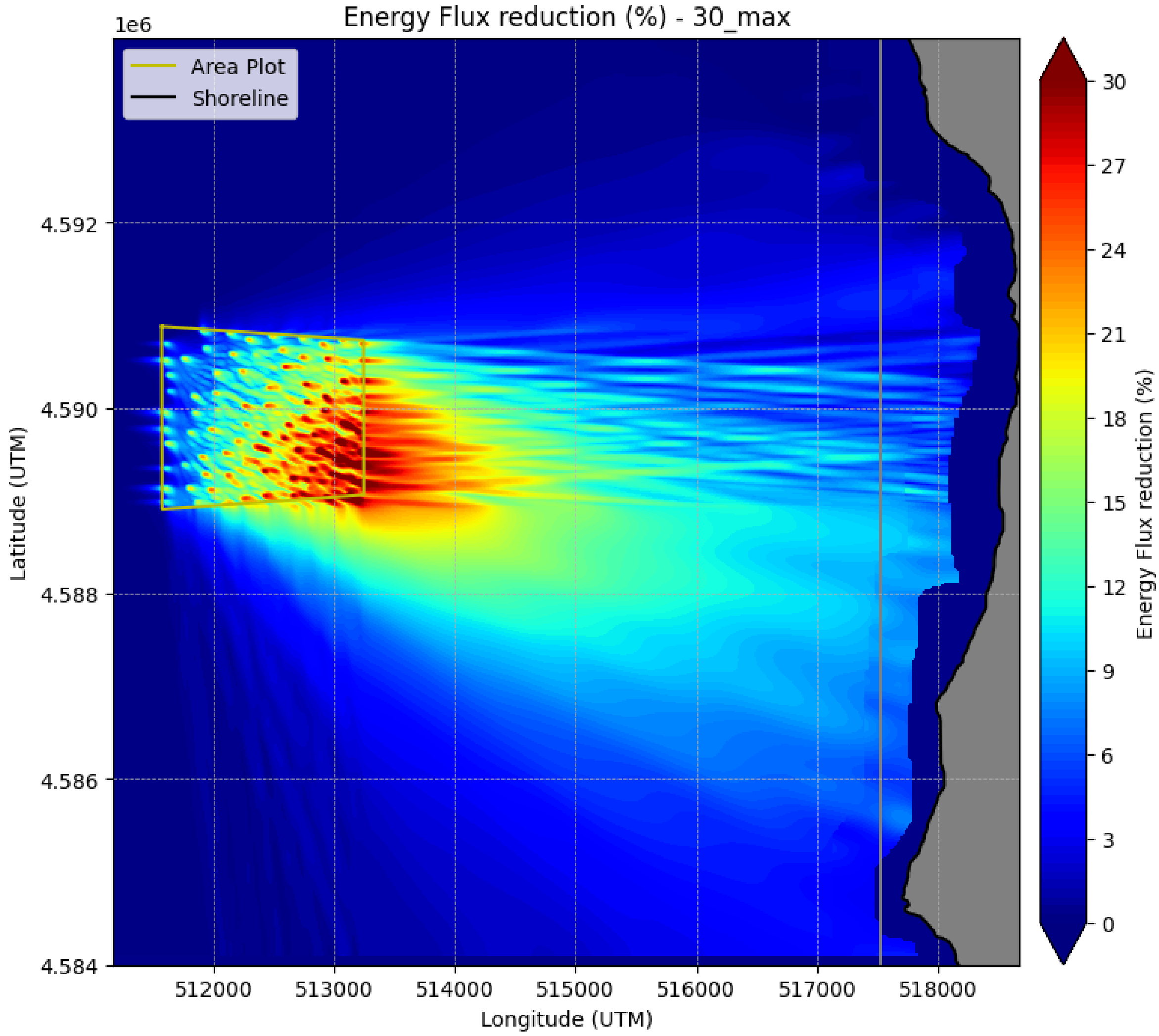

Figure 126 – Wave energy flux reduction (%) of the optimized 30 MW wave farm for Aguçadoura minimal impact case.

Both optimized scenarios also exhibit substantial improvements in power absorption compared to the fixed configuration. The "shield layout" achieves the highest power absorption, with a *q-factor* of 1.03, reaching a 21.52% increase over the fixed layout, while the "low-impact layout" achieved a *q-factor* of 0.95, which represents almost 12% of improvement. These results highlight the efficiency of the optimization process in enhancing the balance between energy extraction and environmental constrains.

The efficiency of the algorithm in addressing different wave impact scenarios is further highlighted in these results. For coastal protection, the "shield layout" significantly reduces wave height in the AOI and enhances power absorption. Conversely, the Impact GA layout achieves its objective of maintaining minimal shoreline changes while still improving power extraction. These findings underscore the versatility and robustness of the GA in achieving specific optimization goals for wave energy farms, demonstrating its adaptability to varying environmental and energy production priorities.

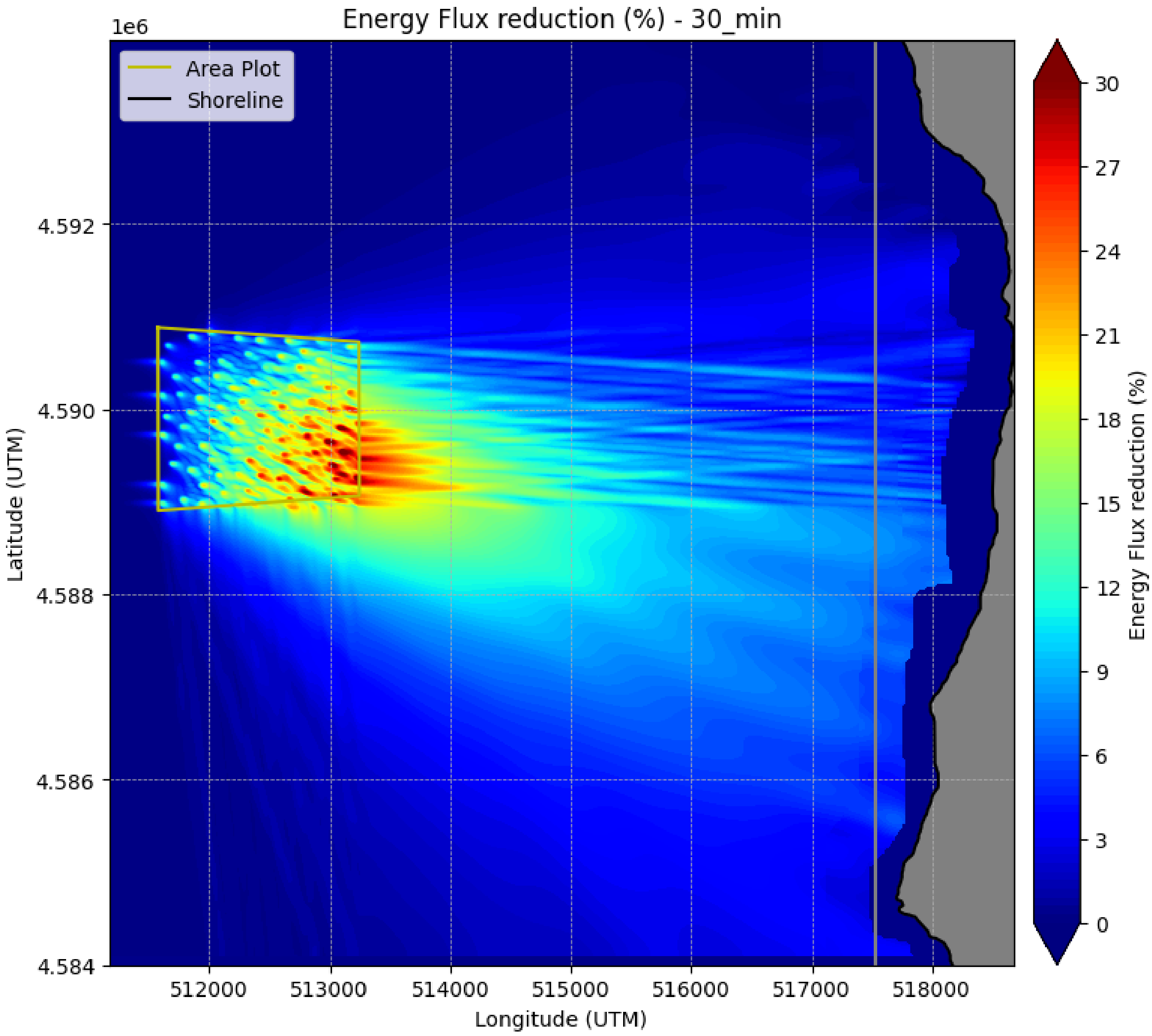

Figure 127 – Wave energy flux reduction (%) of the optimized 30 MW wave farm for Aguçadoura minimal impact case.

6

CONCLUDING REMARKS AND FUTURE DEVELOPMENTS

6.1.Conclusions

The process of developing a framework for optimizing WEC farm layouts is complex and multifaceted, requiring a comprehensive approach that addresses a range of technical and environmental challenges. Key considerations include evaluating models, understanding environmental impacts, optimizing farm layouts through GA, and analyzing the interactions between WEC units within the farm. Knowledge of the wave climate is essential to establish control strategies, create forecast models, and select suitable configurations. Despite the challenges posed by external variables, a well–structured methodology can navigate these complexities to enhance the design and deployment of WEC farms.

This thesis introduces an innovative multi–objective optimization methodology for WEC farm layouts, aiming to balance energy production with environmental constraints. The work integrates hydrodynamic modeling, specifically the SNL–SWAN model, with advanced optimization techniques, such as genetic algorithms, to maximize energy capture while considering environmental impacts. A k–means clustering was employed to optimize the choice of representative sea states aiming to enhance computational efficiency without losing important information. These innovations contribute to the sustainable deployment of renewable marine energy systems and push the boundaries of wave farm design by incorporating both energy generation and environmental sustainability.

Through a series of methodological advancements and real–world applications, this research highlights the effectiveness of the proposed optimization framework for WEC layouts. The methodology began with a comprehensive review of existing approaches, aiming to identify their limitations and uncover opportunities for improvement. This initial step established a solid foundation for developing innovative solutions to address the challenges associated with WEC farm optimization.

Building on this groundwork, the research progressed through the development and refinement of hydrodynamic modeling, which served as a robust evaluation tool for the optimization algorithm. The optimization strategies were then designed and systematically tested using real–world scenarios, allowing for a detailed assessment of the outcomes in terms of both energy production and environmental impact. This framework demonstrated the ability of the genetic algorithm to optimize

WEC layouts effectively, achieving efficient wave energy capture while addressing the complex challenges of mitigating wave impacts on co–located wind farms and coastal areas.

The effectiveness of the optimization methodology was further highlighted by sensitivity analysis, which provided insights into the factors influencing the layout of WEC farms. Key findings included the significant role of WEC positioning, wave distribution, and device spacing in maximizing energy capture and reducing wave–induced impacts. Variations in input data, such as wave direction and meteorological conditions, were shown to be critical in determining optimal device placement. The analysis emphasized the importance of managing trade–offs between objectives, such as maximizing energy production and minimizing wave height, offering a nuanced approach to optimization in real–world settings.

The algorithm's performance was validated through applications to co–located energy parks and coastal protection scenarios. In co–located energy parks, the inclusion of economic parameters in the optimization process reduced computation time and costs while maintaining similar results. For coastal protection applications, the algorithm optimized WEC placements to mitigate wave energy in targeted regions. This approach proved effective in protecting sensitive coastal habitats while balancing the objectives of energy production and environmental sustainability. The ability of the genetic algorithm to refine WEC placement in nearshore settings further demonstrated its capacity to balance competing objectives and enhance the overall efficiency of wave farms.

The key contribution of this research is the development of a new genetic algorithm tailored for continuous domain optimization of WEC positions. This method overcomes the limitations of traditional grided single – objective approaches and integrates seamlessly with the SNL–SWAN hydrodynamic model, offering more flexibility and efficiency in layout optimization. The methodology was tested across various case studies, including different boundary conditions, wave data sources, and WEC types, demonstrating its applicability in optimizing wave energy farms for multi–objective requirements. This research introduces the following innovations:

- **Multi–Objective Optimization Framework**: A framework that balances energy generation and environmental impacts, enhancing the sustainability of wave energy farms;
- **Representative Sea State Selection**: A novel method combining statistical analysis and machine learning to streamline computational demands without compromising result accuracy;
- **Customized Genetic Algorithm**: A purpose–built genetic algorithm designed to integrate energy production and environmental considerations for more realistic optimization results;
- **Practical Case Studies**: Demonstration of the framework’s flexibility in addressing diverse objectives such as economic viability, coastal protection, and environmental sustainability in offshore and nearshore scenarios.

The framework is designed with the potential to accommodate different modeling tools beyond the current integration with the SNL–SWAN hydrodynamic model. While the GA relies on a numerical model to evaluate WEC layouts, it is not strictly tied to any specific model type. For instance, the SNL–SWAN model can be replaced by other spectral phase-averaging models or potentially by phase-resolving models and even computational fluid dynamics (CFD) simulations. Although the computational effort required for phase-resolving models and CFD remains expensive for practical applications at this stage. In the future, advancements in computational power and parallel processing could mitigate these limitations, enabling their use. Moreover, emerging AI techniques, such as advanced machine learning models, could potentially replace traditional numerical simulations altogether by providing accurate energy capture predictions based on trained datasets, significantly reducing computational demands. This flexibility ensures that the framework can adapt to future technological advancements, further enhancing its applicability in diverse contexts.

The findings confirm the robustness and versatility of the proposed framework, positioning it as a foundation for future advancements in wave energy farm design and optimization. This research provides actionable insights for stakeholders, policymakers, and researchers striving for the sustainable development of offshore renewable energy. Additionally, to support further research and development, the GA code, along with selected pre– and post–processing tools, is available on GitHub at https://github.com/FelipeTDuarte/GA_WEC_farm_optimization, therefore facilitating collaboration and accelerating progress toward optimized and efficient wave energy farms.

The research presented in this thesis has been validated and disseminated through several high–impact peer–reviewed publications, reflecting its significant contributions to the field of renewable marine energy. These publications encompass a comprehensive review of WEC layout optimization strategies, the development of multi–objective decision tools for co–located wave–wind energy parks, and the implementation of innovative genetic algorithm–based methodologies for optimizing WEC farm layouts. Additionally, the author's collaboration on studies addressing advancements in wave energy assessment and the dual objectives of energy production and coastal protection further underscores the broader applicability and impact of this work. Collectively, these publications demonstrate the relevance and robustness of the proposed methodologies, advancing the state of the art in sustainable offshore energy systems.

6.2.Future work recommendations

While the proposed framework has demonstrated significant potential, there are several avenues for further research and development:

- **Integration of Additional Objectives:** Future studies could incorporate economic valuation within the WLA, specifically through the integration of LCoE assessments. Additionally, other objectives can be implemented focusing on environmental impact evaluation, particularly in the context of WEC farms installed in nearshore environments, which will further enhance the framework's comprehensiveness.
- **Advanced Machine Learning Techniques:** The application of more sophisticated machine learning methods, such as deep learning, could improve the selection of representative sea states and predict energy outputs, replacing the need of several numerical simulations with even good accuracy.
- **Coupled Models for Multi–Use Platforms:** Expanding the framework to evaluate co–located energy systems, such as hybrid wave and wind farms or systems that integrate aquaculture, could enhance its utility in addressing multi–use scenarios.

- **Real–Time Optimization:** Developing a real–time optimization module that adapts to changing wave conditions could improve operational efficiency and resilience of wave farms.
- **Validation in Different Geographies:** Applying the framework to diverse geographical locations with varying wave climates and socio–economic contexts would enhance its adaptability and global relevance.
- **Policy and Economic Integration:** Incorporating regulatory frameworks, subsidies, and market dynamics into the optimization process would make the framework more applicable to real–world decision–making.

The outcomes of this research lay a strong foundation for the continued evolution of offshore wave energy systems. By addressing the proposed future developments, the framework can become a critical tool in achieving a sustainable and integrated approach to renewable energy exploitation.

BIBLIOGRAPHY

[1] Taveira-Pinto F, Rosa-Santos P, Fazeres-Ferradosa T. Marine renewable energy. Renew Energy 2020; 150:1160–4. https://doi.org/10.1016/j.renene.2019.10.014.

[2] Ritchie H, Rosado P, Roser M. Electricity Mix. Our World in Data 2024.

[3] Teixeira-Duarte F, Clemente D, Giannini G, Rosa-Santos P, Taveira-Pinto F. Review on layout optimization strategies of offshore parks for wave energy converters. Renewable and Sustainable Energy Reviews 2022; 163:112513. https://doi.org/10.1016/J.RSER.2022.112513.

[4] Teixeira-Duarte F, Rosa-Santos P, Taveira-Pinto F. Multi-objective optimization of co-located wave-wind farm layouts supported by genetic algorithms and numerical models. Renew Energy 2025:122362. https://doi.org/10.1016/J.RENENE.2025.122362.

[5] Atan R, Finnegan W, Nash S, Goggins J. The effect of arrays of wave energy converters on the nearshore wave climate. Ocean Engineering 2019;172:373–84. https://doi.org/10.1016/J.OCEANENG.2018.11.043.

[6] Babarit A. On the park effect in arrays of oscillating wave energy converters. Renew Energy 2013;58:68–78. https://doi.org/10.1016/J.RENENE.2013.03.008.

[7] Fernandez GV, Stratigaki V, Vasarmidis P, Balitsky P, Troch P. Wake Effect Assessment in Long- and Short-Crested Seas of Heaving-Point Absorber and Oscillating Wave Surge WEC Arrays. Water (Basel) 2019;11:1126. https://doi.org/10.3390/W11061126.

[8] O'Dea A, Haller MC, Özkan-Haller HT. The impact of wave energy converter arrays on wave-induced forcing in the surf zone. Ocean Engineering 2018;161:322–36. https://doi.org/10.1016/J.OCEANENG.2018.03.077.

[9] Abanades J, Greaves D, Iglesias G. Wave farm impact on beach modal state. Mar Geol 2015;361:126–35. https://doi.org/10.1016/J.MARGEO.2015.01.008.

[10] Abanades J, Greaves D, Iglesias G. Wave farm impact on the beach profile: A case study. Coastal Engineering 2014;86:36–44. https://doi.org/10.1016/J.COASTALENG.2014.01.008.

[11] Abanades J, Greaves D, Iglesias G. Coastal defence through wave farms. Coastal Engineering 2014;91:299–307. https://doi.org/10.1016/j.coastaleng.2014.06.009.

[12] Abanades J, Flor-Blanco G, Flor G, Iglesias G. Dual wave farms for energy production and coastal protection. Ocean Coast Manag 2018;160:18–29. https://doi.org/10.1016/j.ocecoaman.2018.03.038.

[13] Smith HCM, Pearce C, Millar DL. Further analysis of change in nearshore wave climate due to an offshore wave farm: An enhanced case study for the Wave Hub site. Renew Energy 2012;40:51–64. https://doi.org/10.1016/J.RENENE.2011.09.003.

[14] Millar DL, Smith HCM, Reeve DE. Modelling analysis of the sensitivity of shoreline change to a wave farm. Ocean Engineering 2007;34:884–901. https://doi.org/10.1016/J.OCEANENG.2005.12.014.

[15] Mendoza E, Silva R, Zanuttigh B, Angelelli E, Lykke Andersen T, Martinelli L, et al. Beach response to wave energy converter farms acting as coastal defence. Coastal Engineering 2014;87:97–111. https://doi.org/10.1016/j.coastaleng.2013.10.018.

[16] Palha A, Mendes L, Fortes CJ, Brito-Melo A, Sarmento A. The impact of wave energy farms in the shoreline wave climate: Portuguese pilot zone case study using Pelamis energy wave devices. Renew Energy 2010;35:62–77. https://doi.org/10.1016/J.RENENE.2009.05.025.

[17] Bergillos RJ, López-Ruiz A, Medina-López E, Moñino A, Ortega-Sánchez M. The role of wave energy converter farms on coastal protection in eroding deltas, Guadalfeo, southern Spain. J Clean Prod 2018;171:356–67. https://doi.org/10.1016/j.jclepro.2017.10.018.

[18] Abanades J, Greaves D, Iglesias G. Beach morphodynamics in the lee of a wave farm. 2015.

[19] Mendoza E, Silva R, Zanuttigh B, Angelelli E, Lykke Andersen T, Martinelli L, et al. Beach response to wave energy converter farms acting as coastal defence. Coastal Engineering 2014;87:97–111. https://doi.org/10.1016/j.coastaleng.2013.10.018.

[20] Onea F, Rusu L, Carp GB, Rusu E. Wave Farms Impact on the Coastal Processes—A Case Study Area in the Portuguese Nearshore. J Mar Sci Eng 2021;9:262. https://doi.org/10.3390/jmse9030262.

[21] Stokes C, Conley DC. Modelling Offshore Wave farms for Coastal Process Impact Assessment: Waves, Beach Morphology, and Water Users n.d. https://doi.org/10.3390/en11102517.

[22] Rodriguez-Delgado C, Bergillos RJ, Ortega-Sánchez M, Iglesias G. Wave farm effects on the coast: The alongshore position. Science of The Total Environment 2018;640–641:1176–86. https://doi.org/10.1016/J.SCITOTENV.2018.05.281.

[23] Astariz S, Perez-Collazo C, Abanades J, Iglesias G. Towards the optimal design of a co-located wind-wave farm. Energy 2015;84:15–24. https://doi.org/10.1016/j.energy.2015.01.114.

[24] Calheiros-Cabral T, Clemente D, Rosa-Santos P, Taveira-Pinto F, Ramos V, Morais T, et al. Evaluation of the annual electricity production of a hybrid breakwater-integrated wave energy converter. Energy 2020;213:118845. https://doi.org/10.1016/J.ENERGY.2020.118845.

[25] Ramos V, Giannini G, Calheiros-Cabral T, López M, Rosa-Santos P, Taveira-Pinto F. Assessing the Effectiveness of a Novel WEC Concept as a Co-Located Solution for Offshore Wind Farms. J Mar Sci Eng 2022;10:267. https://doi.org/10.3390/jmse10020267.

[26] Rosa-Santos P, Taveira-Pinto F, López M, Rodríguez CA. Hybrid Systems for Marine Energy Harvesting. J Mar Sci Eng 2022;10:633. https://doi.org/10.3390/jmse10050633.

[27] Pérez-Collazo C, Greaves D, Iglesias G. A review of combined wave and offshore wind energy. Renewable and Sustainable Energy Reviews 2015;42:141–53. https://doi.org/10.1016/J.RSER.2014.09.032.

[28] Ramos V, Giannini G, Calheiros-Cabral T, Rosa-Santos P, Taveira-Pinto F. An Integrated Approach to Assessing the Wave Potential for the Energy Supply of Ports: A Case Study. J Mar Sci Eng 2022;10:1989. https://doi.org/10.3390/jmse10121989.

[29] Rosa-Santos P, Taveira-Pinto F, Clemente D, Cabral T, Fiorentin F, Belga F, et al. Experimental Study of a Hybrid Wave Energy Converter Integrated in a Harbor Breakwater. J Mar Sci Eng 2019;7:33. https://doi.org/10.3390/jmse7020033.

[30] Balitsky P, Quartier N, Stratigaki V, Fernandez GV, Vasarmidis P, Troch P. Analysing the Near-Field Effects and the Power Production of Near-Shore WEC Array Using a New Wave-to-Wire Model 2019. https://doi.org/10.3390/w11061137.

[31] Millar DL, Smith HCM, Reeve DE. Modelling analysis of the sensitivity of shoreline change to a wave farm. Ocean Engineering 2007;34:884–901. https://doi.org/10.1016/J.OCEANENG.2005.12.014.

[32] Luczko E, Robertson B, Bailey H, Hiles C, Buckham B. Representing non-linear wave energy converters in coastal wave models. Renew Energy 2018;118:376–85. https://doi.org/10.1016/J.RENENE.2017.11.040.

[33] Project Overview — SNL-SWAN n.d. https://snl-waterpower.github.io/SNL-SWAN/ (accessed January 18, 2023).

[34] Ruehl K, Porter A, Posner A, Roberts J. Development of SNL-SWAN, a Validated Wave Energy Converter Array Modeling Tool. Proceedings of the 10th European Wave and Tidal Energy Conference, 2013.

[35] Ruehl K, Porter A, Chartrand C, Smith H, Chang G, Roberts J. Development, Verification and Application of the SNL-SWAN Open Source Wave Farm Code. Proceedings of the 11th European Wave and Tidal Energy Conference, Nantes, France: 2015.

[36] Porter A, Ruehl K, Chartrand C, Smith H. Development and release of the open-source wave climate environment assessment tool snl-swan. Proceedings of the 3rd Marine Energy Technology Symposium, Washington, DC, USA: 2015.

[37] Göteman M, Giassi M, Engström J, Isberg J. Advances and Challenges in Wave Energy Park Optimization—A Review. Front Energy Res 2020;8. https://doi.org/10.3389/fenrg.2020.00026.

[38] Giassi M, Göteman M. Layout design of wave energy parks by a genetic algorithm. Ocean Engineering 2018;154:252–61. https://doi.org/10.1016/j.oceaneng.2018.01.096.

[39] Dupont V, Gruet R, Kempf V. Ocean Energy Stats & Trends 2023. 2024.

[40] Clark CE, DuPont B. Reliability-based design optimization in offshore renewable energy systems. Renewable and Sustainable Energy Reviews 2018;97:390–400. https://doi.org/10.1016/j.rser.2018.08.030.

[41] Gunn K, Stock-Williams C. Quantifying the global wave power resource. Renew Energy 2012;44:296–304. https://doi.org/10.1016/J.RENENE.2012.01.101.

[42] Pecher A, Kofoed JP. Handbook of Ocean Wave Energy. vol. 7. Cham: Springer International Publishing; 2017. https://doi.org/10.1007/978-3-319-39889-1.

[43] Rusu E, Onea F. A review of the technologies for wave energy extraction. Clean Energy 2018;2:10–9. https://doi.org/10.1093/ce/zky003.

[44] Rebecca Williams FZ, Backwell B, Lee J, Patel A, Hutchinson M, Qiao L, et al. GLOBAL OFFSHORE WIND REPORT 2024. Brussels: 2024.

[45] Arshad M, O'Kelly BC. Offshore wind-turbine structures: a review. Proceedings of the Institution of Civil Engineers - Energy 2013;166:139–52. https://doi.org/10.1680/ener.12.00019.

[46] Rodrigues S, Restrepo C, Katsouris G, Pinto RT, Soleimanzadeh M, Bosman P, et al. A Multi-Objective Optimization Framework for Offshore Wind Farm Layouts and Electric Infrastructures. Energies 2016, Vol 9, Page 216 2016;9:216. https://doi.org/10.3390/EN9030216.

[47] Kempener R, Neumann F. Wave Energy Technology brief. Abu Dhabi: 2014.

[48] MARINA Platform | The European Maritime Spatial Planning Platform n.d. https://maritime-spatial-planning.ec.europa.eu/projects/marina-platform (accessed January 8, 2025).

[49] Off-shore Renewable Energy Conversion platforms – Coordination Action | ORECCA | Project | News & Multimedia | FP7 | CORDIS | European Commission n.d. https://cordis.europa.eu/project/id/241421/reporting (accessed January 8, 2025).

[50] Papandroulakis N, Thomsen C, Mintenbeck K, Mayorga P, Hernández-Brito JJ. The EU-project "TROPOS." Aquaculture Perspective of Multi-Use Sites in the Open Ocean: The Untapped Potential for Marine Resources in the Anthropocene 2017:355–74. https://doi.org/10.1007/978-3-319-51159-7_12/TABLES/3.

[51] Innovative Multi-purpose off-shore platforms: planning, Design and operation | MERMAID | Project | News & Multimedia | FP7 | CORDIS | European Commission n.d. https://cordis.europa.eu/project/id/288710/reporting (accessed January 8, 2025).

[52] Grupo de Trabalho para o planeamento e operacionalização de centros electroprodutores baseados em fontes de energias renováveis de origem ou localização oceânica (Despacho n.º 11404/2022 de 23 de setembro). Relatório do Grupo de Trabalho para o planeamento e operacionalização de centros eletroprodutores renováveis de origem ou localização oceânica. 2023.

[53] Clark CE, Barter G, Shaler K, DuPont B. Reliability-based layout optimization in offshore wind energy systems. Wind Energy 2022;25:125–48. https://doi.org/10.1002/we.2664.

[54] McMillan D, Ault GW. Condition monitoring benefit for onshore wind turbines: Sensitivity to operational parameters. IET Renewable Power Generation 2008;2:60–72. https://doi.org/10.1049/IET-RPG:20070064.

[55] Clark CE, Miller A, DuPont B. An analytical cost model for co-located floating wind-wave energy arrays. Renew Energy 2019;132:885–97. https://doi.org/10.1016/J.RENENE.2018.08.043.

[56] Astariz S, Iglesias G. Accessibility for operation and maintenance tasks in co-located wind and wave energy farms with non-uniformly distributed arrays. Energy Convers Manag 2015;106:1219–29. https://doi.org/10.1016/j.enconman.2015.10.060.

[57] Astariz S, Iglesias G. Enhancing Wave Energy Competitiveness through Co-Located Wind and Wave Energy Farms. A Review on the Shadow Effect. Energies (Basel) 2015;8:7344–66. https://doi.org/10.3390/en8077344.

[58] Astariz S, Perez-Collazo C, Abanades J, Iglesias G. Hybrid wave and offshore wind farms: A comparative case study of co-located layouts. International Journal of Marine Energy 2016;15:2–16. https://doi.org/10.1016/j.ijome.2016.04.016.

[59] Astariz S, Abanades J, Perez-Collazo C, Iglesias G. Improving wind farm accessibility for operation & maintenance through a co-located wave farm: Influence of layout and wave climate. Energy Convers Manag 2015;95:229–41. https://doi.org/10.1016/j.enconman.2015.02.040.

[60] Astariz S, Vazquez A, Sánchez M, Carballo R, Iglesias G. Co-located wave-wind farms for improved O&M efficiency. Ocean Coast Manag 2018;163:66–71. https://doi.org/10.1016/j.ocecoaman.2018.04.010.

[61] Astariz S, Perez-Collazo C, Abanades J, Iglesias G. Co-located wave-wind farms: Economic assessment as a function of layout. Renew Energy 2015;83:837–49. https://doi.org/10.1016/j.renene.2015.05.028.

[62] Astariz S, Perez-Collazo C, Abanades J, Iglesias G. Co-located wind-wave farm synergies (Operation & Maintenance): A case study. Energy Convers Manag 2015;91:63–75. https://doi.org/10.1016/j.enconman.2014.11.060.

[63] Teixeira-Duarte F, Ramos V, Rosa-Santos P, Taveira-Pinto F. Multi-objective decision tool for the assessment of co-located wave-wind offshore floating energy parks. Ocean Engineering 2024;292:116449. https://doi.org/10.1016/J.OCEANENG.2023.116449.

[64] Cui L, Sergiienko NY, Leontini JS, Cohen N, Bennetts LG, Cazzolato B, et al. Protecting coastlines by offshore wave farms: On optimising array configurations using a corrected far-field approximation. Renew Energy 2024;224:120109. https://doi.org/10.1016/j.renene.2024.120109.

[65] Cheng Z, Wen TR, Ong MC, Wang K. Power performance and dynamic responses of a combined floating vertical axis wind turbine and wave energy converter concept. Energy 2019;171:190–204. https://doi.org/10.1016/J.ENERGY.2018.12.157.

[66] Perez-Collazo C, Astariz S, Abanades J, Greaves D, Iglesias G. CO-LOCATED WAVE AND OFFSHORE WIND FARMS: A PRELIMINARY CASE STUDY OF AN HYBRID ARRAY. Coastal Engineering Proceedings 2014;1:33. https://doi.org/10.9753/icce.v34.structures.33.

[67] Silva D, Martinho P, Guedes Soares C. Wave energy distribution along the Portuguese continental coast based on a thirty three years hindcast. Renew Energy 2018;127:1064–75. https://doi.org/10.1016/j.renene.2018.05.037.

[68] Onea F, Rusu L, Carp GB, Rusu E. Wave Farms Impact on the Coastal Processes—A Case Study Area in the Portuguese Nearshore. J Mar Sci Eng 2021;9:262. https://doi.org/10.3390/jmse9030262.

[69] Antunes do Carmo JS. The changing paradigm of coastal management: The Portuguese case. Science of The Total Environment 2019;695:133807. https://doi.org/10.1016/J.SCITOTENV.2019.133807.

[70] Fox-Kemper B, Hewitt HT, Xiao C, Aðalgeirsdóttir G, Drijfhout SS, Edwards TL, et al. Ocean, Cryosphere and Sea Level Change. In: Masson-Delmotte V, Zhai P, Pirani A, Connors SL, Péan C, Berger S, et al., editors. Climate Change 2021: The Physical Science Basis. Contribution of Working Group I to the Sixth Assessment Report of the Intergovernmental Panel on Climate Change, Cambridge, United Kingdom and New York, NY, USA: Cambridge University Press; 2021, p. 1211–1362. https://doi.org/10.1017/9781009157896.011.

[71] Estratégia Nacional para o Mar 2021-2030 - Incentivos MAR2030 n.d. https://mar2030-incentivos.pt/estrategia-nacional-para-o-mar-2021-2030/ (accessed August 19, 2024).

[72] DGPM | Ordenamento do Espaço Marítimo n.d. https://www.dgpm.mm.gov.pt/ordenamento-e-maritimo (accessed August 19, 2024).

[73] Projeto WindFLoat Atlantic | edp.com n.d. https://www.edp.com/pt-pt/inovacao/windfloat (accessed November 14, 2022).

[74] Ramos V, López M, Taveira-Pinto F, Rosa-Santos P. Influence of the wave climate seasonality on the performance of a wave energy converter: A case study. Energy 2017;135:303–16. https://doi.org/10.1016/J.ENERGY.2017.06.080.

[75] REN, APREN. Electricity Generation by Energy Sources in Mainland Portugal in 2024 n.d. https://www.apren.pt/en/renewable-energies/production/ (accessed August 19, 2024).

[76] The European Green Deal n.d. https://ec.europa.eu/stories/european-green-deal/ (accessed August 19, 2024).

[77] WaveRoller - AW-Energy n.d. https://aw-energy.com/waveroller/ (accessed August 19, 2024).

[78] Wave Energy Technology – CorPower Ocean n.d. https://corpowerocean.com/wave-energy-technology/ (accessed August 19, 2024).

[79] Verbrugghe T, Stratigaki V, Troch P, Rabussier R, Kortenhaus A. A Comparison Study of a Generic Coupling Methodology for Modeling Wake Effects of Wave Energy Converter Arrays. Energies 2017, Vol 10, Page 1697 2017;10:1697. https://doi.org/10.3390/EN10111697.

[80] Budal K, Falnes J. A resonant point absorber of ocean-wave power. Nature 1975;256:478–9. https://doi.org/10.1038/256478a0.

[81] Budal K. Theory for Absorption of Wave Power by a System of Interacting Bodies. Journal of Ship Research 1977;21:248–54. https://doi.org/10.5957/jsr.1977.21.4.248.

[82] Engström J, Eriksson M, Göteman M, Isberg J, Leijon M. Performance of large arrays of point absorbing direct-driven wave energy converters. J Appl Phys 2013;114:204502. https://doi.org/10.1063/1.4833241.

[83] Astariz S, Iglesias G. Co-located wind and wave energy farms: Uniformly distributed arrays. Energy 2016;113:497–508. https://doi.org/10.1016/j.energy.2016.07.069.

[84] Astariz S, Iglesias G. Output power smoothing and reduced downtime period by combined wind and wave energy farms. Energy 2016;97:69–81. https://doi.org/10.1016/j.energy.2015.12.108.

[85] Astariz S, Iglesias G. Selecting optimum locations for co-located wave and wind energy farms. Part I: The Co-Location Feasibility index. Energy Convers Manag 2016;122:589–98. https://doi.org/10.1016/J.ENCONMAN.2016.05.079.

[86] Astariz S, Iglesias G. Selecting optimum locations for co-located wave and wind energy farms. Part II: A case study. Energy Convers Manag 2016;122:599–608. https://doi.org/10.1016/j.enconman.2016.05.078.

[87] Carballo R, Iglesias G. Wave farm impact based on realistic wave-WEC interaction. Energy 2013;51:216–29. https://doi.org/10.1016/J.ENERGY.2012.12.040.

[88] Berrio Y, Rivillas-Ospina G, Ruiz-Martínez G, Arango-Manrique A, Ricaurte C, Mendoza E, et al. Energy conversion and beach protection: Numerical assessment of a dual-purpose WEC farm. Renew Energy 2023;219:119555. https://doi.org/10.1016/J.RENENE.2023.119555.

[89] Marchand M. Conscience Project - Concepts and Science for Coastal Erosion Management n.d. http://www.conscience-eu.net/ (accessed October 18, 2024).

[90] EUROSION. EUROSION project n.d. http://www.eurosion.org/ (accessed December 10, 2024).

[91] Dean RG, Dalrymple RA. Water Wave Mechanics for Engineers and Scientists. vol. 2. WORLD SCIENTIFIC; 1991. https://doi.org/10.1142/1232.

[92] Holthuijsen LH. Waves in Oceanic and Coastal Waters. Cambridge University Press; 2010.

[93] López I, Rosa-Santos P, Moreira C, Taveira-Pinto F. RANS-VOF modelling of the hydraulic performance of the LOWREB caisson. Coastal Engineering 2018;140:161–74. https://doi.org/10.1016/j.coastaleng.2018.07.006.

[94] Young IR. Wind generated ocean waves. vol. 2. Elsevier; 1999.

[95] Cavaleri L, Alves JHGM, Ardhuin F, Babanin A, Banner M, Belibassakis K, et al. Wave modelling – The state of the art. Prog Oceanogr 2007;75:603–74. https://doi.org/10.1016/J.POCEAN.2007.05.005.

[96] Chen W, Demirbilek Z, Lin L. Coupling Phase-Resolving Nearshore Wave Models with Phase-Averaged Spectral Wave Models in Coastal Applications. Proceedings of the International Conference on Estuarine and Coastal Modeling, vol. 388, Seattle, Washington, United States: American Society of Civil Engineers; 2010, p. 582–600. https://doi.org/10.1061/41121(388)35.

[97] Rijnsdorp DP, Hansen JE, Lowe RJ. Understanding coastal impacts by nearshore wave farms using a phase-resolving wave model. Renew Energy 2020;150:637–48. https://doi.org/10.1016/J.RENENE.2019.12.138.

[98] Council GWE. Global wind report 2021. Global Wind Energy Council: Brussels, Belgium 2021:6–7.

[99] Brocchini M, Dodd N. Nonlinear Shallow Water Equation Modeling for Coastal Engineering. J Waterw Port Coast Ocean Eng 2008;134:104–20. https://doi.org/10.1061/(ASCE)0733-950X(2008)134:2(104).

[100] Chiang CM. The Applied Dynamics of Ocean Surface Waves 1992;1. https://doi.org/10.1142/0752.

[101] Stoker JJ. Water Waves. Hoboken, NJ, USA: John Wiley & Sons, Inc.; 1992. https://doi.org/10.1002/9781118033159.

[102] Zijlema M, Stelling GS. Efficient computation of surf zone waves using the nonlinear shallow water equations with non-hydrostatic pressure. Coastal Engineering 2008;55:780–90. https://doi.org/10.1016/J.COASTALENG.2008.02.020.

[103] Hasselmann K, Barnett T, Bouws E, Carlson H, Cartwright D, Enke K, et al. Measurements of wind-wave growth and swell decay during the Joint North Sea Wave Project (JONSWAP). Deut Hydrogr Z 1973;8:1–95.

[104] Pierson WJ, Moskowitz L. A proposed spectral form for fully developed wind seas based on the similarity theory of S. A. Kitaigorodskii. J Geophys Res 1964;69:5181–90. https://doi.org/10.1029/JZ069I024P05181.

[105] Janssen P. The Interaction of Ocean Waves and Wind. The Interaction of Ocean Waves and Wind 2004. https://doi.org/10.1017/CBO9780511525018.

[106] Komen GJ, Cavaleri L, Donelan M, Hasselmann K, Hasselmann S, Janssen PAEM. Dynamics and Modelling of Ocean Waves. Dmow 1996:554.

[107] Phillips OM. On the generation of waves by turbulent wind. J Fluid Mech 1957;2:417–45. https://doi.org/10.1017/S0022112057000233.

[108] Hasselmann K. On the spectral dissipation of ocean waves due to white capping. Boundary Layer Meteorol 1974;6:107–27. https://doi.org/10.1007/BF00232479/METRICS.

[109] Tucker MJ., Pitt EG. Waves in ocean engineering 2001:521.

[110] Group TW. The WAM Model—A Third Generation Ocean Wave Prediction Model. J Phys Oceanogr 1988;18:1775–810. https://doi.org/10.1175/1520-0485(1988)018<1775:TWMTGO>2.0.CO;2.

[111] Tolman H. User manual and system documentation of WAVEWATCH III version 3.14. Analysis 2009;166.

[112] Booij N, Ris RC, Holthuijsen LH. A third-generation wave model for coastal regions 1. Model description and validation. J Geophys Res Oceans 1999;104:7649–66. https://doi.org/10.1029/98JC02622.

[113] Rusu E, Guedes Soares C. Numerical modelling to estimate the spatial distribution of the wave energy in the Portuguese nearshore. Renew Energy 2009;34:1501–16. https://doi.org/10.1016/J.RENENE.2008.10.027.

[114] Silva D, Bento AR, Martinho P, Guedes Soares C. High resolution local wave energy modelling in the Iberian Peninsula. Energy 2015;91:1099–112. https://doi.org/10.1016/J.ENERGY.2015.08.067.

[115] Bouws E, Gunther H, Rosenthal W, Vincent CL. Similarity of the wind wave spectrum in finite depth water 1. Spectral form. J Geophys Res 1985;90:975–86. https://doi.org/10.1029/JC090iC01p00975.

[116] Janssen PAEM, Hansen B, Bidlot J-R. Verification of the ECMWF Wave Forecasting System against Buoy and Altimeter Data. Weather and Forecasting 1997:763–84. https://doi.org/https://doi.org/10.1175/1520-0434(1997)012<0763:VOTEWF>2.0.CO;2.

[117] Benoit M, Marcos F, Becq F. Development of a Third Generation Shallow-Water Wave Model with Unstructured Spatial Meshing. Proceedings of the Coastal Engineering Conference 1997;1:465–78. https://doi.org/10.1061/9780784402429.037.

[118] Wu WC, Wang T, Yang Z, García-Medina G. Development and validation of a high-resolution regional wave hindcast model for U.S. West Coast wave resource characterization. Renew Energy 2020;152:736–53. https://doi.org/10.1016/J.RENENE.2020.01.077.

[119] Tolman HL. A Third-Generation Model for Wind Waves on Slowly Varying, Unsteady, and Inhomogeneous Depths and Currents. Journal of Physical Oceanography 1991:782–97. https://doi.org/https://doi.org/10.1175/1520-0485(1991)021<0782:ATGMFW>2.0.CO;2.

[120] Eldeberky Y. Nonlinear transformation of wave spectra in the nearshore zone. PhD. TU Delft, 1996.

[121] Eldeberky Y, Battjes JA. Spectral modeling of wave breaking: Application to Boussinesq equations. J Geophys Res Oceans 1996;101:1253–64. https://doi.org/10.1029/95JC03219.

[122] O'Reilly WC, Guza RT. Comparison of Spectral Refraction and Refraction-Diffraction Wave Models. J Waterw Port Coast Ocean Eng 1991;117:199–215. https://doi.org/10.1061/(ASCE)0733-950X(1991)117:3(199).

[123] Nonlinear interactions of random waves in a dispersive medium. Proc R Soc Lond A Math Phys Sci 1966;289:301–20. https://doi.org/10.1098/RSPA.1966.0013.

[124] Orszag SA. Analytical theories of turbulence. J Fluid Mech 1970;41:363–86. https://doi.org/10.1017/S0022112070000642.

[125] Herbers THC, Burton MC. Nonlinear shoaling of directionally spread waves on a beach. J Geophys Res Oceans 1997;102:21101–14. https://doi.org/10.1029/97JC01581.

[126] Eldeberky Y, Madsen PA. Deterministic and stochastic evolution equations for fully dispersive and weakly nonlinear waves. Coastal Engineering 1999;38:1–24. https://doi.org/10.1016/S0378-3839(99)00021-6.

[127] Janssen TT. Nonlinear surface waves over topography. PhD. TU Delft, 2006.

[128] Holloway G, Hendershott MC. Stochastic closure for nonlinear Rossby waves. J Fluid Mech 1977;82:747–65. https://doi.org/10.1017/S0022112077000962.

[129] Herbers THC, Orzech M, Elgar S, Guza RT. Shoaling transformation of wave frequency-directional spectra. J Geophys Res Oceans 2003;108:3013. https://doi.org/10.1029/2001JC001304.

[130] Vrecica T, Toledo Y. Consistent nonlinear stochastic evolution equations for deep to shallow water wave shoaling. J Fluid Mech 2016;794:310–42. https://doi.org/10.1017/JFM.2015.750.

[131] Toledo Y, Agnon Y. Stochastic evolution equations with localized nonlinear shoaling coefficients. European Journal of Mechanics - B/Fluids 2012;34:13–8. https://doi.org/10.1016/J.EUROMECHFLU.2012.01.007.

[132] Salmon JE, Smit PB, Janssen TT, Holthuijsen LH. A consistent collinear triad approximation for operational wave models. Ocean Model (Oxf) 2016;104:203–12. https://doi.org/10.1016/J.OCEMOD.2016.06.009.

[133] Agnon Y, Sheremet A, Gonsalves J, Stiassnie M. Nonlinear evolution of a unidirectional shoaling wave field. Coastal Engineering 1993;20:29–58. https://doi.org/10.1016/0378-3839(93)90054-C.

[134] Bredmose H, Agnon Y, Madsen PA, Schäffer HA. Wave transformation models with exact second-order transfer. European Journal of Mechanics - B/Fluids 2005;24:659–82. https://doi.org/10.1016/J.EUROMECHFLU.2005.05.001.

[135] Kaihatu JM, Kirby JT. Nonlinear transformation of waves in finite water depth. Physics of Fluids 1995;7:1903–14. https://doi.org/10.1063/1.868504.

[136] Madsen PA, Murray R, Sørensen OR. A new form of the Boussinesq equations with improved linear dispersion characteristics. Coastal Engineering 1991;15:371–88. https://doi.org/10.1016/0378-3839(91)90017-B.

[137] Madsen PA, Sørensen OR. A new form of the Boussinesq equations with improved linear dispersion characteristics. Part 2. A slowly-varying bathymetry. Coastal Engineering 1992;18:183–204. https://doi.org/10.1016/0378-3839(92)90019-Q.

[138] Madsen PA, Sørensen OR. Bound waves and triad interactions in shallow water. Ocean Engineering 1993;20:359–88. https://doi.org/10.1016/0029-8018(93)90002-Y.

[139] Freilich MH, Guza RT. Nonlinear effects on shoaling surface gravity waves. Philosophical Transactions of the Royal Society of London Series A, Mathematical and Physical Sciences 1984;311:1–41. https://doi.org/10.1098/RSTA.1984.0019.

[140] Variational methods and applications to water waves. Proc R Soc Lond A Math Phys Sci 1967;299:6–25. https://doi.org/10.1098/RSPA.1967.0119.

[141] Tsutsumi M, Mukasa T, Iino R. On the generalized Korteweg-deVries equation. Https://DoiOrg/103792/Pja/1195520159 1970;46:921–5. https://doi.org/10.3792/PJA/1195520159.

[142] Hur VM, Johnson MA. Modulational Instability in the Whitham Equation for Water Waves. Studies in Applied Mathematics 2015;134:120–43. https://doi.org/10.1111/SAPM.12061.

[143] Groesen E Van. Wave Groups in Uni-Directional Surface-Wave Models. Journal of Engineering Mathematics 1998 34:1 1998;34:215–26. https://doi.org/10.1023/A:1004355418313.

[144] Marsaleix P, Michaud H, Estournel C. 3D phase-resolved wave modelling with a non-hydrostatic ocean circulation model. Ocean Model (Oxf) 2019;136:28–50. https://doi.org/10.1016/J.OCEMOD.2019.02.002.

[145] Wamit, Inc. - The State of the Art in Wave Interaction Analysis n.d. https://www.wamit.com/manual.htm (accessed December 21, 2022).

[146] Babarit A, Delhommeau G, Kurnia R, Ducrozet G, Gilloteaux J-C. NEMOH-Presentation - LHEEA n.d. https://lheea.ec-nantes.fr/valorisation/logiciels-et-brevets/nemoh-presentation (accessed December 21, 2022).

[147] Crespo AJC, Hall M, Domínguez JM, Altomare C, Wu M, Verbrugghe T, et al. Floating Moored Oscillating Water Column With Meshless SPH Method. Proceedings of the International Conference on Offshore Mechanics and Arctic Engineering - OMAE 2018;11B. https://doi.org/10.1115/OMAE2018-77313.

[148] Devolder B, Stratigaki V, Troch P, Rauwoens P. CFD Simulations of Floating Point Absorber Wave Energy Converter Arrays Subjected to Regular Waves. Energies 2018, Vol 11, Page 641 2018;11:641. https://doi.org/10.3390/EN11030641.

[149] Finnegan W, Goggins J. Numerical simulation of linear water waves and wave–structure interaction. Ocean Engineering 2012;43:23–31. https://doi.org/10.1016/J.OCEANENG.2012.01.002.

[150] Stratigaki V, Troch P, Forehand D. A fundamental coupling methodology for modeling near-field and far-field wave effects of floating structures and wave energy devices. Renew Energy 2019;143:1608–27. https://doi.org/10.1016/J.RENENE.2019.05.046.

[151] Greenwood CE, Christie D, Venugopal V. The Simulation of Nearshore Wave Energy Converters and their Associated Impacts around the Outer Hebrides. 10th Eur. Wave Tidal Energy Conf. (EWTEC 2013) , 2003.

[152] Silverthorne KE, Folley M. A new numerical representation of wave energy converters in a spectral wave model. Proceedings of the 9th European Wave and Tidal Energy Conference (EWTEC), 2011.

[153] Gonzalez-Santamaria R, Zou QP, Pan S. Impacts of a Wave Farm on Waves, Currents and Coastal Morphology in South West England. Estuaries and Coasts 2013;38:159–72. https://doi.org/10.1007/S12237-013-9634-Z/FIGURES/15.

[154] Rodriguez-Delgado C, Bergillos RJ, Iglesias G. Dual wave farms and coastline dynamics: The role of inter-device spacing. Science of the Total Environment 2019;646:1241–52. https://doi.org/10.1016/J.SCITOTENV.2018.07.110.

[155] Veigas M, Ramos V, Iglesias G. A wave farm for an island: Detailed effects on the nearshore wave climate. Energy 2014;69:801–12. https://doi.org/10.1016/J.ENERGY.2014.03.076.

[156] Rusu E, Guedes Soares C. Coastal impact induced by a Pelamis wave farm operating in the Portuguese nearshore. Renew Energy 2013;58:34–49. https://doi.org/10.1016/J.RENENE.2013.03.001.

[157] Bergillos RJ, Rodriguez-Delgado C, Iglesias G. Wave farm impacts on coastal flooding under sea-level rise: A case study in southern Spain. Science of The Total Environment 2019;653:1522–31. https://doi.org/10.1016/J.SCITOTENV.2018.10.422.

[158] Gonzalez R, Zou Q, Pan S. MODELLING OF THE IMPACT OF A WAVE FARM ON NEARSHORE SEDIMENT TRANSPORT. Coastal Engineering Proceedings 2012;1:sediment.66. https://doi.org/10.9753/icce.v33.sediment.66.

[159] Özkan-Haller HT, Haller MC, Cameron McNatt J, Porter A, Lenee-Bluhm P. Analyses of wave scattering and absorption produced by WEC arrays: Physical/numerical experiments and model assessment. Marine Renewable Energy: Resource Characterization and Physical Effects 2017:71–97. https://doi.org/10.1007/978-3-319-53536-4_3/COVER.

[160] Bergillos R, Rodriguez-Delgado C, Iglesias G. Wave farm effects on coastal flooding under climate change. 2019.

[161] Alexandre A, Stallard T, Stansby PK. Transformation of Wave Spectra across a Line of Wave Devices n.d.

[162] Chang G, Ruehl K, Jones CA, Roberts J, Chartrand C. Numerical modeling of the effects of wave energy converter characteristics on nearshore wave conditions. Renew Energy 2016;89:636–48. https://doi.org/10.1016/J.RENENE.2015.12.048.

[163] O'dea AM, Haller MC. ANALYSIS OF THE IMPACTS OF WAVE ENERGY CONVERTER ARRAYS ON THE NEARSHORE WAVE CLIMATE. Marine Energy Technology Symposium 2014.

[164] Jones C, Chang G, Raghukumar K, McWilliams S, Dallman A, Roberts J. Spatial Environmental Assessment Tool (SEAT): A Modeling Tool to Evaluate Potential Environmental Risks Associated with Wave Energy Converter Deployments. Energies 2018, Vol 11, Page 2036 2018;11:2036. https://doi.org/10.3390/EN11082036.

[165] Venugopal V. Wave climate investigation for an array of wave power devices, 2014.

[166] Greenwood C, Christie D, Venugopal V, Morrison J, Vogler A. Modelling performance of a small array of Wave Energy Converters: Comparison of Spectral and Boussinesq models. Energy 2016;113:258–66. https://doi.org/10.1016/J.ENERGY.2016.06.141.

[167] Troch P, Beels C, De Rouck J, De Backer G. Wake effects behind a farm of wave energy converters for irregular long-crested and short-crested waves. 32nd International Conference on Coastal Engineering (ICCE-2010), ICCE 2010 Local Organizing committee; 2010.

[168] Beels C, Troch P, De Backer G, Vantorre M, De Rouck J. Numerical implementation and sensitivity analysis of a wave energy converter in a time-dependent mild-slope equation model. Coastal Engineering 2010;57:471–92. https://doi.org/10.1016/J.COASTALENG.2009.11.003.

[169] Beels C, Troch P, Kofoed JP, Frigaard P, Vindahl Kringelum J, Carsten Kromann P, et al. A methodology for production and cost assessment of a farm of wave energy converters. Renew Energy 2011;36:3402–16. https://doi.org/10.1016/J.RENENE.2011.05.019.

[170] Beels C, Troch P, De Visch K, Kofoed JP, De Backer G. Application of the time-dependent mild-slope equations for the simulation of wake effects in the lee of a farm of Wave Dragon wave energy converters. Renew Energy 2010;35:1644–61. https://doi.org/10.1016/J.RENENE.2009.12.001.

[171] Rijnsdorp DP, Hansen JE, Lowe RJ. Understanding coastal impacts by nearshore wave farms using a phase-resolving wave model. Renew Energy 2020;150:637–48. https://doi.org/10.1016/J.RENENE.2019.12.138.

[172] Rijnsdorp DP, Hansen JE, Lowe RJ. Simulating the wave-induced response of a submerged wave-energy converter using a non-hydrostatic wave-flow model. Coastal Engineering 2018;140:189–204. https://doi.org/10.1016/J.COASTALENG.2018.07.004.

[173] David DR, Rijnsdorp DP, Hansen JE, Lowe RJ, Buckley ML. Predicting coastal impacts by wave farms: A comparison of wave-averaged and wave-resolving models. Renew Energy 2022;183:764–80. https://doi.org/10.1016/J.RENENE.2021.11.048.

[174] Zhang R, Zijlema M, Stive MJF. Laboratory validation of SWASH longshore current modelling. Coastal Engineering 2018;142:95–105. https://doi.org/10.1016/J.COASTALENG.2018.10.005.

[175] Rijnsdorp DP, Smit PB, Zijlema M. Non-hydrostatic modelling of infragravity waves under laboratory conditions. Coastal Engineering 2014;85:30–42. https://doi.org/10.1016/J.COASTALENG.2013.11.011.

[176] Fiedler JW, Smit PB, Brodie KL, McNinch J, Guza RT. Numerical modeling of wave runup on steep and mildly sloping natural beaches. Coastal Engineering 2018;131:106–13. https://doi.org/10.1016/J.COASTALENG.2017.09.004.

[177] Buckley M, Lowe R, Hansen J. Evaluation of nearshore wave models in steep reef environments Topical Collection on the 7th International Conference on Coastal Dynamics in Arcachon, France 24-28 June 2013. Ocean Dyn 2014;64:847–62. https://doi.org/10.1007/S10236-014-0713-X/FIGURES/11.

[178] Jianyang L, Abdelkhalik O, Gauchia L. Optimization of dimensions and layout of an array of wave energy converters. Ocean Engineering 2019;192:106543. https://doi.org/10.1016/j.oceaneng.2019.106543.

[179] Göteman M. Wave energy parks with point-absorbers of different dimensions. J Fluids Struct 2017;74:142–57. https://doi.org/10.1016/j.jfluidstructs.2017.07.012.

[180] Korde UA, Ringwood J. Hydrodynamic Control of Wave Energy Devices. Cambridge University Press; 2016. https://doi.org/10.1017/cbo9781139942072.

[181] Snyder L V, Moarefdoost MM. LAYOUTS FOR OCEAN WAVE ENERGY FARMS: MODELS, PROPERTIES, AND HEURISTIC. Marine Energy Technology Symposium, 2014.

[182] Moarefdoost MM, Snyder L v, Alnajjab B. Layouts for ocean wave energy farms: Models, properties, and optimization. Omega (Westport) 2017;66:185–94. https://doi.org/10.1016/j.omega.2016.06.004.

[183] Thomas GP, Evans D V. Arrays of three-dimensional wave-energy absorbers. J Fluid Mech 1981;108:67–88. https://doi.org/DOI: 10.1017/S0022112081001997.

[184] Sharp C, DuPont B. Wave energy converter array optimization: A genetic algorithm approach and minimum separation distance study. Ocean Engineering 2018;163:148–56. https://doi.org/10.1016/j.oceaneng.2018.05.071.

[185] IEEE Computational Intelligence Society. What is Computational Intelligence? n.d. https://cis.ieee.org/about/what-is-ci (accessed January 5, 2022).

[186] Wang K. Computational Intelligence in Agile Manufacturing Engineering. Agile Manufacturing: The 21st Century Competitive Strategy 2001:297–315. https://doi.org/10.1016/B978-008043567-1/50016-4.

[187] Falnes J. Radiation impedance matrix and optimum power absorption for interacting oscillators in surface waves. Applied Ocean Research 1980;2:75–80. https://doi.org/https://doi.org/10.1016/0141-1187(80)90032-2.

[188] Evans D V. Some theoretical aspects of three-dimensional wave-energy absorbers. Proc. 1st Symp. Wave Energy Utilization, 1979, p. 78–112.

[189] Simon MJ. Multiple scattering in arrays of axisymmetric wave-energy devices. Part 1. A matrix method using a plane-wave approximation. J Fluid Mech 1982;120:1–25. https://doi.org/DOI: 10.1017/S002211208200264X.

[190] Göteman M, Giassi M, Engström J, Isberg J. Advances and Challenges in Wave Energy Park Optimization—A Review. Front Energy Res 2020;8. https://doi.org/10.3389/fenrg.2020.00026.

[191] Falnes J, Budal K. Wave-power absorption by parallel rows of interacting oscillating bodies. Applied Ocean Research 1982;4:194–207. https://doi.org/10.1016/s0141-1187(82)80026-6.

[192] Sarkar D, Contal E, Vayatis N, Dias F. Prediction and optimization of wave energy converter arrays using a machine learning approach. Renew Energy 2016;97:504–17. https://doi.org/10.1016/j.renene.2016.05.083.

[193] Ohkusu M. Hydrodynamic forces on multiple cylinders in waves. International Symposium on Dynamics of Marine Vehicles and Structures in Waves, London: 1974, p. 107–12.

[194] Fitzgerald C, Thomas G. A preliminary study on the optimal formation of an array of wave power devices. Proceedings of the 7th European Wave and Tidal Energy Conference, Porto, Portugal: 2007, p. 11–4.

[195] Child BFM, Venugopal V. Modification of power characteristics in an array of floating wave energy devices. Proceedings of the 8th European Wave and Tidal Energy Conference, Uppsala, Sweden: 2009, p. 309–18.

[196] Borgarino B, Babarit A, Ferrant P. Impact of wave interactions effects on energy absorption in large arrays of wave energy converters. Ocean Engineering 2012;41:79–88. https://doi.org/10.1016/j.oceaneng.2011.12.025.

[197] Child BFM, Venugopal V. Optimal configurations of wave energy device arrays. Ocean Engineering 2010;37:1402–17. https://doi.org/10.1016/j.oceaneng.2010.06.010.

[198] Göteman M, Engström J, Eriksson M, Isberg J, Leijon M. Methods of reducing power fluctuations in wave energy parks. Journal of Renewable and Sustainable Energy 2014;6:043103. https://doi.org/10.1063/1.4889880.

[199] Göteman M, Engström J, Eriksson M, Isberg J. Optimizing wave energy parks with over 1000 interacting point-absorbers using an approximate analytical method. International Journal of Marine Energy 2015;10:113–26. https://doi.org/10.1016/j.ijome.2015.02.001.

[200] Göteman M, Engström J, Eriksson M, Isberg J. Fast Modeling of Large Wave Energy Farms Using Interaction Distance Cut-Off. Energies (Basel) 2015;8:13741–57. https://doi.org/10.3390/en81212394.

[201] McGuinness J, Thomas G. Optimal Arrangements of Elementary Arrays of Wave-Power Devices. 2015.

[202] McGuinness J, Thomas G. Optimisation of wave-power arrays without prescribed geometry over incident wave angle. International Marine Energy Journal 2021;4:1–10. https://doi.org/10.36688/imej.4.1-10.

[203] Cuadra L, Salcedo-Sanz S, Nieto-Borge JC, Alexandre E, Rodríguez G. Computational intelligence in wave energy: Comprehensive review and case study. Renewable and Sustainable Energy Reviews 2016;58:1223–46. https://doi.org/10.1016/j.rser.2015.12.253.

[204] Madiajagan M, Raj SS. Parallel Computing, Graphics Processing Unit (GPU) and New Hardware for Deep Learning in Computational Intelligence Research. Deep Learning and Parallel Computing Environment for Bioengineering Systems 2019:1–15. https://doi.org/10.1016/B978-0-12-816718-2.00008-7.

[205] Bishop CM. Pattern Recognition and Machine Learning. 1st ed. Springer New York; 2006. https://doi.org/10.1007/978-0-387-45528-0.

[206] Shalev-Shwartz S, Ben-David S. Understanding machine learning: From theory to algorithms. Understanding Machine Learning: From Theory to Algorithms 2013;9781107057135:1–397. https://doi.org/10.1017/CBO9781107298019.

[207] GUPTA MM, SINHA NK. Toward Intelligent Systems: Future Perspectives. Soft Computing and Intelligent Systems, Academic Press; 2000, p. 611–20. https://doi.org/10.1016/B978-012646490-0/50028-7.

[208] Kayacan E, Khanesar MA. Fuzzy Neural Networks for Real Time Control Applications: Concepts, Modeling and Algorithms for Fast Learning. Elsevier Inc.; 2015. https://doi.org/10.1016/C2014-0-02444-6.

[209] DTOceanPlus project. DTOceanPlus - Design tools for ocean energy systems n.d. https://www.dtoceanplus.eu/ (accessed January 5, 2022).

[210] Trompoukis XS, Asouti VG, Kampolis IC, Giannakoglou KC. CUDA Implementation of Vertex-Centered, Finite Volume CFD Methods on Unstructured Grids with Flow Control Applications. GPU Computing Gems Jade Edition, Morgan Kaufmann; 2012, p. 207–23. https://doi.org/10.1016/B978-0-12-385963-1.00017-4.

[211] Eiben AE, Smith JE. Introduction to Evolutionary Computing. 2nd ed. Berlin, Heidelberg: Springer Berlin Heidelberg; 2015. https://doi.org/10.1007/978-3-662-44874-8.

[212] Conzalez-Rodriguez AG, Serrano-Conzalez J, Riquelme-Santos JM, Burgos-Payán M, Castro-Mora J, Persan SA. Global Optimization of Wind Farms Using Evolutive Algorithms. Wind Power Systems, 2010, p. 53–104. https://doi.org/10.1007/978-3-642-13250-6_3.

[213] Kubat M. An introduction to machine learning. 2nd ed. Springer International Publishing; 2015. https://doi.org/10.1007/978-3-319-20010-1.

[214] Blanco M, Moreno-Torres P, Lafoz M, Ramírez D. Design Parameters Analysis of Point Absorber WEC via an evolutionary-algorithm-based Dimensioning Tool. Energies (Basel) 2015;8:11203–33. https://doi.org/10.3390/en81011203.

[215] Blanco M, Lafoz M, Ramirez D, Navarro G, Torres J, Garcia-Tabares L. Dimensioning of Point Absorbers for Wave Energy Conversion by Means of Differential Evolutionary Algorithms. IEEE Trans Sustain Energy 2019;10:1076–85. https://doi.org/10.1109/tste.2018.2860462.

[216] Sharp C, DuPont B. A multi-objective real-coded genetic algorithm method for wave energy converter array optimization. International Conference on Offshore Mechanics and Arctic Engineering, vol. 49972, American Society of Mechanical Engineers; 2016, p. V006T09A027.

[217] Giassi M, Göteman M. Parameter optimization in wave energy design by a genetic algorithm. 32nd International Workshop on Water Waves and Floating Bodies (IWWWFB), 23-26th April, 2017, Dalian, China., 2017.

[218] Wu J, Shekh S, Sergiienko NY, Cazzolato BS, Ding B, Neumann F, et al. Fast and effective optimisation of arrays of submerged wave energy converters. Proceedings of the Genetic and Evolutionary Computation Conference 2016, 2016, p. 1045–52.

[219] Ruiz P, Nava V, Topper M, Minguela P, Ferri F, Kofoed J. Layout Optimisation of Wave Energy Converter Arrays. Energies (Basel) 2017;10:1262. https://doi.org/10.3390/en10091262.

[220] Ferri F. Computationally efficient optimisation algorithms for wecs arrays. 12th European Wave and Tidal Energy Conferenc, Technical Committee of the European Wave and Tidal Energy Conference; 2017, p. 798.

[221] Giassi M, Göteman M, Thomas S, Engström J, Eriksson M, Isberg J. Multi-parameter optimization of hybrid arrays of point absorber wave energy converters. 12th European Wave and Tidal Energy Conference (EWTEC), Cork, Ireland, August 27-31, 2017., 2017.

[222] Fang H-W, Feng Y-Z, Li G-P. Optimization of Wave Energy Converter Arrays by an Improved Differential Evolution Algorithm. Energies (Basel) 2018;11:3522. https://doi.org/10.3390/en11123522.

[223] Neshat M, Alexander B, Wagner M, Xia Y. A detailed comparison of meta-heuristic methods for optimising wave energy converter placements. Proceedings of the Genetic and Evolutionary Computation Conference, 2018, p. 1318–25.

[224] Neshat M, Abbasnejad E, Shi Q, Alexander B, Wagner M. Adaptive neuro-surrogate-based optimisation method for wave energy converters placement optimisation. International Conference on Neural Information Processing, Springer; 2019, p. 353–66.

[225] Vatchavayi SR. Heuristic Optimization of Wave Energy Converter Arrays. Master. University of Minnesota, 2019.

[226] Faraggiana E, Masters I, Chapman J. Design of an optimization scheme for the wavesub array. In: Soares CG, editor. Advances in Renewable Energies Offshore - Proceedings of the 3rd International Conference on Renewable Energies Offshore, RENEW 2018, CRC Press/Balkema; 2019, p. 633–8.

[227] Neshat M, Alexander B, Sergiienko NY, Wagner M. Optimisation of large wave farms using a multi-strategy evolutionary framework. Proceedings of the 2020 Genetic and Evolutionary Computation Conference, 2020, p. 1150–8.

[228] Neshat M, Alexander B, Wagner M. A hybrid cooperative co-evolution algorithm framework for optimising power take off and placements of wave energy converters. Inf Sci (N Y) 2020;534:218–44. https://doi.org/10.1016/j.ins.2020.03.112.

[229] Yang B, Wu S, Zhang H, Liu B, Shu H, Shan J, et al. Wave energy converter array layout optimization: A critical and comprehensive overview. Renewable and Sustainable Energy Reviews 2022;167:112668. https://doi.org/10.1016/J.RSER.2022.112668.

[230] Folley M, Babarit A, Child B, Forehand D, O'boyle L, Silverthorne K, et al. A review of numerical modelling of wave energy converter arrays A review of numerical modelling of wave energy converter arrays A REVIEW OF NUMERICAL MODELLING OF WAVE ENERGY CONVERTER ARRAYS 2012. https://doi.org/10.1115/OMAE2012.

[231] Child BFM, Venugopal V. Optimal configurations of wave energy device arrays. Ocean Engineering 2010;37:1402–17. https://doi.org/10.1016/j.oceaneng.2010.06.010.

[232] Göteman M, Engström J, Eriksson M, Isberg J. Fast Modeling of Large Wave Energy Farms Using Interaction Distance Cut-Off. Energies (Basel) 2015;8:13741–57. https://doi.org/10.3390/en81212394.

[233] Bozzi S, Giassi M, Moreno Miquel A, Antonini A, Bizzozero F, Gruosso G, et al. Wave energy farm design in real wave climates: the Italian offshore. Energy 2017;122:378–89. https://doi.org/10.1016/j.energy.2017.01.094.

[234] Sarkar D, Contal E, Vayatis N, Dias F. Prediction and optimization of wave energy converter arrays using a machine learning approach. Renew Energy 2016;97:504–17. https://doi.org/10.1016/j.renene.2016.05.083.

[235] Wolgamot HA, Taylor PH, Eatock Taylor R. The interaction factor and directionality in wave energy arrays. Ocean Engineering 2012;47:65–73. https://doi.org/10.1016/j.oceaneng.2012.03.017.

[236] Vicente M, Alves M, Sarmento A. Layout optimization of wave energy point absorbers arrays. 10th European Wave and Tidal Energy Conference Series, Aalborg, Denmark, 2013.

[237] Moarefdoost MM, Snyder L V, Alnajjab B. Layouts for ocean wave energy farms: Models, properties, and optimization. Omega (Westport) 2017;66:185–94. https://doi.org/10.1016/j.omega.2016.06.004.

[238] Neshat M, Alexander B, Wagner M. A hybrid cooperative co-evolution algorithm framework for optimising power take off and placements of wave energy converters. Inf Sci (N Y) 2020;534:218–44. https://doi.org/10.1016/j.ins.2020.03.112.

[239] Neshat M, Mirjalili S, Sergiienko NY, Esmaeilzadeh S, Amini E, Heydari A, et al. Layout optimisation of offshore wave energy converters using a novel multi-swarm cooperative algorithm with backtracking strategy: A case study from coasts of Australia. Energy 2022;239:122463. https://doi.org/10.1016/J.ENERGY.2021.122463.

[240] Izquierdo-Pérez J, Brentan BM, Izquierdo J, Clausen N-E, Pegalajar-Jurado A, Ebsen N. Layout Optimization Process to Minimize the Cost of Energy of an Offshore Floating Hybrid Wind–Wave Farm. Processes 2020;8:139. https://doi.org/10.3390/pr8020139.

[241] Golbaz D, Asadi R, Amini E, Mehdipour H, Nasiri M, Etaati B, et al. Layout and design optimization of ocean wave energy converters: A scoping review of state-of-the-art canonical, hybrid, cooperative, and combinatorial optimization methods. Energy Reports 2022;8:15446–79. https://doi.org/10.1016/J.EGYR.2022.10.403.

[242] Roberts JD, Chang G, Magalen J, Jones C. Wave Energy Converter Effects on Wave Fields: Evaluation of SNL-SWAN and Sensitivity Studies in Monterey Bay CA. 2014. https://doi.org/10.2172/1156934.

[243] Ris RC, Holthuijsen LH, Booij N. A third-generation wave model for coastal regions 2. Verification. J Geophys Res Oceans 1999;104:7667–81. https://doi.org/10.1029/1998jc900123.

[244] Miles JW. On the generation of surface waves by shear flows. J Fluid Mech 1957;3:185–204. https://doi.org/10.1017/S0022112057000567.

[245] Janssen PAEM. Quasi-linear Theory of Wind-Wave Generation Applied to Wave Forecasting. Journal of Physical Oceanography 1991:1631–42. https://doi.org/https://doi.org/10.1175/1520-0485(1991)021<1631:QLTOWW>2.0.CO;2.

[246] Beji S, Battjes JA. Experimental investigation of wave propagation over a bar. Coastal Engineering 1993;19:151–62. https://doi.org/10.1016/0378-3839(93)90022-Z.

[247] Hasselmann S, Hasselmann K. Computations and parameterizations of the nonlinear energy transfer in a gravity-wave spectrum. Part I: a new method for efficient computations of the exact nonlinear transfer integral. J PHYS OCEANOGR 1985;15:1369–77. https://doi.org/10.1175/1520-0485(1985)015<1369:capotn>2.0.co;2.

[248] Collins JI. Prediction of shallow-water spectra. J Geophys Res 1972;77:2693–707. https://doi.org/10.1029/JC077I015P02693.

[249] Madsen OS, Poon YK, Graber HC. SPECTRAL WAVE ATTENUATION BY BOTTOM FRICTION: THEORY. Coastal Engineering Proceedings 1988;1:34. https://doi.org/10.9753/icce.v21.34.

[250] Holthuijsen LH, Herman A, Booij N. Phase-decoupled refraction–diffraction for spectral wave models. Coastal Engineering 2003;49:291–305. https://doi.org/10.1016/S0378-3839(03)00065-6.

[251] Majidi AG, Ramos V, Giannini G, Rosa Santos P, das Neves L, Taveira-Pinto F. The impact of climate change on the wave energy resource potential of the Atlantic Coast of Iberian Peninsula. Ocean Engineering 2023;284:115451. https://doi.org/10.1016/J.OCEANENG.2023.115451.

[252] Ramos V, Ringwood J V. Exploring the utility and effectiveness of the IEC (International Electrotechnical Commission) wave energy resource assessment and characterisation standard: A case study. Energy 2016;107:668–82. https://doi.org/10.1016/J.ENERGY.2016.04.053.

[253] Akpınar A, Bingölbali B, Van Vledder GP. Long-term analysis of wave power potential in the Black Sea, based on 31-year SWAN simulations. Ocean Engineering 2017;130:482–97. https://doi.org/10.1016/J.OCEANENG.2016.12.023.

[254] Rusu E, Silva D, Guedes Soares C. Evaluation of the shoreline dynamics in a coastal sector of the Portuguese nearshore, 2016, p. 1080–6.

[255] Bento AR, Rusu E, Martinho P, Soares CG. Assessment of the changes induced by a wave energy farm in the nearshore wave conditions. Comput Geosci 2014;71:50–61. https://doi.org/10.1016/J.CAGEO.2014.03.006.

[256] Iglesias G, Carballo R. Wave farm impact: The role of farm-to-coast distance. Renew Energy 2014;69:375–85. https://doi.org/10.1016/J.RENENE.2014.03.059.

[257] SWAN team. USER MANUAL SWAN Cycle III version 41.45AB 2024. https://swanmodel.sourceforge.io/online_doc/swanuse/swanuse.html (accessed August 22, 2024).

[258] SWAN team. SCIENTIFIC AND TECHNICAL DOCUMENTATION SWAN Cycle III version 41.45AB 2024. https://swanmodel.sourceforge.io/online_doc/swantech/swantech.html (accessed August 22, 2024).

[259] SNL-SWAN/bin at master · SNL-WaterPower/SNL-SWAN · GitHub n.d. https://github.com/SNL-WaterPower/SNL-SWAN/tree/master/bin (accessed January 18, 2023).

[260] Deltares. QUICKIN - Generation and manipulation of grid-related parame- ters such as bathymetry, initial conditions and rough- ness: User Manual, Hydro-Morphodynamics & Water Quality. 2024.

[261] Deltares. Delft3D-WAVE - Simulation of short-crested waves with SWAN - User Manual - Hydro-Morphodynamics. 2024.

[262] Camus P, Mendez FJ, Medina R, Cofiño AS. Analysis of clustering and selection algorithms for the study of multivariate wave climate. Coastal Engineering 2011;58:453–62. https://doi.org/10.1016/J.COASTALENG.2011.02.003.

[263] Hegermiller CA, Antolinez JAA, Rueda A, Camus P, Perez J, Erikson LH, et al. A Multimodal Wave Spectrum–Based Approach for Statistical Downscaling of Local Wave Climate. J Phys Oceanogr 2017;47:375–86. https://doi.org/10.1175/JPO-D-16-0191.1.

[264] Draycott S, Davey T, Ingram D, Lawrence J, Day A, Johanning L. Applying site specific resource assessment: Methodologies for replicating real seas in the FLOWAVE facility 2014.

[265] Draycott ST. On the re-creation of site-specific directional wave conditions 2017. https://doi.org/10.1016/J.COASTALENG.

[266] Hamilton LJ. Characterising spectral sea wave conditions with statistical clustering of actual spectra. Applied Ocean Research 2010;32:332–42. https://doi.org/10.1016/J.APOR.2009.12.003.

[267] Wang D, Jin S, Hann M, Conley D, Collins K, Greaves D. Power output estimation of a two-body hinged raft wave energy converter using HF radar measured representative sea states at Wave Hub in the UK. Renew Energy 2023;202:103–15. https://doi.org/10.1016/J.RENENE.2022.11.048.

[268] Eymold WK, Flanary C, Erikson L, Nederhoff K, Chartrand CC, Jones C, et al. Typological representation of the offshore oceanographic environment along the Alaskan North Slope. Cont Shelf Res 2022;244:104795. https://doi.org/10.1016/J.CSR.2022.104795.

[269] Romano-Moreno E, Diaz-Hernandez G, Tomás A, Lara JL. Multivariate assessment of port operability and downtime based on the wave-induced response of moored ships at berths. Ocean Engineering 2023;283:115053. https://doi.org/10.1016/J.OCEANENG.2023.115053.

[270] Romano-Moreno E, Diaz-Hernandez G, Tomás A, Lara JL. Multimodal harbor wave climate characterization based on wave agitation spectral types. Coastal Engineering 2023;180:104271. https://doi.org/10.1016/J.COASTALENG.2022.104271.

[271] Pedregosa FABIANPEDREGOSA F, Michel V, Grisel OLIVIERGRISEL O, Blondel M, Prettenhofer P, Weiss R, et al. Scikit-learn: Machine Learning in Python. Journal of Machine Learning Research 2011;12:2825–30.

[272] Clemente D, Teixeira-Duarte F, Rosa-Santos P, Taveira-Pinto F. Advancements on Optimization Algorithms Applied to Wave Energy Assessment: An Overview on Wave Climate and Energy Resource. Energies 2023, Vol 16, Page 4660 2023;16:4660. https://doi.org/10.3390/EN16124660.

[273] Direção-Geral de Recusos Naturais S e SM (DGRM). TUPEM nº 1/2015. 2015.

[274] Instituto Hidrográfico. Avisos aos Navegantes, aviso 245/22. 2022.

[275] Rosa-Santos P, Taveira-Pinto F, Rodríguez CA, Ramos V, López M. The CECO wave energy converter: Recent developments. Renew Energy 2019;139:368–84. https://doi.org/10.1016/J.RENENE.2019.02.081.

[276] Rosa-Santos P, Taveira-Pinto F, Teixeira L, Ribeiro J. CECO wave energy converter: Experimental proof of concept. Journal of Renewable and Sustainable Energy 2015;7:061704. https://doi.org/10.1063/1.4938179.

[277] Giannini G, Rosa-Santos P, Ramos V, Taveira-Pinto F. On the Development of an Offshore Version of the CECO Wave Energy Converter. Energies 2020, Vol 13, Page 1036 2020;13:1036. https://doi.org/10.3390/EN13051036.

[278] López M, Taveira-Pinto F, Rosa-Santos P. Numerical modelling of the CECO wave energy converter. Renew Energy 2017;113:202–10. https://doi.org/10.1016/J.RENENE.2017.05.066.

[279] Rosa-Santos P, Taveira-Pinto F, Pinho-Ribeiro J, Teixeira L, Marinheiro J. Harnessing the kinetic and potential wave energy: Design and development of a new wave energy converter. Renewable Energies Offshore 2015:367–74.

[280] Ramos V, López M, Taveira-Pinto F, Rosa-Santos P. Performance assessment of the CECO wave energy converter: Water depth influence. Renew Energy 2018;117:341–56. https://doi.org/10.1016/J.RENENE.2017.10.064.

[281] Rodríguez CA, Rosa-Santos P, Taveira-Pinto F. Assessment of damping coefficients of power take-off systems of wave energy converters: A hybrid approach. Energy 2019;169:1022–38. https://doi.org/10.1016/J.ENERGY.2018.12.081.

[282] López M, Ramos V, Rosa-Santos P, Taveira-Pinto F. Effects of the PTO inclination on the performance of the CECO wave energy converter. Marine Structures 2018;61:452–66. https://doi.org/10.1016/J.MARSTRUC.2018.06.016.

[283] Ramos V, Giannini G, Calheiros-Cabral T, López M, Rosa-Santos P, Taveira-Pinto F. Assessing the Effectiveness of a Novel WEC Concept as a Co-Located Solution for Offshore Wind Farms. Journal of Marine Science and Engineering 2022, Vol 10, Page 267 2022;10:267. https://doi.org/10.3390/JMSE10020267.

[284] Taveira-Pinto F, Rosa-Santos P, das Neves L, Ramos JV, Henriques R, Taveira-Printo FVC. Estudo de Caracterização de Riscos e Programa de Intervenção para a Proteção da Restinga de Ofir e Barra do Cávado. Esposende, Potugal: 2021.

[285] PROGRAMA DA ORLA COSTEIRA CAMINHA-ESPINHO RELATÓRIO DO PROGRAMA n.d.

[286] Inundações (Diretiva 2007/60/CE) - Portugal Continental e R.A. Açores - 2º Ciclo | SNIAmb n.d. https://sniamb.apambiente.pt/content/diretiva60ce2007-2%25C2%25BA-ciclo?language=pt-pt (accessed December 18, 2024).

[287] Geoportal do Mar Português n.d. https://webgis.dgrm.mm.gov.pt/portal/apps/webappviewer/index.html?id=df8accb510bc4f33963d9b03bf3674b8 (accessed December 18, 2024).

[288] Aleixo Pinto C, Penacho N, Pires B. PROGRAMA DE MONITORIZAÇÃO DA FAIXA COSTEIRA DE PORTUGAL CONTINENTAL (COSMO): DA CONCEPÇÃO À IMPLEMENTAÇÃO | Portuguese Coastal Monitoring Program (COSMO): From design to implementation. 2021.

[289] Clemente D, Ramos V, Teixeira-Duarte F, Taveira-Pinto FVC, Rosa-Santos P, Taveira-Pinto F. Assessment of electricity production and coastal protection of a nearshore 500 MW wave farm in the north-western Portuguese coast. Appl Energy 2025;379:124950. https://doi.org/10.1016/J.APENERGY.2024.124950.

[290] de Santiago I, Liria P, Garnier R, Bald J, Leitão J, Ribeiro J. DELIVERABLE 3.3 Marine Dynamic Modelling. 2023. https://doi.org/10.13140/RG.2.2.36716.74886.

[291] Hidrografico Mais n.d. https://geomar.hidrografico.pt/ (accessed December 19, 2024).

[292] Rede Nacional de Áreas Protegidas (RNAP) — divgmwebgis.ipma.pt n.d. https://divgmwebgis.ipma.pt/layers/geonode:RNAP (accessed December 19, 2024).

[293] Editais - TUPEM - DGRM n.d. https://www.dgrm.pt/consulta-pblica (accessed December 19, 2024).

[294] HiWave-5 | Wave Power. To Power the Planet n.d. https://www.hiwave-5.eu/ (accessed December 20, 2024).

[295] WaveRoller - AW-Energy n.d. https://aw-energy.com/waveroller/ (accessed December 19, 2024).

[296] Renewable Energy Agency I. Ocean Energy: Technologies, Patents, Deployment Status and Outlook 2014.

[297] Arguilé-Pérez B, Ribeiro AS, Costoya X, deCastro M, Gómez-Gesteira M. Suitability of wave energy converters in northwestern Spain under the near future winter wave climate. Energy 2023;278:127957. https://doi.org/10.1016/J.ENERGY.2023.127957.

[298] Babarit A, Hals J, Muliawan MJ, Kurniawan A, Moan T, Krokstad J. Numerical benchmarking study of a selection of wave energy converters. Renew Energy 2012;41:44–63. https://doi.org/10.1016/J.RENENE.2011.10.002.

[299] Fanti V, Jacob J, Pacheco A, Fortes CJEM, Didier E. Effects of varying the transmission coefficient in SNL-SWAN for a wave farm in Peniche. Developments in Renewable Energies Offshore - Proceedings the 4th International Conference on Renewable Energies Offshore, RENEW 2020 2021:11–8. https://doi.org/10.1201/9781003134572-2/EFFECTS-VARYING-TRANSMISSION-COEFFICIENT-SNL-SWAN-WAVE-FARM-PENICHE-FANTI-JACOB-PACHECO-FORTES-DIDIER.

[300] Fanti V. Application of snl-swan model on the effect of wave farms in the wave propagation. 2019.

[301] CorPower Ocean - Wave Power. To Power the Planet. n.d. https://corpowerocean.com/ (accessed December 20, 2024).

[302] Hersbach H, Bell B, Berrisford P, Hirahara S, Horányi A, Muñoz-Sabater J, et al. The ERA5 global reanalysis. Quarterly Journal of the Royal Meteorological Society 2020;146:1999–2049. https://doi.org/10.1002/QJ.3803.

[303] Cameron McNatt JC, Porter A, Ruehl K. Comparison of Numerical Methods for Modeling the Wave Field Effects Generated by Individual Wave Energy Converters and Multiple Converter Wave Farms. Journal of Marine Science and Engineering 2020, Vol 8, Page 168 2020;8:168. https://doi.org/10.3390/JMSE8030168.

[304] Cameron Mcnatt J, Porter A, Chartrand C, Roberts J. The Performance of a Spectral Wave Model at Predicting Wave Farm Impacts. Energies 2020, Vol 13, Page 5728 2020;13:5728. https://doi.org/10.3390/EN13215728.

[305] Blanco MI. The economics of wind energy. Renewable and Sustainable Energy Reviews 2009;13:1372–82. https://doi.org/10.1016/J.RSER.2008.09.004.

[306] Nielsen JJ, Sørensen JD. On risk-based operation and maintenance of offshore wind turbine components. Reliab Eng Syst Saf 2011;96:218–29. https://doi.org/10.1016/J.RESS.2010.07.007.

[307] Van Bussel GJW, Bierbooms WAAM. Analysis of different means of transport in the operation and maintenance strategy for the reference DOWEC offshore wind farm n.d.

[308] Lee UJ, Jeong WM, Cho HY. Estimation and Analysis of JONSWAP Spectrum Parameter Using Observed Data around Korean Coast. Journal of Marine Science and Engineering 2022, Vol 10, Page 578 2022;10:578. https://doi.org/10.3390/JMSE10050578.

[309] Bretschneider CL. REVISIONS IN WAVE FORECASTING: DEEP AND SHALLOW WATER. Coastal Engineering Proceedings 1957;1:3. https://doi.org/10.9753/icce.v6.3.

[310] Sverdrup HU, Munk WH. Empirical and theoretical relations between wind, sea, and swell. Eos, Transactions American Geophysical Union 1946;27:823–7. https://doi.org/10.1029/TR027I006P00823.

[311] Wilson BW. Numerical prediction of ocean waves in the North Atlantic for December, 1959. Deutsche Hydrographische Zeitschrift 1965;18:114–30. https://doi.org/10.1007/BF02333333/METRICS.

[312] Suh KD, Kwon HD, Lee DY. Some statistical characteristics of large deepwater waves around the Korean Peninsula. Coastal Engineering 2010;57:375–84. https://doi.org/10.1016/J.COASTALENG.2009.10.016.

[313] Goda Y. Revisiting Wilsons Formulas for Simplified Wind-Wave Prediction. J Waterw Port Coast Ocean Eng 2003;129:93–5. https://doi.org/10.1061/(ASCE)0733-950X(2003)129:2(93).

[314] Suh KD, Kwon HD, Lee DY. Some statistical characteristics of large deepwater waves around the Korean Peninsula. Coastal Engineering 2010;57:375–84. https://doi.org/10.1016/J.COASTALENG.2009.10.016.

[315] United States. Army. Corps of Engineers CERC (U. S). Shore protection manual. vol. Volume I. 4th ed. 1984.

[316] Ocean surface wave time series for the European coast from 1976 to 2100 derived from climate projections n.d. https://cds.climate.copernicus.eu/datasets/sis-ocean-wave-timeseries?tab=overview (accessed January 7, 2025).

[317] Product user guide for sea level and ocean wave products - time series and indicators - Copernicus Knowledge Base - ECMWF Confluence Wiki n.d. https://confluence.ecmwf.int/display/CKB/Product+user+guide+for+sea+level+and+ocean+wave+products+-+time+series+and+indicators (accessed January 7, 2025).